

NASA Contractor Report 191428

1N-34
150325
P.230

Shock Tunnel Studies for Scramjet Phenomena, Supplement 6

M. Wendt, M. Nettleton, R. G. Morgan, K. Skinner,
R. Casey, R. Stalker, C. Brescianini, A. Paull,
G. Allen, M. Smart, N. Akman, N. Ward, S. Tuttle,
J. Simmons, S. Sanderson, G. Kelly, A. Neely,
and R. Krek

*University of Queensland
St. Lucia, Queensland, Australia*

Grant NAGW-674
February 1993

(NASA-CR-191428) SHOCK TUNNEL
STUDIES OF SCRAMJET PHENOMENA,
SUPPLEMENT 6 (Queensland Univ.)
230 p

N93-22817

Unclass

G3/34 0150325



National Aeronautics and
Space Administration

Langley Research Center
Hampton, Virginia 23681-0001

Report on Shock Tunnel Studies of Scramjet Phenomena
NASA Grant NAGW 674 - Supplement 6, 1990

As in previous reports, this consists of a series of reports on specific project areas, with a brief general introduction commenting on each report. The introduction is structured by project areas, with the title of the relevant report stated under the project area heading. The reports themselves follow in the order of the project area headings.

The commentary begins with a brief statement of the program of work planned for 1990.

PLANNED PROGRAM FOR 1990

Hypersonic Combustion

Perform initial experiments with hot hydrogen injection, beginning with injection through a central strut, and then proceeding to injection through wall orifices.

Analysis of early results from scaling studies. Compare data obtained in T4 with data obtained in the GASL expansion tube ("Hypulse") in order to explore the effects of frozen oxygen dissociation in the free stream.

Perform initial experiments with a mass spectrometer.

Continue studies of combustion wake structure, using pitot pressure and stagnation point heat transfer traverses.

Continue basic studies of hypersonic combustion, exploiting the new found high pressure capability of the shock tunnel.

Wave Effects

Continue numerical and optical studies of two-dimensional Busemann scramjet configurations.

Surface Heating

Measure heat transfer on a flat plate with a turbulent boundary layer. If possible, combine with skin friction measurements.

Drag and Thrust Production

Employ the "S³" drag balance to measure the drag on a slender cone.

Facility Studies - Expansion Tube

Continue measurements of test section pitot pressure and static pressure, together with measurements of flat plate surface heat transfer. Attempt to determine the degree of frozen dissociation in the test flow.

SCRAMJET STUDIES

Effects of Fuel Injection Parameters in Supersonic Combustion with a Transverse Circular Wall Jet

M. Wendt

Combustion experiments were conducted at a nominal Mach of 4 with hydrogen fuel in a 25x50 mm rectangular duct. A circular orifice wall injector was used, with the centreline of the orifice angled at 30° to the flow direction. The injection orifice was centred on one of the 50 mm walls.

Tests were conducted at stagnation enthalpies of 6, 7 and 10.5 MJ/Kg, and the hydrogen was heated to temperatures of approximately 800 K before injection by using a gun tunnel compression heating rig. These temperatures were checked approximately by monitoring the fuel drainage time from the hot hydrogen reservoir created by operation of the gun tunnel.

The results were compared with those obtained with unheated hydrogen, and indicated that the pressure distributions obtained in the duct were not sensitive to the initial temperature of the hydrogen fuel. Further experiments on simpler configurations are planned in order to further test this conclusion.

Scaling Laws for Measurements in Experimental Scramjet Facilities

M.A. Nettleton

Some physical considerations regarding scaling indicate that simple concepts involving premixed chemical kinetics and Reynold's number effects may not be adequate to describe scaling effects.

Scramjet Testing - Ground Facility Comparisons

R.G. Morgan

Identical models of a scramjet combustor were tested in T4 and in "Hypulse". The model consisted of a duct of circular cross section with injection of hydrogen fuel parallel to the wall. Under comparable test conditions, it was found that the higher

level of free stream dissociation of oxygen in T4 produced the expected higher combustion pressure increment. It was possible to approximately compensate for this effect by reducing the total oxygen content of the test gas in T4.

A Mass Spectrometer for Hypersonic Combustion Studies

K. Skinner

Initial tests of the mass spectrometer in the shock tunnel have been unsuccessful. Subsequent tests of the skimmer system in a shock tube have shown that it is working satisfactorily. Attention is now focussed on the operation of the flight tube.

Supersonic and Hypersonic Hydrogen Mixing and Combustion

R.T. Casey and R.J. Stalker

Studies have been conducted of a nominally two dimensional wake downstream of a transverse in stream injection strut with hydrogen injection into nitrogen and air in two ducts, one 25x50 mm, and the other, 50x50 mm. Near wake studies were conducted mainly in the 25x50 mm duct, and they indicated that the wake was not self similar, in that the rate of growth of the width of the wake did not accord with the rate of change, with downstream distance, of the centreline properties. The rate of growth of the wake could be explained by using incompressible wake data, combined with a convective Mach number effect.

In the far wake (i.e. greater than approximately 35 initial wake widths downstream of the strut trailing edge) the results indicated that self similarity was observed, and the rate of growth of the wake could be explained directly by using incompressible wake data.

A Brief Overview of Wall Injected Scramjet Experiments

C.P. Brescianini

Following previous studies of mixing enhancement with a wall jet, further attempts were made to improve mixing with different mixer configurations. These were not successful.

Numerical Modelling of Sidewall Injected Scramjet Experiments in a High Enthalpy Airflow

C.P. Brescianini, R.G. Morgan and R.J. Stalker

This numerical study of hydrogen injection parallel to the wall of a scramjet was conducted in order to explore reasons for the poor combustion characteristics of such wall jets. The numerical model is not fully predictive, in that constants in the model were adjusted to match heat transfer distributions on the surface downstream of injection. With the use of these constants, the model indicated that the presence of

the wall severely inhibited mixing between the fuel and the air, and that this was responsible for the limited combustion effects observed.

Mach 5 Constant Area Duct Tests

A. Paull

In previous experiments on combustion in constant area ducts, it has usually been necessary to accept substantial irregularities in the pressure distribution along the duct in the absence of fuel injection. These irregularities limit the accuracies of results obtained in the duct. Bearing in mind the desirability of producing data which could be used for code validation, a series of tests was conducted in order to "clean up" the flow before fuel injection tests were initiated. As may be seen from the report, this proved to be more difficult than anticipated.

Parametric Study on Thrust Production in the Two Dimensional Scramjet

G.A. Allen

The thrust production mechanism in a two dimensional thrust nozzle is compounded of the compression waves generated by injection and combustion of the fuel, and by the interaction between the expansion generated by the turning of the surface to form the thrust nozzle and the combustion wake. This is a numerical study, employing the method of characteristics, of the latter phenomenon, for a nozzle with a sharp corner angle.

The study showed that the maximum pressure on the thrust surface reached a peak at an angle close to the value at which maximum thrust per unit length would be expected from a given thrust generating wave. As the surface thrust angle increased further, the thrust also increased, but was distributed over a greater length of surface.

The Glancing Interaction of a Prandtl-Meyer Expansion Fan with a Supersonic Wake

M.K. Smart and R.J. Stalker

Whilst the previous project is a study of thrust generation from a combustion wake interaction with an expansion wave propagating across the wake, this project considers an expansion wave propagating in the plane of the wake. An approximate analysis is presented, and is confirmed by comparison with experiments on the interaction of an expansion fan with the boundary layer on the sidewall of a blowdown wind tunnel.

A Study of Contoured Hypersonic Scramjets

N. Akman and R.J. Stalker

Wave drag effects in scramjets can be studied by extending the concept of the Busemann biplane to incorporate a "Busemann Scramjet". Previous work has involved a small perturbation analysis of this concept, followed by a numerical

analysis applied to cases where flow deflection within the scramjet are too large for a linearized analysis to be effective. This numerical analysis is here extended to take account of the case when the thrust nozzle is contoured, in order to produce the theoretically ideal case of an outlet flow which is parallel to the free stream and eliminates any wave spillage from the system. It is found that the thrust nozzle contouring has a significant effect, reducing the drag of the duct not only at the design Mach number, but also over a wide range of off design Mach numbers.

Shock Induced Heat Release - An Optical Study

N. Ward

This can be seen as an idealised study of scramjet operation with shock induced combustion following fuel-air-mixing in the intake. In this study, an ideal premixed flow is simulated by using the "frozen" free stream in the test section of a shock tunnel with nitrogen test gas. The study involves flow visualisation through use of a differential interferometer, and the report covers progress in bringing the interferometer into operation.

Drag and Thrust Measurement Techniques for Free Piston Shock Tunnels

S.L. Tuttle and J.M. Simmons

A Drag Measurement Technique for Free Piston Shock Tunnels

S.R. Sanderson, J.M. Simmons and S.L. Tuttle

The use of stress waves in a bar to measure drag on models in the shock tunnel (the "S³" force balance) has been successfully applied for cones of 15° and 5° semi-vertex angles respectively. For the 15° cone, force measurements could be obtained within 0.5 millisecon of flow initiation in the shock tunnel, and for the 5° cone (which was 3 x longer than the 15° cone) measurements could be obtained within 0.8 millisecon.

Progress Report on Development and Application of a Skin Friction Gauge

G. Kelly

This project has yielded a working skin friction gauge which has been used to measure the skin friction on a flat plate in a small shock tunnel. The rise time of the gauge is less than 50μsec. Measurements of laminar skin friction have shown satisfactory agreement with predictions.

FACILITY STUDIES - EXPANSION TUBE

High Enthalpy, Hypervelocity Flows of Air and Argon in an Expansion Tube

A. Neely, R.J. Stalker and A. Paull

Experiments were performed with a pilot expansion tube, choosing test conditions which generated flows at medium stagnation enthalpies (approx. 9 MJ/Kg) and at high stagnation enthalpies (approx. 44 MJ/Kg). These conditions were regarded as the limit of likely expansion tube operating conditions in the near future, and were obtained with Argon and Helium driven gas respectively

The theory outlined in the project which follows this one indicates that stagnation enthalpies between these two limits can be obtained simply by changing the mix of Argon and Helium in the driven gas. This theory also indicates that flow disturbances in the test flow can be suppressed by expanding the driven gas to Mach numbers of approximately 4.

This rule was followed in these experiments, and using test section measurements of ~~pitot~~ pressure, static pressure and flat plate heat transfer, it was shown that flows of a quality which is acceptable for aerodynamic testing could be obtained.

Test Flow Disturbances in an Expansion Tube

A. Paull and R.J. Stalker

The test flow disturbances which have limited the utility of expansion tubes in the past are examined theoretically, taking the view that they originate as transverse acoustic waves in the driven gas. The theory succeed in predicting the occurrence and the approximate frequency of fluctuations in the ~~pitot~~ pressure which are observed at large test gas expansion ratios, identifying these as arising from frequency focussing across the expansion. This effect is associated only with transverse acoustic waves, and does not occur with longitudinal waves.

The theory also predicted that the penetration of transverse acoustic waves from the driver, into the test gas, would be inhibited as the ratio of driver gas Mach number to test gas Mach number was increased above a certain critical value. In the case of a driver gas with ratio of specific heats of 5/3, and air test gas, this occurred when the

driver gas Mach number was approximately 4. This effect also was confirmed by experiment.

TEST FACILITIES - REFLECTED SHOCK TUNNEL

Leeward Heat Transfer Comparison Between T4 Data and STS-3 Data

R.M. Krek and R.J. Stalker

The utility of wind tunnel facilities depends, to a very large extent, on their ability to predict flight data. This applies as much to shock tunnels as to other wind tunnels. For high enthalpy wind tunnels, such as T4, the opportunity to test their predictive capability is limited, because of the limited number of vehicles which have flown at hypervelocities. For this reason, the availability of data from the NASA Shuttle Orbiter provided a particularly strong incentive to conduct tests on a Shuttle Orbiter model in T4.

The tests were focussed particularly on heat transfer on the leeward fuselage midplane, since this occurs in a region of extensive flow separation. Not only is this flow difficult to predict theoretically and numerically, but it provides a particularly rigorous test of the flow simulation capability of a short flow duration facility, such as T4.

It was found that flight and shock tunnel results were consistent for both laminar and turbulent leeward surface flows.

**EFFECT OF FUEL INJECTION PARAMETERS ON SUPERSONIC
COMBUSTION WITH A TRANSVERSE CIRCULAR WALL JET**

**Michael Wendt (Mechanical Engineering Department)
The University of Queensland**

LIST OF SYMBOLS

h_6, h_7, h_{10}	---- High speed fuel runs of 6,7 & 10.5 MJ/kg
c_6, c_7, c_{10}	---- As above for low speed
H_{air}	---- High speed injection into air
C_{air}	---- Low speed injection into air
H_{off}	---- Air only run (high speed runs series)
C_{off}	---- Air only run (low speed run series)
HN_2	---- High speed injection into nitrogen
CN_2	---- Low speed injection into nitrogen
H_s	---- Free stream total enthalpy
γ	---- Ratio of specific heats
ϕ	---- Equivalence Ratio
ρ_a	---- Density of air or nitrogen
ρ_f	---- Density of fuel
U_a	---- Velocity of air or nitrogen
U_f	---- Velocity of fuel
AF	---- Tunnel run with air and fuel
NF	---- Tunnel run with nitrogen and fuel
AO	---- Tunnel run with air only

1.0 INTRODUCTION

The favored configuration for fuel injection into a supersonic combustion ramjet is to use a circular wall injector angled at 30° to the flow direction (Ref 1). The injector is centered on the the longer side of a 2*1 cell (Fig 1). The suggestion is that with this configuration, counter-rotating vortices form, giving mixing on all scales. The fuel jet is angled at 30° rather than perpendicular or steeper angles because; i) almost all of its momentum contributes to the thrust, ii) the heat transfer at reattachment behind the jet is less severe , and iii) because the shock formed ahead of the jet is weaker, hence minimizing the stagnation pressure losses in duct.

This configuration was tested at the University of Queensland at three different flight speeds and with two different fuel speeds to ascertain the effect on mixing and combustion.

2.0 APPARATUS

Hypervelocity air and nitrogen flow was produced using the University of Queensland's, free piston reflected shock tunnel (Ref 2). The stagnation region at the end of the shock tunnel is expanded through a Mach 4 contoured nozzle. A section of the expanded flow is fed into the constant area combustion duct. The layout of the supersonic combustion duct is shown in figure 2. It basically comprises of a 25 * 50mm rectangular duct 650mm long. A single circular wall injector angled a 30° to the flow is mounted in the middle of a 50mm wall. Piezoelectric pressure transducers were mounted along the centreline of the top and bottom of the duct. Injection was from the bottom surface.

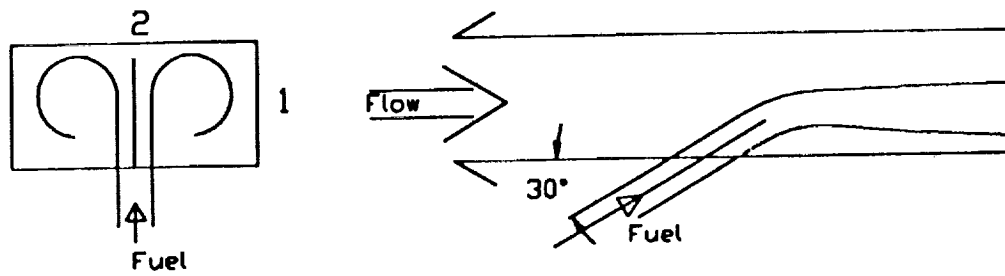


Figure 1 - Wall Injector Configuration

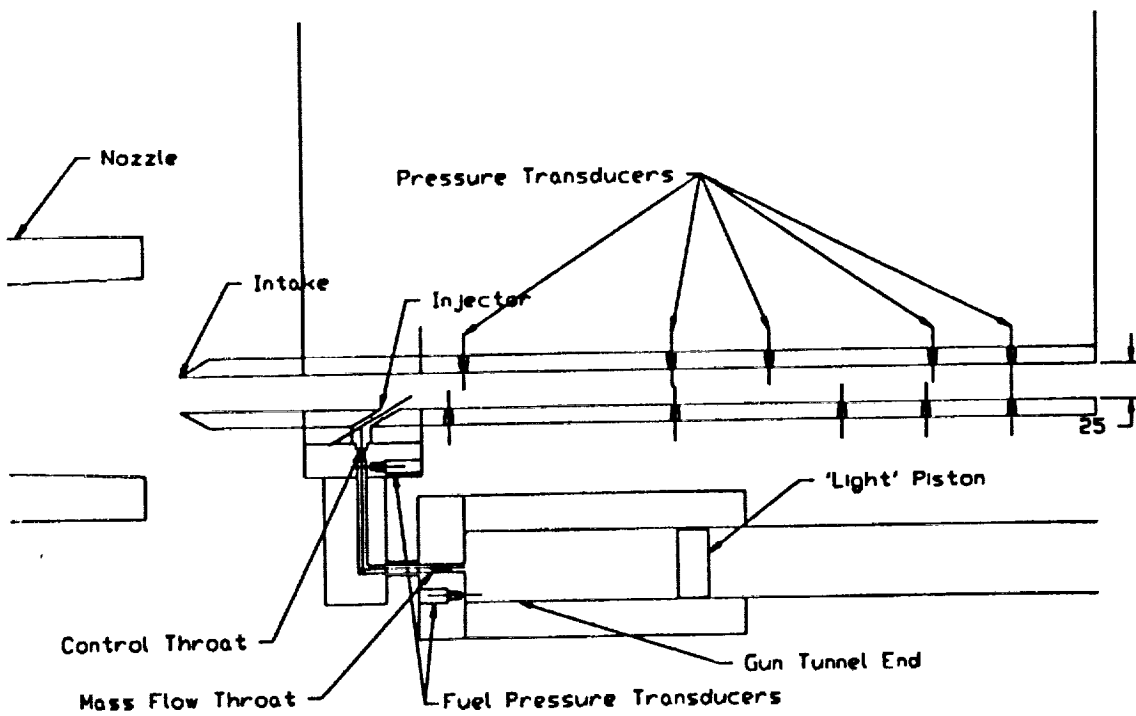


Figure 2 - Layout of Combustion Duct

Low speed fuel was provided by a room temperature Ludwig tube reservoir with a fast acting valve (ref3). The fuel flows from the Ludwig Tube through the valve and is choked at the wall injector. The injector is a constant diameter 7mm hole, 14mm long which is angled at 30° to the surface. A typical pressure versus time trace is shown in figure 3. These runs were performed by Dr R. Morgan and Mr R. Casey.

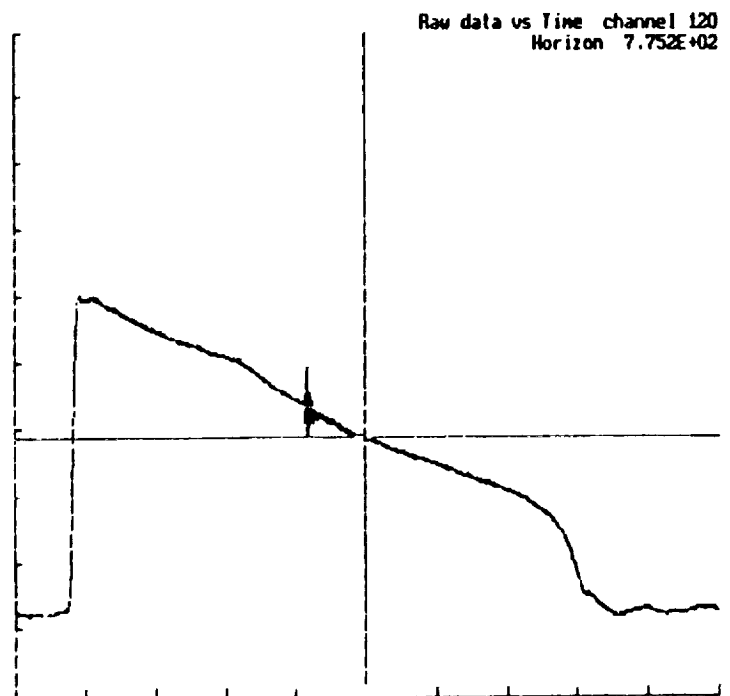


Figure 3 - Low Speed Fuel Line Pressure

To speed up the fuel, it was heated to a stagnation temperature of 900K using a gun tunnel. The layout of the experiment with the gun tunnel in place is shown in figure 4. Hydrogen is compressed in the high pressure end by a 'light' piston. A throat of 3.8 mm in diameter is placed at the exit of the high pressure end and the gas is fed through a 250mm long, 6mm dia. filling line to the 7mm injector used for the low speed experiments. Another throat of 4.5 mm is placed just before the injector to stop unsteady expansion down the filling line. A typical gun tunnel pressure trace is shown in figure 5 and filling line pressure trace in figure 6.

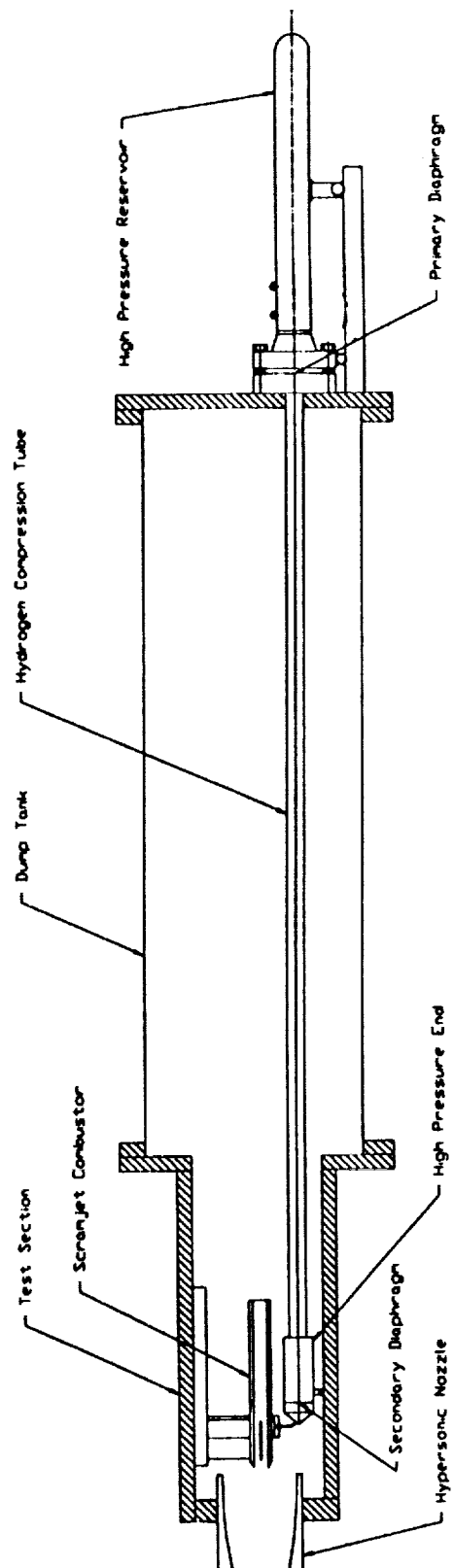


Figure 4 - Layout of Experiment with Gun Tunnel

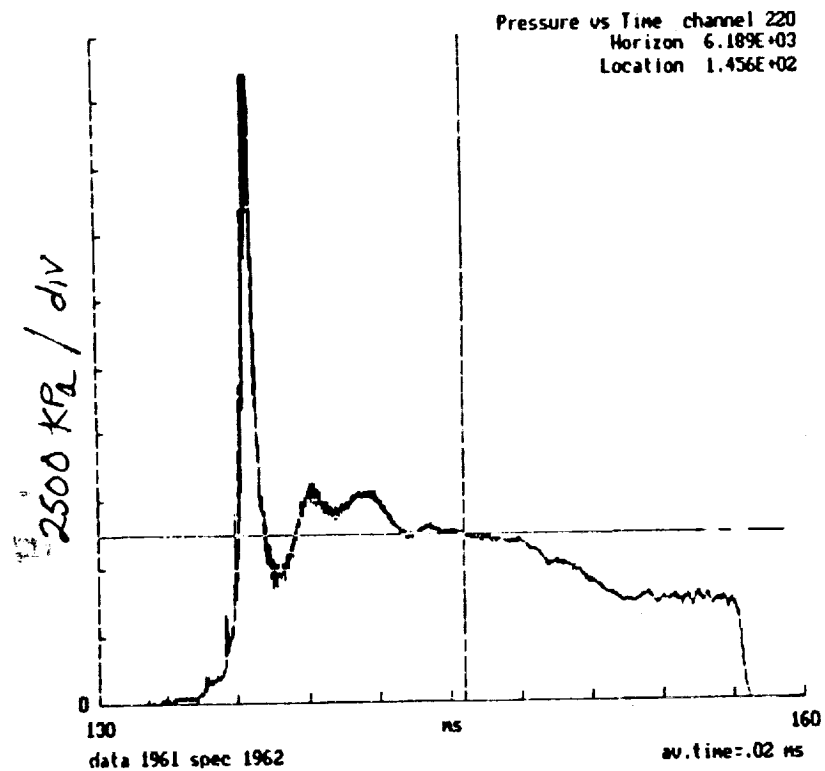


Figure 5 - Gun Tunnel Stagnation Pressure Trace

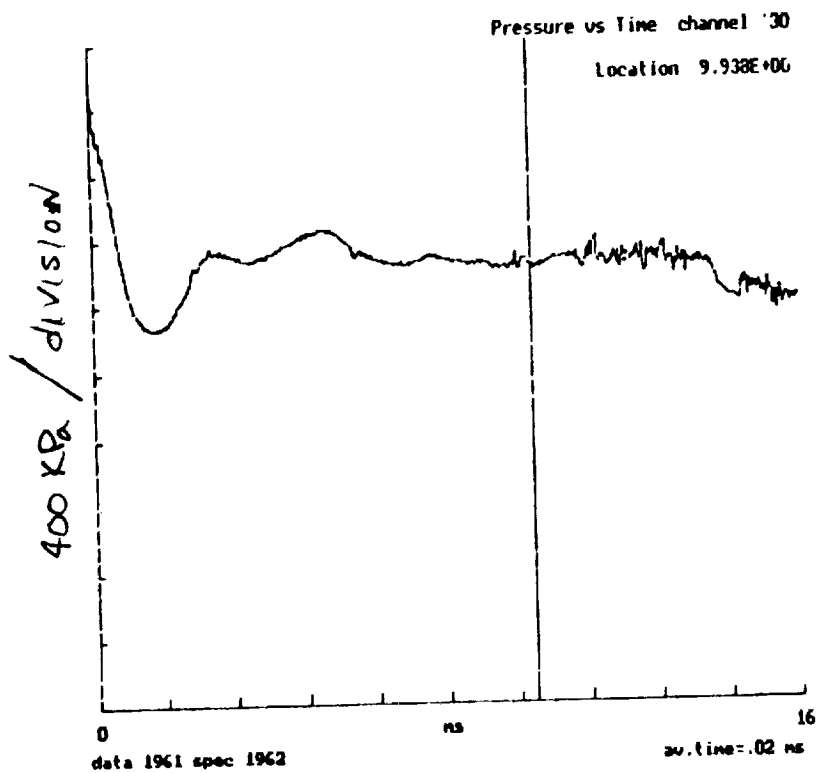


Figure 6 - Gun Tunnel Filling Line Pressure

3.0 RESULTS

The averaged free stream conditions produced by the tunnel before entry into the combustor duct at 'Steady Time' are shown below in Table 1. Steady time is taken at 1.3 millisecs after the beginning of the flow to allow time for the nozzle starting processes. These values were calculated from Dr Morgans 1-D nozzle program 'SHOCK'.

Table 1- Free Stream Conditions

Flight Speed (m/s)	Hs (Mj/kg)	Static Pressure (Kpa)	Static Temp. (K)	Velocity (m/s)	Mach #	Density (kg/m ³)	γ
3500	6	57.7	1171	3077	4.53	.166	1.33
4300	7	56.5	1382	3310	4.51	.137	1.32
5300	10.5	56.3	2090	4016	4.48	.091	1.3

The conditions in the duct were calculated from Mr C. Brescianini's program 'VELCAL'. This program takes the free stream conditions (Table 1) and calculates the stagnation conditions. It then takes these values and the measured fuel stagnation conditions and expands them isentropically into the duct until they reach a common static pressure. Heat loss in the piping and jet angle are not taken into account. A run manifest is shown in Table 2.

Due to variability between shots, each pressure trace is divided by the stagnation pressure trace at the corresponding point in time(i.e. 1.3 millisecs after the start of each trace). A typical pressure vs time trace from a piezoelectric transducer is shown in figure 7. A pressure trace from the shock tunnel stagnation region that supplies the nozzle is shown in figure 8. The 'steady' time is shown as a vertical line in each of these figures.

Table 2 - Run Manifest

Run #	Hs (Mj/kg)	Test Gas	ϕ	Ps (kPa)	Ua (m/s)	Ur (m/s)	ρ_a (kg/m ³)	ρ_f (kg/m ³)	Ua/Ur	ρ_a/ρ_f
1380	6	Air	0	57.7	3077	--	.166	--	---	----
1966	6	Air	0	57.7	3077	--	.166	--	--	--
1381	6	Air	1	62.6	3077	2150	.166	.1	1.43	1.66
1964	6	Air	1.5	65.2	3077	4375	.166	.064	.7	2.93
1382	6	N ₂	1	62.6	3077	2150	.166	.1	1.43	1.66
1965	6	N ₂	1.15	63.6	3077	4210	.166	.063	.73	2.93
1957	7	Air	0	56.5	3310	--	.137	---	-----	-----
1959	7	Air	0	56.5	3310	---	.137	----	---	---
1383	7	Air	1	63	3249	2070	.154	.14	1.57	1.08
1961	7	Air	1.54	60.4	3249	4370	.154	.061	.74	2.53
1962	7	N ₂	.887	63.5	3352	3874	.151	.063	.87	2.4
1384	10.5	Air	1	57	4050	1990	.096	.127	2.04	.75
1960	10.5	Air	1.8	60.4	3958	4310	.1	.06	.92	1.65
1963	10.5	N ₂	1.46	63.5	4045	4131	.102	.063	.98	1.61

Figures 9-14 show the normalized pressure data versus distance. It should be noted that the injector (or bottom) surface pressure increases from the middle of the figure to the bottom. The top surface increases in pressure from the middle of the figure to the top.

Figures 9-11 show the difference in pressure between the air with fuel(AF), nitrogen with fuel(NF) and air only(AO) shots for each flight speed. The difference between low and high speed fuel is also shown on this plot.

Figures 12-14 show the effect of flight and fuel speed for the AF,NF and AO shots respectively.

Figures 15-17 show the AF,NF and AO pressure traces divided against each other. Figure 15 gives the percentage increase of pressure due to the presence of oxygen. Figure 16 plots the difference in pressure due to the presence of the fuel jet. Figure 17 shows the total difference in pressure due to the presence of the fuel jet and oxygen.

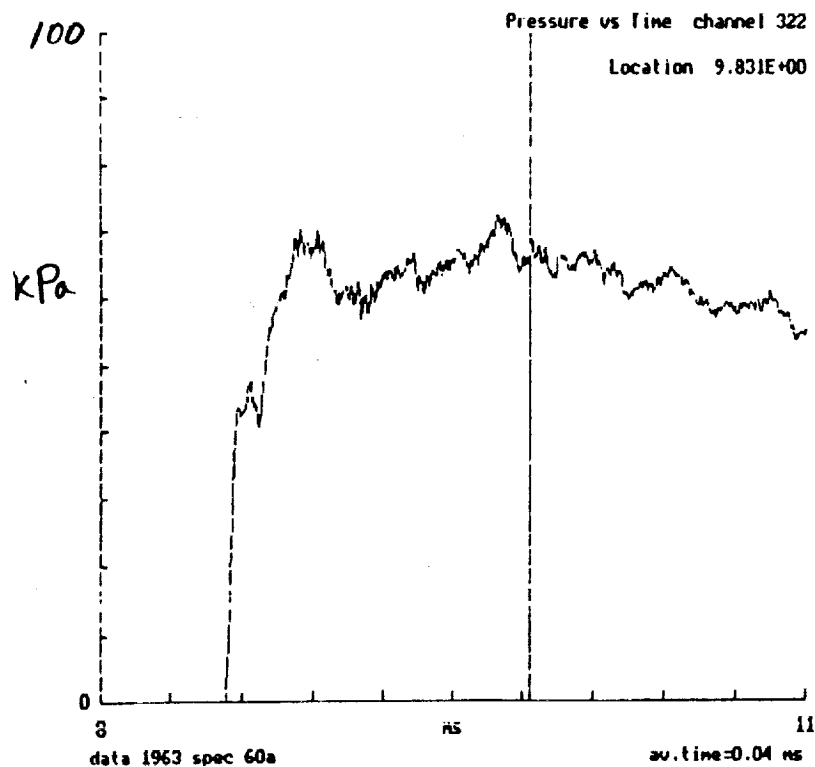


Figure 7 - Static Duct Pressure versus Time

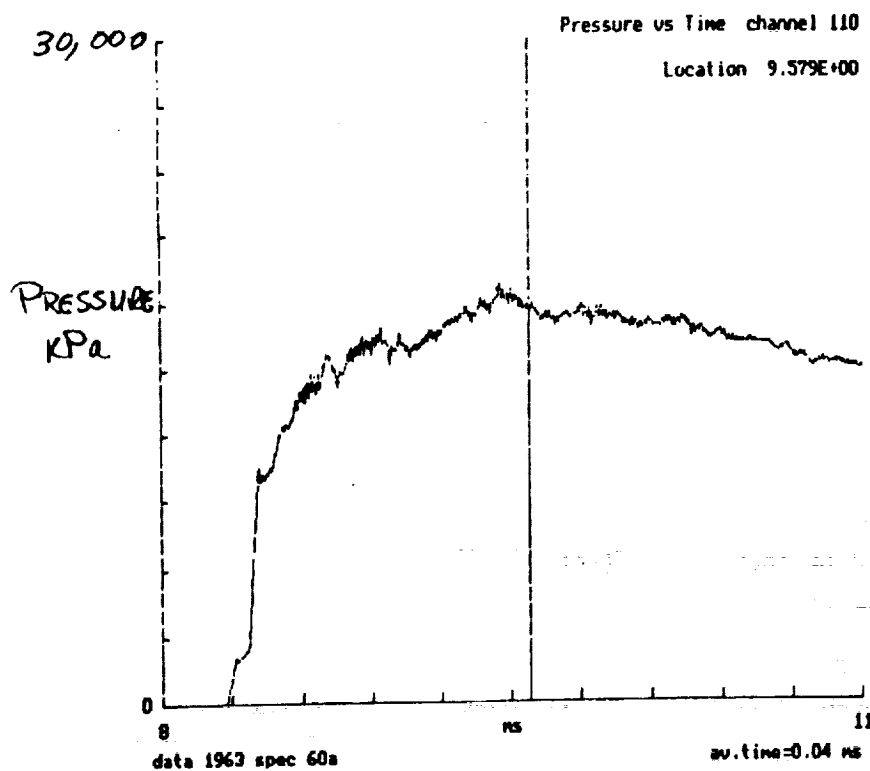


Figure 8 - Stagnation Region Pressure versus Time

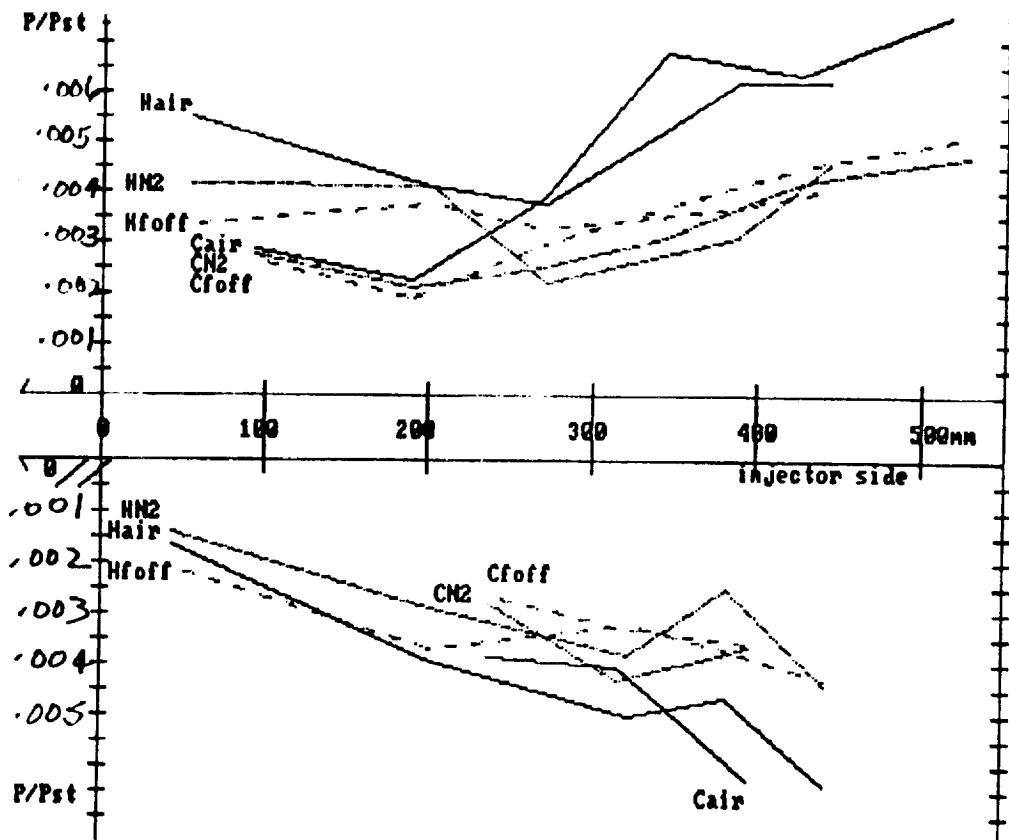


Figure 9 - Normalized Pressure vs Distance 6 MJ/kg

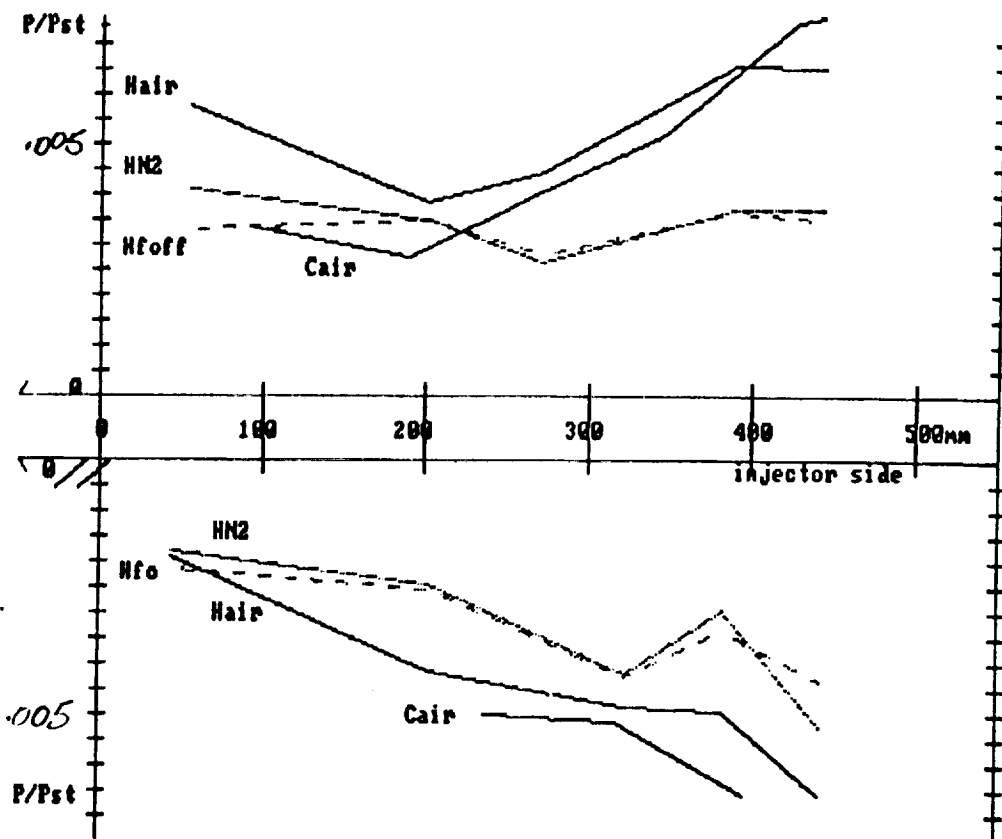


Figure 10 - Normalized Pressure vs Distance 7 MJ/kg

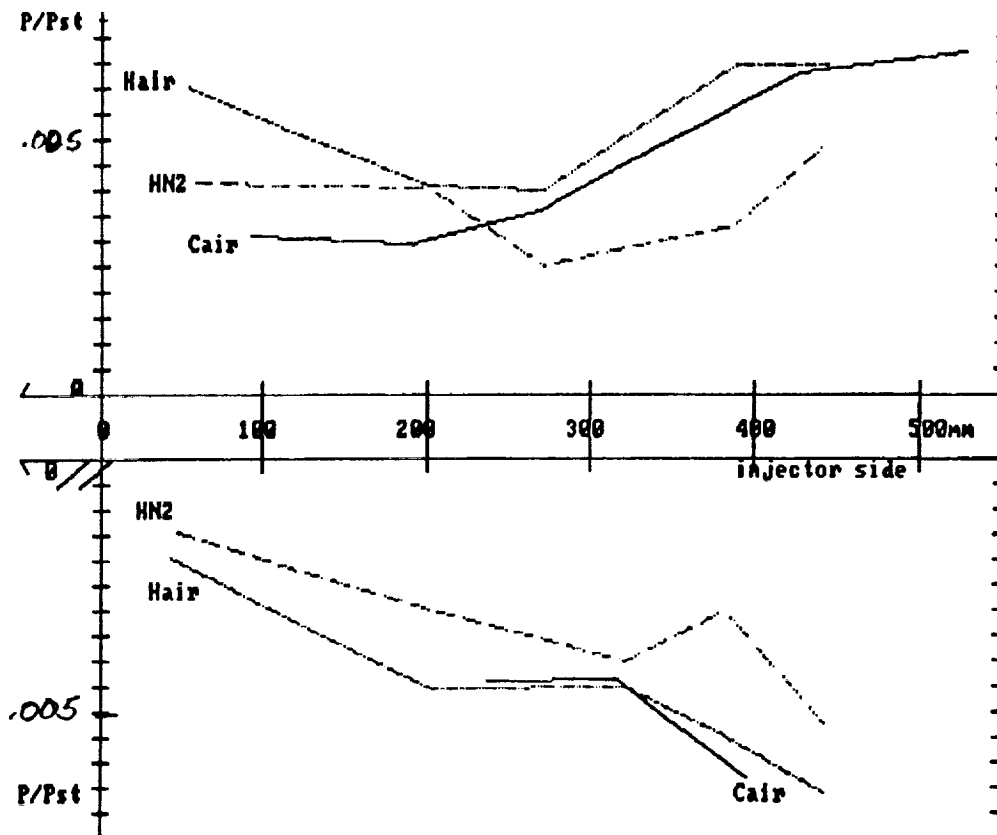


Figure 11 - Pressure vs Distance 10.5 MJ/kg

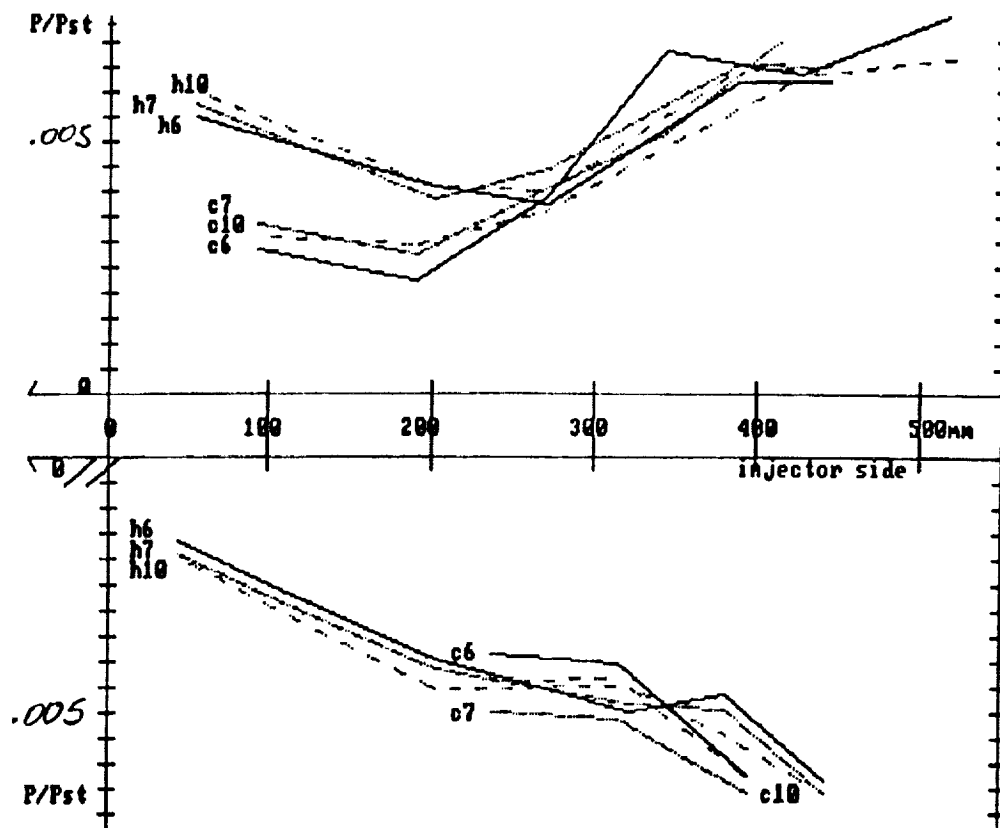


Figure 12 - Fuel into Air vs Distance after Injector

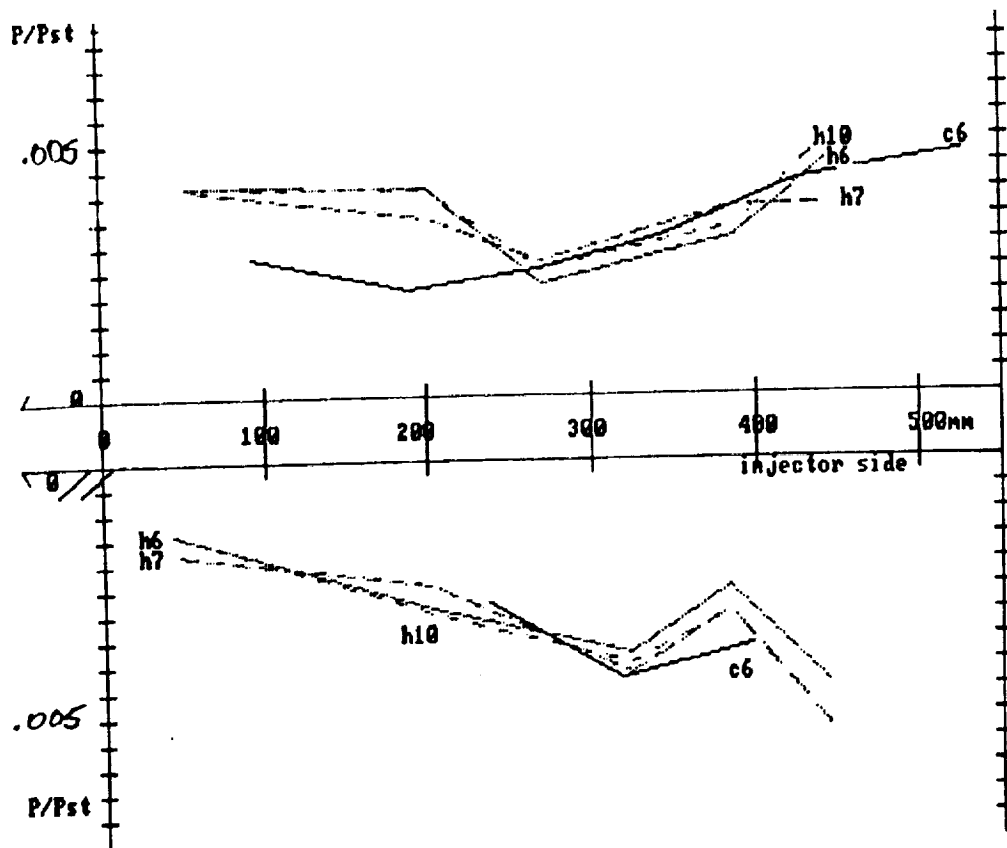


Figure 13 - Fuel into Nitrogen vs Distance after Injector

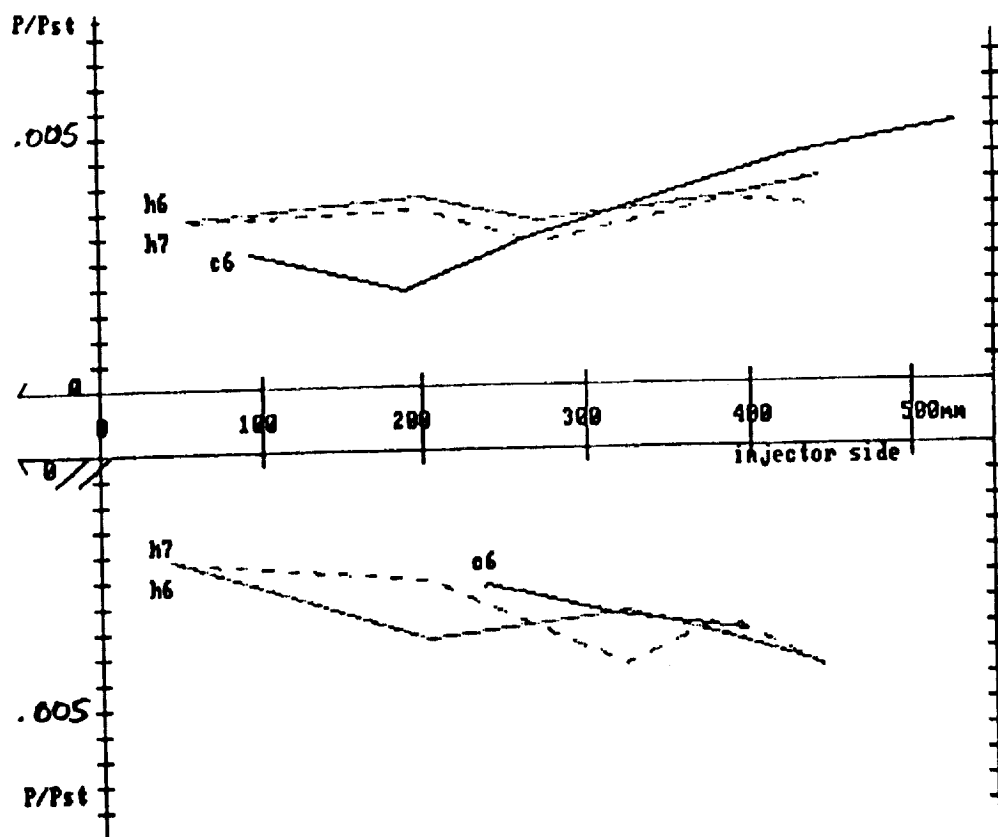


Figure 14 - Air Only vs Distance after Injector

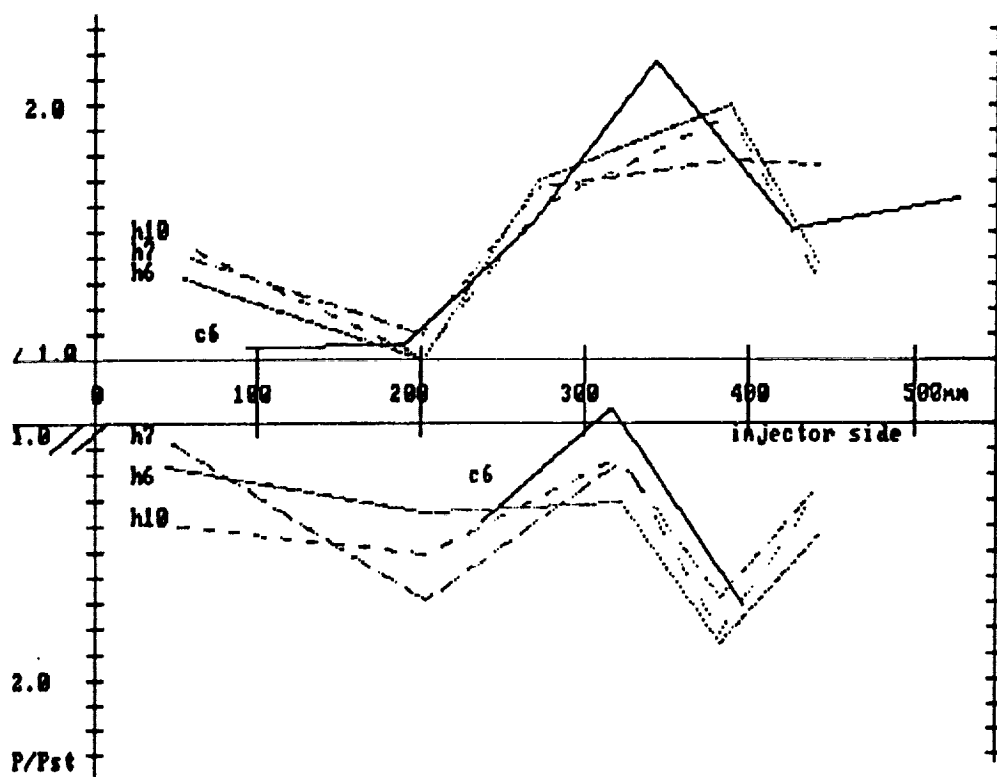


Figure 15 - Air with Fuel/Nitrogen with Air vs Distance

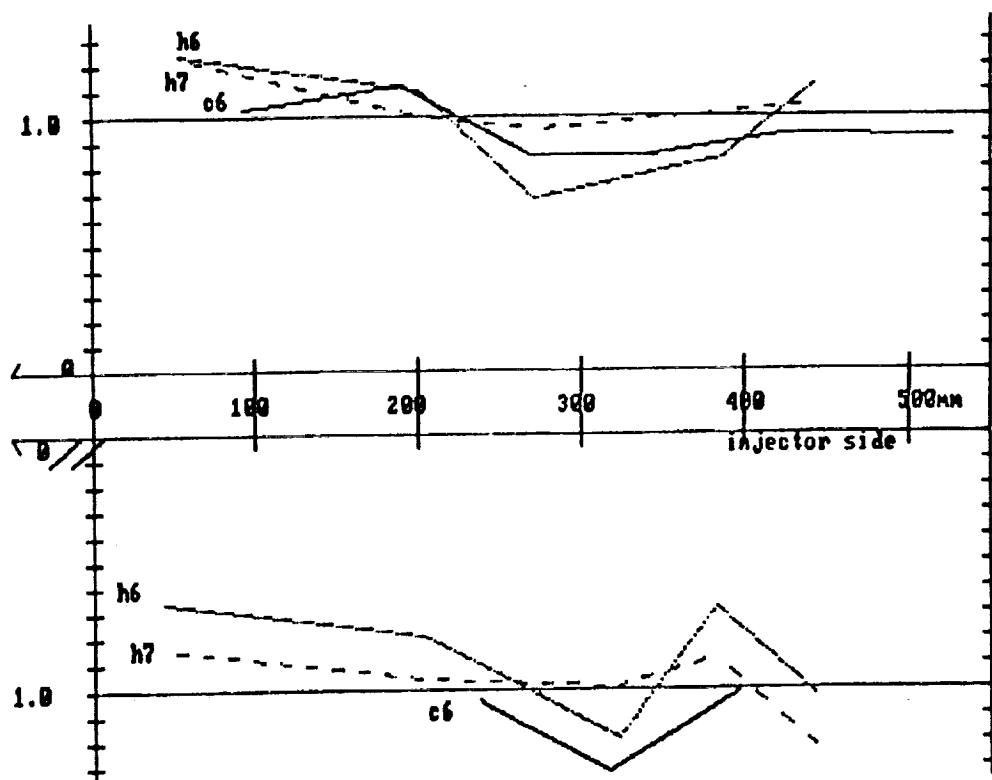


Figure 16 - Nitrogen with Fuel / Air Only vs Distance

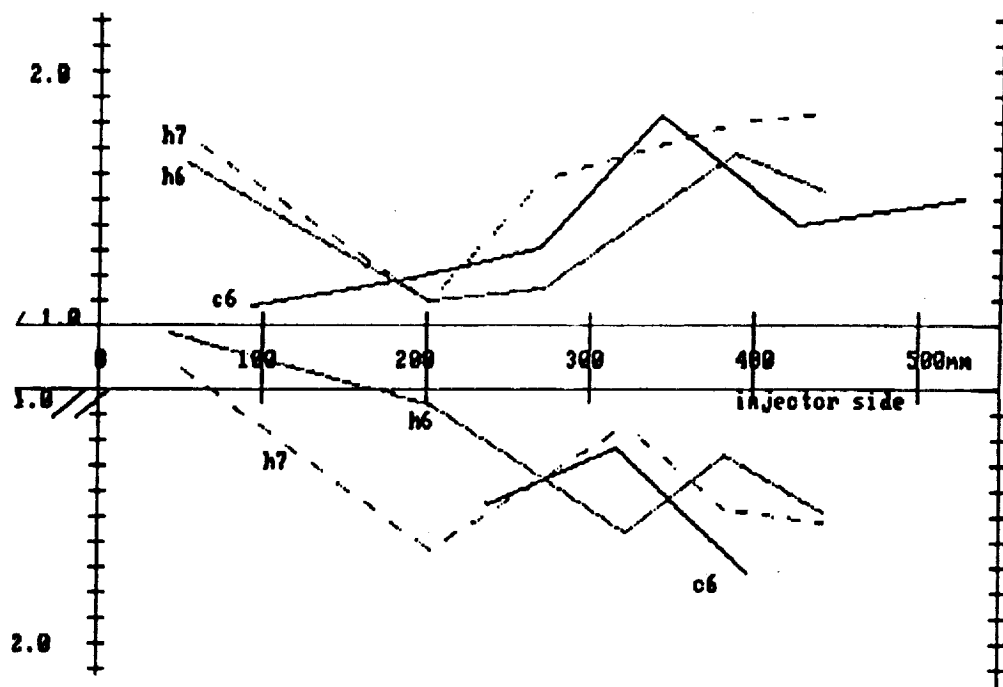


Figure 17 - Air with Fuel / Air Only vs Distance

4.0 DISCUSSION OF RESULTS

Figure 9 gives a full comparison of the low speed and high speed fuel cases for an enthalpy of 6 MJ/kg. This figure shows that up to 250mm after injection, the high speed air with fuel(AF), nitrogen with fuel(NF) and air only(AO) pressures on the upper surface are much higher than the low speed case. At the first transducer on the upper surface the high speed AF,NF and AO are also very different from each other compared to the low speed case where the AF,NF and AO are almost identical. The difference in pressure between the high speed AF,NF and AO pressures is probably due to the shock wave that forms ahead of the jet with a different interaction between AF,NF and AO and nitrogen. The low speed jet would not cause as much interference due to its lower penetration and hence the low speed AF,NF and AO are very similar. However, the difference in pressures between the high speed and low speed AO shots can not be due to this phenomenon.

After about 250mm down the duct, the differences between the high and low speed injection are minimal. The low speed AF separates from the low speed NF and AO from about this point, indicating the beginning of combustion. Figures 10 and 11 show a similar behavior for the 7 and 10.5 MJ/kg runs.

Figure 12 plots all the AF shots to compare the effect of free stream and fuel conditions. Again, after about 250mm, all distributions fall onto a single curve. This result is significant, considering the free stream velocity varies from 3 km/s to 4 km/s, the fuel velocity, 2km/s to 4km/s and the free stream temperature varies from 1100 K to 2100 K. It is also noted that, although the high speed and low speed results differ at the beginning, all the high speed AF and low speed AF traces are the same. Figures 13 and 14, give a similar result for NF and AO respectively.

The low speed fuel injection experiments (runs 1380-1384) were performed with different instrumentation, recording equipment, combustion duct and at an earlier date to the high speed experiments. For this reason, it could be expected that results may not be directly comparable. The best comparison between the two set of experiments is that of the 6Mj/kg fuel off shots. These runs should be the same as they are independent of the fuel jet conditions. Figure 14 shows that although agreement is good from about 250mm to the end, the first few transducers on the top surface do not agree. As has been observed, all the other pressure versus distance plots follow this trend. The most likely source of error is calibration and to eliminate this the AF,NF and AO distributions are divided against each other for each transducer. This gives a percentage increase at each location instead of an absolute value.

If we then look at figure 15, which shows the percentage difference in pressure due to the presence of oxygen, we can observe that all the traces fall (within experimental error) on the same curve. The increase due to the presence of oxygen can be attributed to a combustion reaction. It is also be noted that;

- i) Significant combustion effect occurs from approximately 250mm after injection.
- ii) It appears that the combustion effect is completely independent of the fuel injection parameters. That is, fuel stagnation pressure and stagnation temperature, jet mach number at exit, fuel velocity and fuel density.
- iii) The combustion effect is independent of the parameters of the free stream. That is, the free stream enthalpy, velocity, mach number and density.
- iv) The combustion effect appears to reflect from one side of the duct to the other. That is, peaks in pressure difference on one side of the duct appear to coincide with troughs on the other side. Reflections are spaced at approximately the distance it takes a mach wave to traverse the duct. (i.e. $25 \sin^{-1}(1/M^*) = 105$ mm.).

Figure 16 shows the effect on pressure due to the presence of the fuel jet. Again, reasonable agreement is achieved between conditions. A wave pattern is set up with peaks on one side of the duct corresponding to depressions on the other. The first peak on the upper surface at 50mm-200 mm is most likely due to the shocks forming due to the jet. This corresponds to a lowering of pressure behind the jet (wake?) on the injector surface. The wave reflects and at 300 mm the pattern is reversed.

Figure 17 gives a similar pattern except that the pressure rises are higher and remain greater than for air alone. This suggests it is a superposition of the combustion effect (Fig 15) on the wave effect generated from the fuel jet (Fig 16).

5.0 CONCLUSIONS

From these preliminary studies it was concluded that for the variation of free stream and fuel parameters tested there was had minimal effect(if any) on the degree of pressure rise from combustion that occurred.

REFERENCES:

1. Dr. G. Anderson, NASA Langley Research Center, Private Communication
2. R.J.Stalker,R.G.Morgan,"The University of Queensland Free Piston Shock Tunnel T4, Initial Operation and preliminary Calibration", 4th National Space Engineering Symposium Adelaide, Australia, 12-14 July 1988
3. R.G.Morgan, R.J.Stalker,"Fast Acting Hydrogen Valve",Journal of Physics E. Sci. Inst. Vol. 16, 1983 pp205-207

ADDITIONAL NOTES:

Subsequent to the writing of the report a number of relevant discoveries were made.

Figure 18 shows several shadowgraph photographs that were taken in the same duct at the same conditions. These show a large number of shock/expansion waves in fuel off conditions which should have been wave free. These waves explain the unusual pressure signals found during the experiments (N.B. lines have been drawn on the photographs to increase contrast. Figure 18b shows the difference.) Further experimental work by Dr Allan Paull has led to the conclusion that these waves were caused by the misalignment of the multi-section walls. Experiments with single section walls have removed the possibility of misalignment and hence removed the waves.

Work has also been done by Dr Paull and myself on better vibration isolation for the PCB pressure transducers. The transducers are now mounted in a single heavy block which is attached to the rest of the model by six rubber isolation mounts. Further refinement involves mounting the PCB pressure transducers vibrationally isolated from this heavy block in a similar fashion to the NASA pitot probe (figure 19). The new mount also eliminates the risk of the PCB sealing sleeve buckling and exerting side pressure onto the piezoelectric crystal.

To further examine the experimental results outlined in the report, several conditions were computed by Mr C. Brescianini using the CHARNEL program. The calculation shows the maximum difference expected between the fast and slow fuel is 5% in the H6,C6 case and about 15% in the H10,C10 case. In the H6 case the fuel velocity was 1223 m/s greater than the air whilst the C6 was 927 m/s slower. Noting that the velocity difference is similar suggests this may result in similar mixing and hence similar pressure traces. However, in the H10 case, the difference was 350m/s compared to 2060 m/s, giving explanation for not only a greater difference between the pressure rises but also the greater pressure rise for the slower fuel.

It is also noted that although there is minimal difference between the various tunnel conditions, the computations indicate vast differences between H6 and H10. This was not shown in the experiments where all signals were similar. It is possible that the extraneous shockwaves in the duct have 'swamped' the signal, minimizing all other effects.

A calculation for the fuel stagnation temperature is given below.

From pressure trace (Fig 5): Average pressure = 6200 kPa

Duration = 25 msecs

From Compression Tube: Volume = 0.061 m³

Initial fill pressure = 130 kPa

$$\text{Hence; } m_{H_2} = PV/RT = 6.41(10^{-4}) \text{ kg}$$

$$\dot{m}_{H_2} = m/\Delta t = 0.0257 \text{ kg/sec}$$

$$\text{At throat } \dot{m} = \rho A^* u^*$$

$$\rho = P^*/RT^* = 0.5283 \times 6200000 / (4121 \times 0.8333 \times T_{stag})$$

$$= 953.8 / T_{stag}$$

$$A^* = 1.134(10^{-5}) \text{ m}^2$$

$$u^* = a^* = \sqrt{\gamma RT^*}$$

$$= \sqrt{1.4 \times 4121 \times 0.8333 \times T_{stag}}$$

$$= 69.34 \sqrt{T_{stag}}$$

$$0.0257 = 953.8 / T_{stag} \times 1.134(10^{-5}) \times 69.34 \sqrt{T_{stag}}$$

$$\text{Hence; } \underline{T_{stag} = 852 \text{ K}}$$



Figure 18a - 7MJ/kg Air Only Shadowgraph



Unmodified

Modified

Figure 18b - 6MJ/kg Air Only

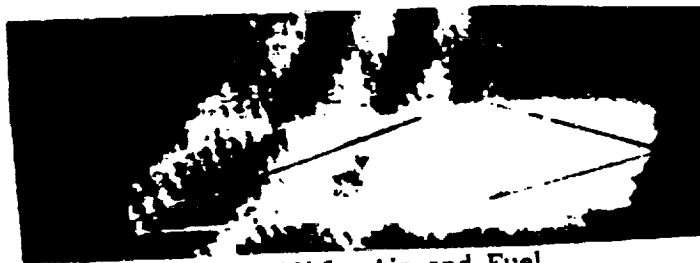


Figure 18c - 6MJ/kg Air and Fuel



No Flow



Flow

Figure 18d - 6 MJ/kg N₂ and Fuel

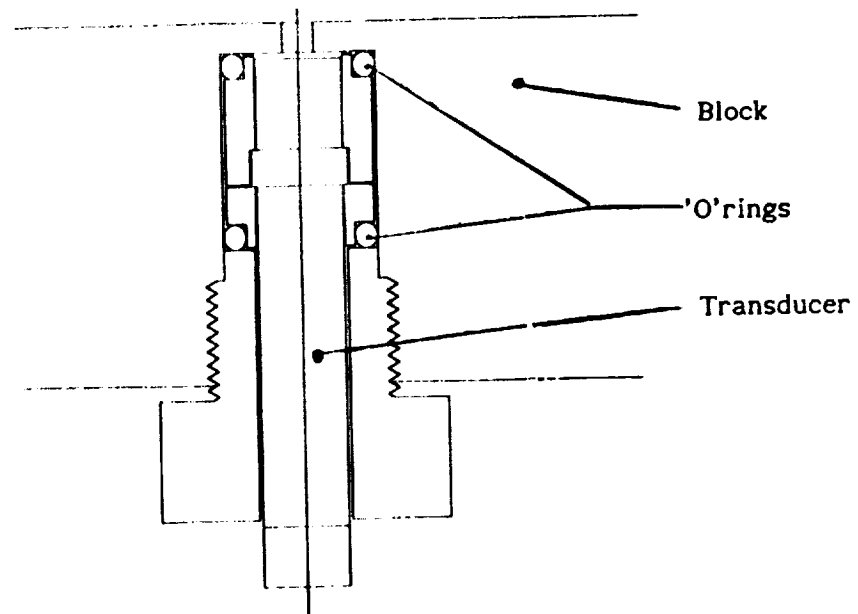


Figure 19 - Transducer Isolation

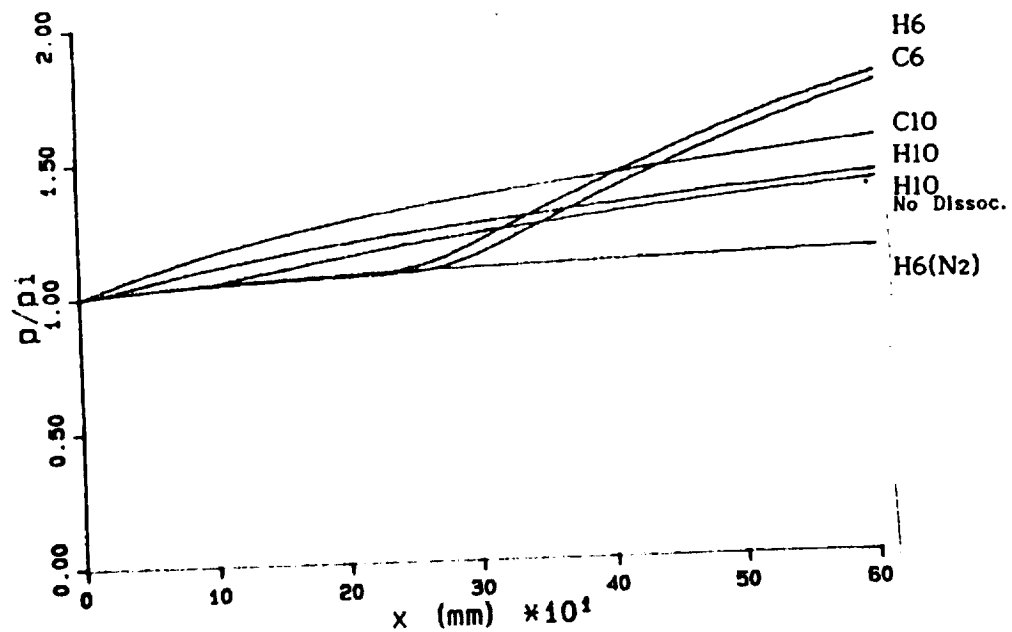


Figure 20 - Pressure vs Distance CHANNEL

Circular wall jets in Rectangular Ducts, Preliminary Summary of Further Experiments and Analysis.

R.G.Morgan, A.Paull, M.V.Pulsonetti.
The Department of Mechanical Engineering,
The University of Queensland.

Following an initial series of experiments using wall injection of hydrogen from circular jets into rectangular ducts, Morgan and Casey (1), additional analysis and extra runs have been performed in the reflected shock tunnel T4.

Following the analysis of Northam and Anderson, Ref 2, the mixing of circular jets can be reduced to a dimensionless problem by using the Langley mixing recipe and normalising length scales by jet spacing. Data from Ref 1 has been replotted in Fig 1, for a 25*50 mm rectangular duct with a single jet from 1 wall, equivalent to jet spacing of 50 mm, and for twin jets from 2 opposite walls with jet spacing of 25 mm. In the non dimensionalised plot all the data is seen to collapse onto a single curve, consistent with the treatment of Ref 2.

The results are for a combustion situation, and evidently ignition times cannot be scaled in the same way. The data is only significant therefore if reaction is sufficiently fast to decouple heat release from the length scaling process, i.e. for a pure diffusion flame where heat release is only mixing controlled. The approach of Morgan, Bakos and Tamagno Ref 3, was used to estimate this effect. Taking the mixing fraction for the two ducts at exit as given by the Langley mixing recipe, and allowing the mixed components to burn with a heat release of 90 MJ/kg of hydrogen, the duct exit pressures can be predicted and are shown in the dimensional plot Fig 2 to give reasonable agreement with the measured pressure levels. The value of 90 MJ/kg is an engineering quantity, lower than the heat release given when burning fully to water, found to give a reasonable approximation to equilibrium combustion heat release at these conditions. In the approach of Ref 3 the mixed layer is assumed to be uniformly mixed, but fuel rich and to burn up all available oxygen. The mixed layer expands on combustion and isentropically compresses the core of unmixed freestream air. The combined evidence of Figs 1 and 2 suggests that to a first order the Langley mixing recipe applies to this situation, and that reaction/ignition delays are not significant.

PRECEDING PAGE BLANK NOT FILMED

Another objective of Ref 1 was to investigate the effects of changing boundary conditions on the mixing and combustion of circular jets in rectangular ducts. Configurations 4A and 4C from Ref 1, reproduced here as Fig 3, have geometrical similarity in the aspect ratio and length scale of the internal mixing cells, but the wall boundary condition on the upper surface of 4A is replaced by a plane of symmetry in 4C. It is not known how the extra boundary layer in 4A will effect the mixing layer. This was studied in Ref 1, but the injector diameters were not matched in the 2 cases, so that a true comparison was not possible. The tests were repeated with 7 mm diameter sonic injectors and the result is shown in Fig 4. It is noticed that a more pronounced wave pattern occurred for configuration 4C, twin mixing cells in a square duct, but there was no significant change in the overall pressure/ distance development. The main features of wave pattern are attributed to the detached shock created due to the obtrusive nature of the injectant, and it is possible that reflection of the wave off the wall boundary layer in the small 25*50 mm duct attenuated and diffused the wave package. For the larger square duct the same wave packages would be created at injection, but they would pass cleanly through the plane of symmetry without attenuation or distortion.

References.

- 1.R.G.Morgan, R.Casey. "Supersonic combustion with transverse circular wall jets". From NASA CR-182096, Oct 1990. Also published in 10 ISOABE, Nottingham, UK, 1991.
- 2.G.Burton Northam, G.Y.Anderson. "Supersonic combustion research at Langley". AIAA-86-0159.
3. R.G.Morgan, R.J.Bakos, J.Tamagno. "Bulk parameter analysis of Expansion shock tunnel tests of a scramjet combustor". GASL TR 321, August 1990.

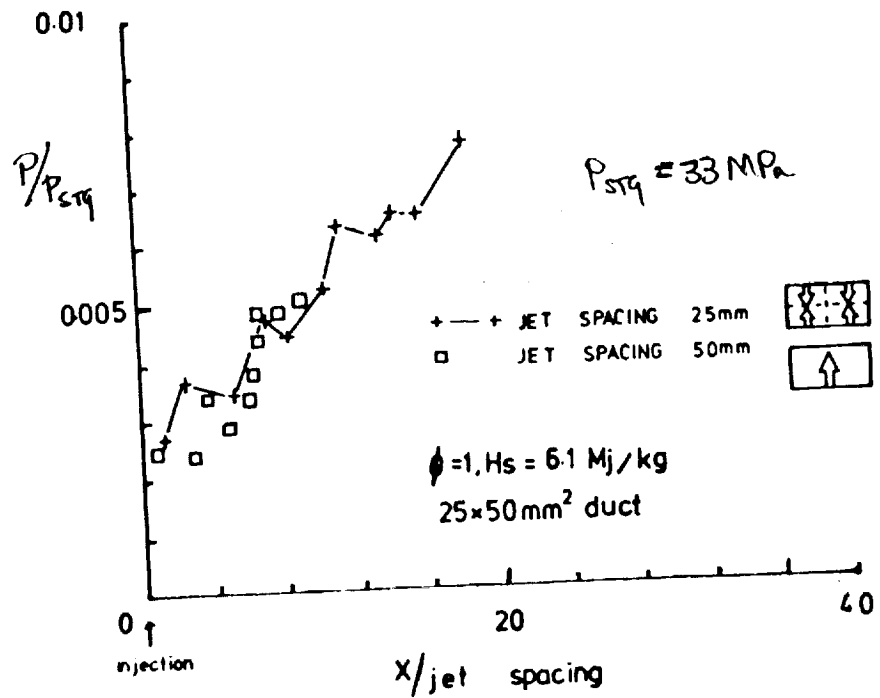


Fig 1 Duct static pressure/ distance, effect of jet spacing.

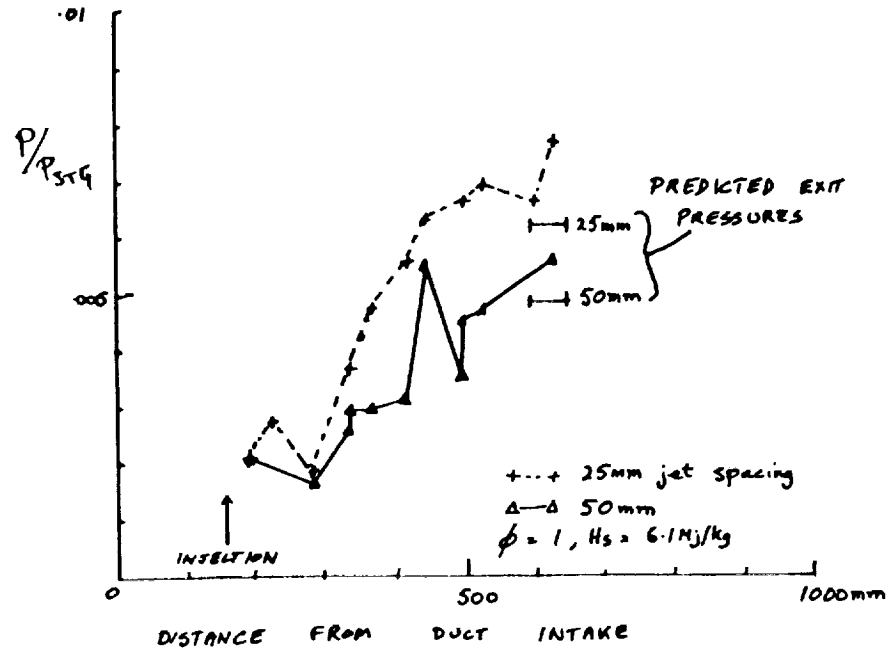


FIG 2 COMPARISON OF PREDICTED DUCT EXIT PRESSURE WITH EXPERIMENT

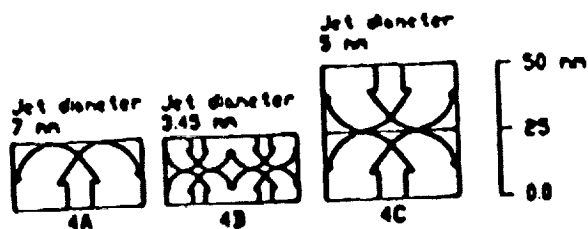


Fig 3 configurations conserving 2:1 aspect ratio

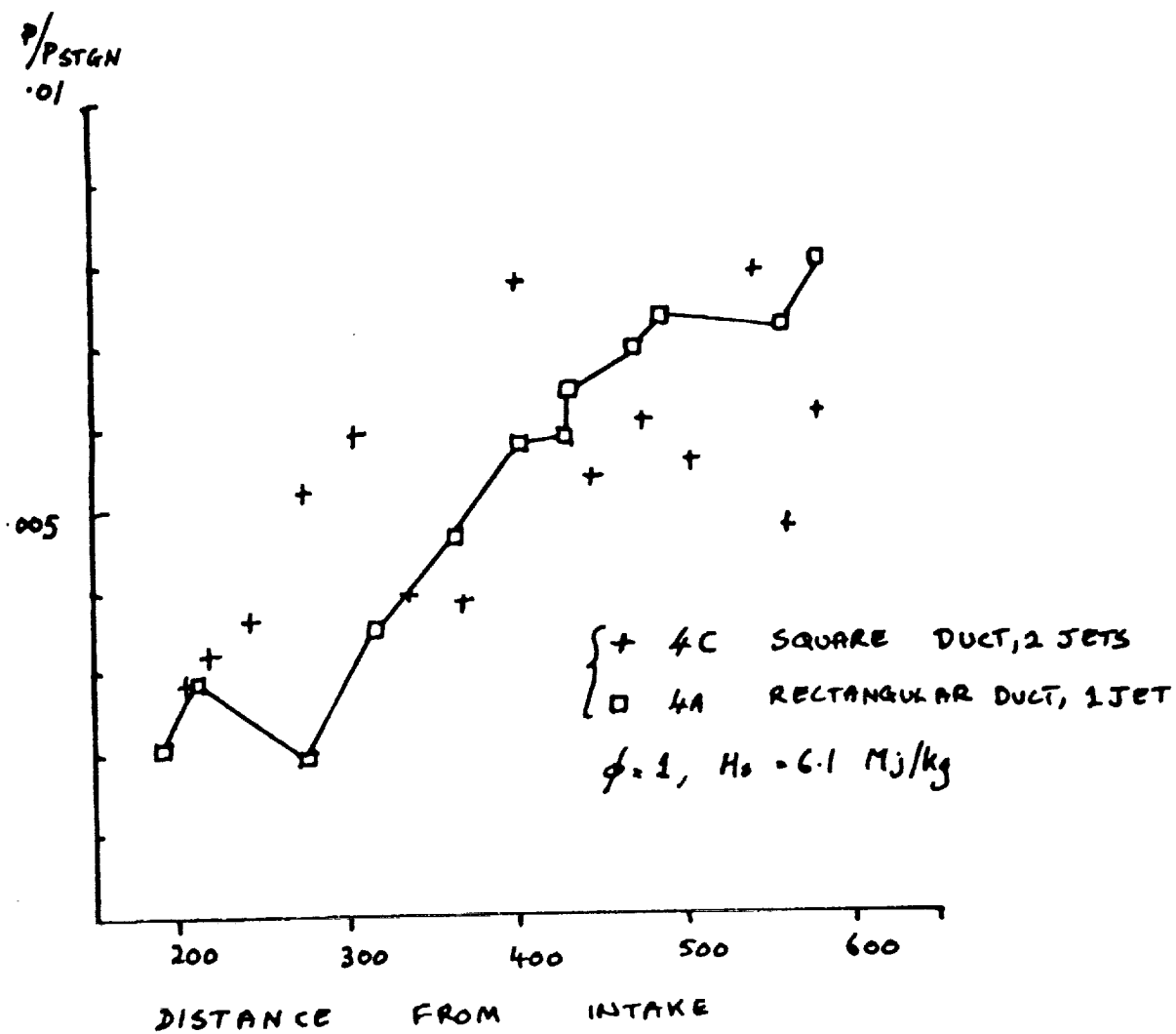


FIG 4 EFFECT OF BOUNDARY CONDITION ON PRESSURE / X

SCALING LAWS FOR MEASUREMENTS IN EXPERIMENTAL SCRAMJET FACILITIES

M.A. Nettleton

Little has been published on the choice of laws governing the scaling of data obtained from experimental models of scramjets to the design of full-scale engines. Undoubtedly this is due to the wide range of possible rate-controlling processes and a lack of understanding of how the readily variable experimental parameters i.e. the properties of the air stream and to a lesser extent those of the fuel stream may affect the governing step. Generally the experiments involve monitoring a steady state property such as specific impulse. The distinction between a steady flame and the transient process of ignition will become apparent later. Now consider some of the possible rate-controlling processes and how they respond to changes in the properties of air and fuel.

- (i) Rate of formation of macro eddies (L-eddies) - the dominant experimental variable in this case is the relative velocity of the air and fuel streams. Variations in the other properties of the two streams should be mainly manifest in terms of any resultant changes in the thickness of the boundary layers within and outside the end of the fuel injector. However nothing is known on the possible effects of a flame on the production of L-eddies in supersonic flows.
- (ii) The final rate of decay of eddies to $\leq \lambda$ at which size molecular mixing takes over (generally a rapid cascade from L to λ is

assumed). Now the important variable is the molecular diffusion coefficient D and

$$D(T,P) = D_0 \left(\frac{T}{T_0} \right)^{1.75} \left(\frac{P_0}{P} \right)$$

The rate of mass flux is given by the product of D and the concentration gradient of the diffusing species (Fick's Law), so that any change in gradient resulting from a change in pressure of the fuel or air will be manifest in a change in the rate of decay.

There may well also be a minor contribution to mass transfer via thermal diffusion so that the mass flux G becomes

$$G = -kD \left[\frac{dn}{dx} + K_T \frac{d(\ln T)}{dx} \right]$$

where K_T is the thermal diffusion ratio.

(iii) The rate of build up of a pool of radicals in a molecularly-mixed but unreacted zone. Note that I have intentionally avoided referring to a conventional chemical induction period. This is because of the possibility of radicals or atomic species being generated externally to the zone e.g. the free-stream being sufficiently hot to be partially disassociated or the presence of an adjacent flame. The rate is then given by the appropriate integration of the rate of mass transfer of active species and the chemical rate of formation in unreacted pockets. Since the

rates of chain branching reactions are very high only in the transient condition of light-up and, only then, in the absence of atomic oxygen in the free-stream is the above a candidate for the rate-controlling step.

(iv) The rate of the 3-body reactions



has frequently been considered as a prime candidate for the slowest process. Its importance is reflected in the very strong influence pressure should exert on its rate. However, there are compelling reasons for challenging the widely-accepted premise that the rates should scale as initial pressure squared. The rates are given by the products of the concentrations (partial pressures) of the species at the temperature and overall pressure in the reaction zone. The relationship between these and the initial temperature and pressure of the unreacted mixture is extremely complex, even when its composition is uniform across the duct section. An acceptable description of the more likely situation of the mixed reaction zone surrounding the periphery of the fuel jet is evidently well beyond our present understanding.

(v) We now consider a novel approach, based on the popular hypothesis of 1960s of the existence of a standing detonation wave in experimental scramjet ducts. Presently we shall regard the front as a real one, that is, with the structure associated with further fronts propagating transversely across the leading wave which is inclined at a suitable angle to the approaching mixed

flow for its forward velocity to match that of the oncoming flow. Then the stability of the front requires that at least one transverse front remains present on the leading wave, so that dimensions of the duct and spacing of the transverse waves must be matched. The spacing of transverse waves is a complex function of the kinetics of the reaction and the presence and nature of any inert diluent, but for mixtures initially at ambient temperatures generally the logarithm of spacing decreases linearly with the logarithm of increasing pressure.

In conclusion it seems probably that current views on scaling laws for results from experiments in scramjet facilities are oversimplified and further effort is required to identify more precisely the physical mechanisms involved and how these are influenced by experimental variables.

Paper No. ISABE 91-194(L)

X ISABE

Nottingham, UK September 1991

SCRAMJET TESTING - GROUND FACILITY COMPARISONS

**R.G. Morgan and R.J. Stalker
University of Queensland
St. Lucia, Queensland, Australia**

**R.J. Bakos, J. Tamagno and J.I. Erdos
General Applied Science Laboratories, Inc. (GASL)
77 Raynor Avenue
Ronkonkoma, New York, USA**

SCRAMJET TESTING - GROUND FACILITY COMPARISONS

R. G. Morgan*, R. J. Bakos**, J. Tamagno**, R.J. Stalker*, J. I. Erdos**

Abstract

The results of a preliminary series of tests to compare the effect of test gas composition on hypersonic combustion are presented. Parallel experiments were performed in the HYPULSE shock expansion tunnel and in the T4 reflected shock tunnel using identical axisymmetric models with wall injection. Test conditions were established at the same stagnation enthalpy and static pressure, with the reflected shock tunnel having approximately 50% by mass of the oxygen in a dissociated form either as atomic oxygen or as NO radicals. The expansion tunnel test gas contained less than 3% of non-molecular oxygen, and therefore closely represented the composition which might be found in flight. The static pressure rise upon combustion was found to be significantly greater when dissociated oxygen was present, and this is attributed principally to the heat of formation of the oxygen adding to the combustion heat release of the fuel at these test conditions. By reducing the total oxygen content of the reflected shock tunnel test gas it was possible to approximately compensate for this effect. The criteria for calculating the appropriate oxygen depletion are discussed, and the results are interpreted in the light of premixed one-dimensional computations.

NOTATION

α	mass fraction of total oxygen in the form of O atoms
α_n	mass fraction of total oxygen in the form of NO molecules
ϕ	fuel/oxygen equivalence ratio
ϕ_a	equivalence ratio referenced to ideal air oxygen content
ϕ^*	$=\phi$ for $\phi_a X_a/X < 1$, $=1$ for $\phi_a X_a/X > 1$
d	combustor internal diameter
h_c	heat of combustion of H_2 from O_2 (90 MJ/kg H_2)
h_f	heat of formation of O atoms from O_2 (15.7 MJ/kg)
h_n	heat of formation of NO molecules from $N_2 + O_2$ (2.93 MJ/kg)
h_m	heat release per mole of combustion products
O_2	mass fraction O_2
N_2	mass fraction N_2
NO	mass fraction NO
Ar	mass fraction Argon
x	combustor model axial location
X	mass fraction of total O content

X_a	mass fraction of total O content in "ideal" air
P	static pressure
u	velocity
ρ	density
T	static temperature
M	Mach number
H_s	stagnation enthalpy
T_s	stagnation Temperature

Subscripts:

C	data from a hydrogen combustion test
M	data from a hydrogen into nitrogen mixing test
Tare	data from a fuel-off test
In	property at facility exit or combustor inlet condition

Introduction

Test facilities for the upper envelope of scramjet flight are currently restricted to reflected shock tunnels and shock expansion tunnels, (References 1 and 2). Both devices have limitations in their simulation capabilities. The reflected shock tunnel, by creating a stagnant high energy reservoir, has test gas with significant residual dissociated species content. The shock expansion tunnel avoids this problem by never stagnating the test gas, but the unsteady wave processes used to generate high energy flow restrict the useful test time, which in turn limits the length scale of models which may be used. The two test facility concepts complement each other and, if the differences between them can be satisfactorily explained in a quantitative way, then they form a powerful base for scramjet testing and evaluation.

Both facility types have been successfully used for scramjet combustor testing. Figures 1 and 2 show sample axial pressure profiles for constant area ducts with hydrogen injection for the T4 free-piston reflected shock tunnel, from Reference 1, and the HYPULSE shock expansion tunnel, from Reference 2.

The results are encouraging in that steady hypersonic flows with mixing and combustion have been demonstrated in pulsed facilities. However, the model geometries and injector configurations were sufficiently different in each case that a direct comparison of the two facilities is not possible. The data from Figure 1 was obtained using a rectangular section duct with a parallel central injector. The model used for the Figure 2 data was an axisymmetric duct with wall injection from around the whole circumference. For the comparisons reported here, an identical axisymmetric model to that tested previously in the expansion tunnel, was tested in a reflected shock tunnel at nearly identical conditions of stagnation enthalpy, static

* Department of Mechanical Engineering,
University of Queensland, Brisbane
AUSTRALIA

** General Applied Science Laboratories, Inc.,
Ronkonkoma, NY USA

pressure and temperature.

The test flow in a reflected shock tunnel is created by means of a steady expansion from the stagnation region occurring behind the reflected shock at the end of the shock tube. The gas in the stagnation region is approximately in a condition of equilibrium composition due to the high density levels and low particle velocity. At the stagnation enthalpies corresponding to flight speeds, the stagnation temperatures are such that significant dissociation occurs to the oxygen and nitrogen molecules. As the flow travels down the expansion nozzle, the temperature drops and the composition shifts toward a reduced dissociation content. However, due to the high particle velocities and low density in the nozzle, reaction rates may in some circumstances be insufficient to maintain equilibrium composition. The test gas at the nozzle exit will therefore have a residual content of the dissociated radicals created in the stagnation region. The higher the stagnation enthalpy, the higher will be the concentration of dissociated gas.

Processing of the test gas in an expansion tunnel is different in several important aspects. The test gas is shock heated in the shock tube portion of the facility where only a fraction of the final flow stagnation enthalpy is added. After shock passage the test flow is expanded in a constant area acceleration tube by means of an unsteady expansion wave. This expansion accelerates the flow from a low supersonic Mach number to hypersonic velocity while increasing the stagnation enthalpy. Because the test gas is never stagnated while at large stagnation enthalpies, it does not experience the high temperatures necessary for dissociation, and is thus delivered with a composition close to equilibrium.

The presence of non-equilibrium levels of dissociated species may affect the flow in several ways. Perhaps most important is that some of the stagnation enthalpy will be stored as atomic heat of formation, and will not be converted directly to thermal or kinetic energy. It is necessary, when comparing the results of reflected shock tunnel tests with real flight, or with other tunnels which do not produce dissociated air, to match the stagnation enthalpy including thermal, chemical and kinetic energy components.

For combustion testing, the presence of free-stream oxygen atoms may have other significant effects, which must be examined closely. There are three main mechanisms by which the free oxygen atoms may be seen to enhance combustion, and influence comparisons made between reflected shock tunnel experiments and real flight.

(i) Combustion heat release When combustion is from atomic oxygen form, the atomic oxygen heat of formation is added to the combustion heat release. This increases the net heat release from approximately 90 MJ to 215 MJ per kg of hydrogen burned. This is clearly a substantial increase and relatively small oxygen dissociation fractions may be significant.

(ii) Ignition delay times Forming of oxygen radicals is a necessary step in the combustion

of hydrogen, and the pre-dissociated shock tunnel flow may be expected to react faster than ordinary air.

(iii) Mixing Effects In some circumstances a scramjet may be considered to be a pure diffusion flame, where reaction rates are so fast that heat release is mixing controlled. Oxygen molecules have different diffusion rates than atoms, and the local chemical composition will affect the rate of heat release. Furthermore, the macroscopic development of the fuel-air mixing layer is dependent on the local flow properties such as Reynolds number, and this may also be influenced by the dissociated oxygen content.

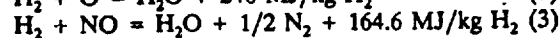
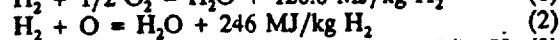
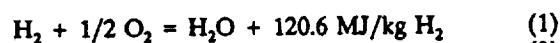
In summary, for a given static pressure, dissociated oxygen increases the partial pressure of the oxygen components, effectively enhancing mixing and combustion.

This paper reports on preliminary experiments and associated analytical work aimed at using the differences between the two facilities to resolve facility-induced effects, developing methods to quantify and compensate for them, so that the results may be related to flight conditions. Only the first mechanism will be addressed, that of predicting, and compensating for, the enhanced heat release due to the chemical enthalpy of the dissociated oxygen. Adjustment of the reflected shock tunnel oxygen content is examined as a way to match the net heat release of combustion, when compared to tests in undissociated air. In this way it is possible to produce pressure profiles which are approximately decoupled from the effects of differing levels of free stream dissociation and allow a direct comparison between reflected shock tunnel experiments and tests using undissociated air.

Analytical Approach

Analysis of the reflected shock tunnel nozzle flow using a one-dimensional, non-equilibrium, chemical kinetics code (Reference 3) indicates that there are two significant dissociation products present (as far as hydrogen combustion is concerned), namely NO and O, in the range of stagnation enthalpies from about 12 to 20 MJ/kg. Similar analysis of the unsteady expansion system in the shock expansion tunnel reveal substantially lower concentration of these species at comparable enthalpies.

The effects of dissociation on hydrogen combustion heat release are quantified in the following manner: Combustion to water from the 3 oxygen-bearing constituents of the test gas proceeds with heat release as indicated below:



(NOTE: These equations are not intended to represent reaction schemes, but are used to calculate differences in heat release for varying reactant compositions.)

Combustion of undissociated air involves only reaction from oxygen molecules, and may be seen to give significantly less heat release than the two other main combustion paths. An approach to matching heat release is to apply a correction to the free stream oxygen concentration as was done in Reference 4. In other words, the reflected shock tunnel tests could be performed with a reduced oxygen concentration intended to reproduce the results of combustion in an expansion tunnel or atmospheric air with the same fluid dynamic properties.

The primary measured experimental parameter in scramjet testing is duct static pressure distribution. Corrections made to oxygen levels should be calculated to produce identical pressure/distance profiles in the two facilities. To match these exactly, a numerical simulation is required which fully evaluates the changes in combustion species composition produced by changing the free stream oxygen level. However, a first-order correction based on the three reaction mechanism identified above has been made and numerical simulations and experimental data used to assess the validity of the approach.

In Reference 4, a chemical equation was constructed from the three reaction mechanism as a function of test gas composition and fuel/oxygen equivalence ratio. This was used to calculate the appropriate oxygen depletion level by conserving heat release per unit mole of combustion products. To first order, this should lead to the same pressure rise, and should create the same wave pattern and flowfield in the two cases. This is considered to be of fundamental importance for scramjet ducts, which can only be analyzed correctly in light of a full wave capturing treatment, Reference 5.

The heat release per unit mole of combustion products is given by

$$h_m = \frac{\phi^* h_c \left(1 + 8\alpha \frac{h_f}{h_c} + 15\alpha \frac{h_a}{h_c} \right)}{\frac{1}{4} \left(2\phi_* \frac{X_*}{X} - \phi^* + \alpha(1 - \phi^*) - \frac{4}{28} \right) + \frac{8}{28X}} \quad (4)$$

From this the modified oxygen mass fraction for the reflected shock tunnel test gas is computed (by equating heat release from (4) to that for the undissociated case) to be:

$$X = \frac{\frac{8}{7} + 2X_*\phi_*}{B \left(A + \frac{32}{28X_*} \right) - A - \alpha(1 - \phi^*) + 2\phi_*} \quad (5)$$

Where

$$A = 2\phi - \phi^* - \frac{4}{28}$$

$$B = 1 + 8\alpha \frac{h_f}{h_c} + 15\alpha \frac{h_a}{h_c}$$

The two terms involving ϕ_* have been added to the original equation for X (as found in Reference 4) to account for matching of fuel mass flow rates in the comparison experiments as opposed to matching of actual fuel/oxygen equivalence ratio which was assumed in the original derivation. Conserving fuel mass flow rate is important for hypersonic combustion comparisons due to its significant influence on mixing. The effect of these terms will be discussed below.

It should be clear that the mass fraction X includes the total oxygen content in all its forms. It is sensitive to O and NO concentrations, which are functions of flow enthalpy, and also equivalence ratio. Note also that the heat release of 120.6 MJ/kg from equation (1), combustion from oxygen molecules, is based on combustion to water alone. The equilibrium composition of a hydrogen flame contains dissociated radicals, and the full heat release is not achieved. A heat release of 90 MJ/kg H_2 is more representative of that developed in a real combustion chamber and is chosen for h_c .

Experimental Conditions and Apparatus

It is not possible to conserve all the flow parameters when choosing test conditions in the two facilities. For example, the molecular weights of the test gases are different, and therefore if flow velocity and temperature are matched then the Mach number will have to be different. The approach taken for comparison was to conserve static temperature and static pressure so as to match combustion conditions as closely as possible. Then matching stagnation enthalpy prescribes velocity, and it is not possible to then simultaneously match pitot pressure.

The test conditions chosen for these tests are given in Table 1 and are based on the nominal Mach 17 stagnation enthalpy (15.3 MJ/kg) operating point of the HYPULSE expansion tunnel. A contoured Mach 5 nozzle was used to obtain the quoted test conditions for the reflected shock tunnel. For the expansion tunnel operating at 15.3 MJ/kg, the test gas diffuser described in Reference 6 is necessary to compress the flow to the static pressures required to support hydrogen/air combustion.

As described previously, the operating principles of the facilities are quite different and therefore so are the time histories of the facility start-up and subsequent flow establishment in the model. For the reflected shock tunnel, a nozzle plenum pressure trace is shown in Figure 3. Operation of the tunnel to achieve 15.7 MJ/kg stagnation enthalpy is at a condition only slightly under tailored, and therefore the stagnation pressure is held approximately constant over a period of 1 msec. A corresponding static pressure history, as measured in the model, is shown in Figure 4, from which a corresponding steady pressure period of 0.75 msec. can be seen.

An expansion tunnel Mach number trace, as derived from pitot and static pressure data measured in a calibration test, is shown in Figure 5 for comparison. It is clear that the steady test period is significantly shorter than for the shock tunnel. To insure flow establishment in the model, heat transfer data are examined for relaxation to steady state.

Figure 6 shows a heat flux trace measured in the model for a fuel-off run. This time history is typical of a laminar heat flux trace, and shows relaxation well within the available steady flow period.

The tests were run with the axisymmetric combustor model shown in Figure 7. Its overall length to diameter ratio is 24, and fuel is injected via a single annular slot located 4.67 model diameters downstream of the inlet. Fuel is injected at Mach 1.9 and radially inward at an angle of 15° from the model axis. The injector throat area to model capture area is 0.062. This choice was made to permit the injected fuel to be pressure matched to the duct inlet pressure at stoichiometric fuel mass flow. Higher equivalence ratios are obtained by raising the fuel plenum pressure accordingly. The model was positioned for both facilities in a free jet configuration, capturing the central uniform core of the facility exit flows.

Model instrumentation includes 13 high frequency, high sensitivity pressure transducers. One was located upstream, and 12 downstream of the injector. An additional transducer was located at the end of the model for the shock tunnel tests. All were positioned at the same azimuthal angle. Thin-film resistance gages were used to measure wall heat transfer. These were located at the same axial locations but diametrically opposed to the pressure transducers. Frequency response for both types of instrumentation is 500 MHz.

Comparison Test Results

As previously noted the reflected shock tunnel experiments were configured around results from HYPULSE tests at a condition equivalent to flight Mach number 17 (as reported in Reference 6). An equivalence ratio of 3 was targeted as it had been shown to give good mixing and combustion in the HYPULSE tests. The corresponding T4 condition, shown in Table 1A, is seen to have a large dissociated radical content.

Results of fuel-off tare runs in the two facilities are shown in Figure 8. Although nominal facility exit pressures were matched, it is clear that a higher average static pressure is achieved in the expansion tunnel tests. A complete explanation for this discrepancy is not available at this time; however, results of calibration tests for the HYPULSE test gas diffuser, as discussed in Reference 6, suggest that the diffuser is producing a weak conical shock system which is captured by the model. It is postulated that this wave system results in a lower average combustor entrance Mach number and a higher average static pressure than would be inferred from the last wall pressure measurement in the diffuser (at $x/d = -1.0$ in Figure 8). Unfortunately, because the diffuser exit pressure was taken as representative of the expansion tunnel average exit pressure (and chosen to be matched in the tests), the reflected shock tunnel tests resulted in the lower duct pressures.

Because duct pressure level is the primary diagnostic used to gauge combustion heat release, it is necessary to remove systematic variations in pressure level between the two experiments. The tare run pressure distributions were

therefore averaged to obtain a scale factor to relate the results of other tests. The success of this method can be seen in Figure 9 which compares the scaled pressure distributions for hydrogen-into-nitrogen mixing runs in the two facilities. It may be seen that the pressure distributions agree quite well.

Figure 10 shows the scaled pressure/distance development for the two cases using air as the test gas. Enhanced combustion in the reflected shock tunnel is clearly evident.

An alternative method of displaying this result is shown in Figure 11. Here the difference between measured combustion run and mixing run pressures are normalized by the average tare pressures and plotted against distance along the duct. The plotted curves are logarithmic regressions of the form $a + b \log x$, fit to the data from the injection station to the end of the duct in both cases. There is considerable scatter of the data about the fit curves which is primarily a result of the actual two-dimensional nature of the flowfields. However, the pressure level increase, due to combustion, is more easily quantified by this procedure.

In attempting to match the expansion tunnel results in the reflected shock tunnel, it was decided first to maintain the actual fuel/oxygen equivalence ratio at 3, and use the procedure outlined above (equation (5) without the modifying terms) to compute a required test gas oxygen content. This leads to a total oxygen content of 0.0675, by mass, for the reflected shock tunnel. The computed test gas composition for this case is shown in Table 1B.

In arriving at this oxygen content a new problem becomes apparent. The reduced oxygen partial pressure in the expansion nozzle leads to increased dissociation, and a further shift in the heat release balance, required by equation (5), toward even lower oxygen content. Furthermore, the requirement of conserving stagnation enthalpy requires stagnation temperature to increase. This is because when the total oxygen content is reduced, less stagnation enthalpy per unit mass of test gas mixture is available in the nitrogen molecules than in the dissociated oxygen atoms which they replace. This again leads to more dissociation. The test gas composition which satisfies the heat release requirement is found through a series of iterations.

The solution for test gas composition now determines what fuel injection conditions are required to achieve the equivalence ratio of 3. The models were designed with identical geometry for both tunnels so that required injector plenum pressures (and thus mass flows) scale approximately with the free stream oxygen mass fraction. This meant that the T4 tests were to be performed with approximately 1/3 the plenum pressure of the HYPULSE tests. This injection pressure corresponds to an equivalence ratio of 1 for the HYPULSE combustion tests, which showed little signs of combustion, mainly due to mixing limitations, Reference 7. Results of tests at this same injection pressure in T4, which are not shown, again confirmed the absence of combustion, even with the elevated dissociation levels.

Fuel/oxygen equivalence ratio had initially been

considered to be a primary parameter to be matched when comparing facilities. However, the mixing process is so sensitive to injection pressure, and it has such an influence on macroscopic flow properties in hypersonic ducted flow, Reference 7, that it is now evident that the injection parameters must be conserved in order to reproduce the same basic flow features in both facilities. This implies that a compromise must be made on equivalence ratio by conserving fuel mass flow rate.

A test with the test gas composition given in Table 1B was subsequently made with the fuel plenum pressure and resultant fuel flow rate matched to the HYPULSE runs at equivalence ratio of 3. The pressure difference results are shown in Figure 12 from which it is seen that combustion takes place, but the heat release is lower than for the HYPULSE condition shown previously in Figure 11. This is because the fuel/oxygen equivalence ratio is approximately 9 for this test and the excess unburnt fuel reduces the heat release per mole of combustion products.

Working from this result, the oxygen content was recomputed by equation (5), this time conserving fuel flow rate. This is accomplished by specifying the fuel-to-ideal-air equivalence ratio, ϕ_a , to be constant at 3 and including the modified terms in (5). The resultant test gas composition is shown in Table 1C where an oxygen content of 0.128 was converged upon. Although no data were taken at this level of depletion, a linear interpolation in X of the T4 regressions has been plotted in Figure 12 to show the anticipated result. This curve is seen to be quite similar in level to the HYPULSE regression curve.

Analyses were performed using a one-dimensional, fully mixed, chemical kinetics code to predict rate limited and equilibrium pressure levels using the hydrogen/air reaction scheme given in Reference 8. The fuel and test gas were mixed in a chemically frozen, constant area process to define start-line conditions for the combustion calculation. The parameter plotted is computed combustion pressure minus the mixing pressure normalized by the nominal facility exit pressure. This parameter is sensitive to combustion heat release, and approximately equivalent to that plotted for the data. The equilibrium levels were computed by allowing the calculation to run for sufficient distance to allow axial gradients to vanish.

Figure 13 shows computed pressure parameter distributions for the T4 and HYPULSE air conditions as given in Tables 1A and 1D. More rapid ignition and enhanced combustion for the T4 air are seen. Comparing these distributions with the data in Figure 11, very similar pressure distributions are noted. In this regard, the analysis of Reference 7 indicated substantial mixing at $\phi_a = 3$ for this injector configuration. Also, by plotting differences between combustion and mixing run pressure distributions, effects due to wall shear, wall heat transfer, and finite rate mixing are approximately canceled. Therefore, the close agreement of experiment with the computations is not surprising, even considering the simplicity of the analysis. And thus, the predicted trend toward greater heat release with increased oxygen dissociation is regarded as confirmation of cause for a similar trend seen in the data.

Similar calculations were done for the oxygen depleted conditions (Table 1B, with $\phi_a = 3$), and the modified conditions (Table 1C, with $\phi_a = 3$). These results are shown in Figure 14. The extremely suppressed pressure rise, which was observed experimentally for case 1B, is well predicted. In comparing case 1C with the HYPULSE prediction, a more rapid ignition is seen for the reflected shock tunnel. However, the down stream behavior and equilibrium pressure levels agree fairly well. Considering the strong agreement already demonstrated, between the predictions and the data, it is clear that an experiment run with the modified oxygen content of $X = 0.128$ should match the HYPULSE pressure data.

Conclusions

A series of experiments have been conducted to compare the effects of oxygen dissociation on hypersonic combustion at conditions simulating flight Mach number 17. It has been demonstrated that the effect of differences in test gas composition on combustion heat release can, to a significant extent, be accounted for by adjusting the oxygen content of the test gas.

These parallel experiments were run in the HYPULSE shock expansion tunnel and the T4 reflected shock tunnel using identical scramjet models at nearly matched levels of stagnation enthalpy, static temperature and static pressure. Despite the nominally identical intake flow conditions, a substantial difference in the duct flow pressures was observed for the two facilities. However, appropriate normalization of the data enabled meaningful comparisons to be made between the two data sets.

Pressure rise due to combustion was found to be clearly greater for the reflected shock tunnel tests run with real air. This difference was shown to be consistent with chemical kinetics calculations which accounted for the dissociated oxygen resident in the test gas.

A first-order correction to the reflected shock tunnel oxygen content to account for enhanced heat release was described and implemented experimentally. It was found that such a correction must be done by conserving fuel flow rate, rather than fuel/oxygen equivalence ratio. This is primarily a result of the large influence that injectant stagnation pressure (hence, mass flow rate) has on the mixing process for ducted hypersonic flow. An initial experiment was run at matched fuel flow rate; however, the oxygen depletion had not been optimized for this fuel flow and the resulting pressure level fell below the expansion tunnel level. Chemical kinetic and equilibrium computations for this test gas, and for an appropriately optimized test gas, indicate that the correct depletion will yield the approximately correct pressure rise.

There remain several aspects of these comparisons which require further investigation. This initial set of experiments addressed only the issue of dissociated oxygen effects on heat release. The influence on ignition, although clearly evident in some of the calculations, was not considered nor were the effects on fuel/air mixing. These issues will require more detailed comparison tests and correlation with more complete CFD simulations.

Additional experiments and numerical simulations are planned for the continuation of this work.

Acknowledgements

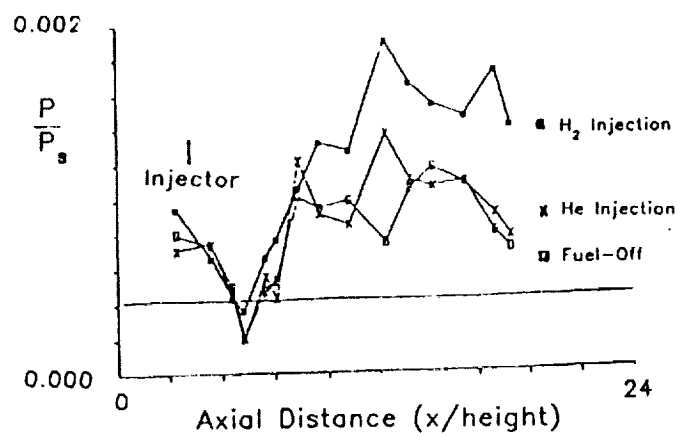
The portion of this work conducted at General Applied Science Laboratories was sponsored by the National AeroSpace Plane Joint Program Office, Mr. Curtis D. Snyder was the Task Manager. The work done at the University of Queensland was funded by a grant from the NASA Langley Research Center, Hypersonic Propulsion Branch, Griffin Y. Anderson - Branch Head. Their support and encouragement are gratefully acknowledged.

REFERENCES

1. Stalker, R.J., Morgan, R.G., Paull, A., and Brescianni, C.P., "Scramjet Experiments in Free Piston Shock Tunnels," Paper No. 28, 8th National AeroSpace Plane Technology Symposium, March 26-30, 1990.
2. Tamagno, J., Bakos, R.J., Pulsonetti, M.V., and Erdos, J.I., "Hypervelocity Real Gas Capabilities of GASL's Expansion Tube (HYPULSE) Facility," Paper 90-1390, AIAA 16th Aerodynamic Ground Testing Conference, Seattle, WA, June 1990.
3. Lordi, J.A., Mates, R.E., and Moselle, J.R., "Computer Program for the Numerical Solution of Nonequilibrium Expansions of Reacting Gas Mixtures," NASA CR-472, 1966.
4. Morgan, R.G., "Dissociated Test Gas, Effects on Scramjet Combustors," NASA CR-182096, October 1990.
5. Stalker, R.J., Morgan, R.G., and Netterfield, M.P., "Wave Processes in Scramjet Thrust Generation," Combustion and Flame, Vol. 71, pp 63-77, 1988.
6. Bakos, R.J., Tamagno, J., Rizkalla, O., Pulsonetti, M.V., Chinitz, W., and Erdos, J.I., "Hypersonic Mixing and Combustion Studies in the GASL HYPULSE Facility," Paper 90-2095, AIAA 26th Joint Propulsion Conference, Orlando, FL, July 1990.
7. Morgan, R.G., Bakos, R.J., and Tamagno, J., "Bulk Parameter Analysis of Hypersonic Combustion Experiments," GASL TR-321, August 1990.
8. "Hypersonic Combustion Kinetics - Status Report of the Rate Constant Committee, NASP High-Speed Propulsion Technology Team," Oldenborg, R. - Chmn, NASP Technical Memorandum 1107, May 1990.

TABLE 1 NOMINAL TEST FLOW CONDITIONS

	Table 1 A T4 real air	Table 1 B T4 6.75% Oxy	Table 1 C T4 12.8% Oxy	Table 1 D HYPULSE
H_0 (MJ/kg)	15.70	15.70	15.70	15.30
T_0 (K)	7880	8350	8180	8355
T (K)	2065	2120	2037	2088
$P/P_{HYPULSE}$	0.927	0.885	0.885	1.000
u (m/s)	4710	4910	4819	5078
M	5.17	5.31	5.30	5.75
N_2	.7320	.9150	.8470	.7507
O_2	.1080	.0063	.0328	.2253
Ar	.0129	.0131	.0131	.0129
N	2.20E-6	3.30E-6	2.20E-6	3.00E-9
O	9.70E-2	5.43E-2	7.90E-2	7.82E-4
NO	.0508	.0114	.0281	.0103
X	.2320	.0675	.1280	.2320
α	.4180	.8100	.6200	.0034
α_n	.1168	.0900	.1200	.0238

Figure 1. Rectangular scramjet combustor data, $H_0 = 8.39$ MJ/kg - T4 Reflected Shock Tunnel Facility.

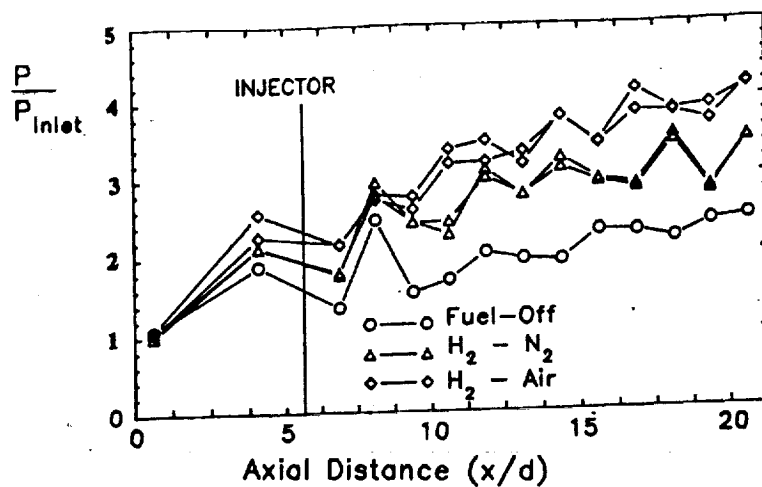


Figure 2. Axisymmetric scramjet combustor data, $H_0 = 15.3 \text{ MJ/kg}$ - HYPULSE Shock Expansion Tunnel Facility.

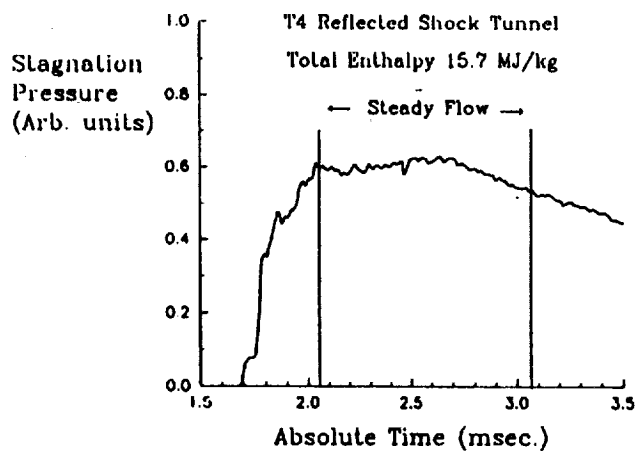


Figure 3. Reflected shock tunnel stagnation pressure trace, $H_0 = 15.7 \text{ MJ/kg}$.

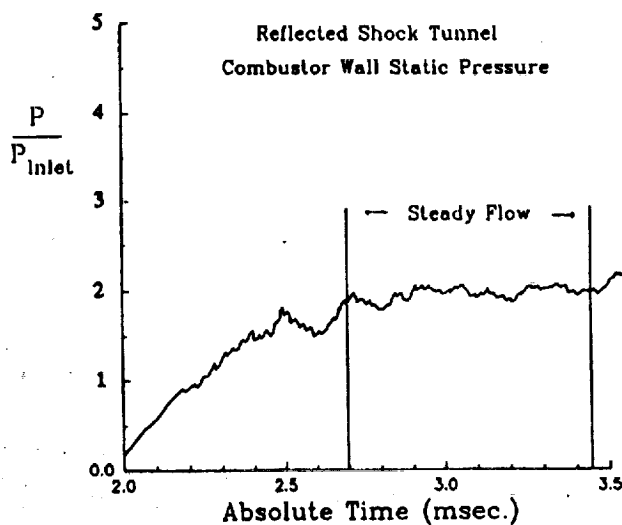


Figure 4. Reflected shock tunnel static pressure trace measured in the combustor model, $H_0 = 15.7 \text{ MJ/kg}$.

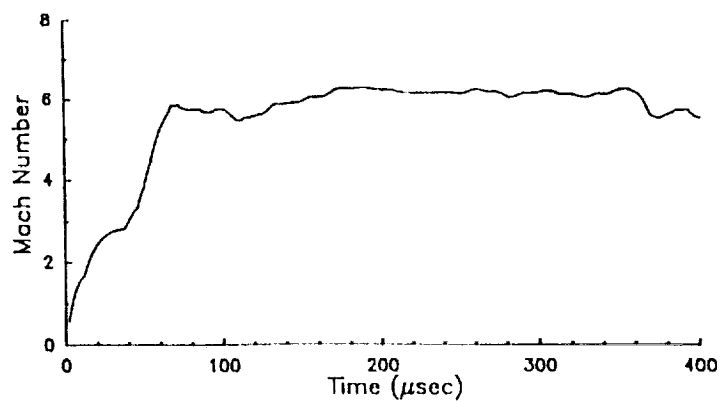


Figure 5. Expansion tunnel diffuser exit Mach number trace, $H_0 = 15.3$ MJ/kg.

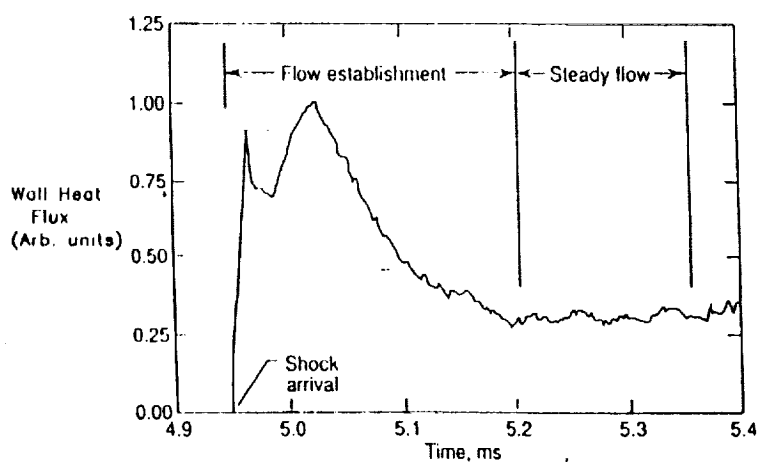


Figure 6. Expansion tunnel combustor wall heat flux trace showing flow establishment and steady flow periods, $H_0 = 15.3$ MJ/kg.

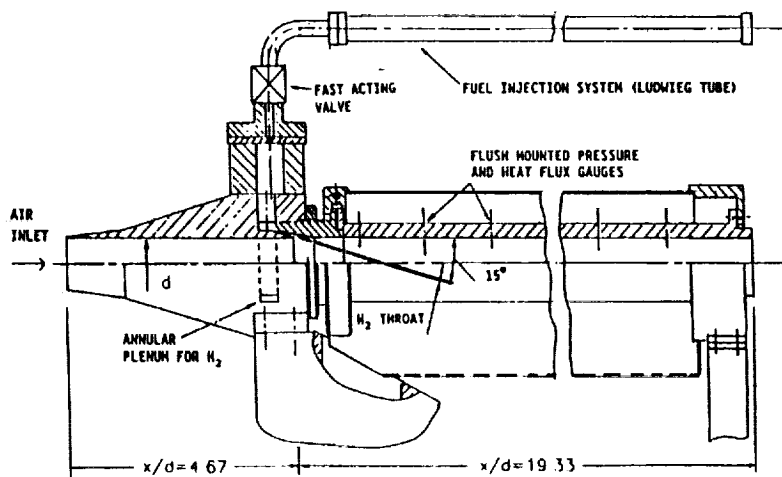


Figure 7. Schematic of axisymmetric combustor model.

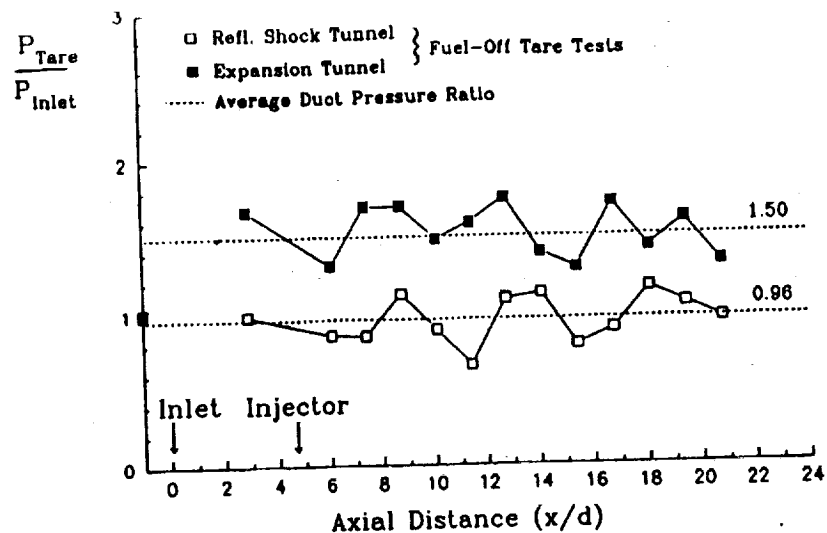


Figure 8. Measured static pressure distributions for fuel-off tare tests in both facilities.

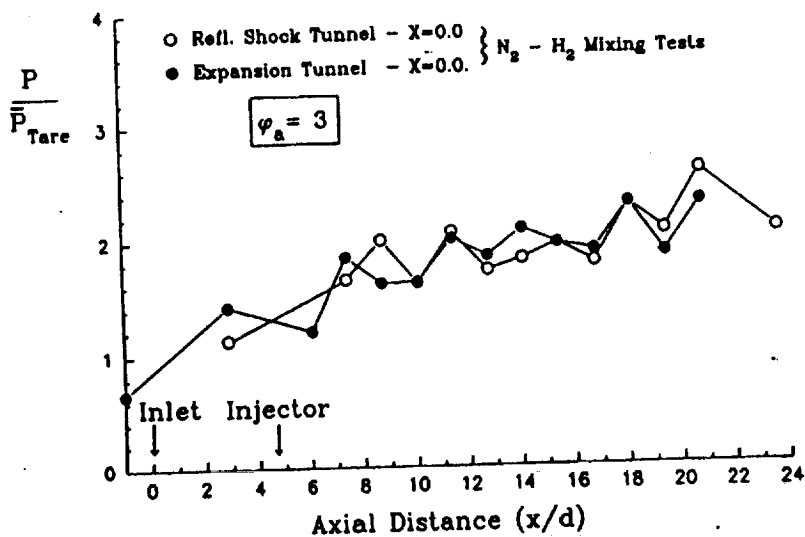


Figure 9. Measured mixing test static pressure distributions shown normalized by the average tare pressure for each facility.

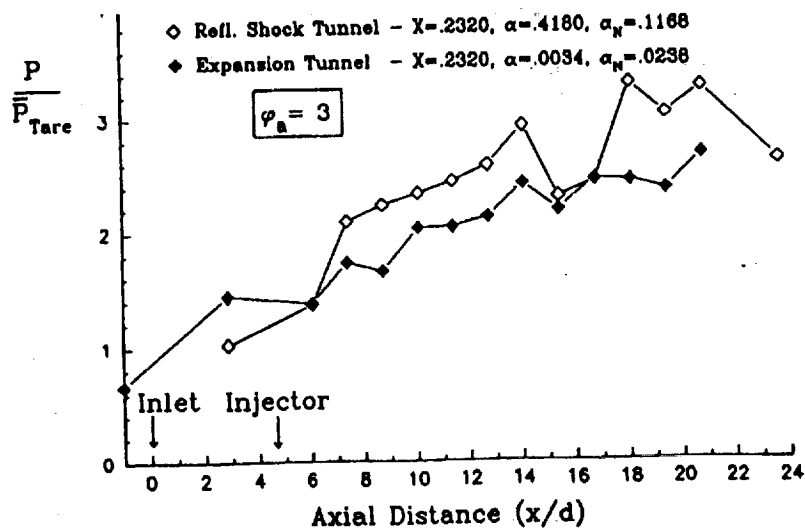


Figure 10. Measured real air combustion test static pressure distributions shown normalized by the average tare pressure for each facility.

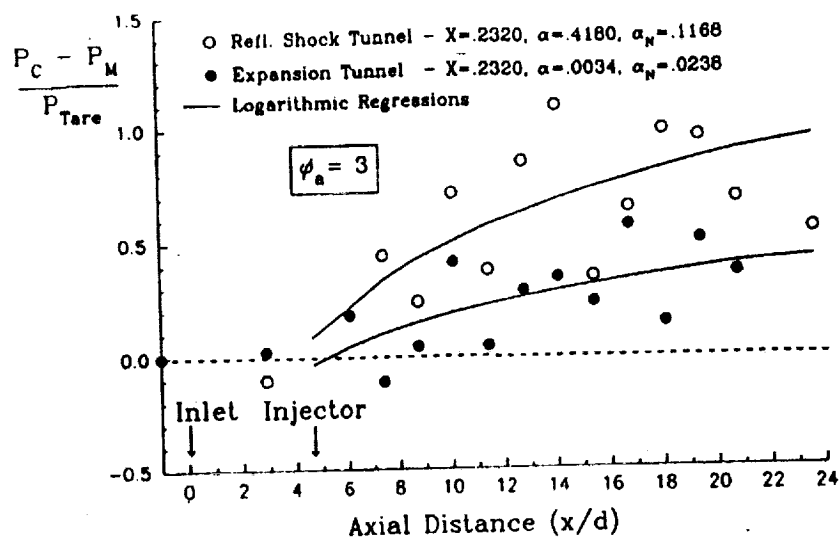


Figure 11. Difference in normalized combustion and mixing run pressures for real air as measured in both facilities.

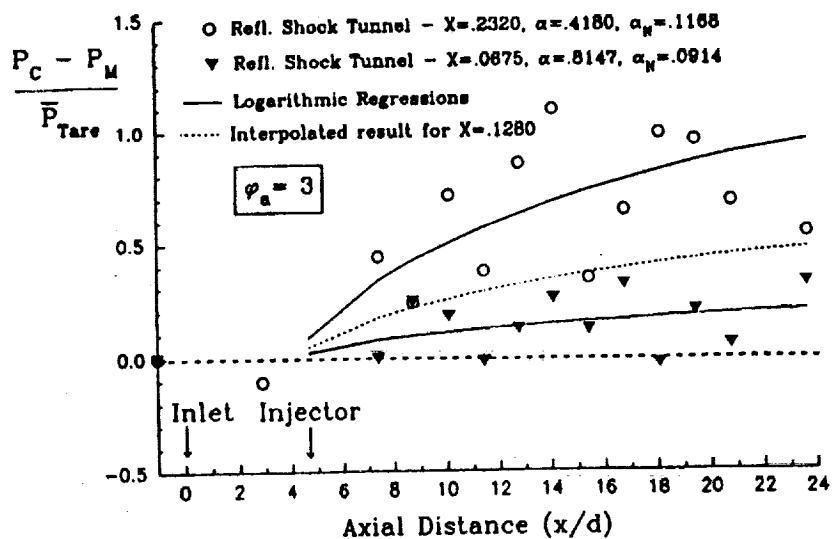


Figure 12. Difference in normalized combustion and mixing run pressures. Comparing reflected shock tunnel real air result with reflected shock tunnel depleted oxygen results.

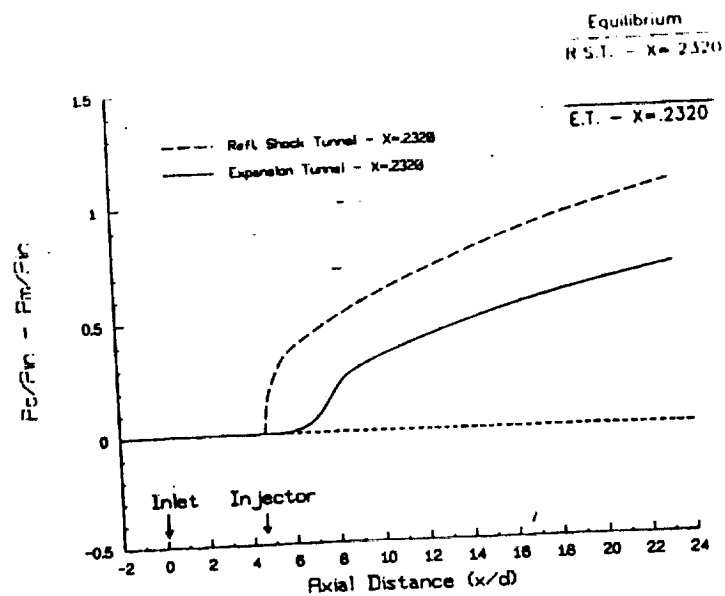


Figure 13. Computed chemical kinetic distributions and equilibrium levels of combustion pressure rise for real air in both facilities.

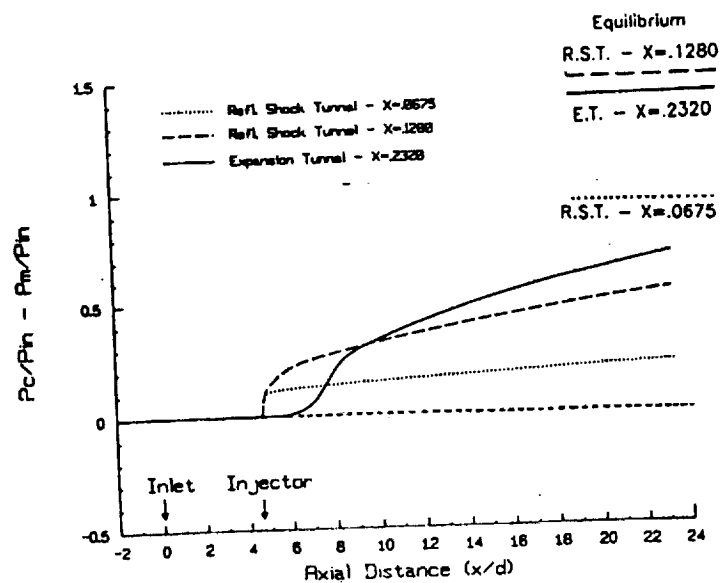


Figure 14. Computed chemical kinetic distributions and equilibrium levels of combustion pressure rise. Comparing reflected shock tunnel using depleted oxygen with expansion tunnel.

A Mass Spectrometer for Hypersonic Combustion Studies

K. A. Skinner B.Sc.(Hons).

Following on from the design discussed in a previous report, the Mass Spectrometer has been constructed and is currently undergoing commissioning in the shock tunnel, T4. A Change to the basic design has occurred during 1990. An extra skimmer has been added to the flow sampling system, making it now a three skimmer system. This has been necessary because of our inability to construct a skimmer with less than a 0.5 mm diameter orifice at its tip. Although a third skimmer has been introduced, no extra evacuated dump volume behind this skimmer has been required. Instead, the flow behind the first skimmer is vented back into the mainstream flow around the outside of the front skimmer. This is possible when the recovery pressure of the flow between the first and the second skimmers is able to be kept higher than the static pressure of the free stream flow. This requirement places limits on the distance between the two skimmers, which are a function of the orifice diameter, inlet Mach number and included skimmer angle. If the distance becomes too large the second skimmer falls behind the recovery shock (thus subjecting the sample gas to a density increase), and if the distance is too small then the second skimmer chokes the flow.

The current skimmer system is shown in figure 1. This arrangement has been tested in the shock tunnel to demonstrate the existence of a molecular beam and to measure the mass flow rate through the third skimmer. The measurement was achieved by using a 1 mm diameter thin film stagnation point heat transfer gauge constructed from a platinum film on a quartz substrate.

A heat transfer rate of 4 W/m^2 was measured 5 mm behind the third skimmer. By making the assumption that the stagnation specific enthalpy contributes only to the directed kinetic energy of the molecular beam and that the stagnation heat transfer is related to the flow velocity and density by the equation:

$$\dot{q} = 1.265 \times 10^{-4} \sqrt{\frac{\rho_{\infty}}{R}} u_{\infty}^3$$

a measure of the mass flux in the molecular beam may be obtained. R is the front radius of the heat transfer gauge. With a stagnation enthalpy of 10.5 MJ/kg, (calculated from T4 operating conditions using ESTC), the above heat transfer measurement was estimated to correspond to a mass flux of 4×10^{-15}

kg/mm²/μsec. If we assume as an order of magnitude estimate that the particles each had a mass of 10 amu., this corresponds to a particle flux of the order of 10¹¹ particles/mm²/μsec. This particle flux is approximately the assumed value of the design stage of the mass spectrometer and with the above specific enthalpy, corresponds to a particle density of 10¹⁰ particles/mm³ in the ionization region. With an electron beam current of 1 mAmp, and an ionization cross section of the order of 10⁻¹⁴ mm², this implies an expected ion production rate of 10⁶ ions/μsec.

Photographs taken of the front skimmer during a shot show that the shock wave was attached to the lip. The mach number of the flow at the front skimmer was approximately Mach 5. The mach number at the second skimmer was approximately Mach 10, but this value can be varied along with the final molecular beam density, if desired.

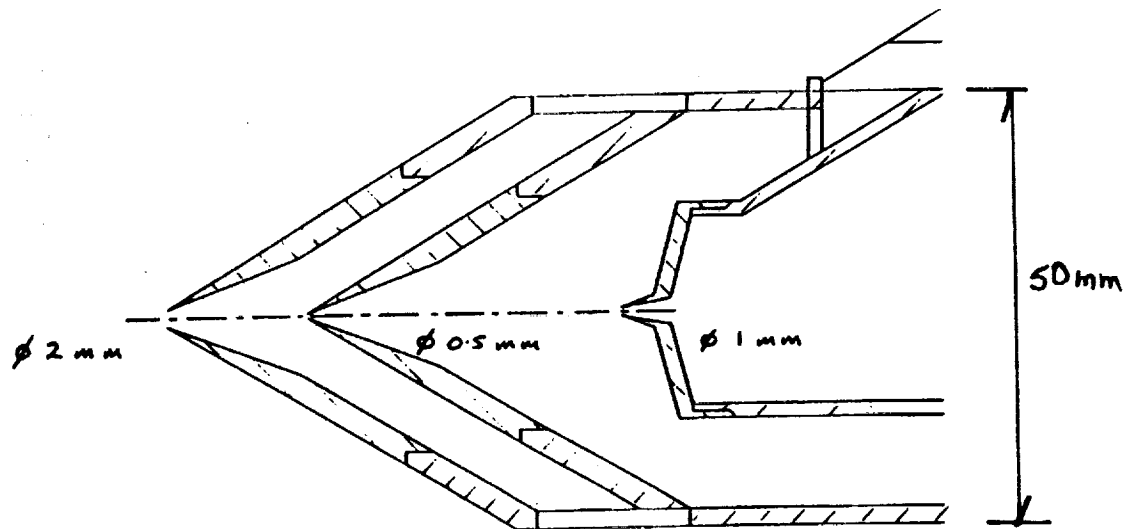


Figure 1.

SUPERSONIC AND HYPERSONIC HYDROGEN MIXING AND COMBUSTION

R.T. Casey and R.J. Stalker

INTRODUCTION

An experimental investigation of two dimensional mixing and combustion of hydrogen has been conducted. The flow has produced by ejecting hydrogen from the trailing edge of a midstream ejection strut in a rectangular duct. Since the velocity of the hydrogen was less than the velocity of the airstream, the structure of the flow was wakelike.

The purpose of the investigation was to compare predictions made by using existing analytical models with measurements of flow parameters in the combustion wake, and thereby to explore the validity of physical concepts which formed the basis of the models.

The analytical models all began with an equivalent turbulent incompressible mixing flow, based upon measurements made in a jet in a coflowing stream (Weinstein, 1956)¹. The effects of combustions and changes in species concentration across the combustion wake were modelled through the Schvab Zeldovich transformations (Kanway, 1975)². These apply strictly only to a laminar wake. The effects of density changes within the boundary layer on the boundary layer profiles were modelled through the Howarth transformation, which also applies strictly only to laminar flows, but has been used with some success in turbulent boundary layers (Baronti and Libby, 1966)³. And the effects of Mach number on the rate of growth of the combustion wake were modelled through the convective Mach number concept (Dimotakis, 1989)⁴.

EXPERIMENTS

The experiments were conducted in two series. The first series was undertaken at the Australian National University, in the shock tunnel T3. It involved quantitative flow visualization of the wake flow by Mach Zehnder Interferometry at flow Mach numbers of approximately 3.5, and was confined to the wake near the injection strut - i.e. up to some 35 initial wake widths downstream of the strut trailing edge. The flow took place in a constant area duct, with a 25 mm x 50 mm rectangular cross section.

The second series was undertaken at The University of Queensland, in the shock tunnel T4. Essentially, it involved pitot surveys of the wake, and focused particularly on the far wake - i.e. up to some 110 initial wake widths downstream of the injection strut trailing edge. Tests were conducted at flow Mach numbers of 4.3 and 5.1, employing a constant area duct with a 50 mm x 50 mm square cross section. A sketch of the model is shown in figs .

RESULTS AND DISCUSSION

Howarth Transformation

For the near wake region, the Howarth transformation, combined with the Schvab-Zeldovich transformations, produced fringe shift profiles which were generally consistent with the experimental results. This is demonstrated in fig. 1. Fig. 1(a) shows the experimental fringe profile, compared with the profile obtained from the incompressible profile without the Howarth transformation, and with the Howarth transformation. It can be seen that the use of the Howarth

transformation causes a substantial change in the fringe profile, and brings it into reasonably close agreement with the measured profile. Fig. 1(b) also displays the same consistency between measured and calculated profiles.

Combustor inlet conditions for these tests were: Air test gas, H_2 fuel.

Test No.	H_u (MJ/kg)	T(k)	p(kPa)	V(ms ⁻¹)	M	ϕ
4577	13.7	3288	141	3970	3.5	1.2
5633	14.5	3560	198	4090	3.5	1.3

For the far wake region, the results presented in figs. 3 and 4 indicate that the Howarth transformation yields a completely unsatisfactory prediction of pitot pressure profiles for H_2 /Air. Since evidence from static pressure distributions along the duct indicates that combustion is taking place in these tests, this result is consistent with the belief (Burggraf 1962)⁵ that the Howarth transformation cannot be applied to non-adiabatic flows. In the cases of both H_2 /Air and H_2 /N₂ flows, the measured pitot profiles were reasonably consistent with profiles obtained by using the Schvab-Zeldovich transformations to calculate concentration and temperature distributions from the incompressible profiles, without subsequently using the Howarth transformation.

Convective Mach Number and Wake Spreading

There are two basic parameters which may be taken as measures of the development of a combustion wake. One is the change in wake centreline flow variables in passing downstream along the wake. This provides a

measure of the rate at which momentum, thermal energy and/or species are being convected from the external flow into the centre of the wake. The other is the increase in the width of the wake in passing downstream. This provides a measure of the rate at which flow variables are convected from the centre of the wake into the external flow. In the case of wakes with self-similar profiles, these two measures must be interrelated but, in the more general case, this is not necessarily so.

The incompressible profiles from which the theoretical models are constructed are self-similar, and so a single factor, called the "spreading coefficient", can be used to characterize both the centreline flow properties and the width of the wake at any downstream station.

As shown by fig. 2, this is no longer true for the near wake. Fig. 2(a) compares values of $b(x)/a$, (the spreading coefficient normalized with respect to the initial half width of the wake) which were derived from measured values of the centreline fringe shift in the wake, with values at the same downstream distance in the incompressible jet. In the incompressible theory the centreline distribution of $b(x)/a$ depends on the magnitude of the difference between the initial jet velocity and the external flow velocity, but not on the sign of the difference - i.e., a wake and a jet yield the same distribution. It can be seen that the measured values of $b(x)/a$, with a normalized velocity difference of 0.66, are in accord with the distributions in the incompressible jet at approximately the same normalized velocity

difference.

The growth of the wake is shown by fig. 2(b). δ^1/δ_1^1 is the ratio of the measured wake width to that predicted by the incompressible model. The theoretical curve shows the wake width, as predicted by using convective Mach number theory, and it is seen that the experiments are in general accord with this prediction.

Thus, the development of the near wake along its centreline is in agreement with incompressible experiments, but the growth of the wake shows a specific effect of compressibility. This is interesting in that it suggests that the mechanisms controlling the centreline properties are the same as in incompressible flow, but the growth of the wake is affected by compressibility phenomena.

For the far wake, as displayed in figs. 3 to 5, the experimental evidence was more consistent. The estimated values of convective Mach number were less than 0.5, indicating that wake widths should be within a factor of 0.7 of the incompressible growth rates. This is generally confirmed by the pitot profiles of figs. 3 and 4, with the exception that the wake of hydrogen in nitrogen appears to be growing more rapidly than predicted by the incompressible model.

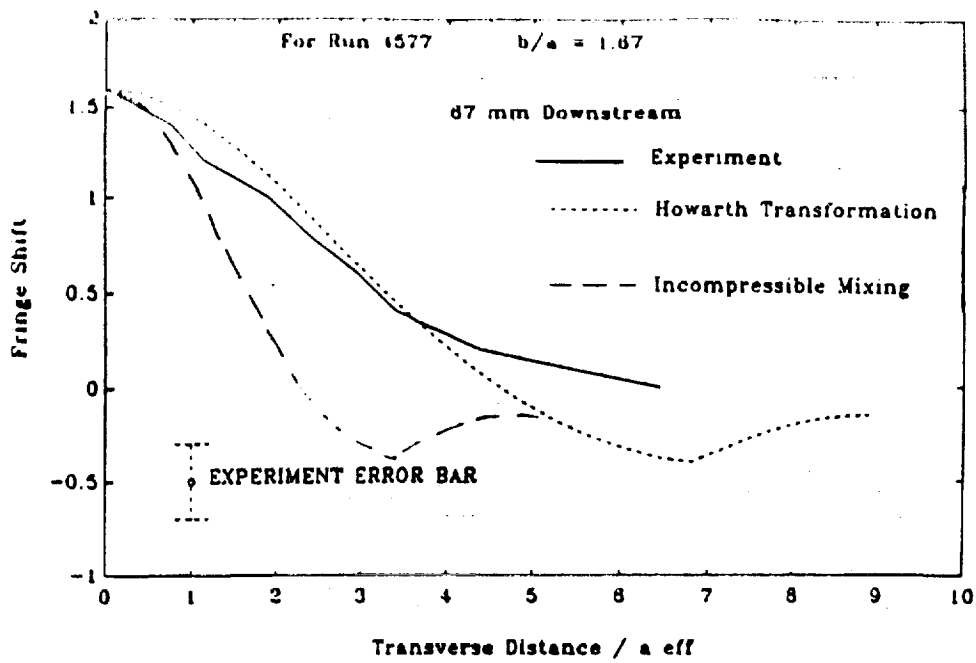
Fig. 5 shows centreline distributions of pitot pressure and, although the distributions were somewhat disturbed by the presence of shock waves and expansion waves in the duct, it can be seen that the measured centreline pitot pressures are reasonably consistent with the

predictions made from the incompressible model.

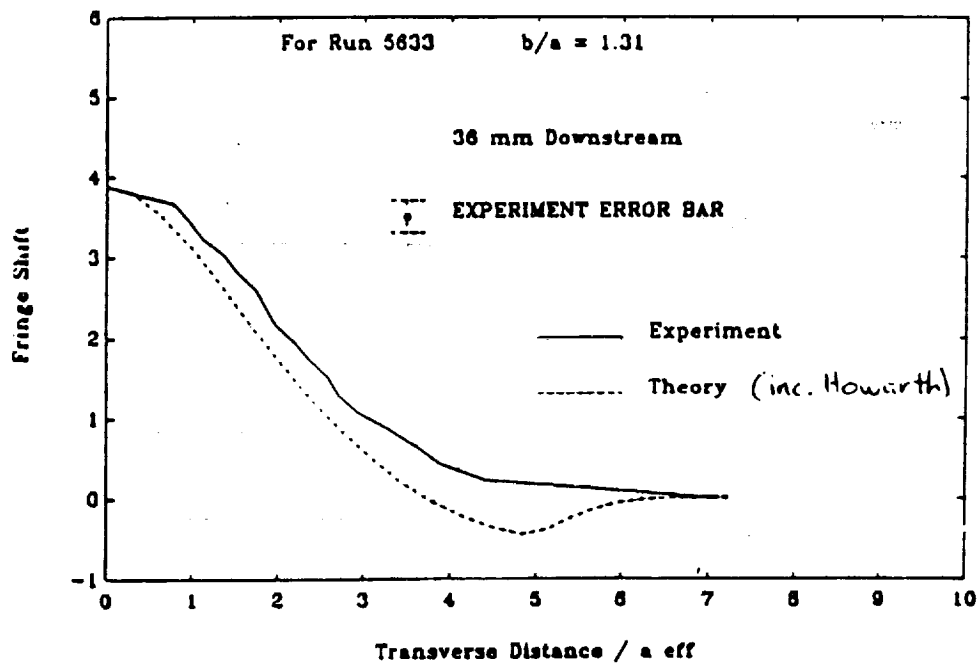
Thus, the development of both the centreline properties and the growth of wake are consistent with the incompressible model for the far wake. In view of the fact that the convective Mach number is relatively low in this region, this should not be surprising.

References

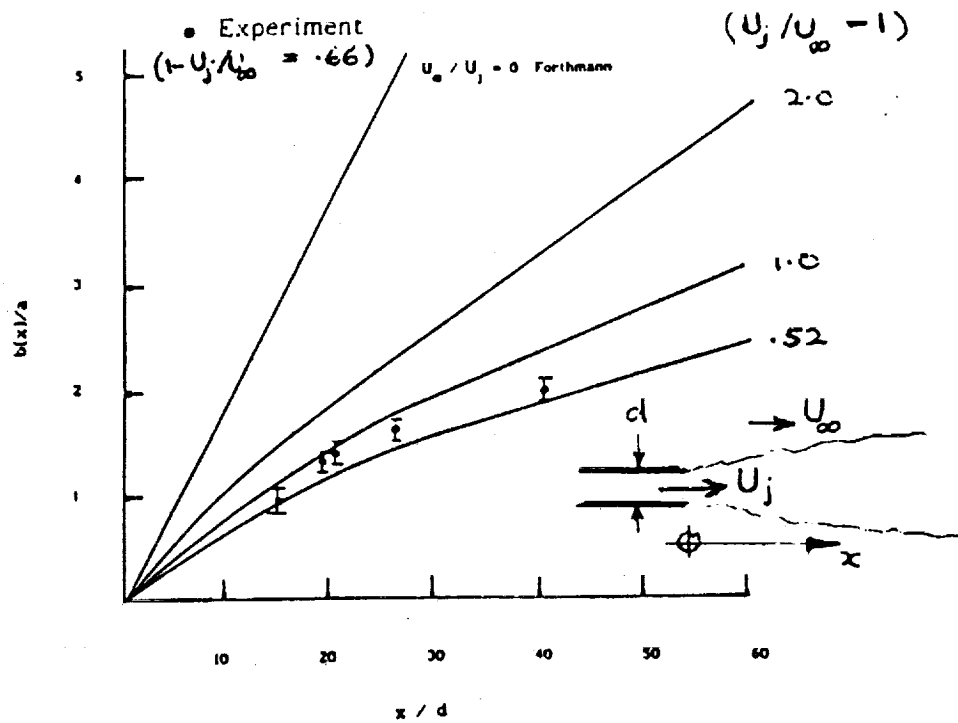
1. Weinstein, A.S., Osterle, J.F. and Forstall, W. (1956), "Momentum diffusion from a slotjet into a moving secondary", *J. Appl. Mech.* pp.437-443.
2. Kanury, A. (1975), "Introduction to Combustion Phenomena", Gordon & Breech, N.Y.
3. Baronti, P.O. and Libby, P.A. (1966), "Velocity profiles in turbulent compressible boundary layers", *AIAA J.* V4. pp.193-202.
4. Dimotakis, P.E. (1989), "Turbulent free shear layer mixing and combustion", *AIAA 27th Aerospace Sci. Mtg.* Jan 9-12, Reno, Nevada.
5. Burggraf, O.R. (1962), "The compressibility transformation and the turbulent boundary layer equations", *J. Aero-Sp. Sci.* pp.434-439.



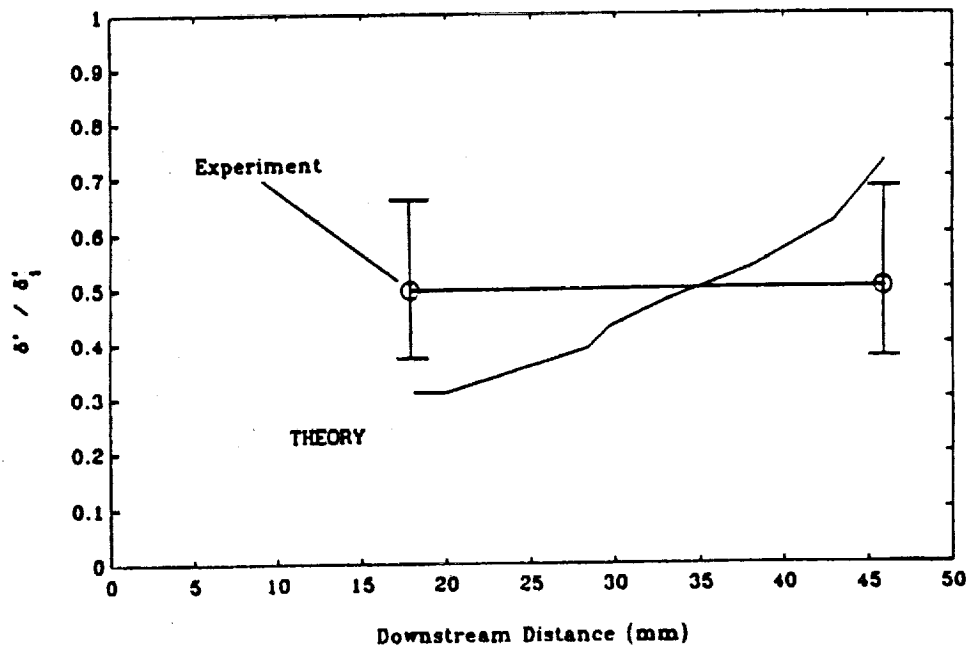
(a) Theoretical and experimental comparison of the fringe profile of run 4577 with a centre line fringe shift of 1.6



(b) Theoretical and experimental comparison of the fringe profile of run 5633 with a centre line fringe shift of 3.8.



(a) Comparison between the spreading coefficients determined from the interferograms and the results of Weinstein [1956].



(b) Compressible to incompressible mixing wake growth rate versus downstream distance for run 5633.

FIG 2. NEAR WAKE MIXING & SPREADING.

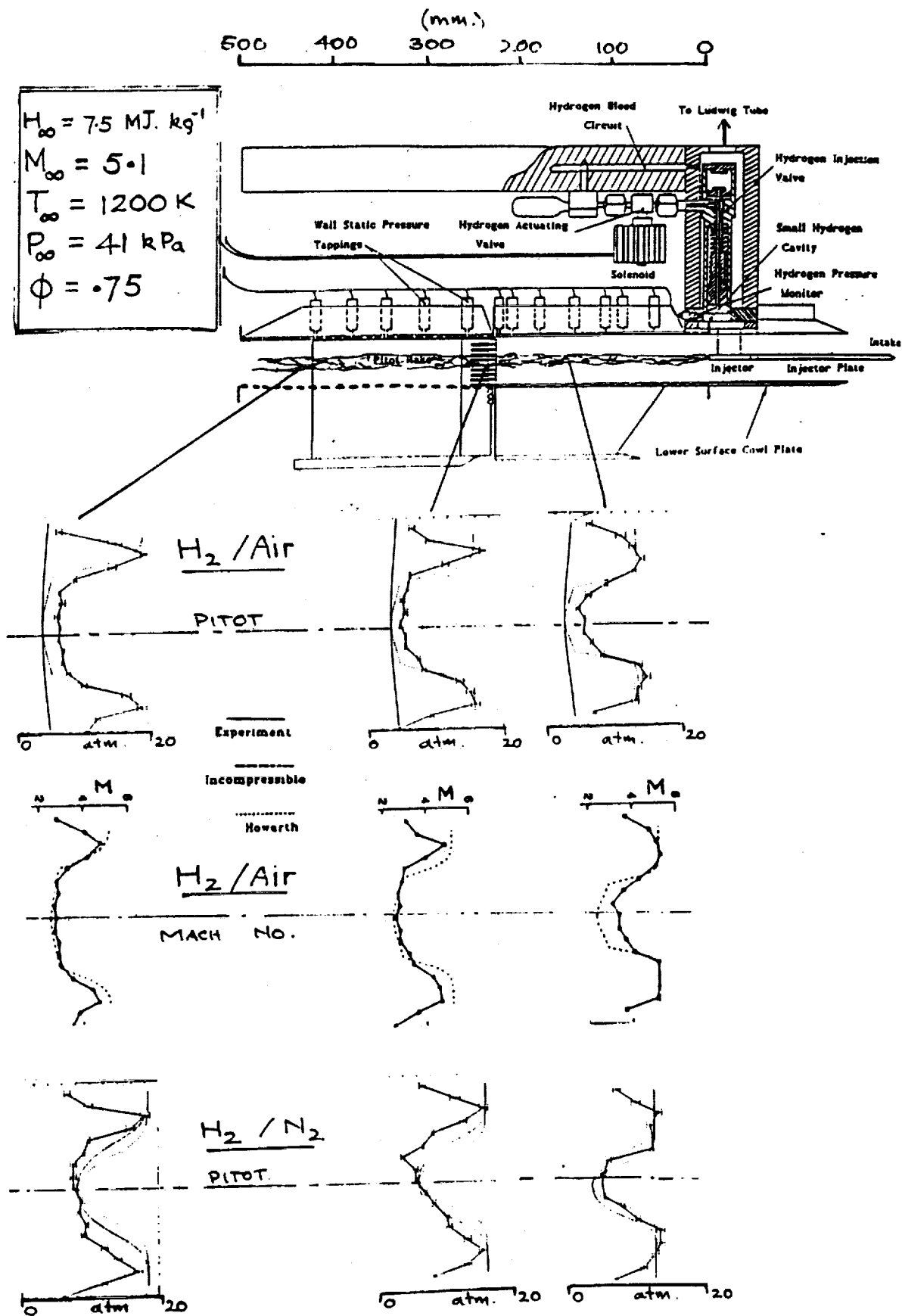
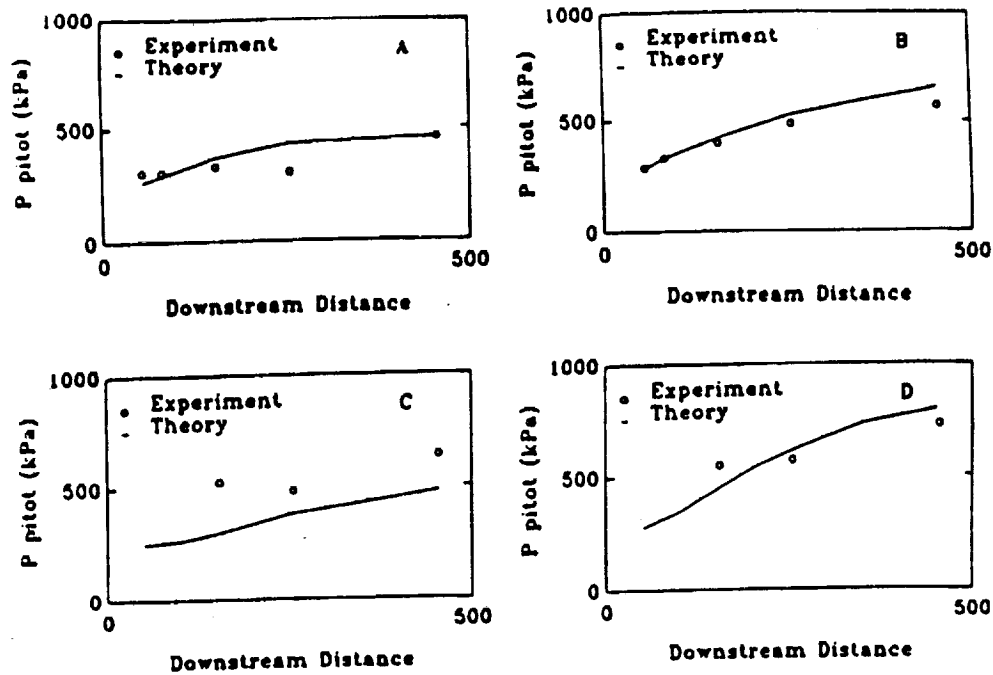


FIG 4. FAR WAKE PROFILES



Theoretical and experimental centre line pitot pressure
 A) Mach 4.31 fuel air. B) Mach 4.4 fuel nitrogen.
 C) Mach 5.06 fuel air. D) Mach 5.21 fuel nitrogen.

FIG 5. FAR WAKE MIXING

A BRIEF OVERVIEW OF WALL INJECTED SCRAMJET EXPERIMENTS

C. P. Brescianini

In this section a brief overview of the experimental work, performed in T4, on supersonic combustion with a wall injected scramjet is presented. The experiments were broken up into two sets. The first set of experiments were performed in 1989, and include shock tunnel run numbers 691-775. These experiments used a wall injected scramjet with a constant area combustion chamber, 25 mm high X 51 mm wide, as shown in Fig. 1. Intake scoops were located in between the exit of the shock tunnel's "Mach 5" nozzle and the inlet to the scramjet. These scoops were required to reduce the Mach number and to raise the static pressure. An example of the experimental static pressure distribution (pressure/ inlet pressure), along the lower wall of the scramjet combustion chamber, is shown in Fig. 3. The computed test conditions for this case (using ESTC¹ and NENZF²) are shown as "condition 3" in Table 1.

Table 1 Test Conditions

test condition	gas	H MJ/kg	p ₀ MPa	T ₀ K	p ₁ kPa	ρ_1 kg/m ³	u ₁ m/s	M ₁	$\alpha_{N2,1}$ %	$\alpha_{O2,1}$ %
3	air	9.4	8.9	2270	38	0.0558	3440	3.6	4.0	22.3
5	air	10.0	12	2070	36	0.0583	3660	4.3	3.8	20.7

The larger pressure rise seen downstream of the injector when hydrogen is injected into air, than when hydrogen is injected into nitrogen (at nominally identical conditions), indicates that substantial combustion has occurred in the former case. Similar results were also found at H = 5.9 MJ/kg conditions, however, no large pressure rises were seen for the H = 3.6 MJ/kg tests.

For run numbers 740-765 a simple "mixer", shown in Fig. 2(a), was placed on the combustion chamber wall, downstream of the fuel injector step. Figure 4 shows the pressure distribution at similar conditions to Fig. 3, except that the mixer has been used. Larger pressure rises are again seen for the hydrogen into air case than for hydrogen into nitrogen, particularly at the rear of the duct. Most of the experiments conducted with the mixer showed larger "average" pressure rises than runs performed without the mixer. (The main exception was at the low enthalpy condition where again no combustion

PRECEDING PAGE BLANK NOT FILMED

was observed). However, it could not be determined if this effect was due improved mixing rates, or some other pressure related effect.

The second set of experiments were performed in 1990, and include shock tunnel run numbers 1478-1550. The scramjet model was similar to that shown in Fig. 1, except that the combustion chamber height was increased to 50 mm. The "Mach 4" nozzle was use on the shock tunnel, and hence no intake scoops were required to produce supersonic flow. For runs 1478-1497 only the tangential wall injector was used to inject fuel. For runs 1498-1517, a single circular perpendicular injector was placed downstream of the injector step. For these runs hydrogen fuel issued from both the tangential and perpendicular injectors simultaneously. For runs 1518-1550 the perpendicular injector was replaced with a "vortex mixer", shown in Fig. 2(b). Figure 5 shows an example of the pressure distribution obtained when only the tangential wall injector was used. The test conditions are shown as "condition 5" in Table 1. Although the hydrogen into air results appear to be slightly higher than the hydrogen into nitrogen results, the pressure rise is minimal, and it is not certain whether combustion has occurred or not.

Fuel into air results with the tangential injector are compared to pressure distributions obtained with the tangential/perpendicular injector and the vortex mixer in Fig. 6. A large pressure spike appears at the rear of the scramjet for runs 1513 and 1518, most likely due to a shock wave emanating from the mixer or the perpendicular fuel stream. The "average" pressure distributions, however, are similar to run 1481 where only the tangential injector was used. If mixing and/or combustion are improved by the addition of the perpendicular injector or mixer, then the benefits do not appear to be seen in the form of higher pressures in the combustion chamber, at least not over the length of model studied here. Tests were also performed at stagnation enthalpies from 3.5 - 11.0 MJ/kg, with similar results.

References

1. McIntosh, M.K., "Computer Program for the Numerical Calculation of Frozen and Equilibrium Conditions in Shock Tunnels," Dept. of Physics, School of General Studies, Australian National University, Canberra, 1968.
2. Lordi, J.A., Mates, R.E., and Morsel, J.R., "Computer Program for the Numerical Solution of Non-Equilibrium Expansions of Reacting Gas Mixtures," NASA CR-472, 1966.

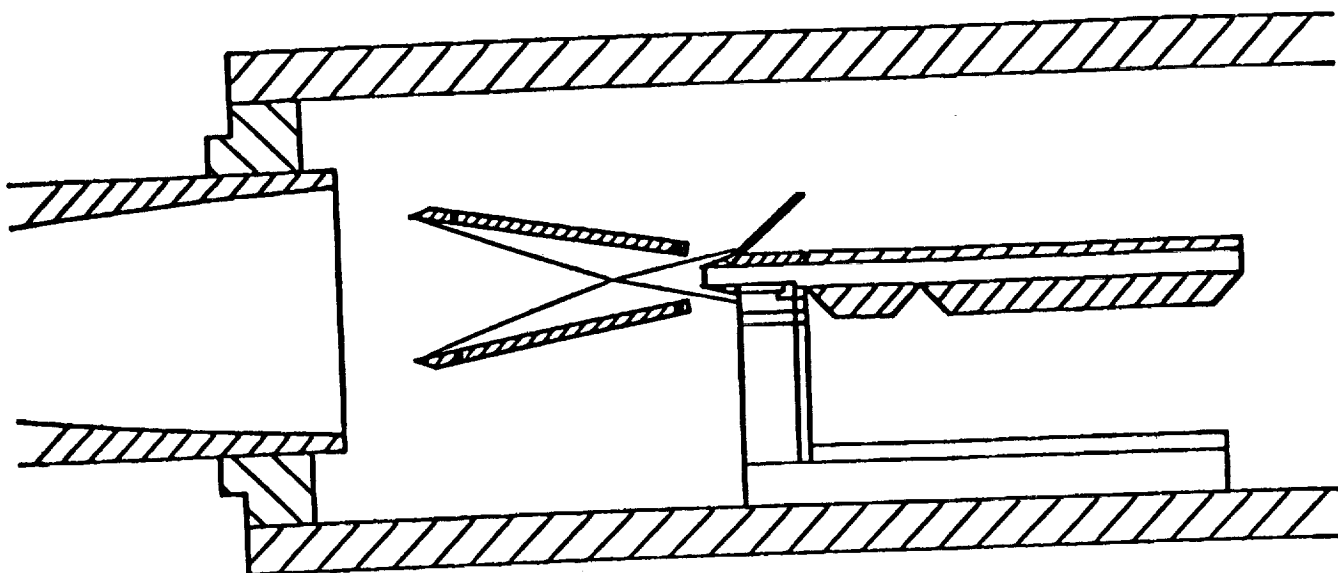


Figure 1 Scramjet Model in Shock Tunnel Test Section

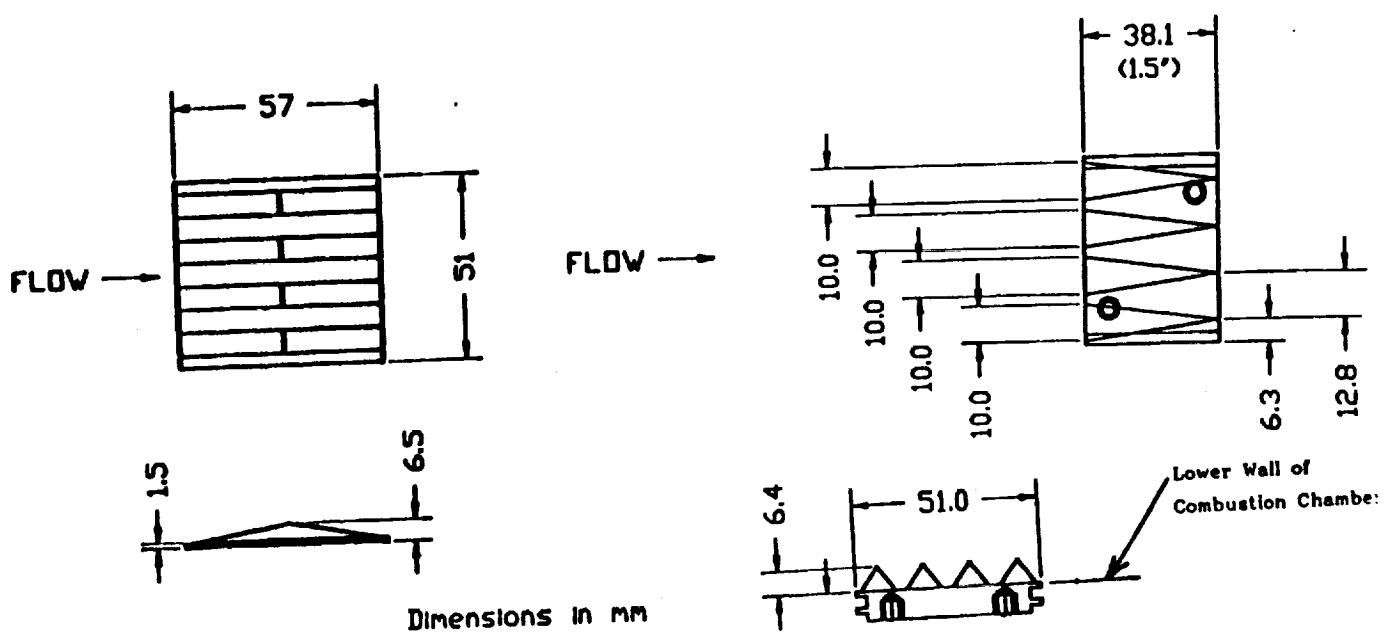


Figure 2(a) Mixer (Runs 740-765)

Figure 2(b) Vortex Mixer (Runs 1518-1550)

2.50

PRESSURE VS POSITION.
 absolute time = 5.000 msc
 flow velocity = 3440.000 mm/msc

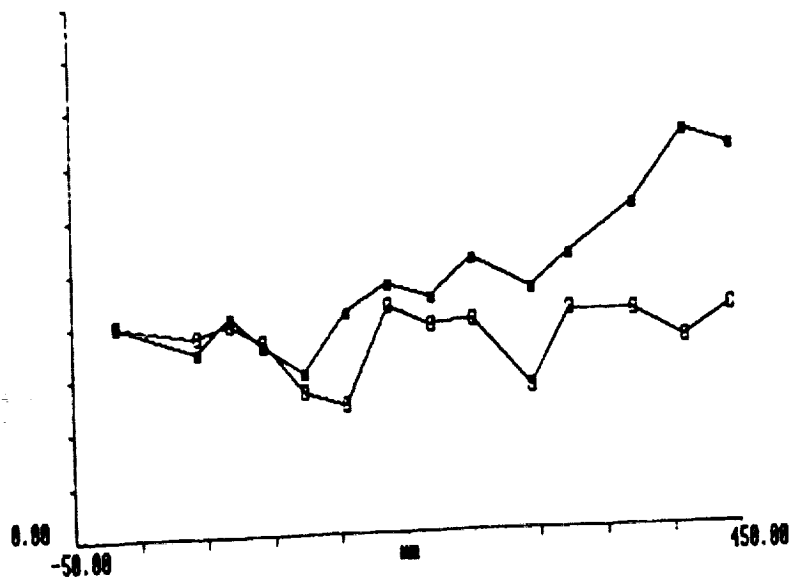


Figure 3 Axial variation in normalized static pressure on lower wall of constant area combustion chamber. Test Condition 3.

■ Run 718 H_2 into Air $\phi = 2.6$ $P_{s,H_2} = 466$ kPa
 □ Run 722 H_2 into N_2 $\phi = 2.5$ $P_{s,H_2} = 437$ kPa

2.50

PRESSURE VS POSITION.
 absolute time = 5.000 msc
 flow velocity = 3440.000 mm/msc

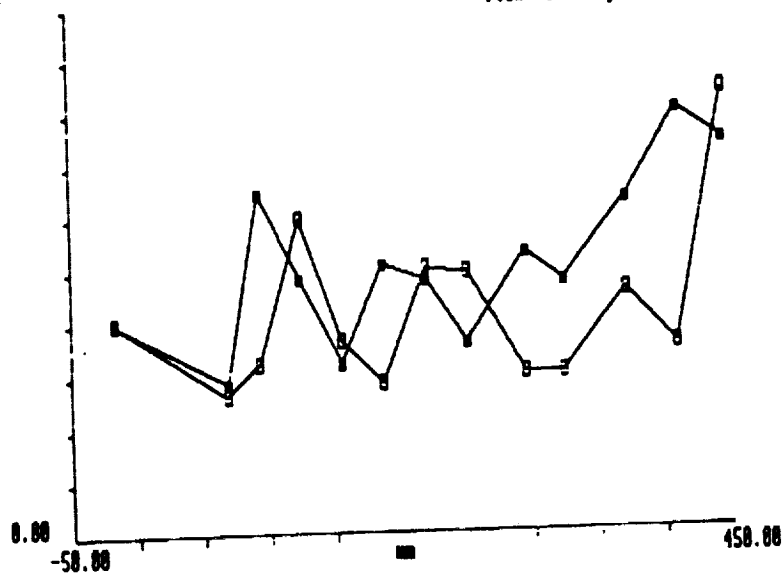


Figure 4 Axial variation in normalized static pressure on lower wall of combustion chamber with mixer. Test Condition 3.

■ Run 757 H_2 into Air $\phi = 2.4$ $P_{s,H_2} = 422$ kPa
 □ Run 758 H_2 into N_2 $\phi = 2.5$ $P_{s,H_2} = 442$ kPa

2.00

PRESSURE VS POSITION.
 absolute time = 5.000 usec
 flow velocity = 3660.000 mm/sec

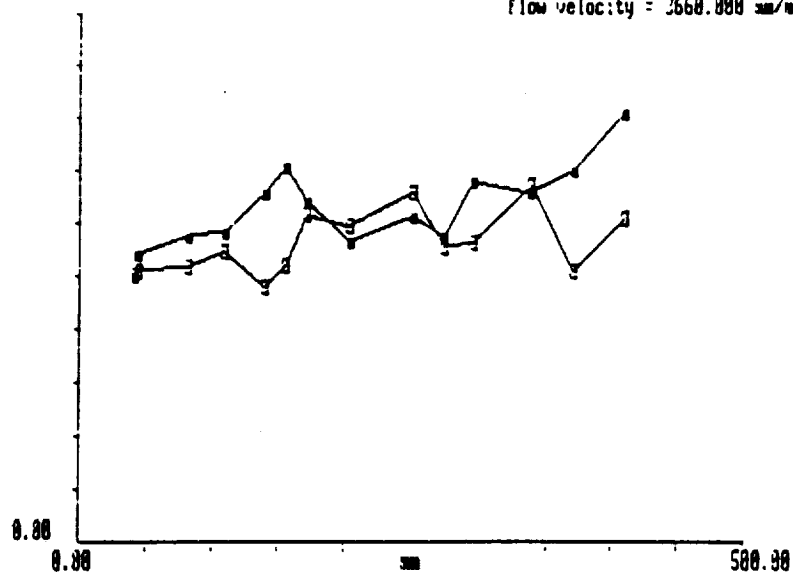


Figure 5 Axial variation in normalized static pressure on lower wall of constant area combustion chamber. Test Condition 5.

- Run 1483 H_2 into Air $\phi = 1.3$ $p_{s,H2} = 484$ kPa
- Run 1485 H_2 into N_2 $\phi = 1.3$ $p_{s,H2} = 479$ kPa

2.50

PRESSURE VS POSITION.
 absolute time = 5.000 usec
 flow velocity = 3660.000 mm/sec

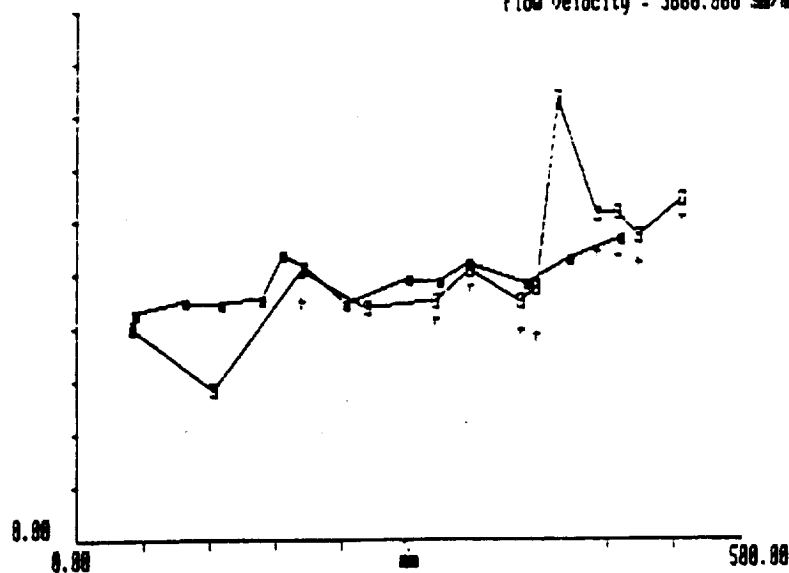


Figure 6 Axial variation in normalized static pressure on lower wall of combustion chamber. Test Condition 5.

- Run 1481 Const. Area. $\phi = 1.2$ $p_{s,H2} = 437$ kPa
- + Run 1513 Perp. Inj. $\phi = 1.2$ $p_{s,H2} = 286$ kPa
- Run 1518 Vortex Mix. $\phi = 1.2$ $p_{s,H2} = 470$ kPa

NUMERICAL MODELING OF SIDEWALL INJECTED SCRAMJET EXPERIMENTS IN A HIGH ENTHALPY AIRFLOW

C.P. Brescianini^{*}, R.G. Morgan^{**} and R.J. Stalker^{***}

University of Queensland, Brisbane, Queensland, Australia

Abstract

A wall injected, hydrogen fueled scramjet is modeled numerically using a steady, two-dimensional, parabolic, Navier-Stokes computer code with a k- ϵ model of turbulence and finite rate chemistry. The numerical results are compared to experimental scramjet data taken in a shock tunnel and are found to be in reasonable agreement. However, the numerical model required adjustment of the initial turbulence length scale, over a large range of sizes, before agreement with experiment could be obtained. This indicates that the numerical approach is not yet fully predictive. The numerical results show that combustion in the scramjet, at the conditions studied, is mainly mixing limited.

Nomenclature

$C_\mu, C_{\epsilon 1}, C_{\epsilon 2}$	constant coefficients appearing in turbulence model
E	constant in Law of the Wall
F_{mass}	mass flux ratio $(\rho u)_{\text{test gas}} / (\rho u)_{\text{H}_2}$
F_{mom}	momentum flux ratio $(\rho u^2)_{\text{test gas}} / (\rho u^2)_{\text{H}_2}$
H_j	fuel injector step height

-
- * Graduate student. Department of Mechanical Engineering.
 - ** Senior Lecturer. Department of Mechanical Engineering.
Member AIAA .
 - *** Professor of Space Engineering. Department of Mechanical Engineering. Member AIAA .

H	stagnation enthalpy
h	static enthalpy
K	hydrogen injector flow rate constant
k	kinetic energy of turbulence
l_ϵ	dissipation length scale $C_\mu k^{3/2} / \epsilon$
l_m	mixing length
m	species mass fraction
\dot{m}	mass flow rate
M	Mach number
P	production rate of turbulence energy
P_H	integration constant in energy wall function
p	pressure
p_{stube}	shock tube filling pressure
Q	time dependant flow quantity
\hat{Q}	quasi-steady flow quantity
\dot{q}	heat transfer rate
\bar{R}	universal gas constant
Re_x	Reynolds number based on axial distance from inlet
Re_{unit}	unit Reynolds number
r	near wall recovery factor
St	Stanton number based on inlet conditions $St = - \dot{q}_w / (H_{aw} - H_w)_i (\rho u)_i$
S_H	near wall Stanton number $S_H = - \dot{q}_w / (H_{aw} - H_w)_c (\rho u)_c$
s	shear stress coefficient $s = \tau_w / (\rho u^2)_c$
T	temperature

t	time
u	axial velocity
U_{shock}	shock speed
v	transverse velocity
W_M	molecular weight
x	axial distance measured from injector
x_o	reference axial distance
y	transverse distance
\dot{w}	species source term
$\alpha_{O_2}^*$	mass of dissociated oxygen (in all forms) divided by total oxygen (%)
α_{O_2}	mass of atomic oxygen divided by total oxygen (%)
γ	ratio of specific heats
δ	boundary layer thickness
η_{MIX}	mixing efficiency defined as the amount of reacted hydrogen (hydrogen mass in the form of water) if all <u>mixed</u> hydrogen and oxygen reacted completely, divided by the same quantity if mixing had been complete
η_{RR}	reaction rate combustion efficiency defined as reacted hydrogen, divided by the amount of reacted hydrogen if the hydrogen and oxygen <u>which are</u> <u>mixed</u> reacted completely
η_{STOICH}	stoichiometric combustion efficiency defined as reacted hydrogen, divided by the amount of reacted hydrogen if mixing was complete and the hydrogen and oxygen reacted completely
η_{TF}	total fuel combustion efficiency

defined as reacted hydrogen, divided by the total amount of hydrogen

κ	von Karman's constant
μ	viscosity
ρ	density
σ	constant used in evaluating transport coefficient
τ	shear stress
τ_{delay}	time delay
ϕ	equivalence ratio

subscripts

aw	adiabatic wall
c	near wall grid point (edge of Couette layer)
eff	effective
i	inlet
j	injector
H	stagnation enthalpy
H ₂	hydrogen
l	laminar
m	species mass fraction
O ₂	oxygen
s	stagnation
t	turbulent
u	momentum
w	wall

superscripts

+	Law of the Wall variable
---	--------------------------

Introduction

The current development of the American National Aerospace Plane (NASP) has led to a revival of interest in high speed propulsion. Most of the high speed air breathing propulsion research has centered around the scramjet (supersonic combustion ramjet) engine. The scramjet engine may be required to operate at extremely high speeds (up to approx. 8 km/s) and high Mach numbers (up to approx. M 25). To verify the viability of the scramjet engine an extensive series of ground tests in wind tunnels must be performed. Testing of scramjet engines requires a wind tunnel facility which can not only produce supersonic gas flow of the correct Mach number, but also the high temperatures and pressures needed to simulate the combustion process. The only type of facilities currently available for performing such "high enthalpy" simulations, at stagnation enthalpies greater than 3.5 MJ/kg (corresponding to flight speeds > 2.7 km/s), are pulsed facilities. These facilities create the extremely high stagnation enthalpy conditions required by heating the test gas with a shock wave. Currently the only operational pulsed facilities which can produce energy levels typical of hypervelocity flight are the HYPULSE expansion tube (Tamagno, Bakos, Pulsonetti and Erdos¹), located at General Applied Science Laboratories, New York, and the free piston shock tunnels, T3 (Stalker²) and T4 (Stalker and Morgan³), located at the Australian National University, Canberra, and the University of Queensland, Brisbane, respectively.^d

Pulse facilities can create the extremely high stagnation enthalpy conditions required, but the price paid is a reduction in the available test time compared to a conventional wind tunnel. In general, shock tunnels have a significant advantage in test time over expansion tubes, however, expansion tubes have the advantage of providing a test flow with significantly reduced dissociation when compared to shock tunnels operating at the same stagnation enthalpy conditions. Using these facilities in a complimentary fashion it is possible to simulate supersonic and hypersonic combustion at speeds up to orbital velocity.

^d Since this paper was originally written, the free piston shock tunnel T5 (Hornung and Sturtevant³³), located at GALCIT, Pasadena, has also been commissioned.

The first scramjet experiments to be performed in the pulse facilities mentioned above, were conducted in the T3 shock tunnel during the early 1980's. A thorough description of the experimental procedure and results can be found in Stalker and Morgan⁴. For these early experiments the hydrogen fuel was injected from the rear of a fuel injection strut located midway between the upper and lower walls of the combustion chamber. This fuel injection configuration was called "central injection". While experimental results with central injection were very encouraging, it was realized that in an actual scramjet engine, the heat load to an injector located in the middle of a high velocity air stream may be unbearably high. A better alternative, from a heat transfer point of view, is to locate the injector along the walls of the combustion chamber. This approach has the second advantage, in that if an excess of hydrogen fuel is injected, the fuel can form an insulating layer along the walls of the combustion chamber. This insulating layer may significantly reduce the heat transfer from the airflow to the combustion chamber walls.

To test the concept of the "wall injected" scramjet a further series of experiments were performed by Morgan, Paull, Morris, and Stalker^{5,6}. The results from these wall injected experiments showed a significantly reduced static pressure rise in the combustion chamber when they were compared to the pressure rises seen with central injection, at the same nominal test conditions. The static pressure rises were taken as indicative of the amount of combustion which had occurred. In an attempt to explain the apparent decrease in combustion the authors of Refs. 5 and 6 postulated the existence of a significant layer of cold hydrogen and air located along the lower wall of the scramjet model. It was presumed that this layer had been quenched by the cold walls of the model to below the temperature required for ignition and combustion. In this study a detailed investigation of the wall injected scramjet flow field is carried out using a CFD (Computational Fluid Dynamics) code, aiming to reproduce the experimental results. By examining the numerical results it was hoped that some of the reasons for the low static pressure rises could be identified.

Shock Tunnel Tests of Wall Injected Scramjet

Description of Wall Injected Scramjet Model

The wall injected scramjet model used in Refs. 5 and 6 is depicted in Fig. 1. The model was nominally 2-dimensional, consisting of a 20 mm high, by 51 mm wide inlet. A 5 mm step was located along the lower wall, 88.5 mm downstream of the model's inlet. Hydrogen fuel (with total temperature equal to room temperature) was injected from the rear of this step into the model's combustion chamber. Two types of nozzles were used in the wall injector to meter the flow of hydrogen. Details of these two nozzles can be seen in Figures 2(a) and 2(b). The hydrogen flow rate was varied by changing hydrogen injection (reservoir) pressure.

Downstream of the wall injector was a constant area combustion chamber. Experimental data consisted of static pressure measurements at the inlet of the scramjet and along the lower wall of the combustion chamber, as well as heat transfer measurements along the lower wall. The final transducer in the combustion chamber (a heat transfer gauge) was located 316 mm downstream of the injector.

The high enthalpy test gas for the experiments was provided by the T3 shock tunnel which was operated in reflected, under-tailored, mode. Under-tailored operation was used to lengthen the time before the test gas (air or nitrogen) was contaminated with driver gas (helium). Typically test times were of the order 0.5 - 1.0 ms. The test gas was expanded from the stagnation conditions at the end of the shock tube, to the free stream test conditions, by a nominally Mach 3.5, contoured, axisymmetric nozzle.

Numerical Modeling

Accurate modeling of all aspects of a short flow duration experiment, including the flow establishment time, requires a time accurate computer code capable of solving the complete Navier-Stokes equations. Such computer codes are currently available, an example of which is the SPARK code^{7,8}. Numerical simulation of pulse facility flows using SPARK have been performed by Rogers and Weidner⁹, and more recently by Jacobs, Rogers, Weidner and Bittner¹⁰. The computational effort required, however, is so large that such solutions have so far been limited to non-reacting cases where turbulent mixing effects are usually ignored.

While time accurate solutions might be the ideal way to model short duration test flows, present day computer limitations mean that it is more

desirable to use a steady state computer code, provided that physically realistic answers are produced. The steady state/ transient flow comparisons made to date in Refs. 9 and 10 are very important in this respect, so that the steady state approach can be verified. So far the results have been encouraging. In Ref. 10 a 500 mm long generic scramjet was modeled with a Mach 5 relaxing test flow to simulate under-tailored shock tunnel operation in T4. The flow was treated as laminar, and hydrogen injection was not considered. The general conclusion was that a flow duration of the order of a few hundred microseconds was probably adequate for establishment of a flow which closely approximated the steady state conditions (within experimental uncertainty). The only significant exceptions to this were the flow properties evaluated at positions where strong shock waves struck the model walls. In these regions a significantly longer flow establishment time was required and the numerical computations were not continued until steady state was reached.

The computer code used in this study is known as CHARMS. The code is an extensive modification of the original CHARNAL code described in Ref. 11. Although not as sophisticated as some of the computer codes currently available to model scramjet combustors (see Anderson, Kumar, and Erdos¹² for a brief summary of some of these codes), CHARMS possesses a few significant advantages. The code is steady, 2-dimensional and parabolic, consequently, the computer resources required to run the code are significantly reduced compared with some of the more recent 3-dimensional, time accurate, full Navier-Stokes codes. Since the flow in the model scramjet is expected to be mostly supersonic with a predominant flow direction, the loss in accuracy in applying a parabolic code, as opposed to a full Navier-Stokes code, is expected to be very small. The main areas where the parabolic assumptions are not accurate are in the small recirculating region near the thick lip of the cylindrical injector, and also the possibility of shock wave/ boundary layer interactions.

Another significant advantage of CHARMS is that it possesses a two-equation, eddy viscosity turbulence model. Although there must be some apprehension in applying any of the currently available turbulence models to the relatively unexplored area of supersonic combustion, the $k-\epsilon$ model remains a much more advanced model than the zero, or one, equation eddy viscosity models which are usually used in the larger, full Navier-Stokes, computer codes.

Previous computations of the wall injected, shock tunnel- scramjet

tests, using steady state codes, have been performed by Rogers, Drummond, and Weldner¹³, and Brescianini and Morgan¹⁴. Whereas these previous References used only "nominal" inlet test conditions, the work here has been extended by using test conditions calculated for each individual shock tunnel run, and also re-evaluated experimental data. The current computations take into consideration the finite rate chemical reactions, and the expected mismatch in the hydrogen and air static pressures at the hydrogen injector.

Description of Computer Program

Conservation Equations

CHARMS solves partial differential equations for the transport of x and y momentum, energy, and species, given by the following equations

$$\rho u \frac{\partial u}{\partial x} + \rho v \frac{\partial u}{\partial y} = \frac{1}{y^i} \frac{\partial}{\partial y} \left(\frac{\mu}{\sigma_u} y^i \frac{\partial u}{\partial y} \right) - \frac{\partial p}{\partial x} \quad (1)$$

$$\rho u \frac{\partial v}{\partial x} + \rho v \frac{\partial v}{\partial y} = - \frac{\partial p}{\partial y} \quad (2)$$

$$\begin{aligned} \rho u \frac{\partial H}{\partial x} + \rho v \frac{\partial H}{\partial y} = & \frac{1}{y^i} \frac{\partial}{\partial y} \left(\frac{\mu}{\sigma_H} y^i \frac{\partial H}{\partial y} \right) + \\ & \frac{1}{y^i} \frac{\partial}{\partial y} \left[y^i \left(\mu \left(\frac{1}{\sigma_u} - \frac{1}{\sigma_H} \right) \frac{\partial (u^2/2)}{\partial y} - \frac{\mu}{\sigma_H} \left(\frac{\partial (v^2/2)}{\partial y} \right) + \right. \right. \\ & \left. \left. \mu \left(\frac{1}{\sigma_k} - \frac{1}{\sigma_H} \right) \frac{\partial k}{\partial y} + \mu \sum_j \left(\frac{1}{\sigma_{m,j}} - \frac{1}{\sigma_H} \right) h_j \frac{\partial m_j}{\partial y} \right) \right] \end{aligned} \quad (3)$$

$$\rho u \frac{\partial m}{\partial x} + \rho v \frac{\partial m}{\partial y} = \frac{1}{y^i} \frac{\partial}{\partial y} \left(\frac{\mu}{\sigma_m} y^i \frac{\partial m}{\partial y} \right) + \dot{w} \quad (4)$$

where

$$H = h + \frac{u^2 + v^2}{2} + k \quad (5)$$

and $i = 0$ for plane flow, 1 for axisymmetric flow.

The density is obtained from the ideal gas relation,

$$\frac{p}{\rho} = \frac{R}{M_w} T \quad (6)$$

where M_w is the local mean molecular weight of the mixture. The solution of the differential equations is accomplished by the finite difference method of Patankar and Spalding¹⁵. The effects of lateral pressure gradients in the flow are calculated using the SIMPLE algorithm as described by Elghobashi and Spalding¹⁶.

The thermodynamic properties of specific heat and static enthalpy are calculated using polynomial equations as functions of temperature. Values for the coefficients used in the polynomials have been taken from the combustion program described in Refs. 17 and 18.

Transport Properties

The transport coefficients appearing in the conservation equations are taken as the effective addition of laminar and turbulent components,

$$\frac{\mu}{\sigma} = \frac{\mu_l}{\sigma_l} + \frac{\mu_t}{\sigma_t} \quad (7)$$

Values for the Prandtl/ Schmidt numbers (σ_H , σ_m) used in the current computations are listed in Table 3. It has been assumed that the Prandtl and Schmidt numbers are equal. A value of unity has been used for $\sigma_{l,u}$ and $\sigma_{t,u}$.

The laminar viscosity, for each component of the gas mixture, is determined by using either a power law relationship or a Sutherland's viscosity law. The local laminar viscosity of the mixture (μ_l) is then found by combining the components using Wilke's formula¹⁹.

The turbulent viscosity is calculated by the well known k- ϵ model of turbulence²⁰. With this model the turbulent viscosity is found from

$$\mu_t = C_\mu \rho \frac{k^2}{\epsilon} \quad (8)$$

where C_μ is a constant, and k and ϵ are found by solving the following transport equations

$$\rho u \frac{\partial k}{\partial x} + \rho v \frac{\partial k}{\partial y} = \frac{1}{y^l} \frac{\partial}{\partial y} \left(\frac{\mu}{\sigma_k} y^l \frac{\partial k}{\partial y} \right) +$$

$$\mu_t \left(\frac{\partial u}{\partial y} \right)^2 = \rho \epsilon \quad (9)$$

and

$$\begin{aligned} \rho u \frac{\partial \epsilon}{\partial x} + \rho v \frac{\partial \epsilon}{\partial y} = \frac{1}{y^1} \frac{\partial}{\partial y} \left(\frac{\mu}{\sigma_\epsilon} y^1 \frac{\partial \epsilon}{\partial y} \right) + \\ C_{\epsilon 1} \left(\frac{\epsilon}{k} \right) \mu_t \left(\frac{\partial u}{\partial y} \right)^2 - C_{\epsilon 2} \left(\frac{\epsilon}{k} \right) \rho \epsilon \end{aligned} \quad (10)$$

simultaneously with the equations governing the mean flow.

The values assigned to the turbulence constants which appear in equations (8-10) are the values given by Launder and Spalding²¹

$$C_\mu = 0.09, \quad C_{\epsilon 1} = 1.44, \quad C_{\epsilon 2} = 1.92$$

$$\sigma_{1,k} = \sigma_{1,\epsilon} = \sigma_{t,k} = 1.0, \quad \sigma_{t,\epsilon} = 1.3$$

Wall Functions

CHARMS makes use of wall functions to relate the fluxes through the wall with the values of the dependant variables at the near wall grid points. The wall functions used assume that the Law of the Wall, given by

$$u^+ = \frac{1}{\kappa} \ln (E y^+) \quad (11)$$

where κ and E are constants, holds in the fully turbulent region close to the wall.

The original CHARNAL code used wall function relations based upon incompressible Law of the Wall variables, however, compressible relations have been incorporated into CHARMS. If ρ and μ are variables (as in compressible flow) it can be shown that the Law of the Wall is theoretically applicable if u^+ and y^+ are defined as follows:

$$u^+ = \frac{u_{eff}}{\sqrt{\tau_w / \rho_w}} \quad (12)$$

and

$$y^+ = \frac{y_c \sqrt{\tau_w \rho_w}}{\mu_w} \quad (13)$$

The near wall Stanton number (S_H) is evaluated from

$$S_H = \frac{s}{\sigma_H \left[\frac{\tau_w}{\tau_\theta} + P_H \sqrt{s} \sqrt{\rho_c / \rho_w} \right]} \quad (19)$$

where

$$\tau_\theta = \frac{u_c}{\int_{u=0}^{u=u_c} 1/\tau \, du} \quad (20)$$

and P_H is an integration constant. This equation is based on the wall function relation given by Spalding²⁶, except that it has been modified here to account for the variation in fluid properties and shear stress throughout the layer. Catalytic wall effects have been ignored in the derivation.

A relation for P_H has been determined by Jayatillaka²⁵ from reference to incompressible data and is given by

$$P_H = 9.24 \left[\left(\frac{\sigma_{1,H}}{\sigma_H} \right)^{3/4} - 1 \right] \left[1 + 0.28 \exp \left(-0.007 \frac{\sigma_{1,H}}{\sigma_H} \right) \right] \quad (21)$$

Chemistry

An 8 reaction, 7 species, finite rate chemistry scheme, described by Evans and Schexnayder²⁷, is used to calculate the species source term, \dot{w} . Evans and Schexnayder have compared this 8 reaction scheme (which treats nitrogen as inert) with a 25 reaction, 12 species scheme that treated nitrogen as reactive. For the experimental test cases that they studied it was found that the 25 reaction system was superior in predicting ignition, however, once ignition had occurred, the 8 reaction system was as good as the 25 reaction system.

Experimental Test Conditions

Computational results are presented for two nominal, experimental inlet conditions reported in Ref. 6, namely the conditions referred to as "4.2 MJ/kg - Mach 3.5" and "8.7 MJ/kg - Mach 3.5" in that report. These test conditions correspond to the mid-range of the likely scramjet envelope,

covering the speeds 2.8 - 4.2 km/s.

The experimental data has been re-evaluated for this study and differs to the data presented in the preliminary report. The main differences are in the heat transfer rates, which had previously been incorrectly integrated from the temperature signals. The experimental data was sampled every 0.016 ms, with typically at least 100 points in time being recorded. All the experimental pressures presented here have been averaged over 5 points in time (or 0.08 ms) to help eliminate noise.

The heat transfer measurements were taken using thin film heat transfer gauges. The gauges measured the temperature of a thin film of platinum painted onto a substrate of Down Corning "Macor" glass ceramic. The variation in temperature was then integrated to obtain the heat transfer rate into the substrate according to the 1-dimensional semi-infinite theory approach of Schultz and Jones²⁸. A value of $2000 \text{ J m}^{-2} \text{ K}^{-1} \text{ s}^{-1/2}$ was used as the thermal product of the substrate.

The stagnation temperature of the test gas in the shock tube was evaluated using a 1-dimensional, equilibrium, computer program ESTC²⁹. The program used the experimentally recorded shock tube filling pressure, incident shock speed, and the stagnation pressure during the test time, as inputs. The results are shown in Table 1.

Table 1 Conditions in Shock Tube

Run No.	Test Gas	P_{tube} kPa	U_{shock} m/s	P_s MPa	T_s K	H MJ/kg
7241	Air	150	2180	13.90	3120	3.9
7281	Air	150	2070	12.46	2880	3.5
7247	Air	54	2980	10.94	4730	7.4
7279	Air	54	2980	13.85	4900	7.7
7235	Air	54	2980	10.68	4710	7.3
7236	N ₂	54	2980	10.88	5600	7.3

The flow conditions at the exit of the shock tunnel nozzle (and thus at the inlet to the scramjet) were then estimated by using a quasi 1-dimensional, nozzle flow program, NENZF³⁰. NENZF takes into consideration the non-equilibrium chemical effects which occur in the shock tunnel nozzle as the test gas expands from stagnation to free stream test conditions. The

1-dimensional nature of the computations, however, does not allow for boundary layer growth in the nozzle or the 2-dimensional nature of the pressure field. A first order correction was made by terminating computations when the predicted static pressure agreed closely with the experimentally recorded static pressure at the inlet to the scramjet. The results are shown in Table 2.

Table 2 Scramjet Inlet Conditions

Run No.	H ^a MJ/kg	T _i K	P _i kPa	ρ _i kg/m ³	u _i m/s	M _i	α _{02,i} %	α _{02,i} %	γ _i
7241	3.9	1080	148	0.478	2240	3.5	17.11	0.12	1.33
7281	3.5	1030	143	0.487	2170	3.5	6.25	0.08	1.34
7247	7.4	2220	147	0.228	2970	3.3	22.14	7.05	1.30
7279	7.7	2340	184	0.270	3040	3.2	22.00	6.99	1.30
7235	7.3	2190	137	0.215	2970	3.3	22.16	7.06	1.30
7236	7.3	2100	119	0.191	3110	3.4	-	-	1.30

^a H = 0.3 MJ/kg for air at 300 K

The experimentally recorded, hydrogen reservoir (injection) pressures, and the type of hydrogen injection nozzle used for each shock tunnel run, are shown in Table 3. The mass flow rate of hydrogen through the injector was calculated from

$$\dot{m}_{H_2} = K P_{S,H_2} \quad (22)$$

where the value of K was determined experimentally to be 3.2×10^{-5} kg/s/kPa for the cylindrical injector. An identical value of K has been assumed here for the source flow injector.

The equivalence ratio was then calculated using this hydrogen flow rate and an air flow rate evaluated from the conditions shown in Table 2. The results are also shown in Table 3.

Table 3 Hydrogen Injection Conditions and Turbulence Constants

Run No.	P_{s,H_2} kPa	ϕ	Inject Nozzle	F_{mass}	F_{mom}	ℓ_c / H_j	$\sigma_{t,H,m}$	$\sigma_{l,H,m}$
7241	993	1.0	cylin.	8.6	8.0	0.06	0.9	0.72
7281	927	1.0	source	9.0	8.2			
7247	993	1.6	cylin.	5.4	6.7	0.003	0.8	0.72
7279	1010	1.3	source	6.4	8.2			
7235	1320	2.2	cylin.	3.8	4.8	0.0008	0.8	0.72
7236	1390	(2.5)	cylin.	3.4	4.4	0.01	0.8	0.72

Initial Conditions for Computer Program

Numerical computations began at the point of hydrogen injection, and marched downstream. The hydrogen conditions at the initial station were estimated by calculating the theoretical throat size (using one-dimensional, isentropic relations, with $\gamma_{H_2} = 1.4$ and $T_{s,H_2} = 300$ K) which would give the experimental hydrogen mass flow rates. The hydrogen was then isentropically expanded, from this theoretical throat size, to the hydrogen injector exit height (taken here as 5 mm).

A step change in the velocity and temperature was assumed at the hydrogen/air interface, and no account was been made for the boundary layer which would exist on the top surface of the injector. If any recirculating regions were present near the injector, their effects were ignored. The hydrogen fuel was assumed to be initially moving parallel to the main airflow.

The air stream conditions at the initial station were taken as identical to those at the scramjet inlet (Table 2), except for a small boundary layer on the upper wall. Computed estimates for the size of the boundary layer are shown in Table 4. The value of Reynolds number/ unit Reynolds number, at an axial distance corresponding to the injector step, would indicate that the boundary layer is most probably laminar or transitional at this point³¹. Nevertheless, because the k- ϵ model employed is designed for fully turbulent flows, the turbulent boundary layer thickness was used. The wall temperature was assumed fixed at 300 K.

Table 4 Boundary Layer Thickness At Injector

Run No.	H	M	Re_x	Re_{unit}	δ_l	δ_t
	MJ/kg			m^{-1}	mm	mm
7241	3.9	3.5	2.2×10^6	24.9×10^6	0.3	1.7
7233	7.4	3.3	0.8×10^6	9.1×10^6	0.4	1.8

The calculated test gas composition indicates that a substantial part of the dissociated oxygen is in the form of NO (compare $\alpha_{O_2}^*$ and α_{O_2} in Table 2). Since the combustion model used in the calculations assumes nitrogen to be inert, the oxygen in the form of NO must be "redistributed" to either O_2 or atomic oxygen. In the following computations the dissociated oxygen fraction has been assumed equal to α_{O_2} .

The initial values of turbulent kinetic energy and dissipation were estimated from

$$k = \max \left[\left(\frac{\ell_c}{\sqrt{C_\mu}} \frac{\partial u}{\partial y} \right)^2, k_{background} \right] \quad (23)$$

and

$$\epsilon = \frac{C_\mu k^{3/2}}{\ell_c} \quad (24)$$

These equations are based upon an assumption that $P/\epsilon = 1$ in the regions of turbulence production. The value of $k_{background}$ was estimated by

$$k_{background} = 4.0 \times 10^{-4} u^2 \quad (25)$$

as suggested by Spalding et. al.¹¹

The dissipation length scale, ℓ_c , required in equations (23) and (24), was adjusted until reasonable agreement was obtained with the computed and experimental heat transfer results downstream of the injector. The final values used are indicated in Table 3. It is unfortunate that a single value of ℓ_c/H_j , suitable for all the test conditions, could not be found. The reduction in ℓ_c/H_j , seen in Table 3, could be due to the corresponding decrease in the mass and momentum flux ratio of the two gas streams at the injector which may decrease the mixing rate. The number of cases studied here, however, is too small to draw any firm conclusions. The initial value

of ℓ_c was assumed constant across the flow except near the walls, where ℓ_c was limited to ensure that the mixing length (ℓ_m) did not exceed κy . The values of κ and E used in the computations were:

$$\kappa = 0.435, \quad E = 9.00$$

These values have been previously suggested by Patankar and Spalding¹⁵, and have been found to give good results for wall jets.

Numerical Results

$$H = 3.9 \text{ MJ/kg}, \quad \phi = 1.0$$

Figure 3(a) shows the computed static pressures, on the lower wall of the scramjet, normalized by the initial air stream static pressure for run number 7241. Also shown on Figure 3(a) are the experimental results obtained using the cylindrical (run 7241, $\phi = 1.0$) and the source flow (run 7281, $\phi = 1.0$) hydrogen injection nozzles. The overall pressure level predicted by the computer program is in good agreement with the experiments, although agreement in the pressure distribution shape is not so good. The widely spaced pressure transducers provide only coarse axial resolution, and it is difficult to make out the exact shape of the experimental pressure distribution. The large troughs in the computed pressure are due to the initial mismatch in the air stream and fuel stream static pressures which results in a strong shock/expansion structure downstream of the injector. The large troughs apparent in the computed profile appear to be missing in the experimental results. This may be due to lack of the lack of resolution, or it may also indicate that the modeling of the initial conditions at the injector needs improving. To treat the flow behind the cylindrical nozzle, shown in Fig. 2(a), as simply a step change between two uniform, parallel velocities is obviously simplistic. The experimentally recorded H_2 reservoir pressures may also be too low, as this pressure is recorded in quite a small plenum chamber, located upstream of the injector. A higher stagnation pressure would result in larger predicted static pressures at the rear of the hydrogen injector, creating a closer match in the fuel/ test gas static pressures, and reducing the strengths of the shock and expansion waves.

The predicted wave structure downstream of the injector can easily be seen on Fig. 4(a), which is a contour map of static pressure normalized by the air stream inlet pressure. On the contour map the flow is travelling from left to right, with hydrogen injection at the lower left hand corner. The

differences in the inlet conditions. The experimental results have been normalized using the theoretical inlet test conditions shown in Table 2.^b

Figure 4(b) shows contours of water mass fraction. No significant water is produced until 40 mm downstream of injection.

Figure 4(c) displays local equivalence ratio contours of 0.2, 1.0, and 5.0^c. The enclosed area represents the region where significant combustion is most likely. According to Huber et. al.³² self ignition may be expected to occur in regions where the local mixture equivalence ratio is approximately 0.2 and the temperatures are above 800 K. The combustion region is seen to spread out into the hot air stream as the flow continues downstream. The spreading rate is slow, however, with the combustion region not even reaching the half way point across the flow by the end of the duct.

Static temperature contours are shown in Fig. 4(d). A significant region of cold gas can also be seen near the lower wall. This cold region appears to be the result of the large amount of injected cold hydrogen, rather than due to significant heat loss through the walls.

Combustion and mixing efficiencies are shown in Fig. 3(d). The reaction rate efficiency, η_{RR} , is seen to be large once ignition has occurred. The finite rate chemistry appears to be limiting the combustion by only a small extent. On the other hand, the mixing efficiency, η_{MIX} , appears to be poor, reaching only 19 % by the end of the duct. Thus, even if reactions were infinity fast, the fraction of the total injected hydrogen which would burn would remain small.

$H = 7.4 \text{ MJ/kg}$, $\phi = 1.6$

Figure 5(a) shows the computed pressure distribution along the lower wall of the scramjet for run number 7247. Two experimental results are again shown. One using the cylindrical hydrogen injector (run 7247, $H = 7.4$, $\phi = 1.6$), and the other the source flow injector (run 7279, $H = 7.7$, $\phi = 1.3$). Both the shape, and the overall pressure level measured at the end of the duct appear to be well predicted. The main source of the large

^b A recovery factor of 0.9 has been used to evaluate H_{aw}

^c The local equivalence ratio contours include hydrogen and oxygen in all forms except H_2O

predicted pressure waves is again the mismatch in the initial hydrogen/air static pressures. The lack of axial distance resolution in the pressure measurements makes it difficult to determine whether such a pressure wave is present in the experimental results. Significant pressure waves due to combustion are also superimposed on the final computed pressure distribution. This can be seen by the significant difference between the pressure profiles obtained when the program is used with and without the chemical reactions.

The 1-dimensional calculations, also shown on Fig. 5(a), predict almost immediate ignition. The ignition process is no doubt aided by the high gas temperatures, and the large fraction of dissociated oxygen initially present in the flow. By the end of the duct the pressure level predicted by the 2-dimensional calculation approaches that of the ideal 1-dimensional case. A significant part of this pressure rise is due to the growing boundary layers, as can be seen by the pressure rise also present in the no reaction case. These boundary layer effects are not considered in the 1-dimensional calculations.

The heat transfer predictions, shown in Fig. 5(b), fall between the two experimental results, although the predictions are closer to the cylindrical injector results, which were used as the initial conditions for the computations. The experimental results collapse significantly when plotted as Stanton numbers on Fig. 5(c). The predicted results, in this case, agree particularly well with the experimental results for the cylindrical nozzle case.

Water contours ,Fig. 6(b), show that almost immediate ignition is predicted after injection. This agrees with the 1-dimensional calculations on Fig. 5(a).

The local equivalence ratio ,Fig. 6(c), and temperature, Fig. 6(d), contours show a very thin flame front spreading out into the hot air stream. The flame front is located well away from any cold gas located near the walls.

Figure 18 shows that 93 % of the mixed hydrogen has reacted (η_{RR}), however, due to the low mixing rate, only 22 % of the total hydrogen available for reaction has been converted to water (η_{STOICH}).

$H = 7.3 \text{ MJ/kg}$, $\phi = 2.2$

The air stream test conditions for run 7235 are similar to run 7247, except in this case the equivalence ratio has been increased to 2.2. The experimental results, see Fig. 7(a), show a slightly higher pressure rise than for run 7247, whereas the computed pressure rises are similar in size. Both the computed and experimental pressure levels are close to the ideal 1-dimensional case by the end of the duct.

The heat transfer results, shown on Figures 7(b) and 7(c), indicate a significant decrease in heat transfer compared with run 7247. This is to be expected because of the increase in flow rate of the insulating hydrogen fuel. It may also be due, to some extent, on the decrease in the mixing rate caused by the decrease in the mass and momentum flux ratios of the two gases. Figure 7(d) shows that the computed mixing and combustion efficiencies are very similar to those predicted for run 7247 by the time the flow reaches the end of the duct.

$H = 7.3 \text{ MJ/kg}$, H_2 into N_2

Run 7236 involves a test where hydrogen is injected into nitrogen, and thus chemical reactions are expected to be negligible. The hydrogen flow rate is similar to run 7235. The experimental pressures, displayed on Fig. 8(a), show an unusually large fall below intake pressure, indicating that the intake pressure reading may have been in error. Nevertheless, the pressures remain fairly flat after this point, as would be expected without combustion. The heat transfer rate, shown on Figures 8(b) and 8(c), are also unexpectedly larger than for the hydrogen into air case.

Discussion

The way in which the quasi-steady experimental results have been presented is worthy of discussion. All of the experimental pressure and heat transfer distributions presented in this study were for simultaneous points in time. In Ref. 10, however, a great deal of success was found in the transient numerical simulations, by normalizing the values with upstream reference values to produce the quasi-steady values. The transformation used was

$$\hat{Q}(x,t) = \frac{Q(x,t)}{Q(x_0, t - \tau_{\text{delay}})} \quad (26)$$

and is based upon the "hypersonic equivalence principle". The time delay, τ_{delay} , was taken as the nominal transit time for a fluid parcel to travel from the reference position.

Although such a transformation has not been applied to the experimental data presented here, it should be noted that if it had been used, then the pressure rises and heat transfer results would be reduced. The conclusions reached in this study would then remain the same, except that the mixing may be even less than what is currently indicated.

Certain points about the present computer simulations should also be considered. First, the effects of "unmixedness" on the reaction rates have not been examined. If unmixedness was taken into consideration it may indicate that there are certain slow reactions which are significant in delaying the overall combustion rate. The effects of including the nitrogen reactions in the chemistry model should also be examined. These nitrogen reactions are expected to be important at the low enthalpy conditions, where the low temperatures can cause significant ignition delays. The nitrogen reactions may also be important at the higher stagnation enthalpies because of the increase in the amount of NO in the air stream produced by the shock tunnel.

Second, the validity of a marching code is fundamentally dependant on the accuracy of the upstream initial conditions. Some of these parameters, such as free stream temperature and velocity, injector boundary layer thickness, and turbulence levels, are not known from direct measurement but are calculated as described earlier. The results of any computed analysis, and the rather unsatisfactory process of adjusting empirical constants to match experimental data, should be interpreted in the light of uncertainties in intake conditions. A concerted effort is currently being made, both in Australia and overseas, to develop instrumentation to more closely define flow parameters.

Finally, the effects of compressibility, and pressure gradients, on the turbulence model need to be looked at in more detail. Although the k- ϵ model usually gives very good predictions in planar, parabolic flows, it must be remembered that it was initially developed with reference to incompressible flows, and its use in high Mach number/ high enthalpy flows, without

modification, may begin to push the model beyond its limitations. The interactions between turbulence and the chemical kinetics also needs to be considered. Developments of advanced turbulence models for used in supersonic, and hypersonic, reacting CFD codes is an area currently requiring serious attention.¹²

Conclusions

Numerical simulations of high enthalpy, wall injected scramjet experiments are presented. The numerical results for the lower enthalpy (3.9 MJ/kg) condition showed reasonable agreement with experiment. The computed results show a significant ignition delay and a low mixing rate between the fuel and air streams.

The numerical results for the higher enthalpy (7.4 MJ/kg) and lower equivalence ratio ($\phi = 1.6$) case showed good static pressure and heat transfer predictions when compared to the shock tunnel experimental data. The numerical results indicated almost immediate ignition but also a low mixing rate.

When the equivalence ratio was increased to 2.2, the heat transfer rate to the walls decreased, as would be expected. Shock tunnel results for hydrogen into nitrogen showed virtually no static pressure rise, indicating that genuine combustion was present for the hydrogen into air experiments.

For both enthalpy conditions the predicted flame front spread outwards into the hot air stream. A layer of comparatively cold gas was found to be present near the lower walls of the scramjet model, however, this cool layer appeared to be due to the large amount of injected cold hydrogen which had not reacted or mixed significantly with the air stream, rather than due to cold model walls. The total amount of mixed hydrogen which had combusted to form water was found to be quite high, while the percentage of the total amount of injected hydrogen which had reacted was small. This indicated that the main combustion limiting factor, after ignition had occurred, was the rate at which the hydrogen mixed with the air stream.

To obtain agreement with experimental heat transfer results the computations required adjustment of the initial turbulence dissipation length scale over a large size range. This means that the code does not yet process a true predictive capability. The CHARMS code, however, has shown itself to be extremely useful in providing information about the scramjet flow field which was not, or could not be, directly measured. The code requires further

experimental data so that any improvements to the code can be validated, especially at the high enthalpy, high Mach number, conditions where previous experimental results have not been available. New data from pulsed facilities will greatly assist in achieving this goal.

Acknowledgments

This work was supported by grants from the NASA Langley Research Center, Hypersonics Propulsion Branch, and the Australian Research Council.

References

¹Tamagno, J., Bakos, R., Pulsonetti, M.V., and Erdos, J., "Hypervelocity Real Gas Capabilities of GASL's Expansion Tube (HYPULSE) Facility," AIAA 16th Aerodynamic Ground Testing Conference, Seattle, WA., AIAA Paper No. 90-1390, June 1990.

²Stalker, R.J., "Development of a Hypervelocity Wind Tunnel," *Aero. Journal of Roy. Aero. Soc.*, Vol. 76, 1972, pp. 374-384.

³Stalker, R.J. and Morgan, R.G., "The University of Queensland Free Piston Shock Tunnel T4 - Initial Operation and Preliminary Calibration," 4th National Space Engineering Symposium, Adelaide, July 1988.

⁴Stalker, R.J. and Morgan, R.G., "Supersonic Hydrogen Combustion With a Short Thrust Nozzle," *Combustion and Flame*, Vol. 57, 1984, pp. 55-70.

⁵Morgan, R.G., Paull, A., Morris, N., and Stalker, R.J., "Scramjet Sidewall Burning - Preliminary Shock Tunnel Results," Department of Mechanical Engineering, University of Queensland, Research Report No. 12/85, NASA Contract NAGW-674, 1985.

⁶Morgan, R.G., Paull, A., Morris, N. and Stalker, R.J., "Further Shock Tunnel Studies of Scramjet Phenomena," Department of Mechanical Engineering, University of Queensland, Research Report No. 10/86, NASA Contract NAGW-674, 1986.

⁷Drummond, J.P., Rogers, R.C., and Hussaini, M.Y., "A Detailed Numerical Model of a Supersonic Reacting Mixing Layer," AIAA Paper No. 86-1427, 1986.

⁸Drummond, J.P., "A Two-dimensional Numerical Simulation of a Supersonic, Chemically Reacting Mixing Layer," NASA Technical Memorandum 4055, 1988.

⁹Rogers, R.C. and Weidner, E.H., "Numerical Analysis of Pulse Facility Transient Flow Through a Supersonic Combustor Model," 24th Joint Propulsion Conference, Boston, Massachusetts, AIAA Paper No. 88-3261, July 1988.

¹⁰Jacobs, P.A., Rogers, R.C., Weidner, E.H., and Bittner, R.D., "Flow Establishment in a Generic Scramjet Combustor," 26th Joint Propulsion

Conference, Orlando, FL., AIAA Paper No. 90-2096, July 1990.

¹¹Spalding, D.B., Launder, B.E., Morse, A.P., and Maples, G., "Combustion of Hydrogen - Air Jets in Local Chemical Equilibrium (A Guide to the CHARNAL Computer Program)," NASA CR-2407, 1974.

¹²Anderson, G., Kumar, A., and Erdos, J., "Progress in Hypersonic Combustion Technology with Computation and Experiment," AIAA Second International Aerospace Planes Conference, Orlando, FL., AIAA Paper No. 90-5254, Oct. 1990.

¹³Rogers, C.R., Drummond, J.P., and Weidner, E.H., "Numerical Analysis of Shock Tunnel Data for Hydrogen Injection into Supersonic Air Flows," 24th JANNAF Combustion Meeting, Monterey California, Oct. 1987.

¹⁴Brescianini, C.P., and Morgan, R.G., "Numerical Modelling of Sidewall Injected Scramjets," Shock Tunnel Studies of Scramjet Phenomena - Supplement 3, Department of Mechanical Engineering, University of Queensland, 1987. Also available as NASP CR-1023, 1988 and NASA CR-181721, 1988.

¹⁵Patankar, S.V. and Spalding, D.B., *Heat and Mass Transfer in Boundary Layers*, 2nd. Edition, Int. Textbook Co. Ltd. (London), 1970.

¹⁶Elghobashi, S. and Spalding, D.B., "Equilibrium Chemical Reaction of Supersonic Hydrogen-Air Jets (The ALMA computer program)," NASA CR-2725, 1977.

¹⁷McLain, A.G. and Rao, C.S.R., "A Hybrid Computer Program for Rapidly Solving Flowing or Static Chemical Kinetic Problems Involving Many Chemical Species," NASA TM-X-3403, 1976.

¹⁸Bittker, D.A. and Scullin, V.J., "General Chemical Kinetics Computer Program for Static and Flow Reactions, With Application to Combustion and Shock-Tube Kinetics," NASA TN D-6586, 1972.

¹⁹Wilke, C.R., "A Viscosity Equation for Gas Mixtures," *The Journal of Chemical Physics*, Vol. 18, No. 4, 1950, pp. 517-519.

²⁰Launder, B.E., Morse, A., Spalding, D.B., and Rodi, W., "Prediction of

Free Shear Flows - A Comparison of the Performance of Six Turbulence Models," *Proceeding of Free Shear Flows Conference*, NASA SP-321, 1972.

²¹Launder, B.E. and Spalding, D.B., "The Numerical Computation of Turbulent Flows," *Computer Methods in Applied Mechanics and Engineering*, Vol. 3, 1974, pp. 269-289.

²²van Driest, E.R., "Turbulent Boundary Layers in Compressible Fluids," *Journal of the Aeronautical Sciences*, Vol. 18, No. 3, 1951, pp. 145-160.

²³Hopkins, E.J., Keener, E.R., and Polek, T.E. "Hypersonic Turbulent Skin- Friction and Boundary Layer Profiles on Nonadiabatic Flat Plates," *AIAA Journal*, Vol. 10, No. 1, 1972, pp. 40-48.

²⁴White, F.M., *Viscous Fluid Flow*, McGraw-Hill Book Company, New York, 1974, pp. 627.

²⁵Jayatillaka, C.V.L., "The Influence of Prandtl Number and Surface Roughness on the Resistance of the Laminar Sub-layer to Momentum and Heat Transfer," *Progress in Heat and Mass Transfer*, Vol. 1, Ed. by Grigull, U., and Hahne, E., Pergamon Press, London, 1969, pp. 193-329.

²⁶Spalding, D.B. "GENMIX - A General Computer Program for Two-Dimensional Parabolic Phenomena," Pergamon Press, Oxford, 1977.

²⁷Evans, J.S. and Schexnayder, C.J. Jr., "Influence of Chemical Kinetics and Unmixedness on Burning in Supersonic Hydrogen Flames," *AIAA Journal*, Vol. 18, No. 2, 1980, pp. 188-193.

²⁸Schultz, D.L., and Jones, T.V., "Heat-Transfer Measurements in Short-Duration Hypersonic Facilities," Dept. of Engineering Science, University of Oxford, AGARD-AG-165, 1973.

²⁹McIntosh, M.K., "Computer Program for the Numerical Calculation of Frozen and Equilibrium Conditions in Shock Tunnels," Dept. of Physics, School of General Studies, Australian National University, Canberra, 1968.

³⁰Lordi, J.A., Mates, R.E., and Morsel, J.R., "Computer Program for the Numerical Solution of Non-Equilibrium Expansions of Reacting Gas Mixtures,"

NASA CR-472, 1966.

³¹He, Y. and Morgan, R.G., "Transition of Compressible High Enthalpy Boundary Layer Flow Over a Flat Plate," Tenth Australasian Fluid Mechanics Conference, University of Melbourne, Dec. 1989.

³²Huber, P.W., Schexnayder, C.J. Jr., and McLinton, C.R., "Criteria for Self-Ignition of Supersonic Hydrogen-Air Mixtures," NASA TP-1457, 1979.

³³Hornung, H., and Sturtevant, B., "Challenges for High-Enthalpy Gasdynamic Research During the 1990's: Plans for the GALCIT T5 Laboratory. GALCIT Paper FM 90-1, 1990.

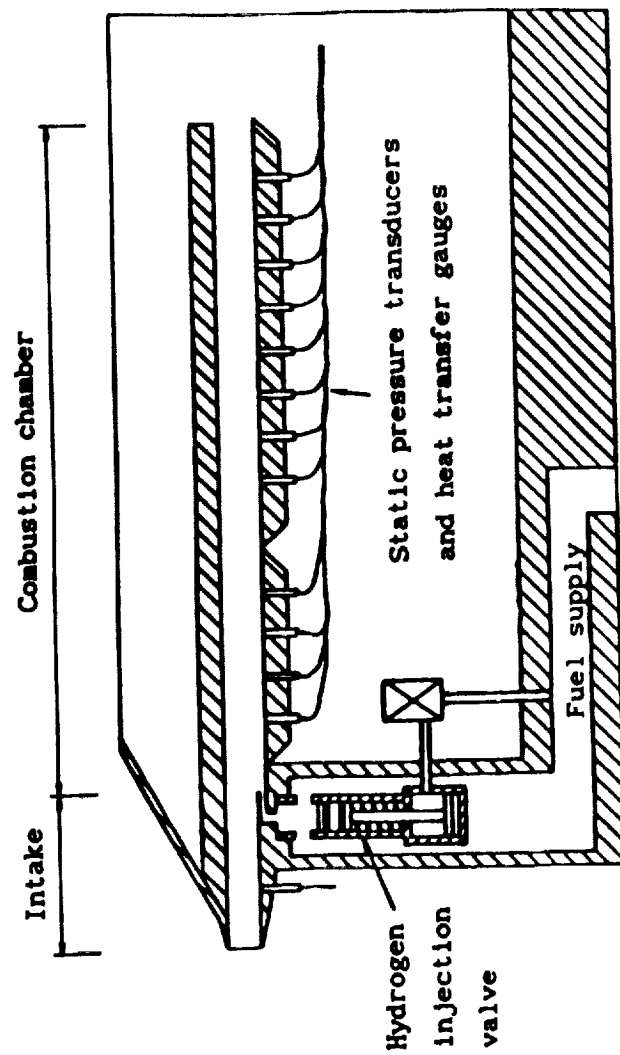


Fig. 1 Schematic of model scramjet

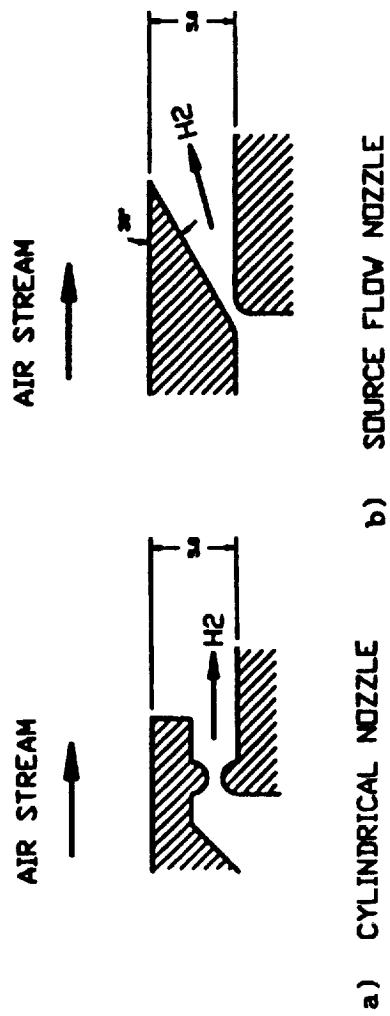
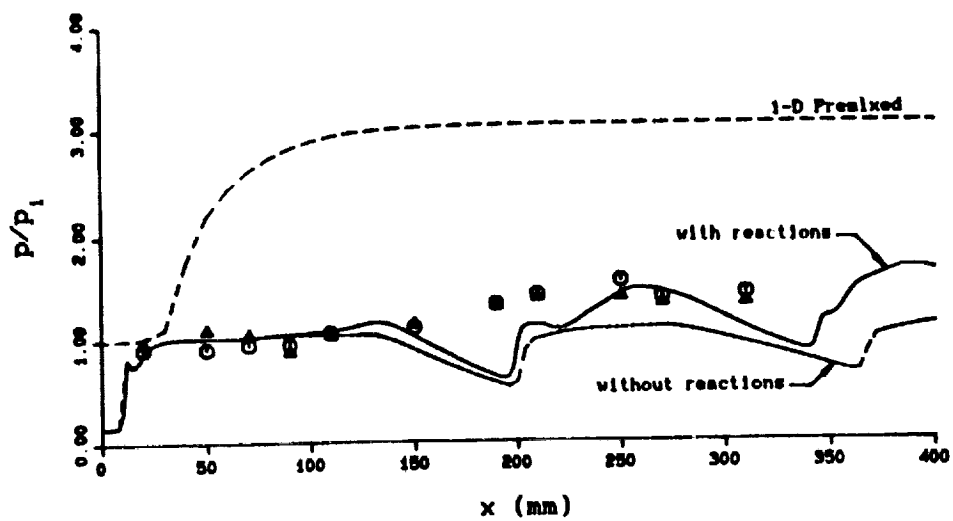
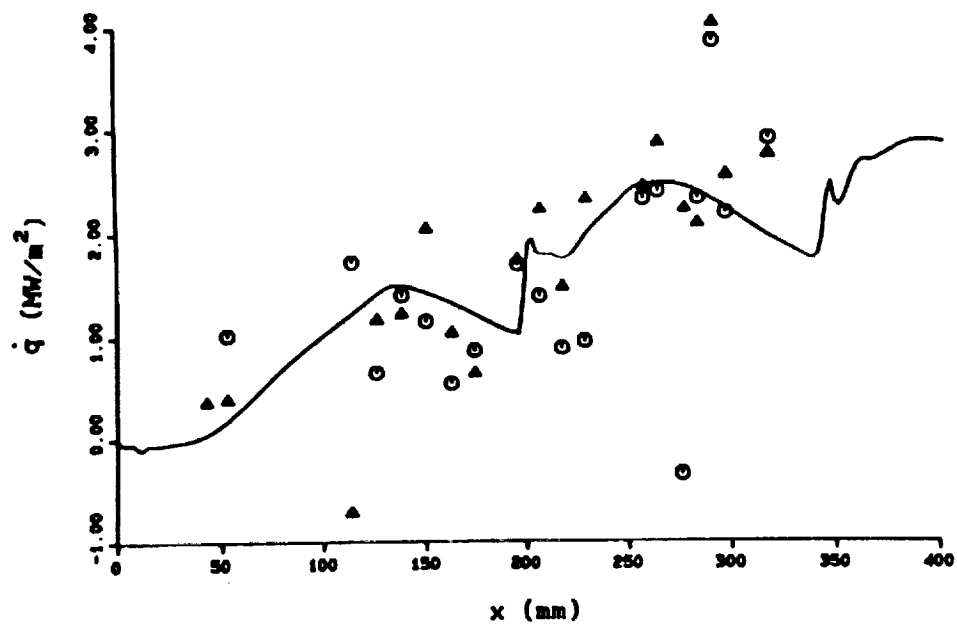


Fig. 2 Hydrogen wall injectors

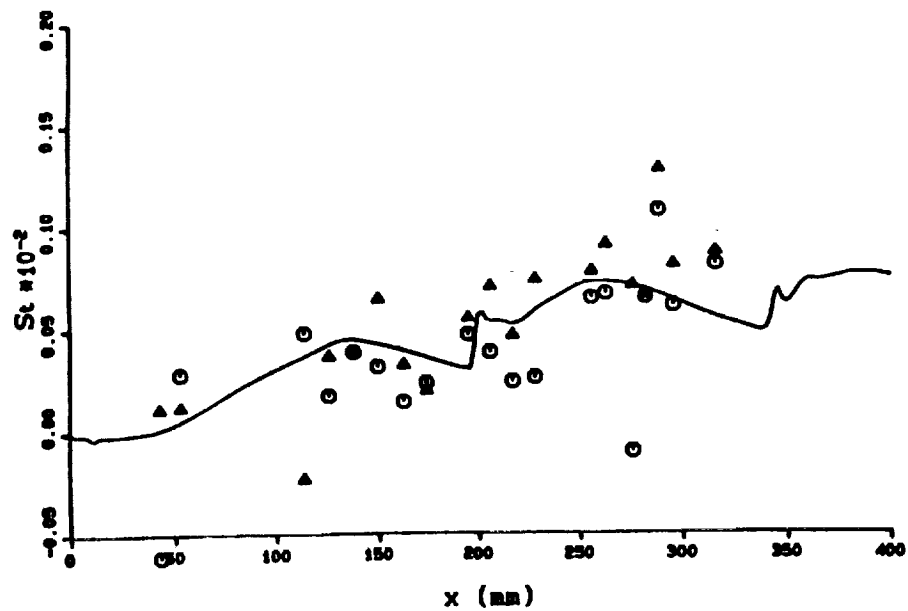
a)



b)



c)



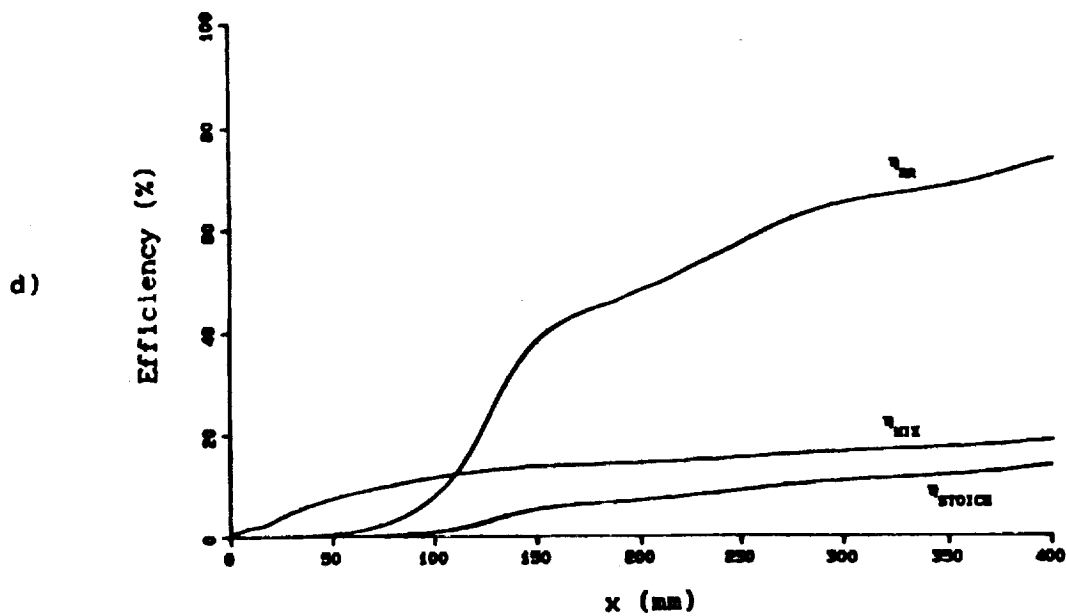


Fig. 3 Axial variation in a) normalized static pressure; b) heat transfer rate; c) Stanton number; d) combustion and mixing efficiencies; along the lower wall of a constant area scramjet combustor.

Run 7241, $H = 3.9$ MJ/kg, $\phi = 1.0$

Experimental results :

⊙ cylindrical injector	run 7241
▲ source flow injector	run 7281

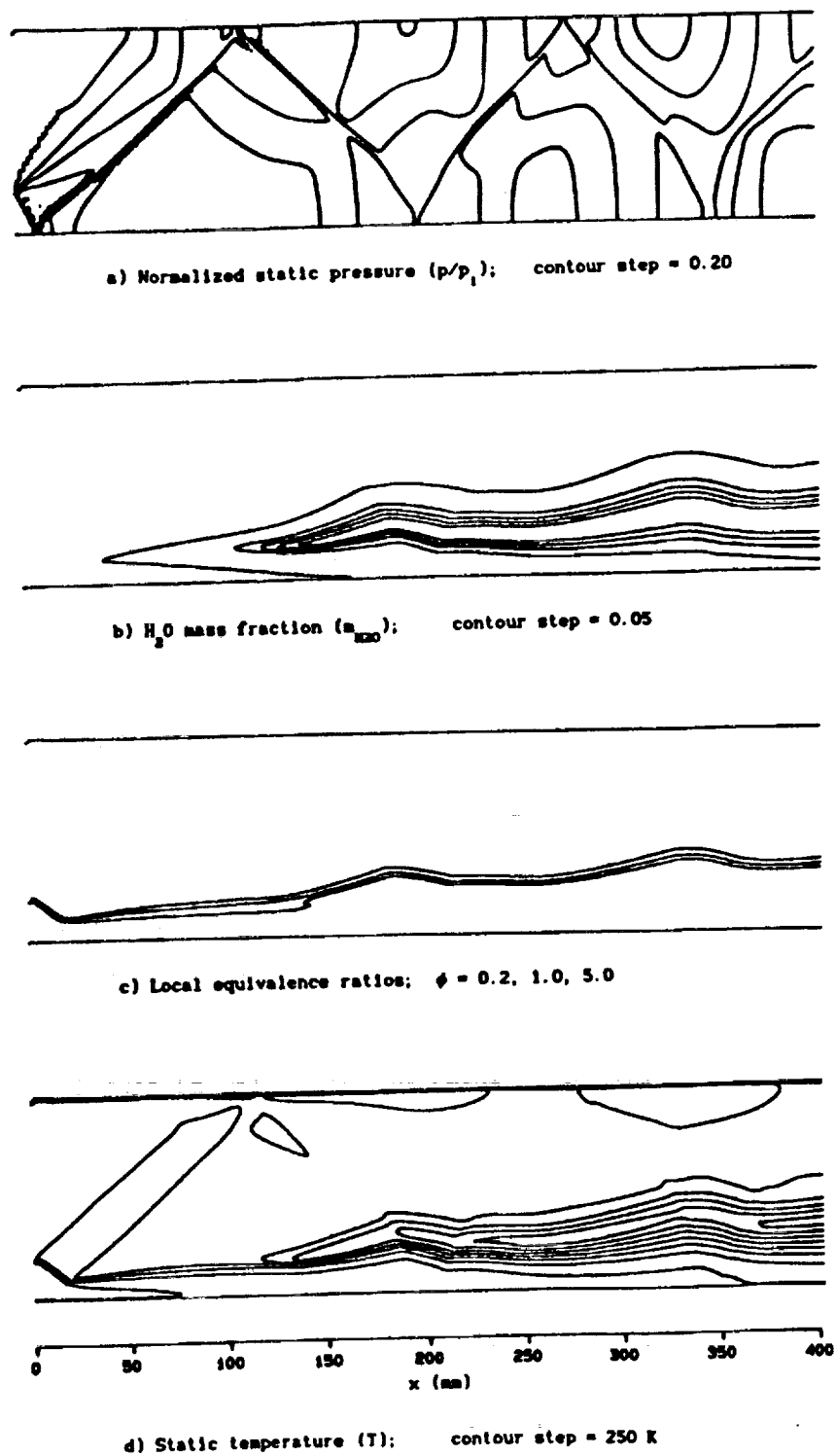
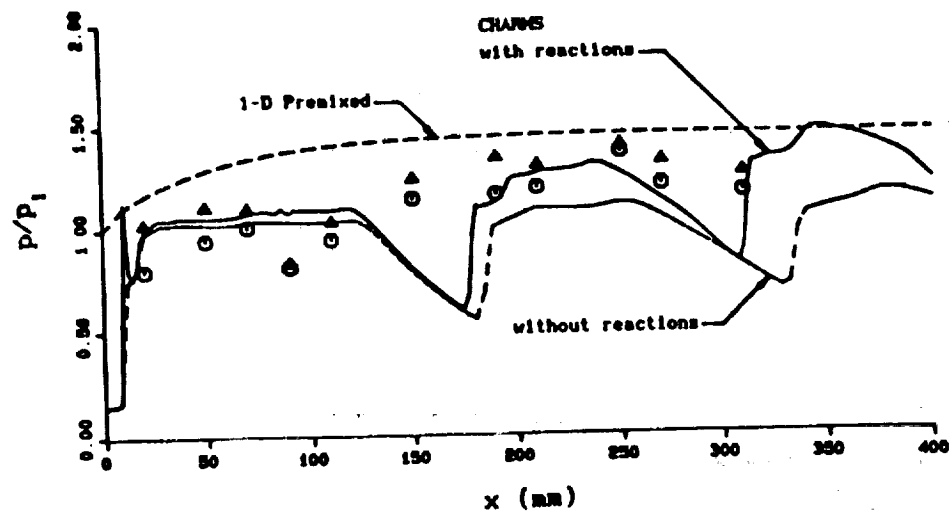
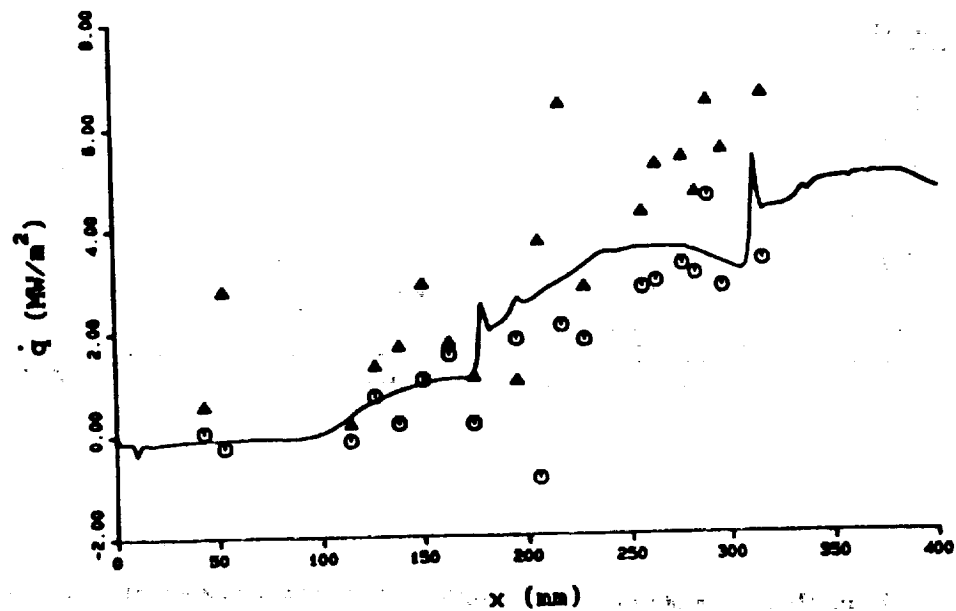


Fig.4 Contour maps, Run 7241, $H = 3.9$ MJ/kg, $\phi = 1.0$

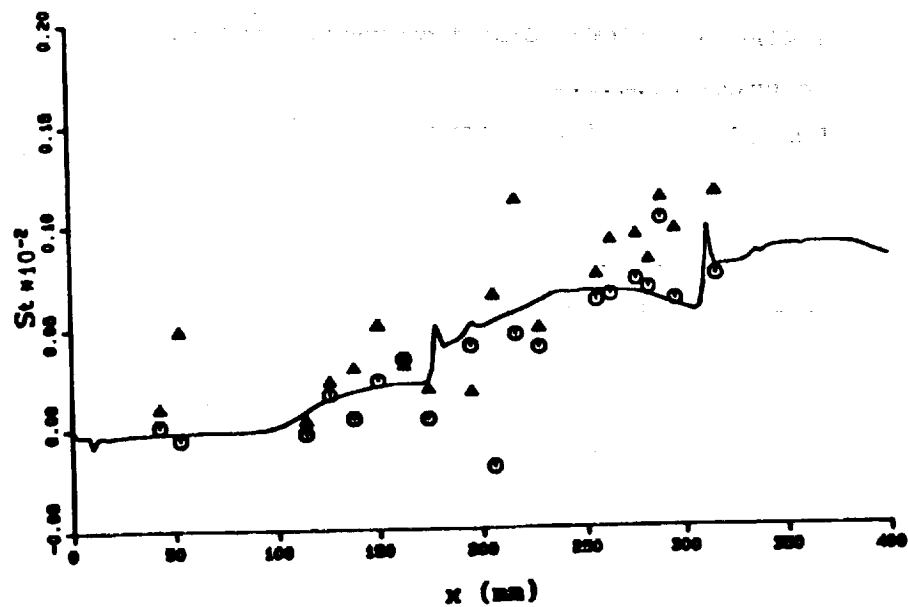
a)



b)



c)



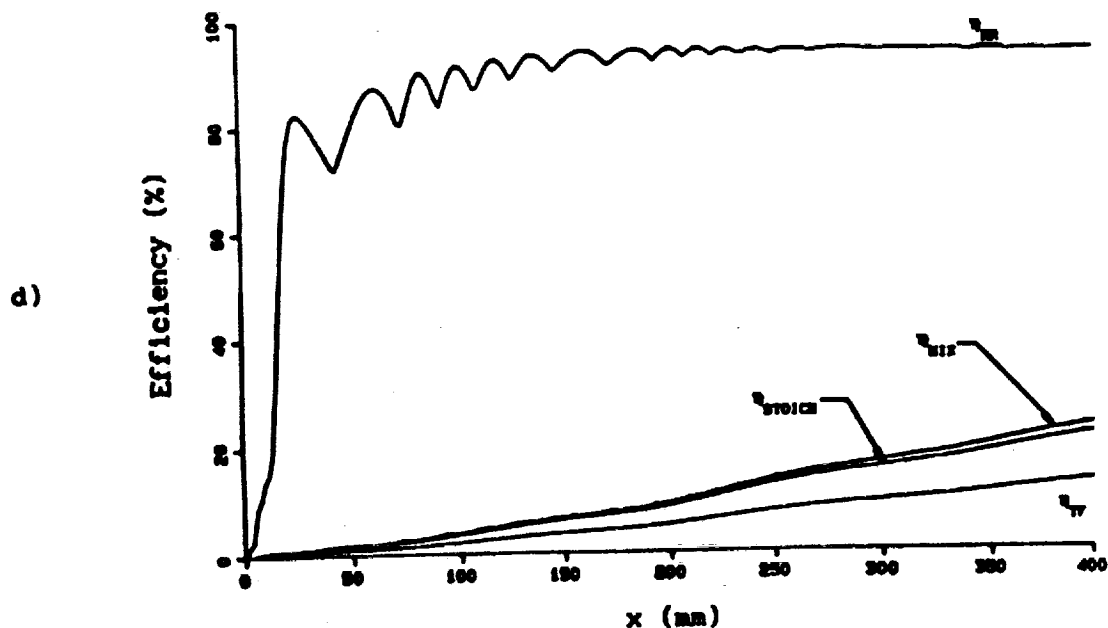


Fig. 5 Axial variation in a) normalized static pressure; b) heat transfer rate; c) Stanton number; d) combustion and mixing efficiencies; along the lower wall of a constant area scramjet combustor.

Run 7247, $H = 7.4 \text{ MJ/kg}$, $\phi = 1.6$

Experimental results :

○ cylindrical injector run 7247

▲ source flow injector run 7279

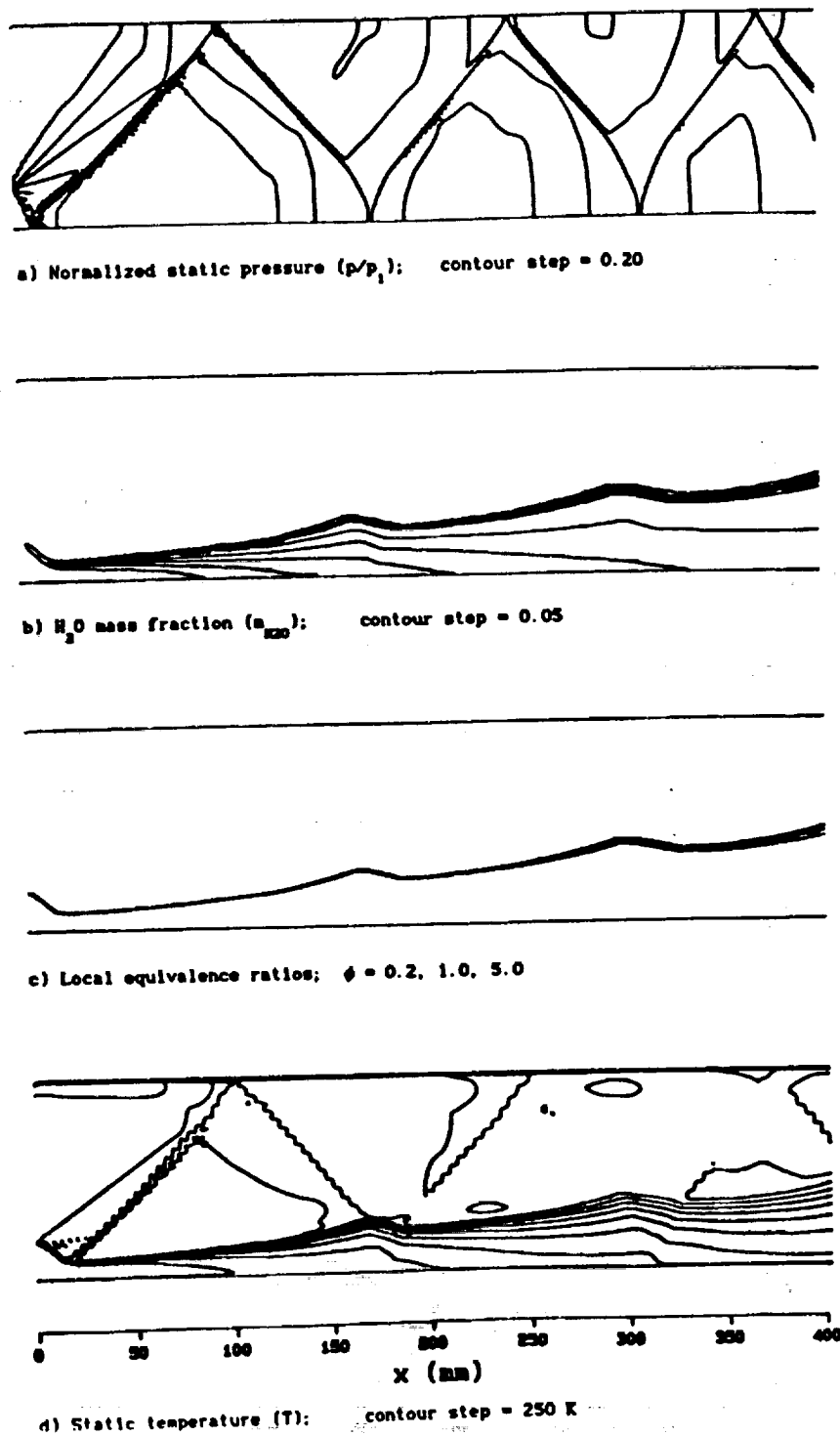
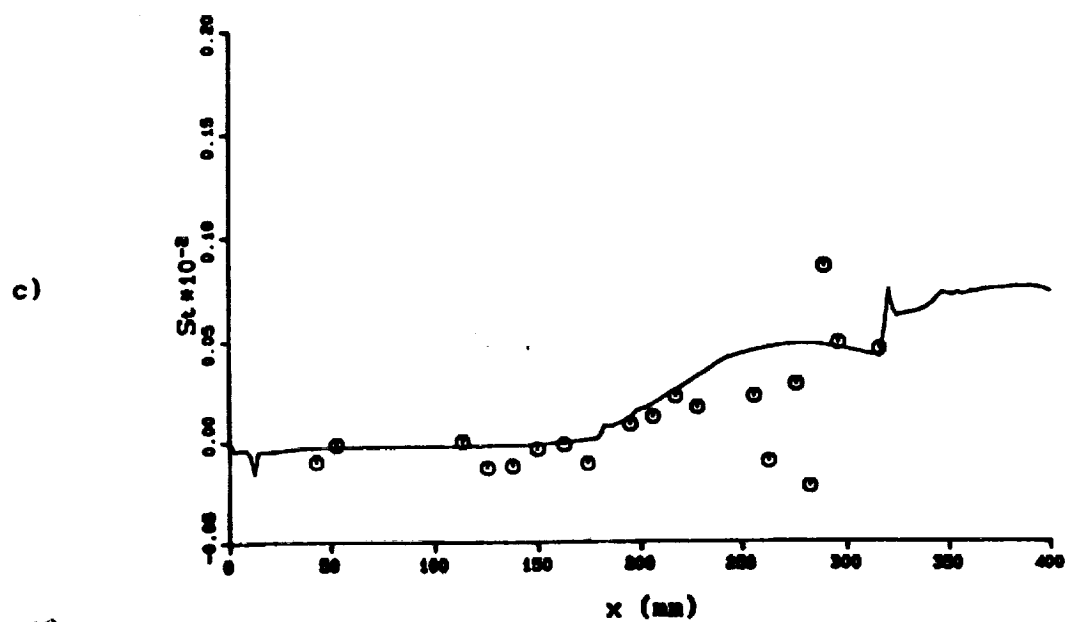
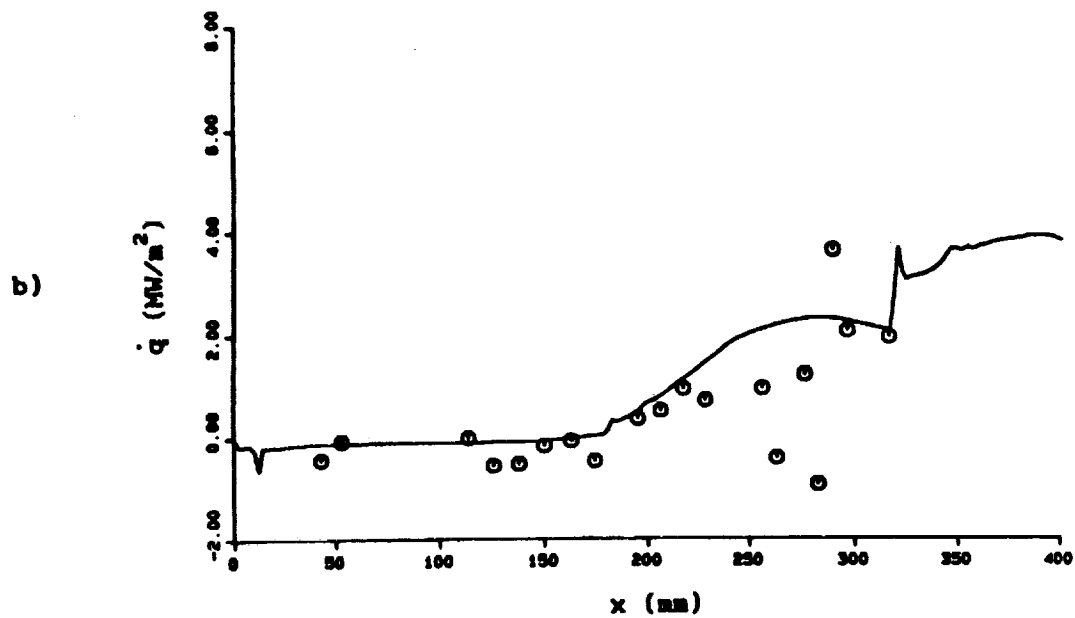
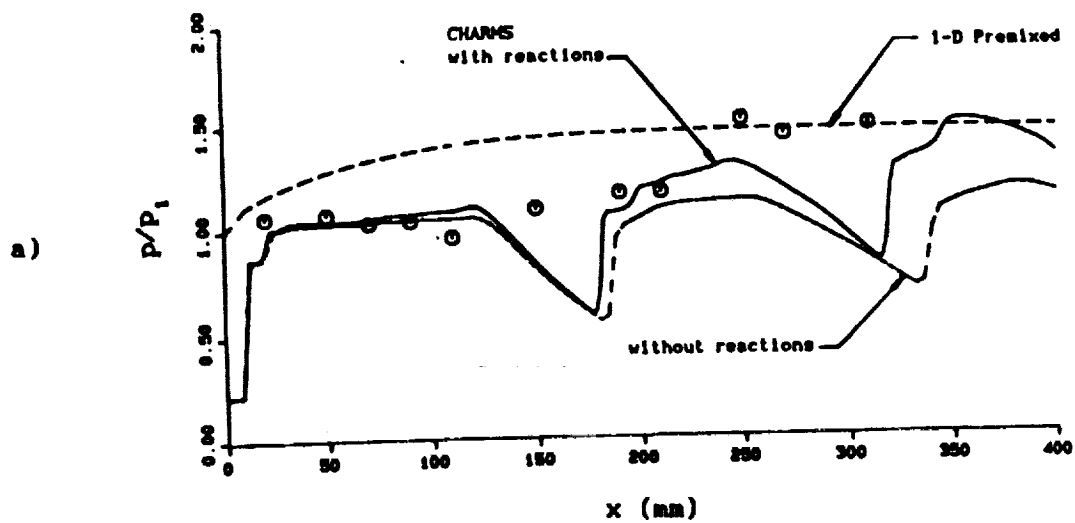


Fig.6 Contour maps, Run 7247, $H = 7.4$ MJ/kg, $\phi = 1.6$



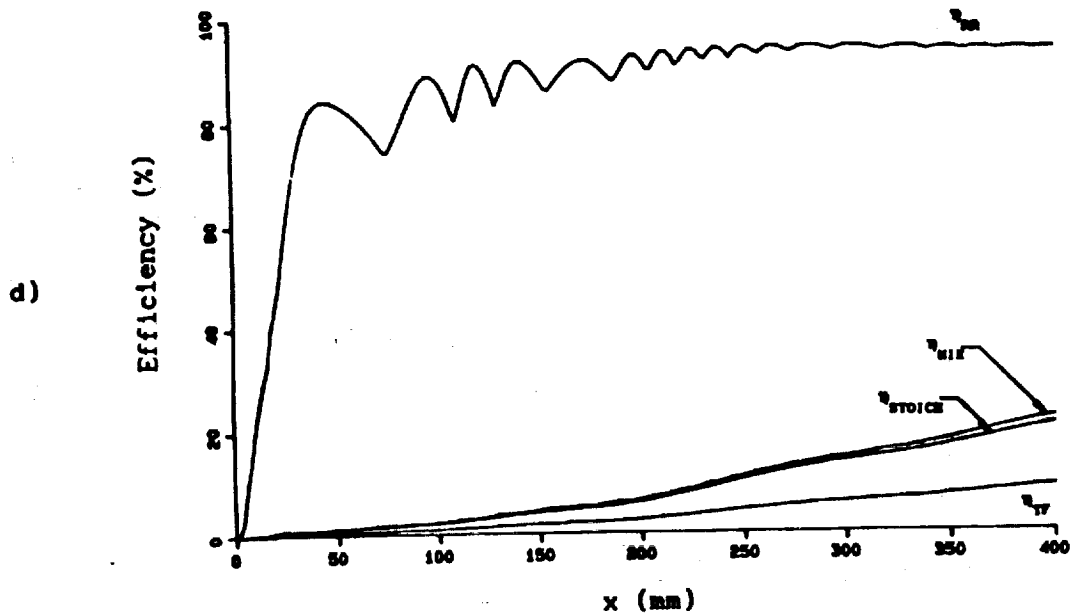


Fig. 7 Axial variation in a) normalized static pressure; b) heat transfer rate; c) Stanton number; d) combustion and mixing efficiencies; along the lower wall of a constant area scramjet combustor.

Run 7235, $H = 7.3$ MJ/kg. $\phi = 2.2$

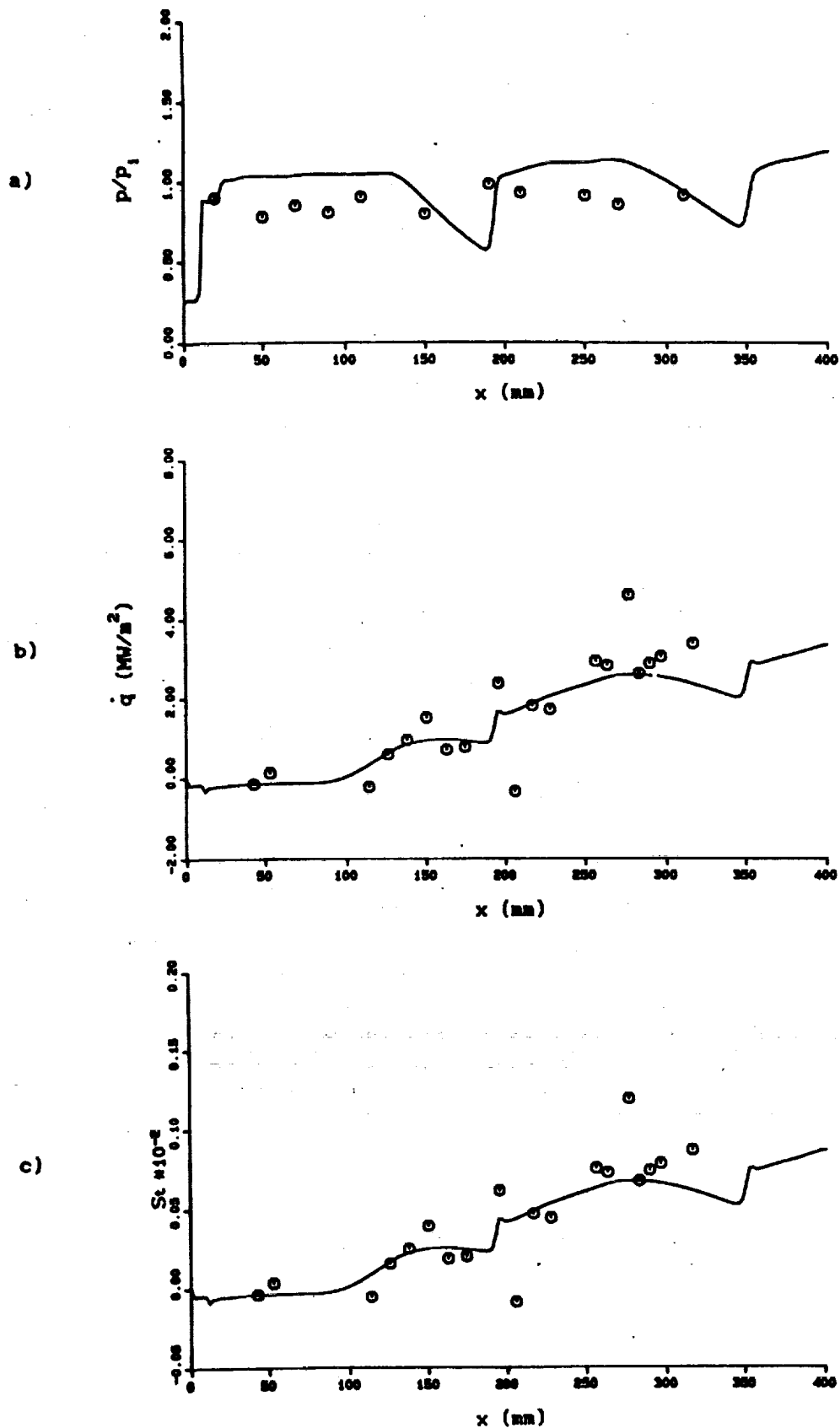


Fig. 8 Axial variation in a) normalized static pressure; b) heat transfer rate; c) Stanton number; along the lower wall of a constant area scramjet combustor Run 7236. $H = 7.3$ MJ/kg. H into Nitrogen

MACH 5 CONSTANT AREA DUCT TESTS

A. Paull

A series of tests were initiated to determine the combustion length of hydrogen in a square duct (49.5mm x 52.1mm) when injected from the wall into a free stream in which the Mach number was nominally 5. However, it became acutely apparent that the flow down the duct was being disturbed from unknown sources even when the injection ports were covered. The pressure fluctuations (see Figure 1) which were measured along the centreline of a wall in a nominally square duct could be as much as 50% in excess of the mean pressure. For combustion experiments this is simply not good enough because the static pressure has a significant effect on the combustion length. Hence, if the duct has regions of higher pressure, combustion may be induced by this region. Thereby an incorrect result would be obtained if it was assumed that the pressure at which combustion occurred was that at the intake. In fact, for the conditions which were initially used for the combustion tests, pressure rises attributed to combustion were only observed downstream of the pressure rise produced by the unknown disturbances.

Sources for these unwanted pressure rises were then sought. Four main areas were considered.

- (1) Transducer calibration
- (2) Model alignment
- (3) Leading edge effects and
- (4) Model irregularities.

1. Transducer Calibration.

It was noted above that pressure rises observed in the duct were also closely associated with the onset of combustion. This would indicate that the pressure fluctuations observed in the duct were real and it was unlikely that inaccurate calibration of the pressure transducers was the primary cause for these fluctuations. Notwithstanding, it is important to obtain accurate calibrations of all transducers in any experiment.

Prior to all experiments performed in T4 new calibrations of all the transducers are made. The transducers are usually mounted in a container which can be exposed to a sudden known pressure rise. It has always been

observed that this technique usually produces a calibration which is different to that of the manufacturers. Furthermore, a different calibration is obtained by each experimenter. (Calibrations were generally within $\pm 10\%$ of the mean). This indicates that something changes between each calibration.

The transducers used in the experiments reported here were PCB 113A. The transducers were mounted as specified by the manufacturer using a steel sleeve to prevent the front face from touching the model (see Figure 2). However, this technique is successful only if care is taken in assembly and in the manufacture of the transducer mount. If there is any imperfection of the transducer mount then either the steel sleeve will press onto the transducer or there will be a leak past the transducer. Both problems will produce incorrect measurements.

The steel sleeve could be prevented from touching the transducer by not screwing the floating clamp nut (see Figure 2) up too tight. However, if it is not tight enough leaking will occur. An aura of good luck is sometimes needed to obtain a workable balance. As such an aura is generally elusive some leaking occurs and as a consequence the manufacturers calibration is inaccurate. (Totally unacceptable results are obtained if the sleeve touches the the sides of the transducer).

It can be seen that if the transducer is first calibrated in a special calibrating rig and is then removed and remounted in the model then this approach is also inaccurate. There is no guarantee that the leak rate when mounted in the model will be the same as the leak rate when mounted in the calibration rig. However, this source of error is eliminated by calibrating the transducers when they are mounted in the model.

It should be understood that the leak is only very small, in fact so small it can only be detected by the apparent difference in gauge sensitivity. Ideally, the leak would be totally eliminated, but until such times that a suitable mounting technique becomes available the practice of calibrating the transducers after they have been mounted in the model would appear to be a satisfactory solution to inaccurate transducer calibrations.

The technique used to calibrate the transducer was to employ a large pressure vessel as a reservoir which would be pressurized to 80 kPa gauge. The reservoir was connected to the gauge mounted in the model by a hose and a fitting which would seal on the model and cover the transducer. A fast acting valve was then opened to expose the gauge to this pressure. The hose from the vessel to the gauge was approximately

1.5 metres long and had flexible walls. This resulted in a pressure rise as seen in Figure 3.

As can be seen this technique would not provide an accurate absolute calibration of a transducer. (An absolute calibration can be obtained by using a shorter stiffer hose). However, this technique was applied in turn to each transducer. One transducer (usually the one furthest upstream) was then used as a reference and the output voltages from the other transducers were divided by that of the reference transducer (see an example in Figure 5). This provided a relative calibration for all the transducers in the model. It can be seen that from the normalized trace in Figure 5 that the calibration of transducer on channel 130 is 0.9707 times the calibration of the reference transducer on channel 110. To obtain an absolute calibration the calibration of the reference transducer must be obtained independently. However, even if this could not be obtained, the relative calibration was all that was required to determine whether or not the duct had unwanted disturbances. It was also shown that the relative calibration was repeatable to within $\pm 1\%$.

From Figures 3 and 4 it can be seen that the relative calibration is constant over a range of pressures. By necessity this is required, otherwise one of the gauges has a non linear response to pressure and therefore is useless. If a nonlinear response did occur the mounting of the gauge was inspected and usually found to be at fault. However, if no fault in the mounting could be found the gauge was replaced. It can be seen that this technique not only provides an easy way to obtain relative calibrations but also checks how constant this calibration is in time and over a range of pressures.

As a further check of the gauge calibration, gauges that were measuring low values of pressure were interchanged with gauges measuring high pressures. Minor differences were detected, however, as was expected, the overall presence of a large disturbance was still observed.

2. Model Alignment.

One obvious source of large pressure rises is the misalignment of the model to the flow. Particular care was taken to align the model with the flow. This was checked by measuring the pressures along opposite walls. They were found to be symmetrical for the first 350 mm of the duct, but there was some asymmetry appearing further downstream. This could not be explained.

3. Leading Edge Effects.

It is well known that a blunt leading edge is a mechanism for producing a disturbance which can propagate into the duct. It is believed that the effects of leading edge bluntness were eliminated by making the leading edges razor sharp. The leading edge radius was less than 0.1 mm.

It is also well known that the boundary layer which starts in the duct at the leading edge will produce a weak shock which eventually decays. As the shock is weak it will travel approximately along a Mach line. From the conditions listed in Table 1 and with the aid of Figure 5 it can be seen that weak shocks originating at the leading edges would produce pressure rises along the centreline at 136, 259, 408, and 518 mm from the leading edges. Note that the two transducers furthest upstream in Figure 1 were not on the centreline but were located 12 mm off the wall. Thus, from Figure 5, it can be seen that a pressure rise should be observed between these transducers at approximately 204 mm from the leading edge. From Figure 1 it can be seen that the position of the pressure rises is in relatively good agreement with that predicted for a weak disturbance originating from the leading edge. There is no apparent record in Figure 1 of the disturbance arriving from the side walls between the first two offcentre transducers. However, the time history record of the first transducer had oscillations with a magnitude of the order of 10% of the mean and with a period of approximately 0.5 ms. This could be one of at least two things. It could be the result of insufficient vibrational isolation or it could be the result of an instability in the location of the disturbance which is expected in this region. The disturbance could be wandering back and forth across this transducer thus producing an oscillation in the pressure. At the time frame in which Figure 1 was taken the pressure was at its lowest value of its fluctuation. Thus, the low value of the pressure measured on the first transducer in Figure 1 may be misleading.

A two-dimensional parabolic Navier-Stokes solver (Brescianini (1991)) was used to determine the shock strength generated by a fully turbulent boundary layer which starts at the leading edge. This worst case produced a pressure rise of the order of 10% of the intake pressure. Thus, the magnitude of the rise is considerably greater than that predicted. This could not be explained.

3.1. Contoured Intakes.

Having eliminated leading edge bluntness and having observed the location

of the disturbance would be consistent with originating at the leading edge, it was believed that a significant proportion of the disturbance resulted from the formation of the boundary layer. Hence, efforts were concentrated on reducing the effect produced by the boundary layer.

In an attempt to eliminate this disturbance it was observed that Jacobs (1989) had produced a relatively clean flow in a larger duct by expanding the flow at the intake to the duct from nominally Mach 4 to Mach 5. It was thought that the pressure drop experienced at the leading edge somehow decreased the pressure irregularities down the duct. Hence, a similar intake was designed for the smaller duct used here. It was assumed that the intake gas was frozen, ideal and inviscid. The intake was designed to expand the gas from Mach number 4.49 to 5.58. A Mach number of 4.49 could be obtained by using the appropriate nozzle at the end of the shock tube. Figure 6 is the profile of the intake. The flow in the duct was assumed to be two-dimensional, i.e. the side walls of the duct were not contoured. Pressures were measured downstream of the end of the contour on the same walls which were contoured.

Figure 7 is the pressure measured down the duct when the intake flow was at the designed conditions. It can be seen that the disturbances still have unacceptable magnitudes. Conditions at the intake were varied, however, this did very little to eliminate or change the nature of the disturbances.

An attempt was made to account for the boundary layer in the design by initially over expanding by an extra 2 degrees and then fairing back to the original contour by using a parabolically fitted contour. The pressure measurements from this attempt were also unacceptable (see Figure 8). The only encouraging thing about this attempt was that the disturbances were less broad than those measured previously (compare Figures 7 and 8).

4. Model Irregularities.

It was concluded that all attempts to remove the disturbances in the duct by changing the intakes were failing for reasons which had not been addressed. When the model was checked for alignment it was noted above that the disturbance was becoming asymmetric in the last quarter of the duct. This suggested that there was a problem with the symmetry of the duct.

The duct was constructed originally to be as versatile as possible and therefore was made from fourteen different pieces which were screwed

together. A lot of effort was made to ensure the duct was true for its entire length and that there were no points at which leaks could occur. However, if there was asymmetry appearing in the pressure either side of the duct, then this would suggest that the alignment was not good enough. It was not believed that better alignment could be obtained with the existing model. Hence a new model was built which was simply to assemble and easy to align. The dimensions of the duct were 54.5mm x 55mm with an error of less than ± 0.1 mm.

This model to date has only had limited testing, however from Figure 9 it can be seen that the results are encouraging. There are still some pressure fluctuations which start at 275 mm from the leading edge, however, this is a far better result that was recorded previously (Figure 1). It is currently believed that these fluctuations result from the formation of the boundary layer. Techniques for removing this effect are being pursued.

5. Conclusions

1. The inadequacies in the pressure gauge mountings produces different sensitivities to those specified by the manufacture. Calibrations should always be done in the assembled model.
2. Small misalignments in the model can lead to large disturbances.

Table 1. Table of conditions.

Figure	Run No.	Total Enthalpy	M_0	V_0 m/s	P_0 kPa	ρ_0 kg/m ³	M_1	P_1 kPa
1	2012	10.4	5.27	4004	23.5	0.053	--	--
7	2062	8.06	4.47	3455	92.5	0.202	5.53	21.5
8	2072	7.07	4.58	3269	74.5	0.190	5.98	12.6
9	2197	9.19	5.42	3794	13.5	0.036	--	--

Notation

P pressure

M Mach number

V velocity

ρ density

subscript 0 condition at nozzle exit

subscript 1 condition downstream of contoured intake (were applicable)

References

Brescianini C.P., Morgan R.G and Stalker R.J.
Numerical Model of Sidewall Injected Scramjet Experiments in a High
Enthalpy Air Flow. Appears in this report.

Jacobs P.A. and Stalker R.J.
Pressure-Length Correlations in Supersonic Combustion. Shock Tunnel
Studies of Scramjet Phenomena, NASA grant NAGW-674-Supplement 5 1989.

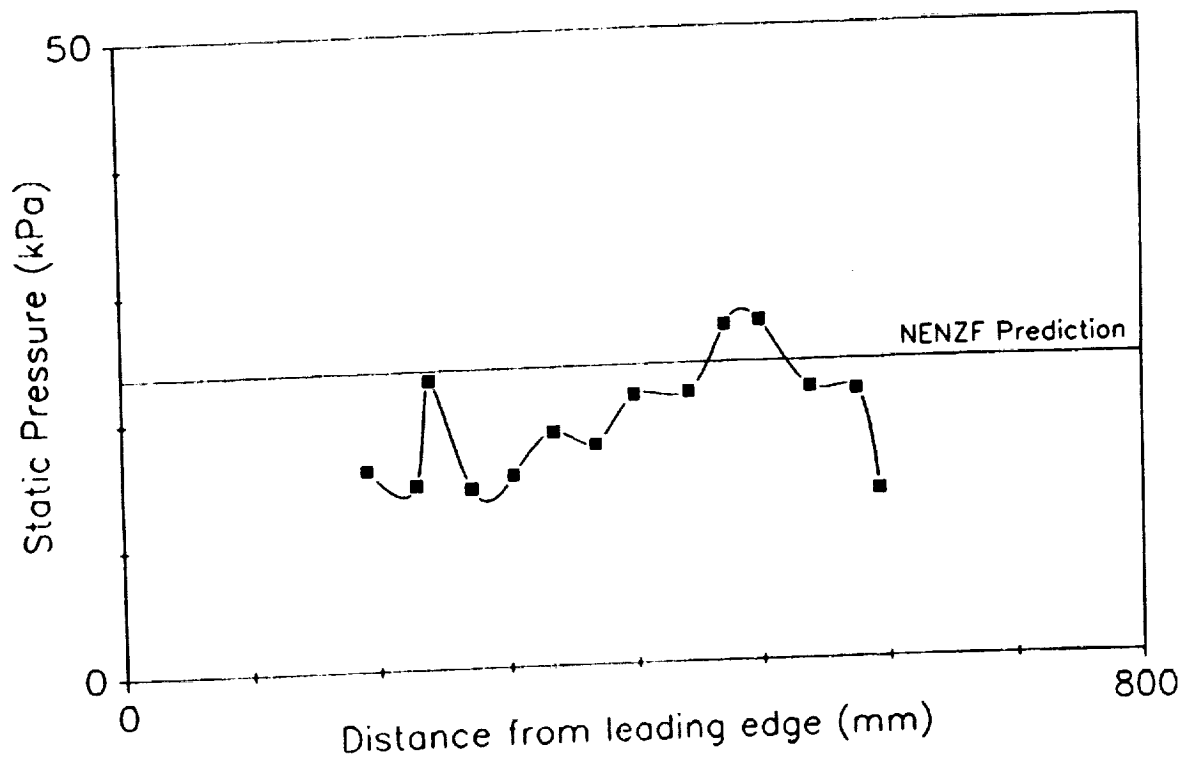
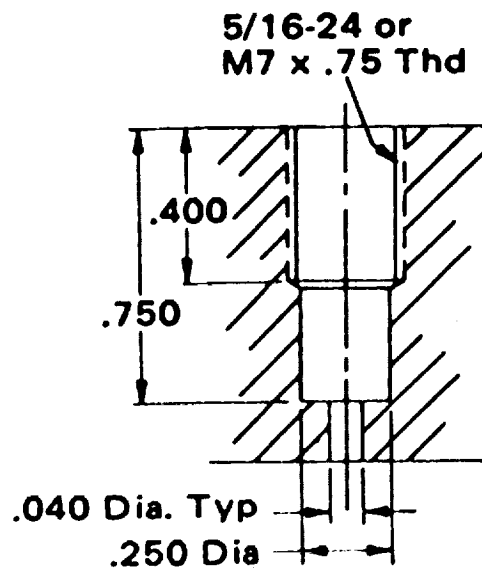
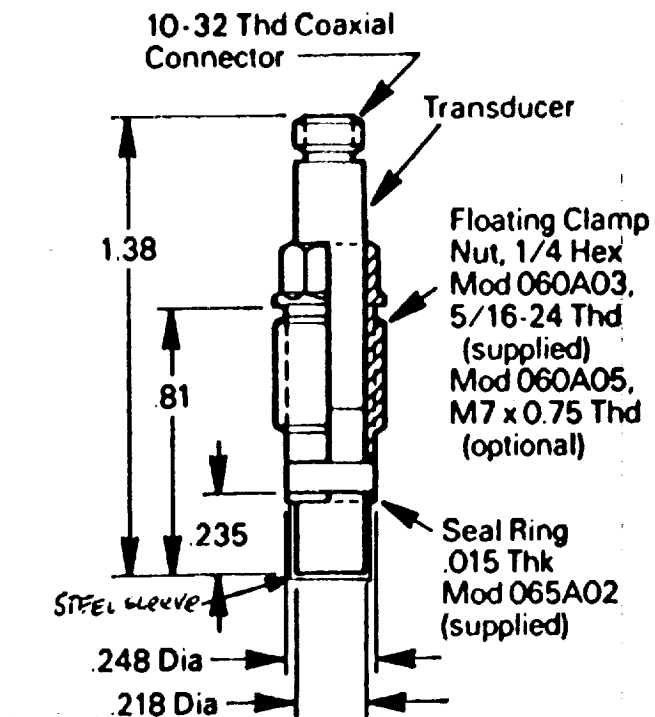


Figure 1. Pressure down a duct measuring 49.5x52.1 mm. See Figure 5 for transducer locations. All readings were made on the wall measuring 52.1 mm. Averaged over 0.02 ms.



TRANSDUCER MOUNT

DIMENSIONS IN INCHES

Figure 2. Transducer mounting.

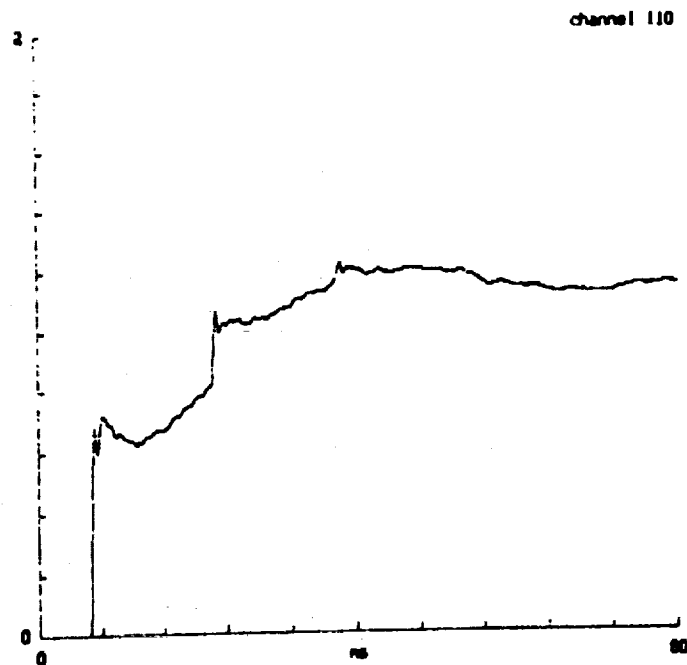


Figure 3. Voltage as a function of time measured during calibration of a transducer. Averaged over 0.05 ms.

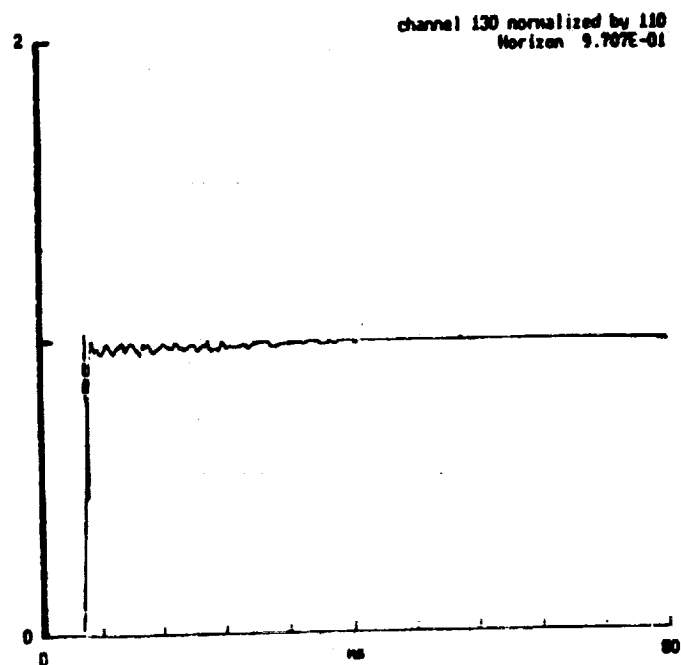


Figure 4. Voltage of channel 130 divided by that of channel 110 (see Figure 3) as a function of time. This result is used to determine the relative calibration factor of the gauge connected to channel 130 to that of 110. Both records averaged over 0.05 ms before division.

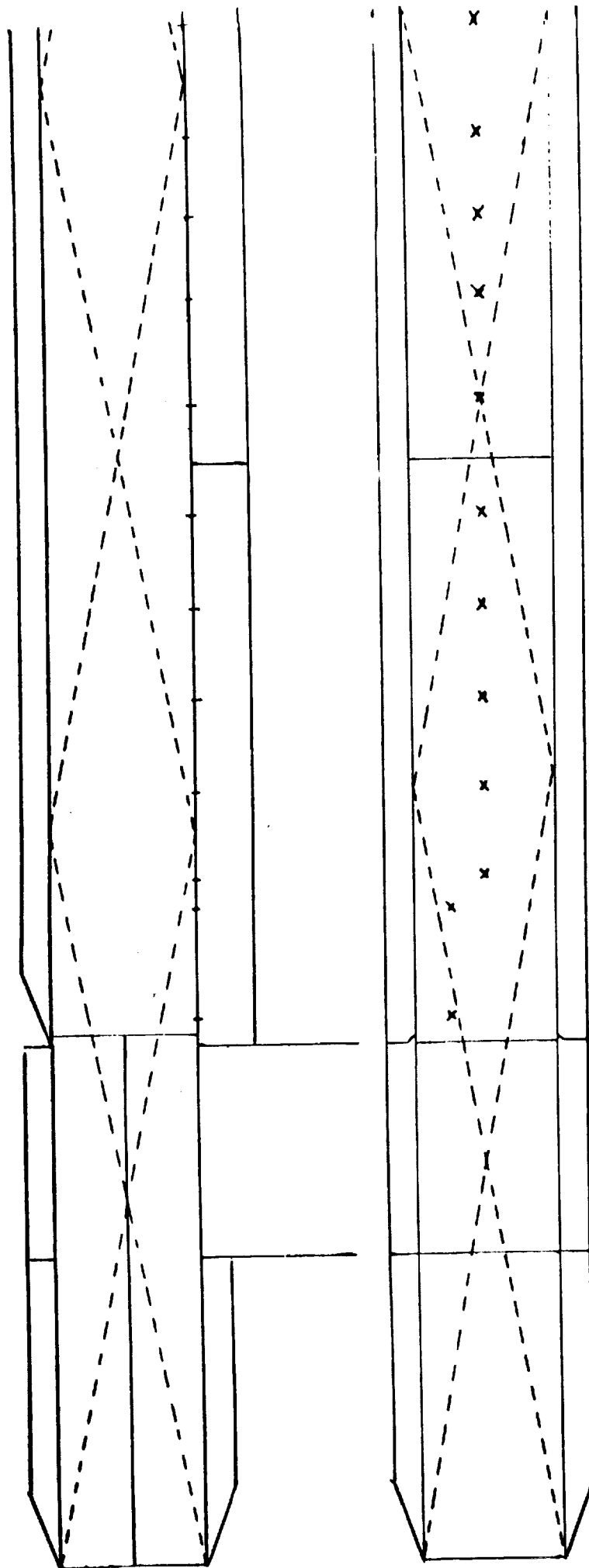
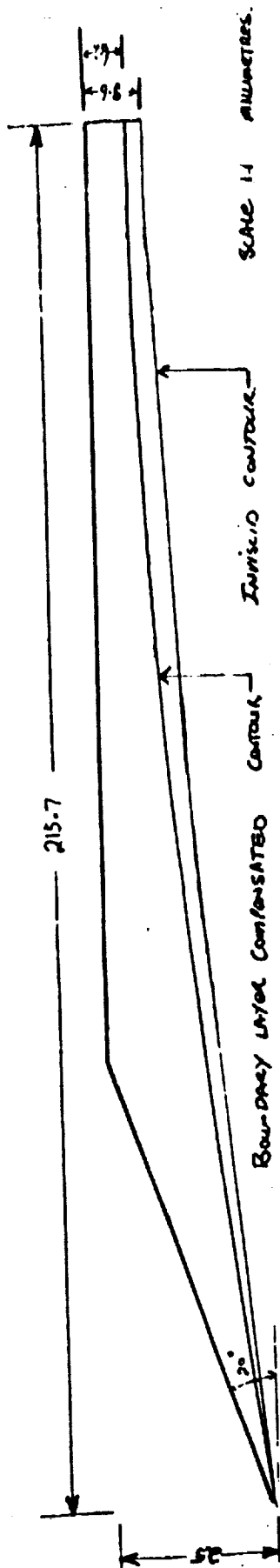


Figure 5. Diagrammatic representation of the duct used in obtaining the pressures displayed in Figure 1. Dotted lines represent Mach lines for the conditions obtained from Table 1. X and ticks represent transducer locations. All other lines represent joins in the model.



INTAKE PROFILES

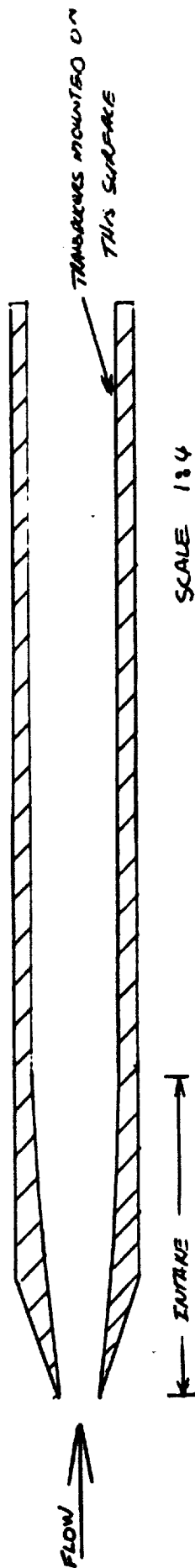


Figure 6. Schematic of the contoured intake.

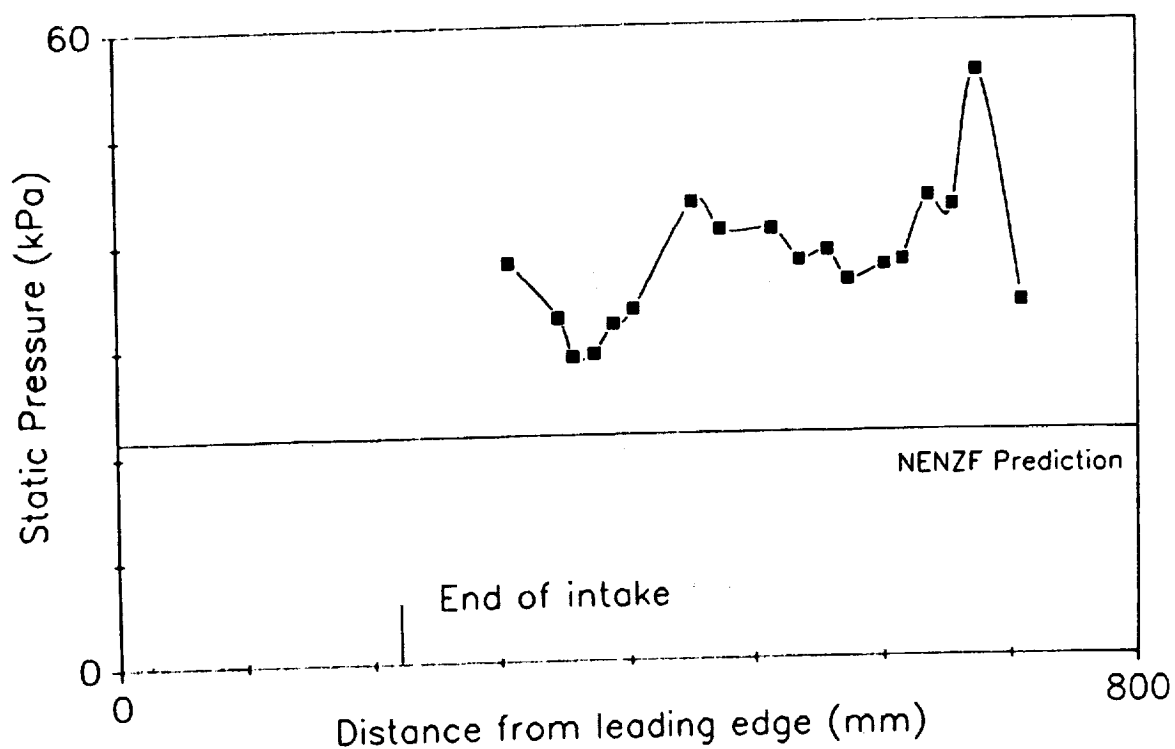


Figure 7. Pressures as a function of position measured inside a duct with dimensions 49.5x52.1 mm with a contoured intake which did not account for the boundary layer. Pressure tapplings were in the 52.1 mm side. The first two tapplings were 12 mm off the side wall. The remainder were along the centreline. Averaged over 0.02 ms.

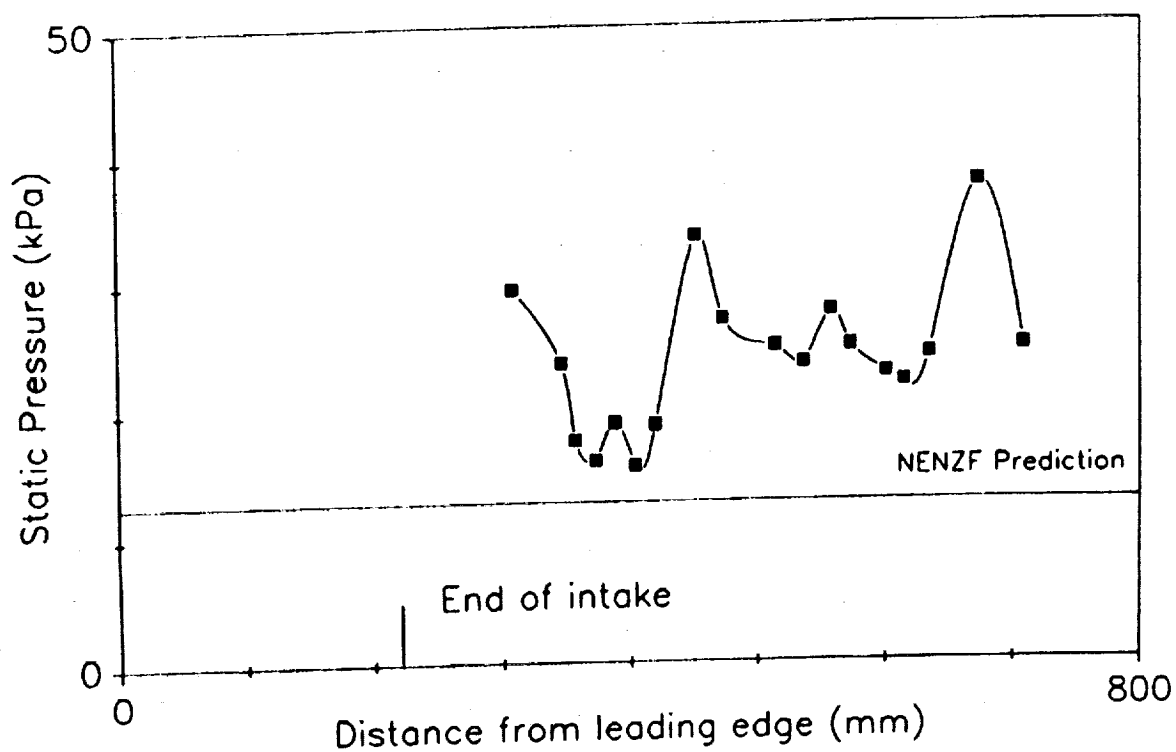


Figure 8. Pressures as a function of position measured inside a duct of dimensions 49.5x52.1 mm with a contoured intake which did account for the boundary layer. Pressure tapings were in the 52.1 mm side. The first two tapings were 12 mm off the side wall. The remainder were along the centreline. Averaged over 0.02 ms.

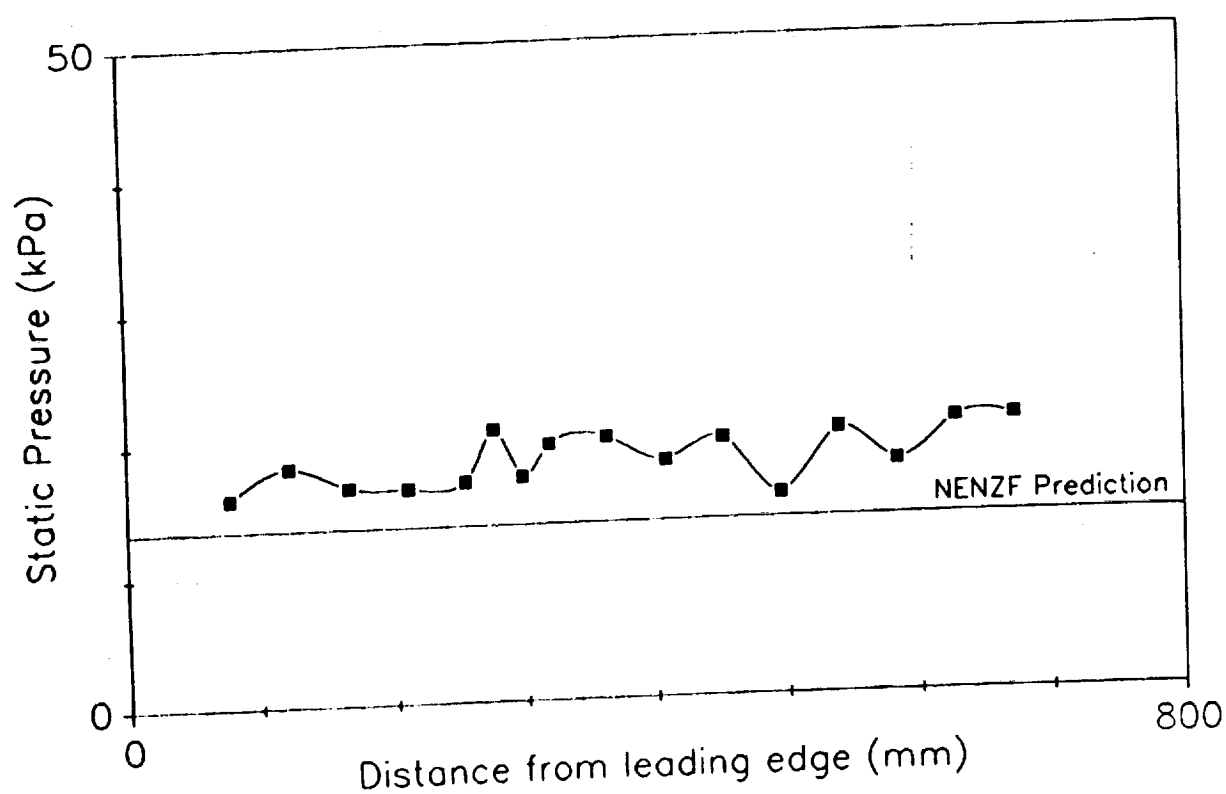


Figure 9. Centreline pressures as a function of position measured inside a duct of dimensions 54.5x55.0 mm. Averaged over 0.02 ms.

PARAMETRIC STUDY ON THRUST PRODUCTION IN THE TWO DIMENSIONAL SCRAMJET

Gary A. Allen, Jr.
University of Queensland
Brisbane, Australia

Abstract

The paper examines thrust production in the two dimensional scramjet. The method of analysis used is the nonhomotropic (nonisentropic) method of characteristics. This method is used in developing a computer program which takes a Mach number distribution as input and determines the thrust produced on the scramjet's diverging section. The Mach number distribution is found experimentally or through another numerical method. The resulting program is essentially a postprocessor which determines thrust for different scramjet geometries for a given Mach number distribution. In the paper some optimal angles for maximum pressure are described.

1. Introduction

There are many possible scramjet geometries with different thrust production processes. In this paper we will examine one of the simplest geometries which is the two dimensional open duct scramjet. The particular thrust production process which we will study occurs where the burnt and quenched fuel-air mixture has passed over the diverging section of the scramjet. A phenomena of particular interest in this paper is the influence upon thrust by the variation of diverging section angle.

Our theoretical model for the thrust production process was the steady, compressible, two dimensional Euler equations, assuming a perfect gas. The Euler equations were solved through a computer program using a numerically integrated form of the nonhomotropic method of characteristics. The advantages in using this simple theoretical model were in the resultant computer program being small, extremely fast and usable on a low cost personal computer.

2. Theory

The use of characteristics in studying the scramjet is by no means original. Antonio Ferri in his classic paper [1] on axisymmetric scramjets used characteristics with a simple combustion model. In a paper by R.J. Stalker, et al. [2] the thrust production process for a two dimensional scramjet was described using diverging and converging Mach waves based on an approximate theory developed by Weinbaum [3]. Our approach to this problem employs the physical model used by Stalker, et al. with a nonisentropic (or more precisely a nonhomotropic) characteristics method as shown in Vincetti and Kruger [4].

The fundamental equations are the steady, two dimensional, compressible Euler equations cast in Cartesian coordinates:

$$\frac{\partial(\rho u)}{\partial x} + \frac{\partial(\rho v)}{\partial y} = 0 \quad (1)$$

$$\rho \left[u \frac{\partial u}{\partial x} + v \frac{\partial u}{\partial y} \right] = - \frac{\partial p}{\partial x} \quad (2)$$

$$\rho \left[u \frac{\partial v}{\partial x} + v \frac{\partial v}{\partial y} \right] = - \frac{\partial p}{\partial y} \quad (3)$$

Where ρ is density, u is velocity in the x direction, v is velocity in the y direction, p is pressure. The x direction is parallel to the local streamline. The y direction is normal to the local streamline. If we assume the flow is isentropic along the streamline (but not necessarily isentropic normal to the streamline), we may recast equations (1)-(3) into the more simplified form:

$$\frac{\partial \theta}{\partial \eta} = - \frac{[M^2 - 1]^{\frac{1}{2}}}{\gamma M^2 P} \frac{\partial p}{\partial \eta} \quad (4)$$

$$\frac{\partial \theta}{\partial \xi} = \frac{[M^2 - 1]^{\frac{1}{2}}}{\gamma M^2 P} \frac{\partial p}{\partial \xi} \quad (5)$$

Where θ is the streamline angle with respect to an axis in inertial space, M is the Mach number, γ is the ratio of specific heats, η is the coordinate along the characteristic (Mach wave) which is deflected by an angle μ from the streamline. ξ is the coordinate along the characteristic which is deflected by an angle minus μ from the streamline. Figure 1 depicts the streamline with these different coordinate systems and the two characteristics.

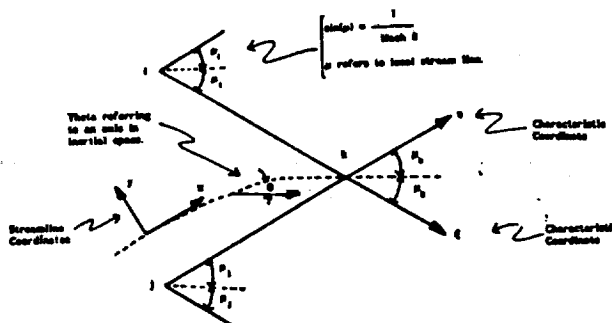


Figure 1.

Streamline, Characteristics and Coordinate System

If we were to assume the flow was completely isentropic (a false assumption for the scramjet problem), then we could further simplify equations (4) & (5) into the classical Method of Characteristics solution form:

$$\frac{\partial}{\partial \eta} (\omega - \theta) = 0 \quad (6)$$

$$\frac{\partial}{\partial \xi} (\omega + \theta) = 0 \quad (7)$$

Where ω is the Prandtl-Meyer function which is defined as:

$$\omega = \left[\frac{\gamma - 1}{\gamma + 1} \right]^{\frac{1}{2}} \text{ARCTAN} \left[\left[\frac{\gamma + 1}{\gamma - 1} (M^2 - 1) \right]^{\frac{1}{2}} \right] - \text{ARCTAN} [(M^2 - 1)^{\frac{1}{2}}] \quad (8)$$

It should be mentioned there is a nonhomentropic formulation which uses the Prandtl-Meyer function as a dependent variable. This form can be found in Liepmann and Roshko [5]. Using the Prandtl-Meyer function for the nonhomentropic case seems advantageous since this formulation is quite compact and accurate for the isentropic regions of the flow. Unfortunately the use of the Prandtl-Meyer function in nonhomentropic flow requires carrying the temperature as a dependent variable in the vorticity terms. This would create a host of added and unnecessary problems. Therefore it was concluded the pressure-theta technique shown in equations (4) & (5) was the superior approach.

The classical Method of Characteristics method shown in equation (6) & (7) can be integrated exactly. We may not assume the scramjet problem is fully isentropic. Therefore we must employ the nonhomentropic formulation as shown in equations (4) & (5) which need to be integrated numerically. If a first order finite difference technique is used on equations (4) & (5) then the following is derived:

$$\theta_k - \theta_j = - \frac{(M_j^2 - 1)^{\frac{1}{2}}}{\gamma M_j^2 P_j} (P_k - P_j) \quad (9)$$

$$\theta_k - \theta_i = \frac{(M_i^2 - 1)^{\frac{1}{2}}}{\gamma M_i^2 P_i} (P_k - P_i) \quad (10)$$

The solution procedure assumes all conditions are known at points i and j as seen in Figure 1. The values for P_k and θ_k are found directly from

equations (9) & (10). However to propagate the solution, the Mach number for point k needs to be calculated as well. This Mach number is found by assuming the flow is isentropic along streamlines. The usual procedure seen in textbooks is to extrapolate the path of the streamline backwards to the line connecting points i and j. The values for pressure and Mach number are then found by interpolation along this line. Once the Mach number and pressure have been found on the stream line then one can calculate pressure at point k by utilizing the isentropic chain. Our experience has indicated the use of both points i and j in the extrapolation/interpolation process made the computation overly implicit and magnified error. A better method was to extrapolate upstream to the next Mach wave and perform the interpolation there.

In principle this method can deal with shock waves since the theory allows for changes in entropy along a streamline. However this theory was usable only because the combustion process was assumed to be quenched before it encountered the scramjet's thrust producing expansion fan. Unfortunately it is likely that induced shock waves would cause local reignition of the fuel-air mixture introducing complicated chemical and real gas effects which were not modeled by the theory. Therefore the computer program developed with this theory looks for the coalescence of Mach waves which would indicate the formation of a shock wave. When a shock wave is detected, the program prints out a warning message. Fortunately induced shock waves do not occur until the scramjet is near its operating limit. Therefore induced shock waves were not a serious limitation to this method.

3. Computer Program

The computer program developed in this study was optimized for both speed and minimum memory requirement (25 CPU seconds on an IBM-PC/AT). The basic scramjet geometry described by the computer program is depicted in Figure 2.

The computation starts at the leading Mach wave which is the first Mach wave of the expansion fan radiating from the diverging section corner as shown in Figure 2. The fuel/air mixing layer along the leading Mach wave is divided into forty characteristic pairs. The air region above the fuel/air layer region is divided into another forty pairs up to the top of the duct. The scramjet is assumed to be an open duct type, viz. no upper surface.

The expansion fan is divided into five regions where each region is subdivided into seven sectors. Six hundred and forty characteristic pairs are generated for each region. When the next region is calculated, all but the last sector of characteristic pairs from the previous region are thrown away resulting in the computer's data memory requirement being kept below 64 kilobytes. This 64 kilobyte memory restriction is a consequence of using personal computers with the Intel 80x86 microprocessor.

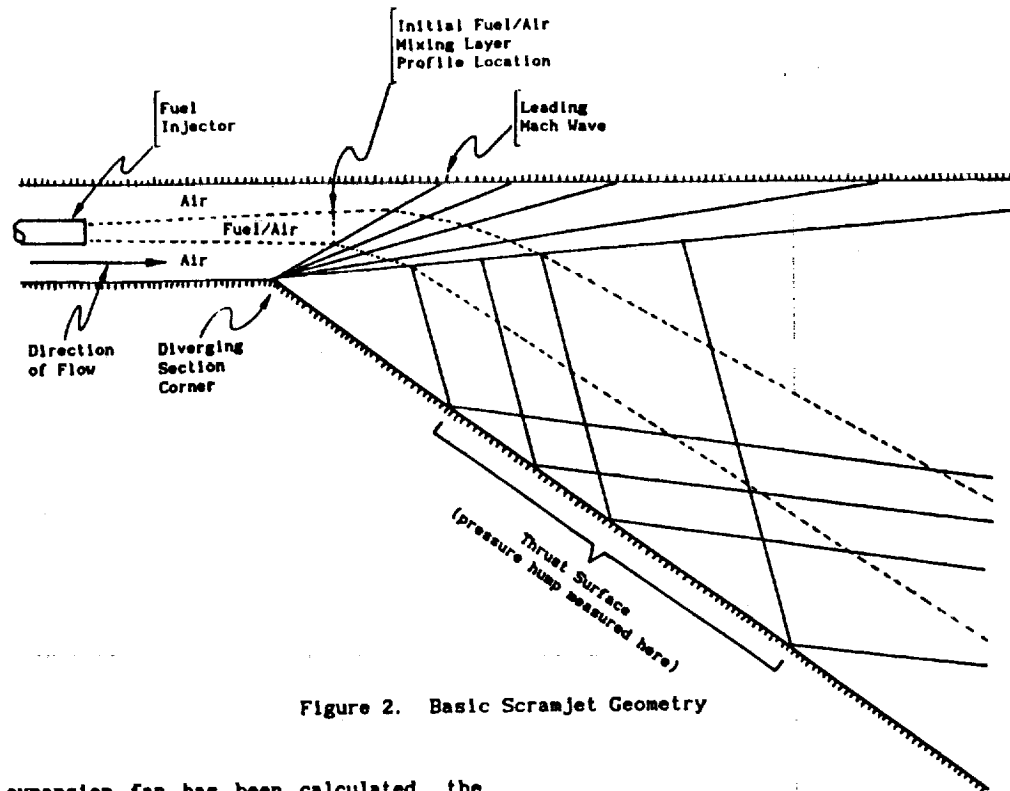


Figure 2. Basic Scramjet Geometry

Once the expansion fan has been calculated, the program then calculates the characteristics down to the surface of the diverging section (thrust surface). The characteristics are each evaluated to determine if they cross prior to encountering the thrust surface. If the characteristics do cross, then it is assumed a shock wave has formed resulting in the computer program generating a warning message. Characteristics reflecting away from the thrust surface are not checked to see if they cross since it is not believed that reflected induced shock waves are significant to thrust production.

The characteristics leading to the thrust surface are divided into ten regions each with six hundred and forty characteristic pairs. Calculation of total thrust is found by integrating the local wall pressure over the thrust region using the trapezoidal rule.

The scramjet is assumed to always have central fuel injection since our experimental data used central injection. Wall injection can also produce a central fuel/air mixing layer by fuel being injected away from the wall and passing some lateral distance before combustion begins.

The fuel/air mixing layer as it encounters the leading Mach wave is described by a Gaussian distribution for the Mach number. The initial velocity vector is assumed to be parallel to the wall. The initial static pressure is assumed to be uniform across the duct. The Gaussian distribution for Mach number is matched to the duct air layers on both boundaries of the fuel/air mixing layer. The ratio of specific heats is assumed to be uniform throughout the scramjet. It should be emphasized that these initial conditions are input parameters based on experimental data and are not actually calculated.

The program was tested against a nozzle designing program written by P. Jacobs [6] to establish its basic validity. The nozzle designing program was developed to solve for homentropic flow with Riemann invariant characteristics. It was found the two programs generated results with very good agreement even though the characteristic mesh resolution and solution procedures were different.

4. Program Initialization Data

The experimental data used for initializing this computer program was taken from the R.J. Stalker, et al. paper. The data was generated in the T-3 shock tunnel at the Australian National University, Canberra. Table 1 shows the test conditions for the three experiments used. This data roughly corresponds to a flight Mach number of about eight.

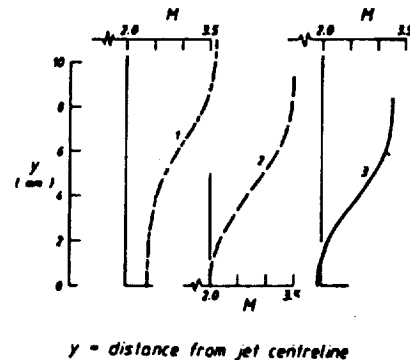


Figure 3. Mach Number Profiles Prior to the Expansion Fan (from ref. [2])

Test Case No.	1	2	3
Stagnation Enthalpy (MJ/kg) ^a	4.3	6.1	8.7
Precombustion Pressure (kPa) ^b	140	180	160
Precombustion Temperature (K)	1300	1900	2500
Precombustion Velocity (km/sec)	2.42	2.85	3.26
Precombustion Mach Number	3.50	3.35	3.40
Ratio of Specific Heats, γ	1.35	1.32	1.32

^aExperimental error $\pm 3\%$, ^bExperimental error $\pm 5\%$

Table 1. Experimental Test Conditions (from ref. [2])

The initial Mach number profiles in the duct used for the parametric study are shown in Figure 3. These Mach number profiles are measured normal to the duct's axis of symmetry in the fuel/air mixing layer just prior to where the duct's flow encounters the leading Mach wave (see Figure 2).

The actual dimensions of the experimental scramjet were not provided in the original Stalker paper. They are now provided in Figure 4.

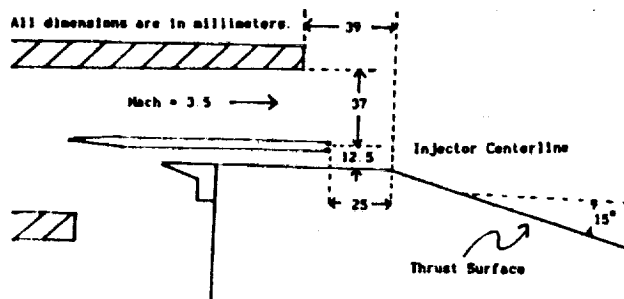


Figure 4 Physical Dimensions of the Experimental Scramjet

5. Diverging Section Angle Effect on Thrust

The angle of the T-3 experimental diverging section was fifteen degrees (see Figure 4). The vertical axis in Figure 5 uses the pressure parameter $\Delta P/P$. This pressure parameter is based on static pressures and is defined as:

$$\frac{\Delta P}{P} = \frac{\text{Pressure(Fuel On)} - \text{Pressure(Fuel Off)}}{\text{Pressure(Precombustion)}} \quad (11)$$

The precombustion pressure was measured in the duct just prior to the leading Mach wave of the expansion fan. The Fuel On and Fuel Off pressures were measured from a set of pressure taps on the thrust surface. The Fuel On value was the wall pressure measured when combustion had occurred. The Fuel Off value was the wall pressure measured when combustion had not occurred due to the fuel (hydrogen) not being injected. The horizontal axis in Figure 5 is the radial distance in millimeters downstream from the diverging section corner as shown in Figure 2.

The broken horizontal line corresponds to the Fuel Off value for pressure. An interesting development in Figure 5 is the region between 230 mm and 310 mm where the pressure has dropped below the Fuel Off value. The scramjet is actually producing negative thrust in that region. The Mach waves which created this negative thrust emanate from the fuel-air mixing layer where the thrust surface reflected Mach waves of the main thrust hump also cross. This negative thrust region also reflects Mach waves resulting in the thrust surface pressure oscillating as a decaying sinusoidal converging to the Fuel Off value.

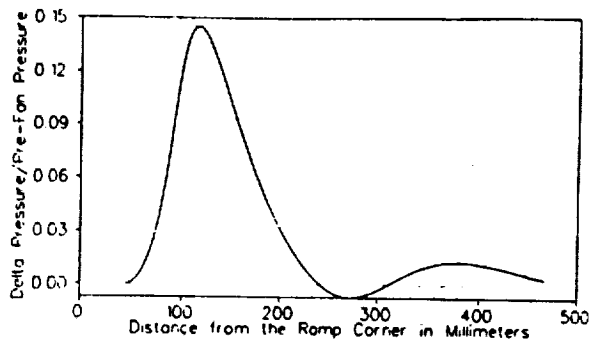


Figure 5. Pressure Distribution at 15 Degrees for Case 3

A parametric study was performed which involved varying the angle of the diverging section. The results of this study are depicted in Figures 6.1-6.3 which correspond to the three cases examined experimentally. These plots are truncated where the primary thrust hump reaches the Fuel Off value.

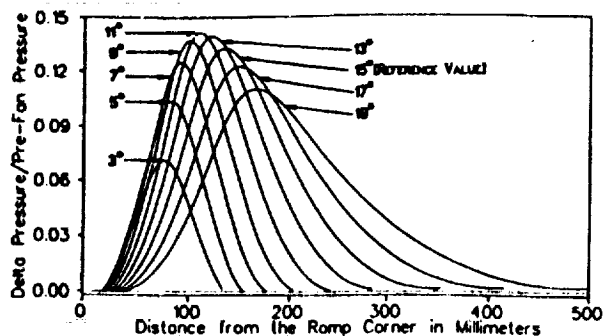


Figure 6.1. Variation of the Diverging Sections Angle for Case 1

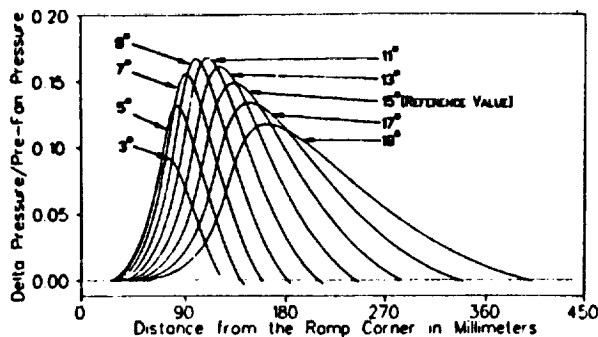


Figure 6.2. Variation of the Diverging Sections Angle for Case 2

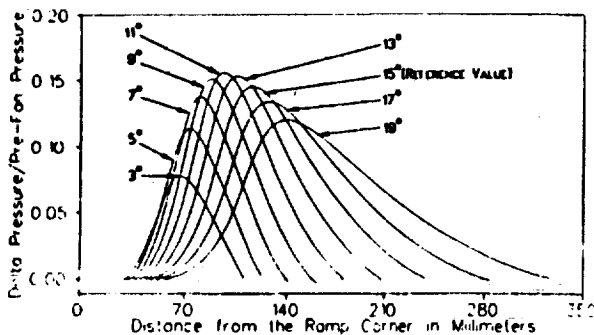


Figure 6.3. Variation of the Diverging Sections Angle for Case 3

Each plot shows nine different pressure traces for different diverging section angles starting with an angle of three degrees and going through a range of angles at two degree increments to a final diverging section angle of nineteen degrees. It was observed that the maximum pressure occurred in Figure 6.1 at a ramp angle of 11.40 degrees. In Figure 6.2 the maximum pressure occurred at a ramp angle of 9.95 degrees. In Figure 6.3 the maximum pressure occurred at a ramp angle of 11.05 degrees.

Thrust was calculate by integrating the pressure over the entire length of the trace. Plots showing thrust as a function of diverging section angle for the three test cases are shown in Figure 7.

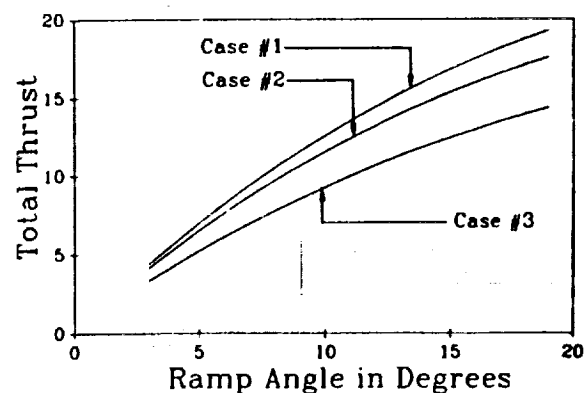


Figure 7. Scramjet Thrust as a Function of Diverging Section Angle

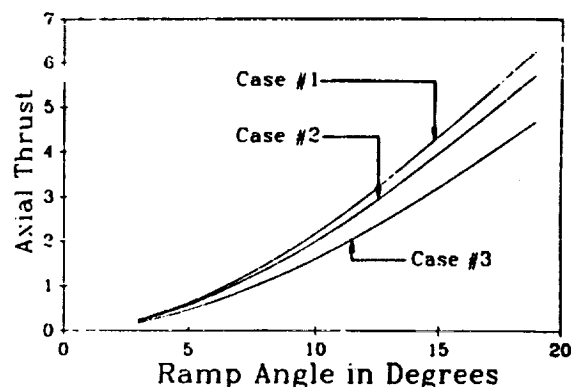


Figure 8. Scramjet Axial Thrust as a Function of Diverging Section Angle

Before this study was performed, it was speculated that the Euler equations might reveal an optimum diverging section angle which yielded maximum thrust. Figure 7 shows the total thrust increased monotonically as diverging section angle increased. Axial thrust is the component of total thrust which would overcome drag in a hypersonic vehicle. Figure 8 shows axial thrust increased as diverging section angle increased. Obviously the Euler equation model for thrust production would breakdown where the diverging section angle increased sufficiently to cause flow separation from the wall. Also our model of a scramjet assumed the thrust surface was infinitely long. Clearly in an actual scramjet the thrust surface must have a finite length. The relevance of thrust surface length was demonstrated in Figures 6.1 - 6.3, where the pressure hump increased in length with an increase in diverging section angle. At some angle the pressure hump would spill off of the thrust surface. Although it was not revealed by our approach with the Euler equations, for a scramjet with a finite length thrust surface there would be an optimal diverging section angle for maximum thrust production.

6. Numerical Error

The main source of error in the numerical method comes from the uncertainty in extrapolation of the streamline's path. This uncertainty in the streamline's position degraded the accuracy of the interpolation process. This in turn reduced the accuracy of the solution at point k thus propagating the error. When the flow field was fully isentropic (and therefore streamline path independent), the computation was extremely accurate. Figure 9 shows this type of flow with one pressure trace calculated by the classical Prandtl-Meyer technique versus a second trace calculated by the nonhomentropic technique.

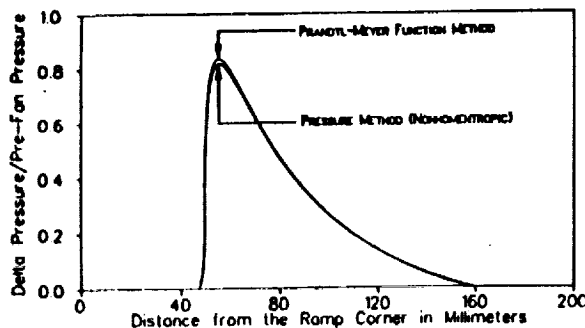


Figure 9. Comparison of the Prandtl-Meyer versus Pressure Solution Methods

Figure 10 shows the consequence of error in streamline tracking and interpolation for a nonhomentropic flow. One trace in Figure 10 is calculated by taking the initial conditions across a duct with uniform pressure and velocity direction. The solution is propagated down the duct by the method of characteristics to the leading mach wave of an expansion fan and then passed through the fan. The second trace involves having the initial conditions imposed directly on the leading mach wave and then passed through the expansion fan. The two traces should be identical but are different due to errors accumulated in the streamfunction tracking and interpolation in the duct. It would appear this error never exceeded ten percent of the exact value.

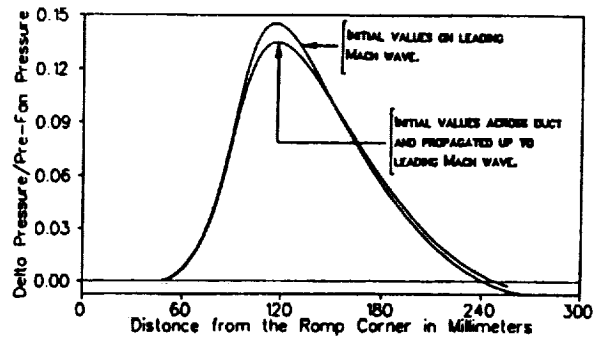


Figure 10. Traces Differing due to Error in Stream Function Tracking

7. Experimental Verification

The R.J. Stalker, et al. paper which provided the initialization data for this work also provided experimentally measured pressure distributions of the scramjet thrust surface. Unfortunately it was found these pressure distributions were contaminated by a reflected shockwave which originated from the trailing edge of the fuel injector strut. Fortunately there existed from the same experimental study unpublished cases gathered by R.G. Morgan where the fuel injector was moved 15 centimeters and 20 centimeters further upwind in the scramjet channel. Consequently the fuel injector strut shockwave would in these cases reflect from the lower channel surface prior to reaching the diverging section corner and thus not contaminate the thrust surface data. The Mach number distributions for these two cases were the same as in Case 2 of the original paper but scaled up in size to allow for the 15 or 20 cm. additional distance the fuel/air mixing layer propagated down the scramjet channel. These new Mach number distributions are shown in Figures 11.1 and 11.2.

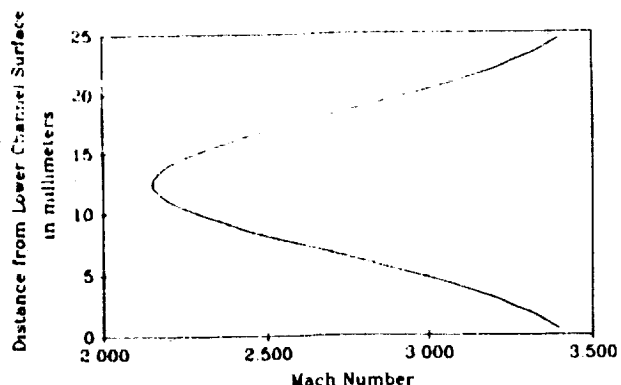


Figure 11.1. Mach Number Distribution for Case 2 with 15 cm. Displacement

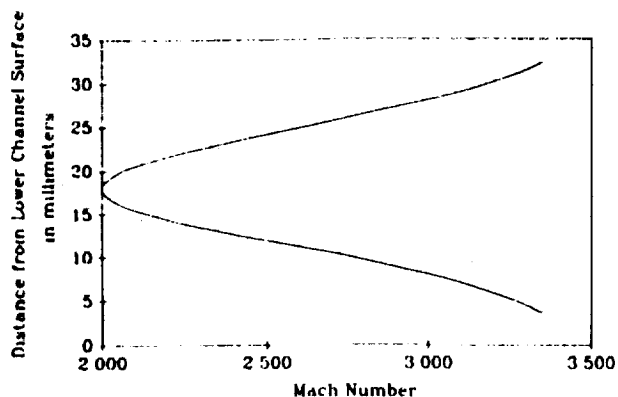


Figure 11.2. Mach Number Distribution for Case 2 with 20 cm. Displacement

The resultant pressure distributions calculated for these Mach number distributions with the experimental data collected by R.G. Morgan are shown in Figures 12.1 and 12.2.

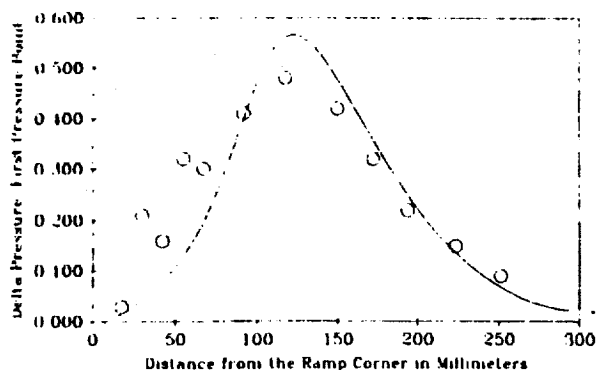


Figure 12.1. Pressure Distribution for Case 2 with 15 cm. Displacement

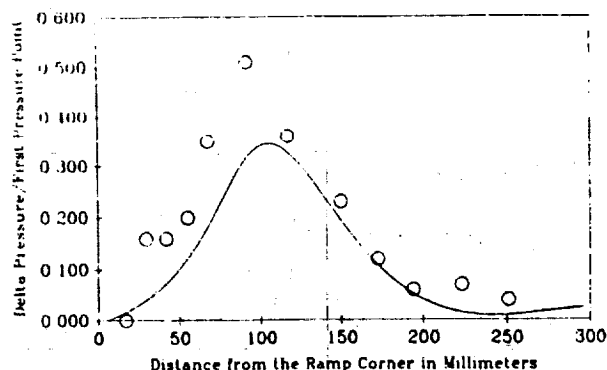


Figure 12.2. Pressure Distribution for Case 2 with 20 cm. Displacement

The theoretical versus experimental data in Figures 12.1 and 12.2 correlates as well as one would expect for shock tunnel data. Unfortunately these results are by no means conclusive. An attempt was made to calculate the Mach number distribution directly (without going through a scaling argument) using the CHARNAL program. CHARNAL was developed at NASA Langley and solves the compressible Navier Stokes equations using a k- ϵ turbulence model and also models hydrogen combustion in air. CHARNAL predicted significantly wider Mach number distributions than those previously used. When the CHARNAL Mach number distributions were used as input for the characteristics program, the resultant pressure distributions were shifted 50 millimeters downstream. However the CHARNAL results are in doubt since unpublished experiments performed by Robert Casey at the University of Queensland T-4 shock tunnel facility indicated that CHARNAL predicted significantly wider Mach number distributions compared to those he measured experimentally. It is suspected the k- ϵ turbulence model in CHARNAL may not be adequately modeling viscous diffusion in the fuel/air mixing layer.

8. Conclusions

In this paper we have investigated the thrust production process in the two dimensional scramjet using a high speed computer program written for small personal computers. We have shown that for specific diverging section angles the peak pressure on the thrust surface achieves a maximum value. However we have also shown the axial thrust does not have a maximum value for a specific diverging section angle provided the thrust surface is infinitely long. Rather the axial thrust increases monotonically with diverging section angle.

Computer investigations of the scramjet are usually restricted to the province of super computers doing runs on the order of CPU hours. This study has demonstrated that useful information can be obtained from a small and fast computer program using the Method of Characteristics.

References

1. Ferri, A., *Journal of the Royal Aero. Society* 68:575-597 (1964).
2. Stalker, R.J., Morgan, R.G., and Metterfield, M. P., *Combust. Flame* 71: 63-77 (1988).
3. Weinbaum, S., *A.I.A.A. Journal* 4:217-226 (1966).
4. Vincenti, W.G., and Kruger, C., *Introduction to Physical Gas Dynamics*, John Wiley & Sons, New York, 1965.
5. Liepmann, H. W., and Roshko, A., *Elements of Gasdynamics*, John Wiley & Sons, New York, 1967, p. 295.
6. Jacobs, P.A., *An Interactive Graphics Program for Computer-Assisted Calculation of Isentropic Supersonic Flows*, Report 7/88 Department of Mechanical Engineering, University of Queensland, 1988.

The glancing interaction of a Prandtl-Meyer expansion fan with a supersonic wake

M. K. SMART* and R. J. STALKER
Department of Mechanical Engineering
University of Queensland, Australia

ABSTRACT

The glancing interaction of a Prandtl-Meyer expansion fan with a supersonic wake is examined. The particular supersonic wakes of interest are the combustion wake generated by a vertical strut injected scramjet, and the side wall boundary layer of a supersonic wind tunnel. A physical structure for the interaction is defined, and an approximate analysis of the downstream behaviour of the wake is presented. The phenomenon of wake over-turning by the glancing expansion fan is introduced, based on this analysis. This over-turning produces a high pressure zone on the expansion generating surface, which for the vertical strut injected scramjet, is part of the thrust nozzle. Combustion wake over-turning is suggested to be a major thrust producing mechanism in this form of scramjet.

Pressure measurements were taken on the expansion generating surface of a glancing interaction involving the side wall boundary layer of a small supersonic wind tunnel. Results from the analysis presented were found to be consistent with these measurements.

NOMENCLATURE

A	cross-sectional area of the bulge
M	flow Mach number
m	mass flow rate into the groove per unit length along the expansion surface
m_b	mass flow rate into the bulge per unit length along the expansion surface
P	flow pressure
P_{eq}	equivalent pressure over the expanded wake thickness (δ_2), which generates the same thrust as the spreading pressure field
P_E	expanded free stream pressure in experiments
P_F	undisturbed free stream pressure in experiments
ΔP	pressure rise on wedge due to boundary layer over-turning in experiments
R	bulge radius
R_o	forebody radius of bulge

*Now at WBM Pty Ltd, Brisbane, Australia.
Manuscript received 3 January 1990, revised version received 28 November 1990, accepted 19 December 1990.
Paper No 1764.

T	flow temperature
V	flow velocity
x	distance along the expansion surface
α	over-turning angle of the wake
β	ratio of thrust per unit upstream width of the wake, to the thrust per unit upstream width of the mainstream
λ	angle of the interaction line relative to the mainstream flow direction
δ	wake thickness
ν	turning angle of the wake through interaction
θ	turning angle of the mainstream through the interaction
$d\theta$	turning angle of the mainstream through the incremental interaction
γ	ratio of specific heats
ρ	flow density
ϵ	non-dimensional wake thickness parameter
Σ	$\int_0^1 \tan \alpha(\epsilon) d\epsilon$

Subscripts

M	mainstream
W	wake
1	upstream of the interaction
2	downstream of the interaction
x	component in the direction normal to the interaction line
z	component in the direction tangential to the interaction line
N	normal to the expansion surface
P	parallel to the expansion surface

1. INTRODUCTION

Consider a two-dimensional wake in a supersonic flow. The Mach number in the wake also is taken to be supersonic, but is lower than the surrounding stream. Bounding the wake on the spanwise side is a plane surface. As shown in Fig. 1, a sharp convex corner at the surface generates a centred Prandtl-Meyer expansion, which propagates across the wake to participate in a glancing interaction.

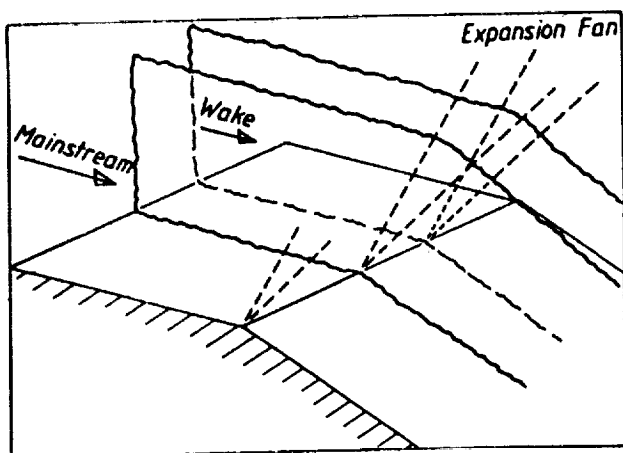


Figure 1. Flow configuration.

This type of flow situation is common on supersonic vehicles, when the wake of a wing or a fin interacts with the expansion waves generated by downstream parts of the vehicle. However, it is of more immediate interest for two other situations. As shown in Fig. 2(a) the first occurs in a supersonic combustion ramjet (Scramjet). In this case the wake is formed by fuel injection, from a strut, into the combustion chamber duct. The fuel mixes and burns with the stream tubes of supersonic air passing through the duct, raising the temperature and speed of sound, and lowering the Mach number, in a manner which is not uniform across the duct. This produces the wake structure which is of interest here. Of course, if the combustion chamber is long enough the wake structure degenerates into a uniform Mach number distribution, but it is unlikely that this state will be realised in practice. Therefore, scramjet thrust production is expected to involve supersonic wakes, and the use of expansions to release energy from them.

Such a process has been studied in two dimensions in Ref. 1. There the expansion was due to the wave generated by a corner located in a plane which is parallel to the plane of the wake. This would be represented in Fig. 2(a) by divergence of the sidewalls of the duct, rather than the bottom surface divergence which is shown in the Figure. In the two dimensional case it was found that the mechanism of thrust production was peculiar to supersonic flow, with the low Mach numbers in the wake interacting with the expansion wave to generate thrust producing compression waves. The present study can be seen as an extension of this work, exploring the way in which a similar mechanism might operate in a three dimensional flow, represented here by placing the corner at right angles to the plane of the wake.

The second situation occurs when an expansion fan participates in a glancing interaction with a boundary layer, as shown in Fig. 2(b). In this case the wake becomes the low Mach number boundary layer and if the viscous flow in the subsonic sublayer close to the wall is neglected, this interaction can be seen to be similar to that involving the combustion wake, with the wall being a plane of symmetry. The upstream effects of this interaction are expected to be small⁽²⁾, indicating that downstream effects are likely to be of most interest. This is also a feature which is similar to the combustion wake.

The discussion in this paper concentrates on the downstream effects of the glancing expansion-wake interaction just described. The phenomenon of wake flow over-turning in response to the expansion is investigated first. This is seen to produce a wake flow downstream of the interaction with a velocity component directed towards the expansion generat-

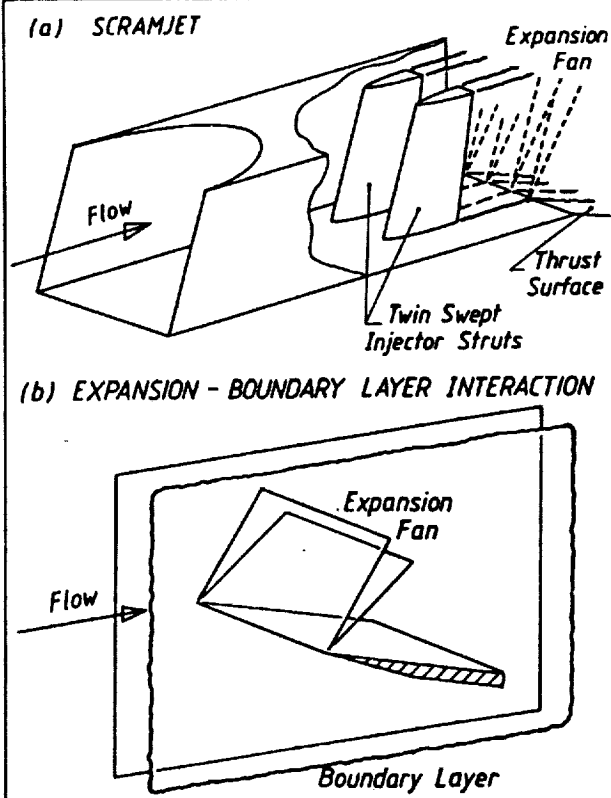


Figure 2. Examples of expansive interactions.

ing surface. As a consequence of this velocity component, part of the surface experiences a pressure rise. An approximate analysis for predicting this pressure rise is presented, and is found to be consistent with experimental measurements of an interaction involving the side wall boundary layer of a small supersonic wind tunnel.

2. FLOW OVER-TURNING

The interaction between a wake and a Prandtl-Meyer expansion is modelled by assuming that the wake is thin. The analysis then bears a resemblance to that used for glancing shock-boundary layer interactions⁽²⁾. However, unlike a shock-boundary layer interaction, the pressure change impinging on the boundary layer in this case occurs smoothly over the finite angular width of a Prandtl-Meyer fan.

In order to accommodate this difference, the separable nature of the Prandtl-Meyer fan is used. The interaction is modelled as a large number of very weak expansion fans impinging on the wake one after another. As shown in Ref. 2, the equations of motion of a boundary layer, when expressed in terms of perturbations to the dependent variables (i.e. pressure, density and velocity) turn out to be linear if the perturbations are small with respect to undisturbed values. Thus, the interaction of each of the very weak expansion fans with the wake can be treated independently of the others, and, provided that the resulting perturbations are not too large, the results can be added to yield a description of the overall reaction.

The expected physical structure of the interaction of a very weak expansion fan with a wake is shown in Fig. 3. Viewed in plan in Fig. 3(a), the pressure change in the wake is seen

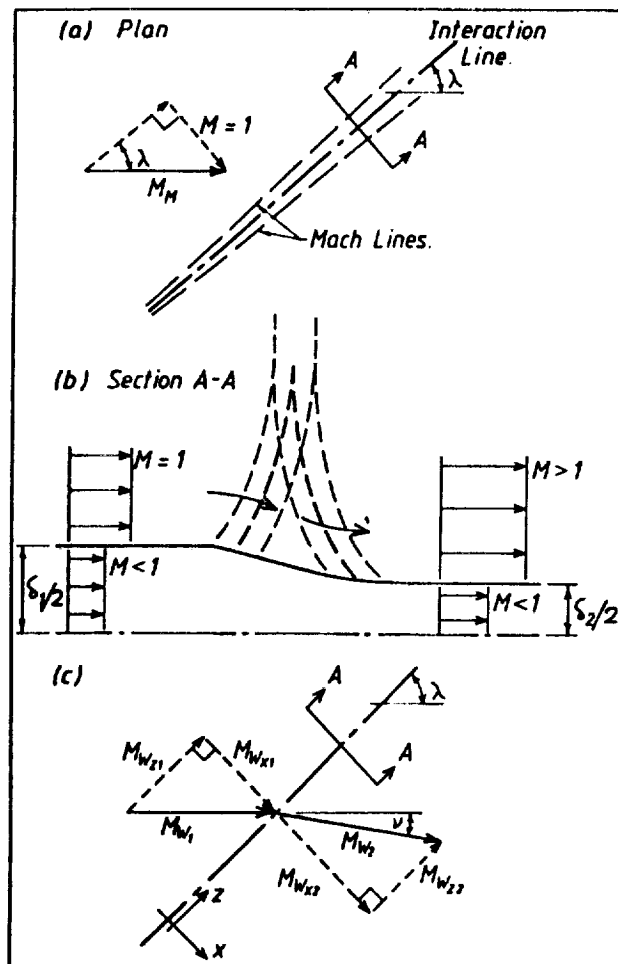


Figure 3. Weak expansion wave interaction.

to occur across a region which is thin with respect to its spanwise extent. The flow can then be described in terms of the cross-sectional view shown in Fig. 3(b). For simplicity, the wake is regarded as a uniform flow, with a subsonic component of Mach number in the direction normal to the leading Mach line of the expansion. Initially, the mainstream has a sonic component of Mach number normal to the leading Mach line, but it becomes supersonic in passing through the interaction.

Streamlines far out in the mainstream will cross the expansion without deflection in the plane of view of Fig. 3(b) (they deflect normal to this plane). The falling pressure impinging on the wake causes it to thin as it enters the interaction and, as it does so, expansion waves which do cause flow deflection in the plane of view will propagate into the mainstream. In order to match the no deflection condition well out into the mainstream, these waves must be cancelled by other expansions propagating back towards the wake. As shown in the Figure, these cause the edge of the wake to deflect back towards the mainstream, thus allowing the edge of the wake to resume the upstream flow direction as it emerges from the interaction. The expansion waves in the mainstream therefore form a 'lambda' pattern in the plane of view, and thereby allow the mainstream to accommodate the thinning of the wake.

The over-turning effect in the wake takes place in the plane of the wake itself. In order to calculate the effect it is noted that, if an interaction line is formed by bisecting the angle between the leading Mach line and the trailing Mach line of

the expansion, as displayed in Fig. 3(a), then it can be shown that there is no net component of pressure gradient along the interaction line. Thus, referring to Fig. 3(c), the turning of the flow in the wake can be determined by first resolving the upstream and downstream wake Mach numbers, M_{w1} and M_{w2} respectively, into their components normal to and parallel with the interaction line. The weak expansion is specified by the angle $d\theta_M$ (not shown in the figure) through which the mainstream flow turns as it passes through the interaction. The pressure drop associated with the thin expansion is assumed to occur instantaneously along the interaction line. The interaction line is swept at angle λ to the oncoming mainstream flow, and the wake turning angle, v , is in the sense shown in Fig. 3(c).

It should be noted that the interaction model assumes that derivatives of the flow properties in the 'z' direction are zero, meaning that the flow is cylindrically symmetric. Following Ref. 3, it is acknowledged that this will not be true close to the corner which generates the expansion. However, Ref. 3 also indicates that a close approximation to a cylindrically symmetric situation will be developed within a distance of the order of ten wake thicknesses from the corner. Provided it is accepted that substantial errors may occur close to the corner, a cylindrically symmetric analysis can be used for all the flow.

For cylindrical symmetry, the 'z' component of velocity remains constant across the interaction. Treating the flow in the wake as one-dimensional and isentropic, it then follows that the components of M_{w2} normal to and parallel with the interaction line are

$$M_{w2} = \sqrt{\frac{2}{\gamma-1} \left(\frac{T_1}{T_2} \left(1 + \frac{\gamma-1}{2} M_{w1}^2 \right) - 1 \right)} \quad \dots (1)$$

and

$$M_{w2} = M_{w1} \sqrt{\frac{T_1}{T_2}} = M_{w1} \cos \lambda \sqrt{\frac{T_1}{T_2}} \quad \dots (2)$$

where

$$\frac{T_1}{T_2} = \frac{1 + \frac{\gamma-1}{2} M_{w2}^2}{1 + \frac{\gamma-1}{2} M_{w1}^2} = \left(\frac{P_1}{P_2} \right)^{\frac{\gamma-1}{\gamma}} \quad \dots (3)$$

The resultant wake Mach number downstream of the interaction, M_{w2} , the wake turning angle through the interaction, v , and the reduction in thickness of the wake as it passes through the interaction may simply be calculated as follows.

$$M_{w2} = \sqrt{M_{w1}^2 + M_{w2}^2} \quad \dots (4)$$

$$v = \phi_1 - \phi_2 \quad \dots (5)$$

where $\phi_1 = \cos^{-1}(M_{w1}/M_{w1})$
 $\phi_2 = \cos^{-1}(M_{w2}/M_{w2})$

and

$$\frac{\delta_1}{\delta_2} = \left\{ \frac{1 + \frac{\gamma-1}{2} M_{w1}^2}{1 + \frac{\gamma-1}{2} M_{w2}^2} \right\}^{\frac{\gamma+1}{2(\gamma-1)}} \frac{M_{w2}}{M_{w1}} \quad \dots (6)$$

An example of flow over-turning is evident in Fig. 19(a) of Ref. 3. In that figure experimental surface streamline patterns, obtained by the china-film technique, are displayed for a glancing interaction of a 3° Prandtl-Meyer expansion with a flat plate boundary layer in an $M = 1.85$ mainstream. At some twenty boundary layer thicknesses downstream of the interaction, the surface streamlines are almost straight, indicating that they have ceased to respond to the low momentum cross flow of the low speed portion of the boundary layer. However, the deflection of the surface streamlines is $5^\circ \pm 1^\circ$ with respect to the upstream flow direction. This is well in excess of the mainstream flow deflection of 3° , and indicates that over-turning of the main part of the boundary layer is persisting well downstream of the interaction. It is interesting to note that a reasonable mean value for the boundary layer Mach number is 1.48, and if this is used for M_w in equations (1)-(5), it is found that $\nu = 4.1^\circ$. Whilst the accuracies involved are such that this cannot be seen as a quantitative check of the theory, it does indicate a reassuring order of magnitude consistency with the observed phenomenon.

As indicated earlier, the analysis for a weak expansion fan can be extended to a strong expansion fan by invoking a superposition process. Given a single weak fan analysed according to the preceding analysis, the exit conditions from this interaction may be fed as input to a second weak interaction. In doing this it must be noted that the mainstream and the wake have been turned different amounts through the first interaction, and hence the direction of the respective flows fed to the second interaction are different. The second weak interaction may then be analysed. This procedure is continued until the analysis for a full strong interaction has been performed. It is well suited to implementation on a computer where parameters such as weak incremental expansion strength and Mach number may be easily varied.

3. THRUST DUE TO A COMBUSTION WAKE

At this point it is interesting to consider the thrust due to over-turning as it occurs in the interaction of an expansion fan with a combustion wake. Using once again a uniform profile for the wake, a configuration which is particularly simple to analyse is first chosen, where the surface downstream of the expansion generating corner is adjusted to accommodate the over-turning. As shown in Fig. 4, this involves local deflection of the surface in a groove which just matches the width and deflection of the over-turned wake, and therefore allows it to pass downstream without any further pressure rise.

As the pressure in the groove is the same as the pressure on the surrounding surface after the corner, the larger deflection of the groove surface ensures that its component of surface pressure in the upstream direction is greater than for the mainstream part of the surface. Hence more thrust is generated by the over-turned wake than by the mainstream. Allowing for the thinning of the wake which occurs in passing through the expansion, it can readily be shown that β , the ratio of the thrust per upstream unit width of the wake to the thrust per upstream unit width of the mainstream is given by

$$\beta = \frac{\delta_2 \tan \nu}{\delta_1 \tan \theta} \quad \dots (7)$$

As an example of over-turning induced thrust, combustion wake data from Ref. 1 is employed to indicate that a typical

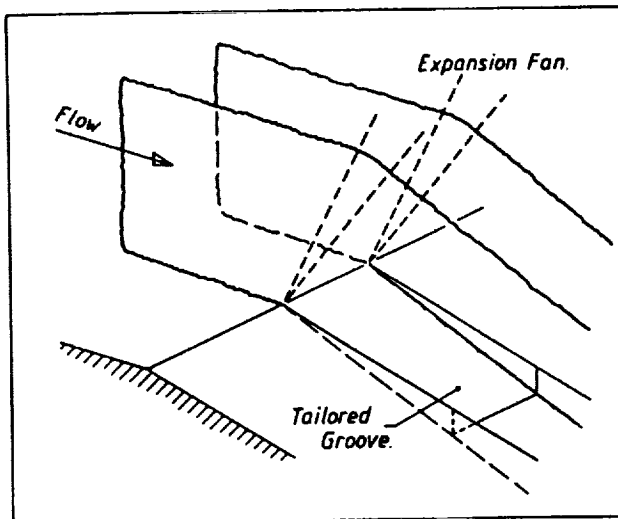


Figure 4. Thrust by local surface deflection.

mean wake Mach number of 2.7 would correspond to a mainstream Mach number of 3.5. For a corner expansion angle of $\theta = 15^\circ$, calculations yield a wake turning of $\nu = 19.76^\circ$ (over turning angle $= 4.76^\circ$) and $\delta_2/\delta_1 = 0.893$. The wake then produces 19.7% more thrust than the mainstream. This thrust increment due to wake over-turning could make a significant contribution to the thrust budget of a scramjet.

Combustion wake over-turning will also generate thrust on a flat expansion surface downstream of the corner. However, unlike the tailored groove surface, this more practical configuration produces a complex supersonic flowfield. As indicated in Fig. 5(a) the crossflow towards the surface which is associated with over-turning in the wake causes accumulation of fluid at the downstream surface and leads to 'bulging' of the wake as more and more wake fluid arrives there. Comparing this with the tailored groove configuration, all wake fluid which previously filled the groove in the expansion surface, now fills the developing bulge above it. Wake fluid entering the bulge will undergo a small pressure rise as it straightens to follow the flat surface, and the growing bulge will deflect surrounding mainstream streamlines. Hence the wake bulge and the region of the mainstream about it form a spreading zone of elevated pressure on the expansion surface, contributing to a thrust. In order to obtain an estimate of the thrust increment generated on a flat surface, the features described above have been incorporated into an analytical flow model through a series of simplifying assumptions. The approximations inherent in these assumptions are ultimately tested in Figs 10 and 11, where it is seen that they yield predictions of surface pressure that are consistent with experiment. The model is summarised in the following paragraphs.

The major thrust producing feature of the flow is expected to be the growth of the wake bulge on the flat constraining surface. Estimates indicate that changes in the thickness of the planar wake above the bulging region will produce effects on the thrust increment which are small enough to be ignored. Given this, the elevated pressure generated on the flat surface outside the wake bulge is, to a first order, equivalent to that about a full body of the bulge shape in a supersonic stream at the expanded mainstream Mach number (the bulge being a half body with the flat surface as a plane of symmetry). To complete the pressure distribution, the pressure is assumed uniform inside the bulge section, the magnitude being equal to that at the bulge surface. Hence the pressure distribution generated on the flat surface, and

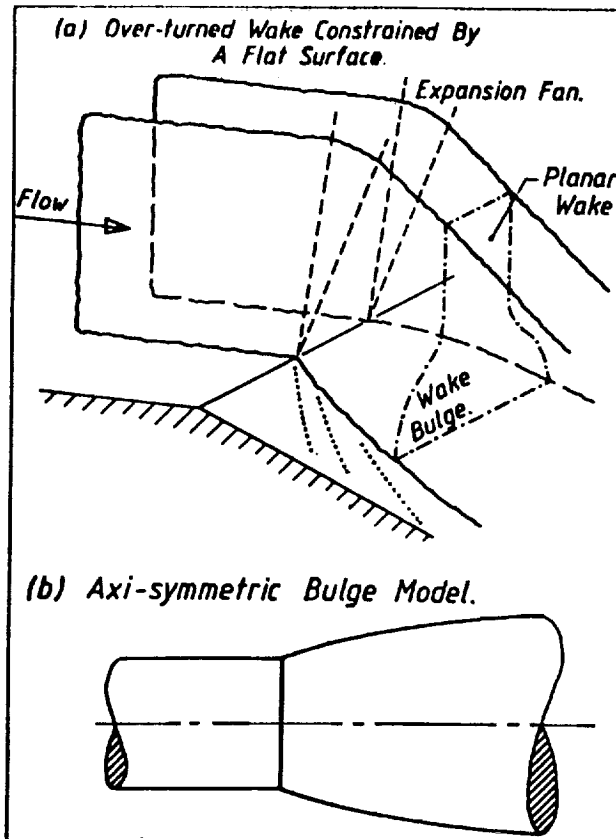


Figure 5. Wake bulge model.

therefore its thrust increment, is dependent solely on the wake bulge development along that surface.

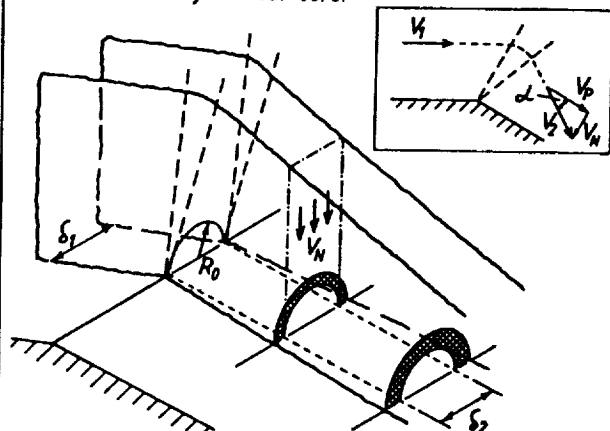
Consistent with the assumption of uniform internal pressure, the bulge is assumed to be circular in cross section as shown in Fig. 5. Of course, this state will only be obtained some distance downstream of the corner when the local compression and expansion waves generated there have suffered sufficient cross-stream reflections to allow nearly uniform pressure to occur over the bulge cross-section. It is by taking the view that only very few reflections are required to produce effectively uniform pressure across the bulge section, that the assumption of semi-circular bulge formation close to the corner can be seen as a reasonable approximation.

The axisymmetric body shown in Fig. 5(b) consists of a cylindrical forebody of radius R_0 equal to half the expanded wake thickness ($R_0 = \delta_2/2$), followed by an axisymmetric profile which is dictated by the wake mass flow into the bulge region. The two profiles join at the corner. At this point a slope discontinuity occurs corresponding to the initial wake growth close to the corner. A body of this shape is used to model the expanded wake thrust increment.

The tailored configuration of Fig. 4 points towards a simple method for the calculation of the wake bulge geometry. In this configuration, all over-turned wake fluid was allowed to flow smoothly into a recess in the expansion surface. It therefore seems reasonable that all fluid which entered the groove in Fig. 4, will now contribute to the bulge growth in the flat plate configuration of Fig. 5. Referring to Fig. 6(a), the wake mass flow rate into the bulge per unit length, denoted dm/dx , is then simply

$$\frac{dm}{dx} = \rho_2 V_N \delta_2 \quad (\text{kg/sm}) \quad (8)$$

(a) Bulge Development Based On Mass Redistribution About A Cylindrical Core.



(b) Bulge Profile Based On Combustion Wake Data.

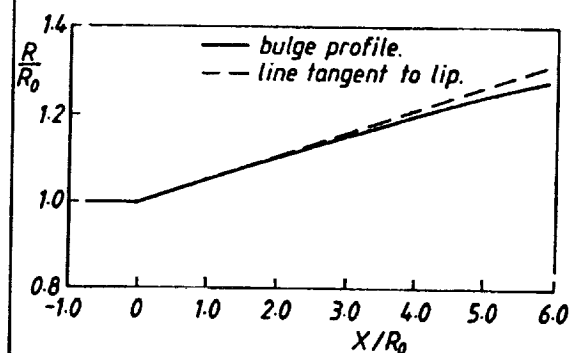


Figure 6. Bulge development.

This rate is uniform along the expansion surface. The wake flow velocity parallel to the expansion surface, V_p , is also constant. The wake mass flow rate into the bulge with respect to distance along the expansion surface, per unit length, dm/dx , is then simply

$$\frac{dm}{dx} = \left(\frac{dm}{dt} \right) / V_p = \rho_2 V_N \delta_2 / V_p \quad (\text{kg/m}^2) \quad (9)$$

As wake fluid enters the bulge it will be redistributed in some manner, and experience a pressure rise. The density variation corresponding to this rise is expected to be small. Its contribution to the bulge profile development will then be of second order and is ignored in this analysis. The relationship between dm/dx and the rate of rate of change of bulge cross-sectional area long the expansion surface, dA/dx , is then

$$\frac{dm}{dx} = \rho_2 \frac{dA}{dx} \quad (\text{kg/m}^2) \quad (10)$$

From equations (9) and (10), and the fact $V_N/V_p = \tan \alpha$ and $\delta_2 = 2R_0$, dA/dx is given by

$$\frac{dA}{dx} = 2 R_0 \tan \alpha \quad (11)$$

The rate of change of bulge radius along the surface is then

$$\frac{dR}{dx} = \frac{2R_0}{\pi R} \tan \alpha \quad (12)$$

Given that $R = R_0$ at the corner ($x = 0$) as shown Fig. 6(a), equation (12) may be integrated to yield the bulge profile

$$\frac{R}{R_0} = \sqrt{1 + \frac{4 \tan \alpha}{\pi} \frac{x}{R_0}}, \quad \frac{x}{R_0} \geq 0 \quad (13)$$

The slope at the discontinuity at $x = 0$ is

$$\Delta \left(\frac{dR}{dx} \right) = \frac{2}{\pi} \tan \alpha \quad (14)$$

The profile based on the combustion wake data of Ref. 1 is shown in Fig. 6(b). Note that the profile is quite slender for the small values of over-turning angle produced.

A number of techniques are available for determination of the supersonic flow field past this axis-symmetric shape. The one chosen here is a second order perturbation technique by Van Dyke⁽⁴⁾ which uses an approximate solution to the supersonic perturbation equation including terms up to a second order. This technique has been shown to produce results for slender quasi-cylindrical bodies close to those from the method of characteristics.

Using the axisymmetric profile shown in Fig. 6(b) and an expanded Mach number of 4.47 corresponding to the $M = 3.5$ mainstream expanded 15° , a first order estimate of the pressure distribution generated on the flat surface due to combustion wake over-turning is shown in Fig. 7. In order to determine the thrust ratio β for this distribution, an equivalent pressure (P_{eq}) generated over the expanded wake thickness δ_2 which produces the same thrust as the spreading pressure field is calculated. β is then

$$\beta = \frac{\delta_2 P_{eq}(x)}{\delta_1 P_2} \quad (15)$$

For the flow in question $\delta_2/\delta_1 = 0.893$ once again, and P_{eq} peaks at $1.41 P_2$ at the corner and decreases close to linearly to $1.37 P_2$ at $x = 80$ mm. It follows that $\beta = 1.259$ at the corner and drops to $\beta = 1.223$ at $x = 80$ mm.

A direct comparison of these β values with those calculated for the grooved configuration is not possible due to the different wave drag generated by the two geometries⁽¹⁾. However, it is encouraging to note that the β values for both are of the same order.

The flow configuration just examined corresponds to that produced by a vertical strut injector in a scramjet, followed by a straight thrust surface. The pressure distribution on the flat surface calculated here suggests that if the combustion wake from the injector is fully developed, then significant thrust may be extracted from the wake with minimal thrust surface length. This is a promising result for scramjet propulsion where the engine mass is a prime consideration.

4. ANALYSIS FOR A CONTINUOUS WAKE

For simplicity, the over-turning analysis described earlier for a glancing Prandtl-Meyer expansion-wake interaction used a uniform supersonic layer for the wake. Extending this analysis to include a real continuously varying Mach number wake, it is noted again that the analysis follows that used for a shock-boundary layer interaction⁽²⁾. In such an analysis, with interaction lengths which are not too short, the interaction with the mainstream of each stream tube in the boundary

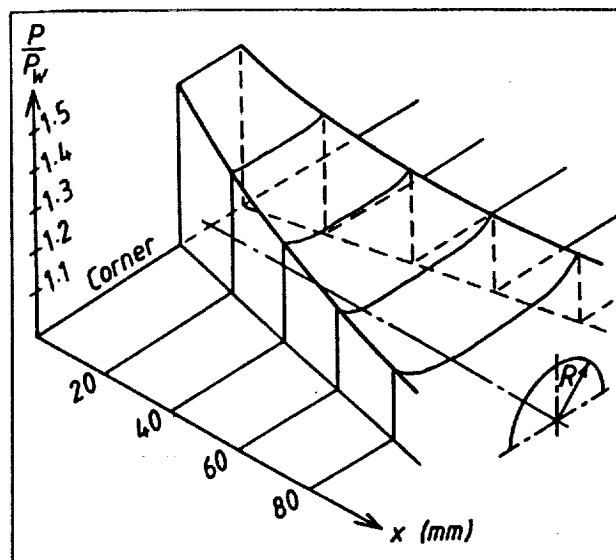


Figure 7. Pressure distribution generated on flat expansion surface by combustion wake.

layer is essentially independent of the presence of other streamtubes. The same approximation is used here.

In the case of the over-turning analysis for a supersonic boundary layer, it may appear that the picture is complicated by the presence of the slow viscous flow close to the wall. However, in developing the 'triple deck' model of a shock boundary layer interaction, Lighthill⁽⁵⁾ showed that this viscous sublayer does not take a direct part in the interaction, serving only to determine the effective distance from the wall at which the flow takes on an inviscid character. This distance tends to be small. For example, for the experiments reported in Section 5, the viscous sub-layer makes up approximately 2% of the boundary layer thickness. At this distance the Mach number is approximately one-third of the mainstream Mach number. This layer therefore makes only a small contribution to the over-turned mass flow, and so its effect may be ignored.

Given this, the preceding analysis may be easily extended to a continuous profile combustion wake or boundary layer. Applying it to the interaction of a weak fan with each streamtube in a wake, the entire wake will thin as before and a continuous distribution of Mach number and streamtube direction will occur downstream of the interaction. Invoking a superposition process once again, the passage of each stream tube through a strong interaction may be determined with similar attention to the variation of flow direction and Mach number as was required for the uniform wake.

Turning attention to the calculation of thrust due to over-turning of a combustion wake, it also may be easily extended to include a continuous wake profile. The simplest configuration to analyse, in which the surface downstream of the corner is adjusted to accommodate the over-turning, is shown in Fig. 8.

Note that for the continuous combustion wake the groove is now curved and deflection peaks at the wake centre line where the Mach number is a minimum. Thrust ratio β will now vary across the groove. The total β for the wake can be determined by integration.

To determine the thrust increment generated on a flat expansion surface downstream of the corner, the same procedure introduced for the uniform wake is used. Even though there is no distinct interface between the continuous wake and the mainstream, the flow is expected to be

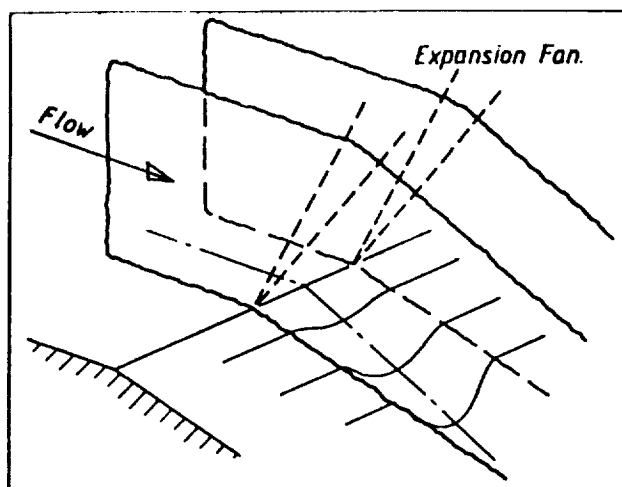


Figure 8. Continuous groove thrust surface.

dominated by a growing wake bulge along the surface, as for the uniform wake. Hence the mainstream and the wake will be separated again and the pressure distribution on the flat surface will be calculated from the flow past an axi-symmetric body in a supersonic stream. This distribution will then take the same form as shown in Fig. 7 for the uniform wake.

The calculation of the bulge profile will be slightly different. The mass flow rate into the bulge is assumed to be equal to that flowing into the groove shown in Fig. 8. This will need to be integrated across the wake, and will remain constant with distance downstream of the corner. Following then the same procedure as for the uniform wake, it can be shown that the bulge profile is

$$\frac{R}{R_0} = \sqrt{\frac{4\Sigma x}{\pi R_0} + 1} \quad \dots (16)$$

where $\Sigma = \int_0^1 \tan \alpha(\epsilon) d\epsilon$

and

$$\epsilon = 2\mu/\delta_2$$

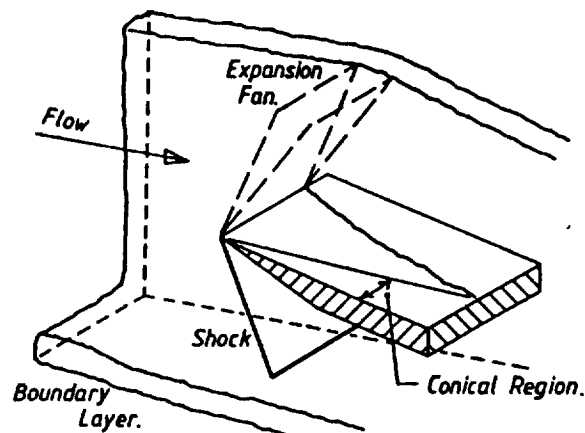
where μ is the distance across the wake

It is found that for the $M = 3.5$ combustion wake data used earlier that the extension to the more exact continuous layer analysis did not greatly change the magnitude of the generated pressure distribution, changing the value of Σ in equation (16) only by some 5%. This is because this wake was such that the Mach number everywhere was greater than 50% of the mainstream value. However, for profiles such as boundary layers, where the Mach number can vary greatly from that in the mainstream, it has been found that the effect of a continuous profile is much more significant. For example, an insulated wall turbulent boundary layer yields a value of Σ approximately 25% greater than the value of $\tan \alpha$ obtained from the mean boundary layer Mach number.

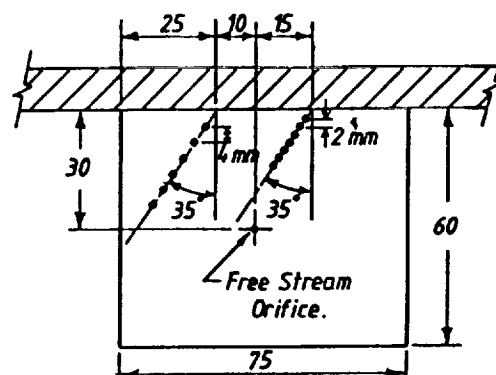
5. EXPERIMENTS—GLANCING EXPANSION FAN AND BOUNDARY LAYER INTERACTION

To corroborate the physical structure of the glancing Prandtl-Meyer expansion-wake interaction presented up to this

(a) Test Section Flow Characteristics.



(b) Transverse Pressure Orifice Distribution.



(c) Side Wall Pressure Orifice Distribution.

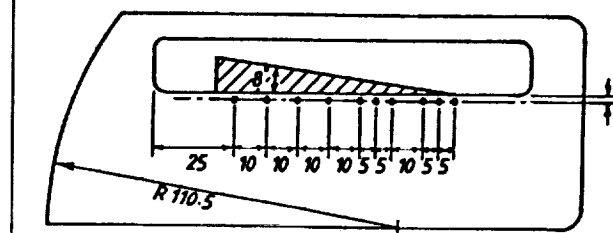


Figure 9. Experimental configuration.

point, a series of experiments were performed on the interaction of a fin induced expansion with a side wall boundary layer in a small supersonic blowdown tunnel. A tunnel at the University of Queensland, Brisbane, Australia, of asymmetric construction to a design by Stalker and Winarto⁽⁶⁾ was used. It enabled a range of uniform Mach number to be obtained in a $134 \times 102 \text{ mm}^2$ test section by use of a sliding lower nozzle block. The experimental configuration is sketched in Fig. 9(a), and consisted of an 8° rotatable wedge mounted normal to the side wall. Pressure orifices were mounted in the wedge and also in the side wall very close to the expansion side of the wedge as shown in Figs 9(b) and (c). The average wall boundary layer thickness for the experiments was $\delta_{av} = 12 \text{ mm}$, hence the wedge mounted pressure orifice arrays extend well into the mainstream. These two arrays begin at the wall at 2.5 and 5 boundary layer thicknesses downstream of the wedge leading edge and are swept back for ease of mounting.

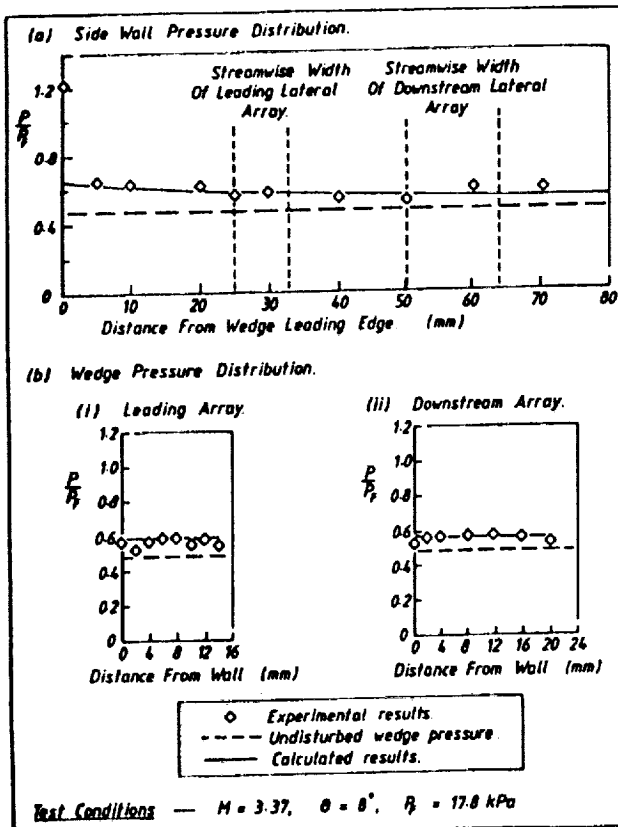


Figure 10. Experimental results

Experiments were performed for Mach numbers of 3.37 and 2.62. The flow characteristics of the test section limited the maximum expansion angle for smooth supersonic flow past the wedge, and useful experiments were able to be performed up to an expansion angle of 10° at $M = 3.37$ and 9° at $M = 2.62$. The complete series of experiments are documented in Chapter 6 of Ref. 7. All pressures are normalised with respect to the free stream test section pressure, P_F , measured on the test section side wall upstream of the wedge. The mainstream wedge pressure, P_w , was calculated from the free stream conditions and the measured wedge expansion angle.

Experiments were first performed with zero expansion angle for both Mach numbers. Wedge pressure levels were expected to be close to the free stream, and were found to be within 2%. Given this, any pressure increment above the undisturbed wedge pressure experienced in the remainder of the experiments must correspond to boundary layer overturning. All experiments with positive expansion angle displayed consistent behaviour and a typical result is shown in Fig. 10 for $M = 3.37$ and $\theta = 8^\circ$. The wall mounted array results showed good correlation with calculations along its length. Pressure peaked near the wedge leading edge as expected, and at a consistent level of $\Delta P/P_F = 0.18$ for the $M = 3.37$, $\theta = 6, 8$ and 10° experiment and $\Delta P/P_F = 0.10$ for the $M = 2.62$, $\theta = 6, 8$ and 9° experiments, (ΔP is the pressure increment above P_w). Consequently the peak incremental pressure rise factor, denoted $\Delta P/P_w$, increased with expansion angle. The pressure levels decreased along the wedge in the flow direction at a rate roughly consistent with calculations. The final two tappings in all $M = 3.37$ experiments experienced some upstream influence from the confused flow downstream of the wedge. This effect was not apparent in the $M = 2.62$ experiments.

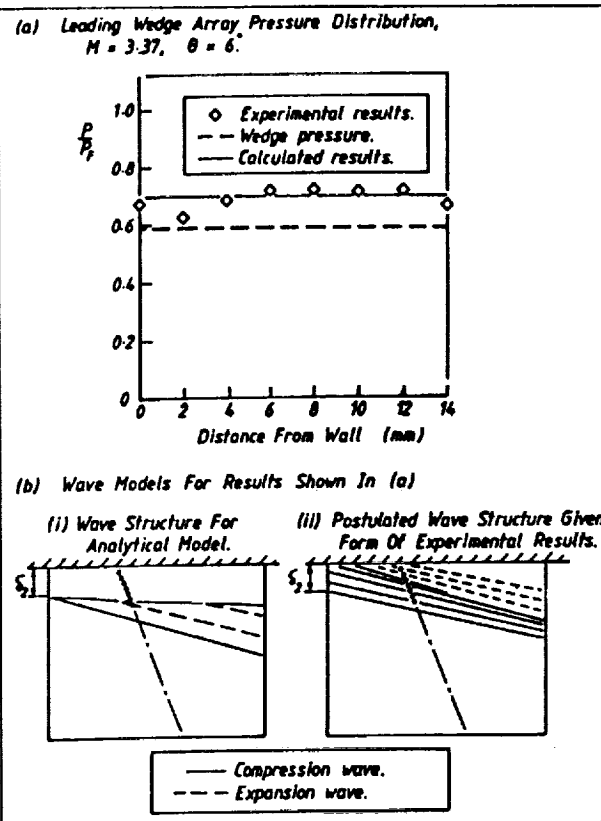


Figure 11. Wave structure near wedge.

The upstream lateral array showed average pressure levels consistent with calculations, however, the form of the distribution along the array was different. A graph of the distribution for $M = 3.37$ and $\theta = 6^\circ$ is shown in Fig. 11(a). The difference in form is thought to be due to an omitted effect of the continuous nature of the boundary layer. In calculations, the bulging layer was treated as a solid body and disturbances from it propagated into the mainstream from its surface (the bulge-mainstream interface). A wave pattern of the lateral flow produced by this configuration is shown in Fig. 11(b). In reality no distinct interface exists between the mainstream and the layer and the constraint of the layer overturning will initiate waves across its span.

Examining Fig. 11(a), the farthest tapping from the wall experiences some compression, due to waves beginning in the outer regions of the layer where the Mach number deficit relative to the mainstream is not large. The central tappings show a strong compression zone. This region is possibly influenced by waves from the initial constraint of the inner portion of the layer at the wedge leading edge. The tappings nearest the wall detect lower pressure. This may correspond to expansion waves from the region of the layer downstream of the wedge leading edge. A possible wave diagram which corresponds to the measured pressure levels is shown in Fig. 11(b).

The wall tapping adjacent to each lateral array is also shown in the lateral distribution graphs. In all cases, the wall tapping shows consistently higher pressure than the closest wedge tapping which is in both cases 2 mm from the wall. The reason for this phenomenon is not clear.

The downstream lateral array result showed a spreading of the elevated pressure as expected. With this spreading the form of the lateral pressure distribution smoothed, and both the form and level of pressures recorded were reasonably

close to those predicted from calculations.

These results indicate that the calculation procedure predicted with reasonable accuracy the pressure distribution along the wedge close to the tunnel side wall for a range of expansion angles. The average pressure level along the lateral array 2.5 boundary layer thicknesses downstream of the wedge leading edge was also able to be predicted. By five boundary layer thicknesses from the wedge leading edge, both the magnitude and form of the lateral distribution was able to be obtained with the procedure.

6. CONCLUSIONS

A physical model of the glancing interaction between an expansion fan and a supersonic wake was presented in this paper. The following conclusions can be made from this work.

- (i) The glancing interaction of an expansion fan with a supersonic wake turns the wake more than the mainstream. The wake also thins as it passes through the interaction.
- (ii) In the case of the wake being a combustion jet, the cross flow associated with over-turning produces accumulation of fluid on the surface downstream of the corner which initiated the expansion. This leads to a region of elevated pressure adjacent to the wake and therefore a thrust. Based on surface pressure distributions calculated using an analytical procedure formulated from the model this phenomenon is considered to be a major thrust producing mechanism in a vertical strut injected scramjet.
- (iii) Experiments involving the interaction of a side wall boundary layer with an expansion fan generated by a tilted wedge, showed good correlation between wedge pressure measurements and calculated results. The discrepancy in the form of a lateral pressure distribution

found to occur 2.5 boundary layer thicknesses from the wedge leading edge, can be explained using the physical model of the interaction presented. It is therefore attributed to simplifying assumptions used in the calculation procedure. Five boundary layer thicknesses from the wedge leading edge however the form of the calculated lateral pressure distribution does approach that of the measurements.

- (iv) Glancing expansion-Boundary layer interactions appear to be dominated by the Lighthill inviscid middle deck of the boundary layer as has been found previously for weak shock interactions.

7. REFERENCES

1. STALKER, R. J., MORGAN, R. G. and NETTLEFIELD, M. P. Wave processes in scramjet thrust generation, *Combustion Flame*, 1988, 71, pp 63-77.
2. STALKER, R. J. Sweepback effects in turbulent boundary layer-shock wave interactions, *J Aero/Space Sci*, May 1960, 27, pp 348-354.
3. MEE, D. J., STALKER, R. J. and STOLLERY, J. L. Glancing interactions between single and intersecting oblique shock waves and a turbulent boundary layer, *J Fluid Mech*, 1987, 170, pp 411-433.
4. VAN DYKE, M. D. First and second order theory of supersonic flow past bodies of revolution, *J Aeronaut Sci*, 1951, 18, pp 161-169.
5. LIGHTHILL, M. J. On boundary layers and upstream influence. II: Supersonic flows without separation, *Proc R Soc A*, 1953, 217, pp 487-501.
6. WINARTO, H. and STALKER, R. J. Design parameters and performance of two-dimensional, asymmetric, 'sliding block', variable Mach number, supersonic nozzles, *Aeronaut J*, 1984, 88, (876) pp 270-280.
7. SMART, M. K. Analysis of a Scramjet Nozzle Exhaust, Master of Engineering Science Thesis, Department of Mechanical Engineering, University of Queensland, Brisbane, Australia. 1988.

A STUDY OF CONTOURED HYPERSONIC SCRAMJETS

N. Akman, R.J. Stalker

The University of Queensland,
Department of Mechanical Engineering,
Queensland, 4072.

1.0 INTRODUCTION

In their earlier report, the authors have presented a study of wave drag in hypersonic scramjets with straight line geometry (Figure 1). The design Mach number is defined as the Mach number at which the shock wave from the leading edge of one plane meets the opposite plane at the shoulder. The part of the centered expansion fan generated at the shoulder cancels the reflected shock wave and results in a symmetrical wave distribution according to the linearized theory in which the width of the expansion fan and the altered flow properties in the regions of wave interactions are ignored.

The inefficiency of the linearized theory was highlighted in the calculation of the wave drag, oblique shock angles, and the flow properties in the complex regions of wave interactions.

However, the straight line geometry has failed to simulate the assumption of the linearized theory which states that the flow at the

outlet is parallel to the flow at the inlet. The authors have studied a surface contoured duct geometry with elongated divergent section. This model gives an outlet flow which is parallel to that at the inlet and eliminates any wave spillage from the system.

In this report, the authors present the performance of the surface contoured hypersonic scramjet at various Mach numbers and at the design Mach number of 6 with heat addition at the throat at the deflection angle of 6 degrees. The the study is extended to the effects of varying deflection angle on the surface contouring.

2.0 THE GEOMETRY OF THE SCRAMJET

The contoured geometry of the scramjet is given in Figure 2. In this geometry the thrust surface is contoured to align with the flow direction in the region of interaction between the reflected expansion fan and the surface. The reflected expansion fan is contained within the duct with the elongated geometry rather than part of it spilling out of the duct as was the case in the straight line geometry (Figure 3).

The surface contouring along the drag surface just before the shoulder is used to counteract the smearing of the reflected shock wave and slightly increased to encompass the reflected shock in this region. This eliminates the flow from further reflecting and gives similar conditions assumed in the linear theory. The drag coefficient obtained at the design Mach number by the code is better compared to that obtained with the linearized theory since the parallel flow assumption

is satisfied with the contoured geometry.

The height of the throat with the surface contouring together with slightly extended convergent region equals to the height at the throat with the straight line geometry. However, the outlet area is 3 percent greater than the inlet area. This is a direct result of the entropy increase across the shock waves. If the energy loss due to the entropy increase across the shock waves to be recovered, the outlet area needed is 3.1 percent greater than the inlet area if calorifically perfect gas is assumed.

3.0 RESULTS

The ratio of the biplane wave drag to that of monoplane is given in Figure 4. If the results of the contoured surface is compared to those with the straight line geometry, it is seen that the wave drag obtained with the contoured surface is lower than the wave drag obtained with the straight line geometry at all Mach numbers. This is due to the increased outlet area and the elongated divergent region. The effect of the elongated divergent region is more evident when the reflected shock waves meet the surface due to the increased length rather than missing it. With the straight line geometry, the biplane wave drag reaches to that of monoplane at Mach number 15. The reflected shock wave with the contoured geometry meets the surface up even at Mach number 20. This increases the thrust produced within the systems hence reducing the overall drag.

2.1 Heat Addition

As it was in the case of the scramjet with the straight line geometry, the heat is added at the throat without the addition of mass or change in the compressibility factor. The thrust obtained under these idealized conditions varies linearly with the amount of heat added until the conditions of choking is obtained.

As it was mentioned earlier an elongated divergent region is needed to eliminate part of the reflected expansion fan spilling from the system at the design Mach number. For this configuration the thrust region is 90 percent greater than that with the straight line geometry. The overall increase in the length of the Busemann scramjet is 45 percent. To study the shortening effect in the thrust region at the design Mach number with heat addition, the scramjet is recontoured to align the flow direction at the surface when the heat added at the throat equals to the combustion heat of one kilogram stoichiometric hydrogen. This reduces the length of the surface contoured scramjet. With this configuration the increase in the length of the expansion region due to the surface contouring is halved.

The ratio of the biplane drag coefficient to that of monoplane drag coefficient as a function of added heat is given in Figure 6. The thrust obtained with the surface contoured geometry is higher in all cases.

3.2 The Effect of the Deflection Angle

The surface contouring of the scramjet is repeated for deflection angles of 2, 4, 5 and 8 degrees. The flow angle leaving the scramjet is 0.02 degrees in each case. The increase in the length of the divergent region and in the overall length of the scramjet as a function of the deflection angle are given in Figure 7. The increase in the length of the scramjet indicates the increasing width of the expansion fan as the deflection angles get bigger.

4.0 CONCLUSIONS

When the surface of the scramjet is contoured in order to eliminate the internal waves further reflecting from the surface at the design Mach number, the flow at the outlet is parallel to the flow at the inlet. This allows the wave drag produced within the system to be better compared with the results obtained from the two-dimensional linear theory. At the design Mach number the system fails to give zero wave drag due to the finite dimensions of the expansion fans and the altered flow properties in the regions where the waves interact each other. Therefore, the numerical result is more realistic than their counterparts obtained by the linear theory.

At Mach numbers where the linear theory predicts that the biplane drag coefficient to be equal to the monoplane drag coefficient, the code gives smaller wave drag. This is again more accurate since the code takes into account of varying flow properties in the complex regions of wave interactions.

The Figure 4 shows the inefficiency of the straight line geometry in the absence of the added heat to the system. However, when the heat is added to the system, the benefits of the surface contouring diminish since the thrust surface where the pressures are high due to the heat are smaller.

5.0 REFERENCES

1. Liepmann H. W., Roshko A., Elements of Gas Dynamics, New York, Wiley, 1957.
2. Maurice H., Numerical Methods In Fluid Dynamics, 2nd rev. ed., Berlin New York, Springer-Verlag, 1984.

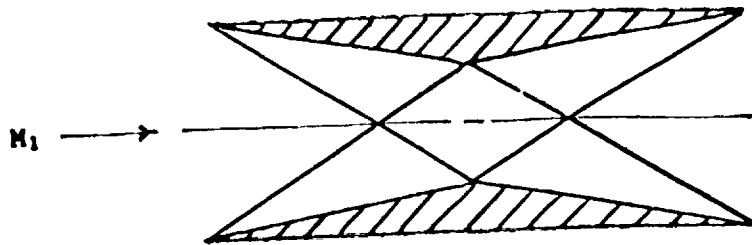


Figure 1. Scramjet with the straight line geometry (Busemann biplane).

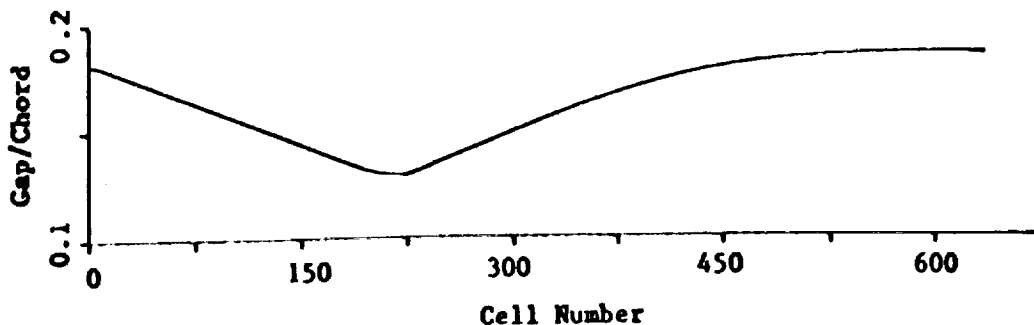
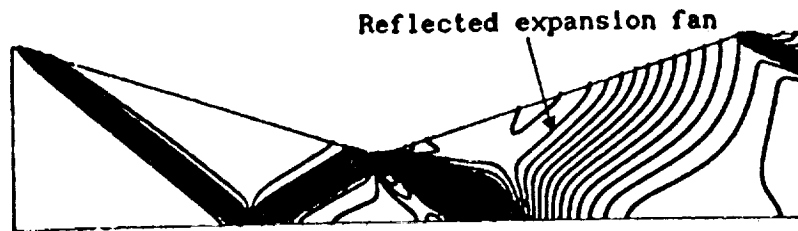
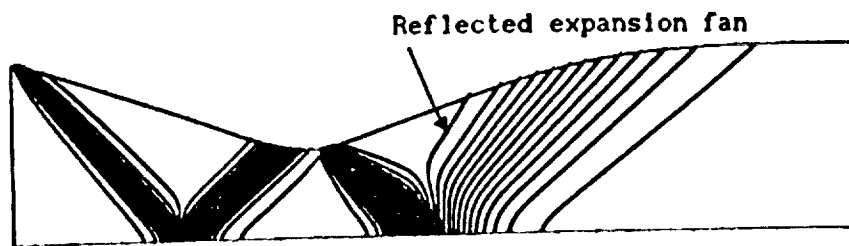


Figure 2. The geometry of the surface contoured scramjet.



a. Straight line geometry



b. Surface contoured geometry

Figure 3. The shock waves and the expansion fans within the scramjet.

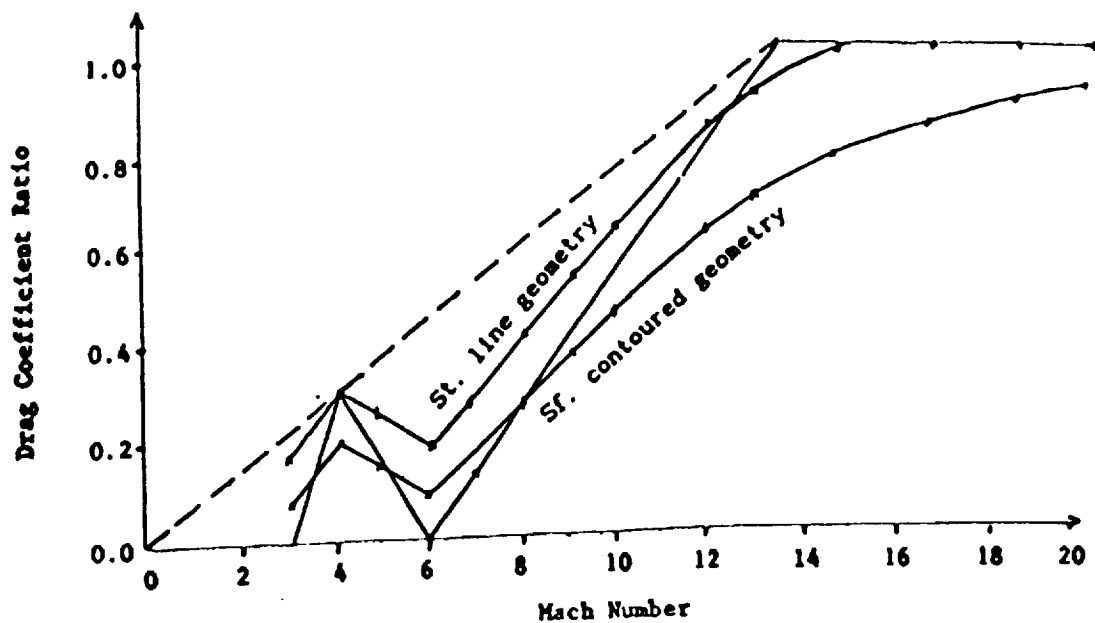


Figure 4. The ratio of the biplane drag to the monoplane drag (Design Mach number = 6, deflection angle = 6°)

SHOCK INDUCED HEAT RELEASE

AN OPTICAL STUDY

Report for the year March 1990 to March 1991

by Nicholas Ward

INTRODUCTION

In the past scramjet studies have involved injecting fuel into high pressure and temperature flow within the scramjet duct and investigating the effects of the heat release following its combustion. A difficulty of such studies has always been in differentiating between heat release effects and mixing effects emanating from the injector. This study was designed to avoid this confusion by eliminating an injector and investigating instead heat release brought about by recombination of dissociated nitrogen in the incoming flow. The heat release brought about by this recombination closely resembles that resulting from combustion of fuel. In this way even weak waves resulting from heat release could be detected and studied.

Recently interest has shifted from scramjet configurations involving fuel injection within the duct to configurations where fuel is mixed into the flow far upstream of the intake shocks. In this situation the flow reaching the scramjet is premixed and needs only to cross the intake shocks in order to induce combustion and subsequent heat release. This is the situation under study here. Dissociated nitrogen in the flow is 'premixed' and requires only to cross the intake shocks for recombination and subsequent heat release to take place. Thus this study can give insights into the behaviour of this new scramjet configuration.

This is an optical study. It involves the use of a double pass differential interferometer to examine the density gradients in a scramjet intake and duct during hypervelocity flow. This flow is generated by the T4 shocktunnel. In this way a detailed examination of the flow for each shot can be carried out throughout the duct and any waves generated by heat release can be detected. Coupled with this is a computational prediction of the expected theoretical recombination at all points throughout the scramjet duct. Comparison with recombination observed optically can then be carried out.

PRECEDING PAGE BLANK NOT FILMED

Previous to March 1990 most work had revolved around the development of the differential interferometer. A basic system had been assembled and aligned, but despite improvements the image quality was still quite poor and breakdowns were frequent. Also, a computer program had been developed to give basic flow paths after a shock taking into account dissociation and recombination and, in preparation for experiments in the T4 shocktunnel, a scramjet model had been designed and built.

REPORT

At the start of 1991 the image quality from the differential interferometer was poor and desperately in need of further refinement. One big problem was the background speckle pattern superimposed on the image due to the laser light source travelling through a multimode optic fibre before entering the optics system. It was decided to eliminate this by replacing the optic fibre with mirrors to convey the laser beam undistorted from the laser to the optics. This improved the situation dramatically, but also facilitated the discovery of a low quality plane mirror in the system which had to be replaced with one of superior flatness. This done the image quality was quite good, with adequate (if a bit uneven) illumination of the image, good parallel fringes and a sharp silhouette of the model in the test section.

To this time the system had been developed using the helium-neon laser which runs coaxially through the ruby laser cavity as the light source. It was now time to get the system working with the pulsed ruby laser itself. This involved checking that both lasers were indeed truly coaxially aligned, finding a safe and appropriate power for the ruby laser, developing a triggering system and incorporating into the optics a narrow band filter to cut out luminosity of the T4 flow and other interfering light sources. This was all carried out successfully.

Lasers can be very unreliable machines, and I was shortly to be reminded of this. Within a matter of weeks I was beset with a shattered reflector tube around the ruby and the breakdown of a selection of electronics components in the high voltage power supply and water cooling units. These were all repaired, the main cost being time, and subsequently the system was ready to be tested on real flow situations generated by the T4 shocktunnel.

The first set of experiments carried out on the T4 shocktunnel using this optics system was in August 1990. These showed quite reasonable detail around the leading shocks from the duct intake wedges. Interference fringes could be traced across the shocks and their curvature after these leading

shocks was quite noticeable. See Figure 1. Fringe detail back further in the duct was not so clear though, apparently due to the intake shocks reflecting along the duct. Efforts to change the position of the duct entrance and allow the intake shocks to escape proved unsuccessful.

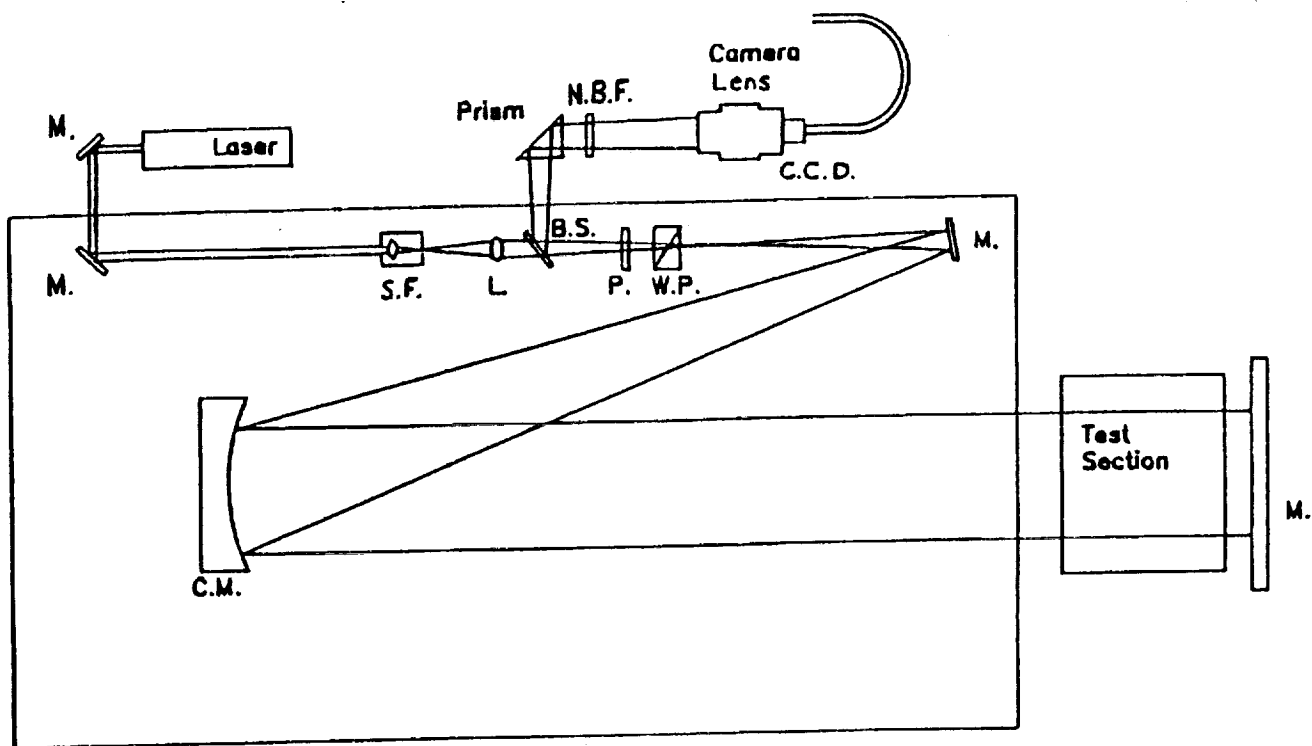
Analysis of these first results proved the value of the differential interferometer system. From the position and curvature of the fringes behind the intake shocks the axial component of the dissociation fraction gradient could be calculated and hence an indication of the recombination rate in this region. Also, an apparent relaxation zone around these intake shocks was observed.

In order to attempt to clear up the fringe pattern in the duct so that useful observations could be made in this region in future experiments it was decided to carry out some modifications to the model. The duct plates were replaced with a selection of interchangeable segments and bolt holes were elongated into slots in the support beams to allow for tailoring of the duct during experiments to allow the intake shocks to escape before entering the duct.

A second set of experiments were carried out in early November 1990. For these a pitot probe was placed above the model to check the synchronisation of the image to the test flow period and other parameters were recorded to allow estimation of dissociation fraction α and temperature, pressure and mach number of the test flow. The model was modified in situ between T4 shots as were the experimental flow conditions. Although some detail of the fringe pattern within the duct was observed, and this did suggest that some recombination was taking place in the duct, this was only when the duct was drastically narrowed and the resulting images were of low quality and could not be reliably reproduced. See Figure 2. It was concluded that image quality and reproducibility had to be improved still further.

The problems with image quality were tackled on three fronts. Beam separation in the test section caused by the wollaston prism was of the order of ten millimetres and subsequently there was a large 'shadow' area around the silhouette of the model in which fringe information was lost. To reduce this two new smaller angle wollaston prisms were ordered. The second area which could be improved was the sharpness of the imaging of the test section. To do this a two lens system was designed and ordered which would focus the test section perfectly onto the image plane. Finally and most importantly the numerous fine background fringe patterns and unevenness in the illumination apparent in the images had to be dealt with. It was suggested that this may be due to the very long coherence length of the laser light used amplifying

FIGURE 3. Final optics configuration



ABBREVIATIONS

L.	Lens
M.	Plane Mirror
C.M.	Concave Mirror
B.S.	Beam Splitter
P.	Polaroid
W.P.	Wollaston Prism
S.F.	Spatial Filter
N.B.F.	Narrow Band Filter
C.C.D	CCD Camera

any imperfections in the system, and it was decided to try a multiple core fibre bundle to destroy this coherence. Other areas which it was decided to look at were the use of a spatial filter to eliminate uneven illumination from the laser beam after it left the ruby cavity and before it entered the optics, and to investigate the effect on the image quality of such optics components as the beamsplitter and the narrowband filter.

While awaiting the arrival of components to enable the above investigations into image quality to be carried out work was begun on the development of a new computer program to take a set of T4 experimental conditions and predict the dissociation fraction α throughout the duct. This was later extended to present this α distribution graphically against position in the duct. This program now allows selection of optimum experimental conditions for the study of recombination effects in the scramjet duct. Also, some new intake wedges were designed and built to supplement those already used and allow maximum variability of shock positions and flow conditions in the scramjet duct.

ADDENDUM

The image quality and reliability has since been improved dramatically with the inclusion of a spatial filter to improve the beam quality leaving the ruby laser, the upgrading of the beamsplitter and the narrow band filter, and the remounting of the camera lens to allow for the accurate focussing of the test section. A new smaller angle wollaston prism is also in use. The differential interferometer is now working at its optimum. See Figure 3 for final optics configuration.

A DRAG MEASUREMENT TECHNIQUE FOR FREE PISTON SHOCK TUNNELS

S.R. Sanderson*, J.M. Simmons** and S.L. Tuttle***
The University of Queensland
St. Lucia, Queensland, Australia

Abstract

A new technique is described for measuring drag with 100 μ s rise time on a non-lifting model in a free piston shock tunnel. The technique involves interpretation of the stress waves propagating within the model and its support. A finite element representation and spectral methods are used to obtain a mean square optimal estimate of the time history of the aerodynamic loading. Thus, drag is measured instantaneously and the previous restriction caused by the mechanical time constant of balances is overcome. The effectiveness of the balance is demonstrated by measuring the drag on cones with 5° and 15° semi-vertex angles in nominally Mach 5.6 flow with stagnation enthalpies from 2.6 to 33 MJ/kg.

I. Introduction

Hypervelocity impulse facilities, such as free piston shock tunnels, have an important role in the development of technologies for hypersonic flight. They are capable of generating the high enthalpy flows associated with external aerodynamics of spaceplanes at near orbital velocities and the internal aerodynamics of scramjet propulsion systems. Important model test parameters are drag and thrust but their measurement is complicated greatly by the very short test times of impulse facilities.

Bernstein¹ has produced a comprehensive review of the force measurement techniques used in short duration facilities during the period 1955-70. With the decline of interest in hypersonic flight, few papers appeared after 1970. Bernstein outlines the two modelling assumptions that are inherent in force balances prior to the new techniques described here - the model behaves as a rigid body and the members of the force balance structure are simple, lumped parameter elements. Balances are then categorized as stiffness-dominated force balances or inertia-dominated accelerometer balances. As the time scale over which a force balance must operate is reduced, the stiffness of the balance members must be increased. Eventually a situation is reached where the distributed mass and stiffness of the balance members are no longer insignificant. Traction along the length of the balance structure elements are then no longer constant and accelerometers placed on the model do not accurately reflect its motion.

From the literature¹⁻⁸ we conclude that for practically sized models, stiffness-dominated

balances are only suitable for test times greater than about 200 ms. Inertia-dominated accelerometer balances can lower this acceptable test time to only about 10 ms. None of the papers reviewed describes a technique that is appropriate for testing in the 1 ms flows experienced in free piston shock tunnels.

Aerodynamic force measurement in free piston shock tunnels is currently based on surface pressure measurements made at discrete pressure tappings on the surface of the model. Integration of the discretized pressure distribution to obtain drag is feasible only if model geometry is simple and if drag due to skin friction is insignificant. This paper describes a novel approach to direct measurement of drag, including skin friction, by interpreting the transient stress waves propagating within the model and its sting support. To date, shock tunnel models are restricted to configurations that generate negligible lift. The mechanical configuration of the drag balance is derived from the Hopkinson pressure bar⁹ and modifications of it that have been used for dynamic testing of materials subjected to large transient stresses^{10,11}

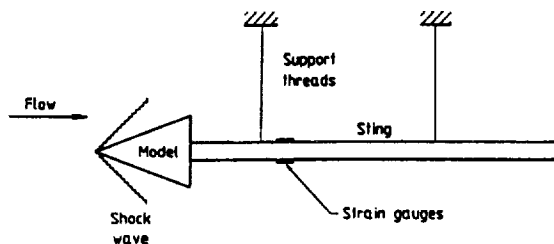


Fig. 1. Diagram of new drag balance.

II. Modelling the Drag Balance

The new drag balance is shown diagrammatically in Figure 1. The model for testing, in this case a cone at zero incidence and so subjected to drag only, is attached to a sting in the form of a slender cylindrical elastic bar. The sting is suspended by several vertical threads so that it is free to move in the axial (freestream) direction. The time-history of drag applied to the model can be inferred from the output of strain gauges that respond to the passage of stress waves along the sting. The strain gauges are placed near the model end of the sting in order to maximize the observation time before the onset of complications caused by the return of stress waves reflected from the free (downstream) end of the sting.

Finite Element Representation

An axisymmetric mathematical representation of the elastic model and the sting, based on a finite element method, is used to interpret experimental data. It is achieved for a cone on a hollow

* Presently, Graduate Student, California Institute of Technology

** Professor and Dean, Faculty of Engineering
Member AIAA

***Graduate Student, Mechanical Engineering

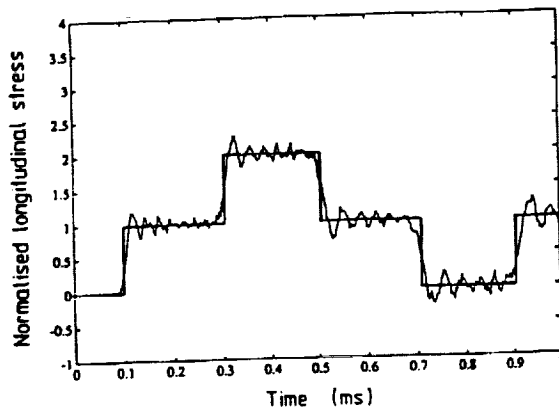


Fig. 2. Comparison of computed and analytical (straight lines) solutions for stress at mid-point of bar in uniform bar test case. Stress is normalized by static stress.

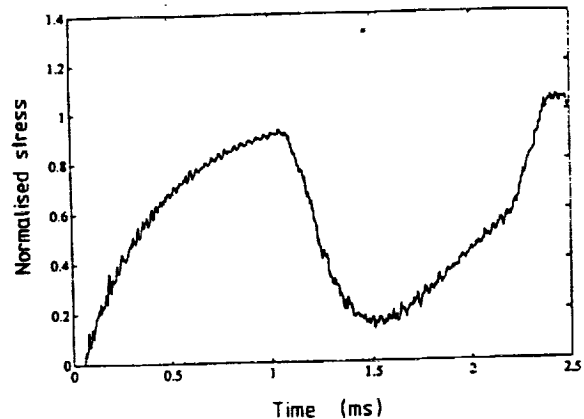


Fig. 4. Finite element solution (fine mesh) for stress at gauge location due to step uniform pressure applied to 15° cone. Stress is normalized by static stress.

cylindrical sting by spatial discretization with a finite element code based on that by Bathe¹². The computational effort involved in the direct integration of the resulting second order differential equations was minimized by using the Bulirsch-Stoer algorithm¹³.

Numerical Results

The finite element method was validated by computing the stress wave processes following the application of a step load to the free end of a free/fixed circular steel bar. The system was approximated by a mesh of axisymmetric bilinear quadrilateral elements. Axial stress at the midpoint of the bar, normalized with respect to the static stress, is shown in Figure 2, with the one-dimensional analytical solution superimposed. Oscillations in the numerical solution arise from the coarseness of the mesh and non-one-dimensional wave propagation modes. The computed solution is seen to be valid after a considerable number of wave reflections.



Fig. 3. Finite element mesh for 15° cone and sting.

The finite element method was next applied to the drag balance. The axisymmetric mesh is shown in Figure 3 for a cone with 15° semi-vertex angle (a cone with 5° semi-vertex angle was also modelled). Except for a small stainless steel tip, the cone is constructed from aluminium. A tubular brass sting extends to a length of 2 m (not shown). The aerodynamic loading in time is modelled as a step uniform pressure acting on the surface of the cone, with base pressure assumed to be negligible. The output of the balance is the axial stress in the sting, as would be measured by strain gauges bonded to the surface of the brass tube 200 mm behind the

base of the cone. Convergence of the numerical solution has been demonstrated¹⁴ by changing the fineness of spatial and temporal discretization. The solution is shown in Figure 4. Oscillations are inevitable in a mathematical model that is analogous to an undamped array of masses and springs.

Effect of Load Distribution

For the operation of a static drag balance in the absence of lift it is sufficient to make only one measurement to define the drag force. When the model cannot be treated as a rigid body, the output of the drag balance depends on both the magnitude of the drag and its distribution over the surface of the model. Conversely, from a single measurement it is not possible to define uniquely the loading that produced the measured response. In reality, the loading distribution can be adequately described by a small number of parameters, and hence by a small number of measurements. To avoid the need for a numerically accurate prediction of the stress waves propagating within the model, it is best to maximize the number of wave reflections within the model. These wave processes then need only be accurate in a general sense with any errors being averaged over a number of reflections. This results in a drag balance that has low sensitivity to loading distribution. Finite element computations¹⁴ of the step responses, for both a uniform pressure distribution and a point load at the vertex of the cone, show no discernible sensitivity to load distribution for the 15° cone. Slight sensitivity to loading distribution is shown for the 5° cone for which the wave reflections within the longer model are more apparent. However, the difference in loading distribution between a uniform pressure and a point load is extreme in terms of practical application.

III. Using the Computed Response to Obtain Drag

The dynamic behaviour of a time-invariant, causal, linear system with single input $u(t)$ and single output $y(t)$ is described by the integral

$$y(t) = \int_0^t g(t - \tau) u(\tau) d\tau \quad (1)$$

The preceding finite element analysis can be used to obtain the unit impulse response function $g(t)$ from the computed step response. In this section the inverse dynamic problem is solved. A method is described for interpreting the noisy measured output to obtain the unknown aerodynamic drag $u(t)$ acting on the shock tunnel model.

For the discrete time problem, $u(t)$, $y(t)$ and $g(t)$ are replaced by the discrete time series u_i , y_i and g_i ; $i = 0, 1, 2, \dots$. The sampling interval is Δt and $t = i \Delta t$. The convolution integral (1) becomes the summation,

$$y_i = \sum_{j=0}^i g_{i-j} \cdot u_j \quad (2)$$

Inverse dynamics problems are studied in many disciplines. Unfortunately, they are often poorly conditioned. Difficulties arise through the amplification of measurement noise by the inversion procedure¹⁵⁻¹⁸. The description of the problem is now expanded to include measurement noise $n(t)$ added to $y(t)$. In discrete time the noise is n_i , the output of the system is y_i and the measured output is $z_i = y_i + n_i$.

The inverse problem may be interpreted as a mean square estimation problem. We define the error function, J , as

$$J = \sum_{i=0}^{N-1} |u_i - \hat{u}_i|^2 \quad (3)$$

The real and estimated inputs to the system are u_0, \dots, u_{N-1} and $\hat{u}_0, \dots, \hat{u}_{N-1}$ respectively and N is the length of the data. Thus the inverse problem comprises determining the estimator, $\hat{u}_0, \dots, \hat{u}_{N-1}$, where,

$$\sum_{k=0}^i \phi_{i-k} z_k = \sum_{k=0}^i g_{i-k} \cdot \hat{u}_k; \quad i=0,1,\dots,N-1, \quad (4)$$

such that the expected value of the error function J , given by (5), is minimized,

$$\bar{J} = E \left\{ \sum_{i=0}^{N-1} |u_i - \hat{u}_i|^2 \right\}; \quad i=0,1,\dots,N-1 \quad (5)$$

Here $E \{ \cdot \}$ denotes the expectation given the data.

z. We omit the reference to the data and henceforth all expectations may be taken as conditional on z .

Since each term of the summation is greater than or equal to zero, an equivalent requirement for an optimal estimate is that

$$\bar{J}_i = E \left\{ |u_i - \hat{u}_i|^2 \right\} \quad (6)$$

be minimum for $i = 0, \dots, N-1$. Generally, mean square estimation problems such as this may be solved by application of the orthogonality principle¹⁹. For \bar{J}_i to be a minimum we require that

$$E \left\{ (u_i - \hat{u}_i) \bar{z}_i \right\} = 0; \quad i=0,1,\dots,N-1 \quad (7)$$

That is, the estimation error, $(u_i - \hat{u}_i)$, is orthogonal to the data, \bar{z}_i . Note that we must reconstruct the aerodynamic load before its effect is sensed by the strain gauges. This is apparent from consideration of the implicit form of (4) for u . Hence we must implement an acausal algorithm to solve the inversion problem and consequently we define the error function, J , for both future and past times. The non-causal nature of the inversion problem precludes the use of the more common Wiener-Hopf and Kalman¹⁹ prediction and filtering results. Whilst these techniques may be applied to the acausal smoothing problem, the implicit nature of the right hand side of (4) distinguishes the smoothing and inversion problems. Press et al¹³ note that an elegant solution to the inversion problem may be obtained using spectral methods and they derive the result in a deterministic manner. Continuing with the current stochastic formulation we note that Parseval's identity may be used to define the error function in the frequency domain,

$$\bar{J} = E \left\{ \sum_{j=0}^{N-1} |U_j - \hat{U}_j|^2 \right\} \quad (8)$$

Equivalently,

$$\bar{J}_j = E \left\{ |U_j - \hat{U}_j|^2 \right\}; \quad j=0,1,\dots,N-1 \quad (9)$$

and for an optimal estimate (7) implies,

$$E \left\{ (U_j - \hat{U}_j) \bar{Z}_j \right\} = 0; \quad j=0,1,\dots,N-1 \quad (10)$$

Using the convolution property of the Fourier transform we write (4) as,

$$\hat{U}_j = \frac{\phi_j \bar{Z}_j}{G_j}; \quad j=0,1,\dots,N-1 \quad (11)$$

Substituting for \hat{U}_j in (10) gives,

$$E \left\{ \left(U_j - \frac{\phi_j \bar{Z}_j}{G_j} \right) \bar{Z}_j \right\} = 0; \quad j=0,1,\dots,N-1 \quad (12)$$

Note the intractability of the above substitution in the time domain.

Since $Y_j = G_j U_j$,

$$E \left\{ \frac{Y_j \bar{Z}_j}{G_j} - \frac{\phi_j \bar{Z}_j \bar{Z}_j}{G_j} \right\} = 0; \quad j=0,1,\dots,N-1 \quad (13)$$

For $G_j \neq 0$, this implies that

$$E \left\{ (Z_j - N_j) \bar{Z}_j - \phi_j \bar{Z}_j \bar{Z}_j \right\} = 0,$$

where N_j represents the measurement noise. It follows that

$$E \left\{ Z_j \bar{Z}_j (1 - \phi_j) - N_j (\bar{Y}_j + \bar{N}_j) \right\} = 0.$$

Since n_j and y_j are uncorrelated,

$$(1 - \phi_j) E \{ Z_j \bar{Z}_j \} - E \{ N_j \bar{N}_j \} = 0, \text{ and}$$

$$\phi_j = \frac{S_{zz,j} - \nu}{S_{zz,j}} ; \quad j=0,1,\dots,N-1 \quad (14)$$

Thus, given the power spectral density of the data S_{zz} and the noise variance ν as a design parameter, (14) determines the optimum filter, ϕ . Combining the filter with the impulse response function in (11) we obtain the mean square optimal solution of the inverse problem,

$$\hat{U}_j = F^{-1} \left[\frac{\phi_j \bar{Z}_j}{G_j} \right] ; \quad j=0,1,\dots,N-1 \quad (15)$$

Here F^{-1} denotes the inverse discrete Fourier transform to be evaluated using standard FFT algorithms¹³.

A further consequence of the use of discrete Fourier transforms is the implicit assumption of N-periodicity of the signals. This conflicts with the causal nature of the physical system as defined by (1). By padding all time series to twice their length with trailing zeros, causality is enforced for the first half of the signal¹³. Subsequent application of the discrete Fourier transform provides the desired acausal filter properties.

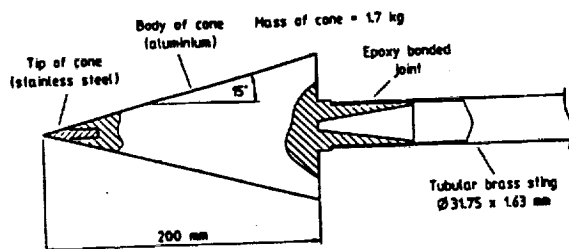


Fig. 5. Model-sting geometry for prototype balance.

IV. Implementation of a Drag Balance

This section contains a description of experiments conducted with the 15° cone to evaluate a prototype drag balance in the University of Queensland T4 free piston shock tunnel. Preliminary experiments with the 5° cone are also included.

Model and Sting

The model-sting geometry for the 15° cone is shown in Figure 5. The 15° semi-vertex angle results in a weak bow shock wave behind which the composition of the nitrogen test gas can be assumed to be frozen at the composition existing at the exit of the shock tunnel nozzle. The ratio of surface area to frontal area is low so that skin friction is only a minor component of the total drag. The mass of the aluminium cone is 1.7 kg. The main difference with the 5° cone is that its 425 mm

length and small vertex angle increase the surface-to-frontal area ratio, thereby giving rise to significant skin friction. Details of the model and sting design considerations are presented by Sanderson¹⁴ and Tuttle²⁰.

The sting was constructed from hollow brass tubing to make its bending stiffness high relative to its axial stiffness, thereby simplifying the supporting of it in the test section to minimize non-one-dimensional effects. For consistency with the finite element representation, a continuous contact surface between the model and the sting was achieved with an epoxy adhesive. The sting was suspended horizontally in the test section with two vertical wires. This provides vibration isolation in the horizontal plane. Bending effects from tunnel vibration excitation in the vertical direction are cancelled by using two diametrically opposed foil resistance strain gauges cemented to the sting 200 mm from the base of the cone. To shield the sting from the flow, the sting and the supporting wires were enclosed in a close fitting shroud. The freely suspended model could not reach significant velocity during the 1 ms duration of the test flow.

Data Acquisition

The outputs of the drag balance and the general shock tunnel instrumentation were recorded on an 11 bit digital event recorder, each channel of which recorded 2048 samples with a sampling time of 5 μs.

Obtaining the Impulse Response

The unit impulse response function is obtained from the finite element computation by differentiation of the step response of the balance. The computed step response in Figure 4 exhibits non-physically significant oscillations associated with the spatial discretization of the governing equations. To avoid differentiating these oscillations a ninth-order polynomial is first fitted to the computed step response. The discretized impulse response is scaled to represent the response of the balance to a load of 1 N applied for 5 μs (one sampling interval).

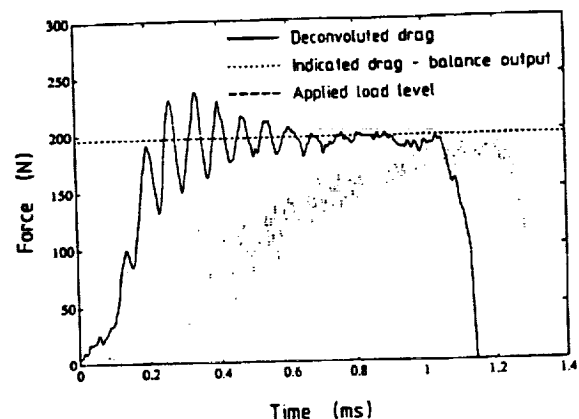


Fig. 6. Vertical dynamic calibration with 15° cone.

V. Experimental Results

Dynamic Calibration of Balance

The drag balance was calibrated dynamically to validate the deconvolution procedure. A known weight was suspended from the vertex of the cone by a highly stressed steel wire which, when cut, provided a rapid step unloading of the model. This process was performed with the model and sting suspended both vertically from the free end of the sting and horizontally in the test section of the shock tunnel. The vertical test is considered to be the more accurate, but the horizontal test was needed to show that the sting suspension system in the test section has an insignificant effect on the performance of the balance¹⁴. The raw balance output from a vertical test on the 15° cone with a statically calibrated strain gauge bridge, the drag history deconvoluted from it and the level of applied loading are compared in Figure 6. The computed drag measurement is a valid estimate of the applied load until the arrival of the stress wave reflected from the rear end of the sting.

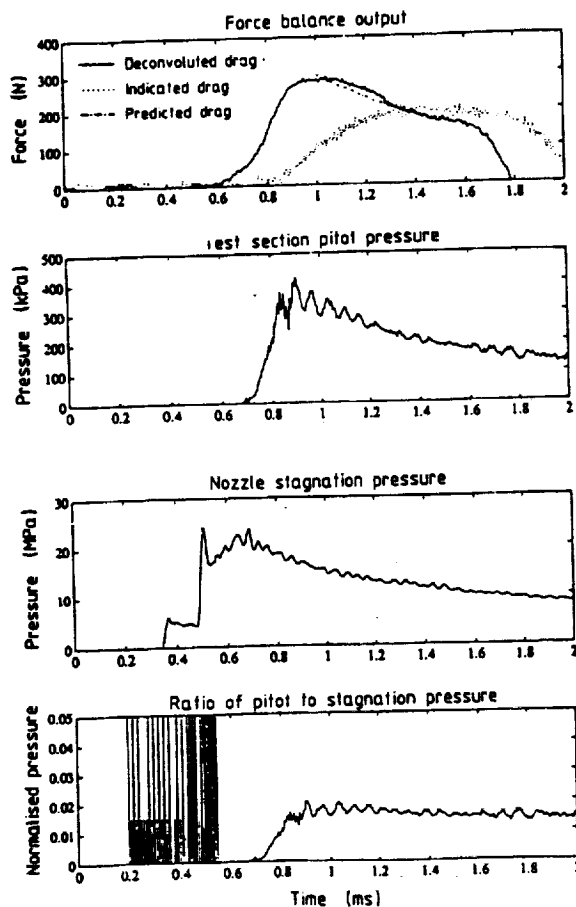


Fig. 7. Experimental results with 15° cone for nozzle stagnation enthalpy of 3.96 MJ/kg and the following test section conditions: Mach number = 6.9, velocity = 2640 m/s, static pressure = 6.64 kPa, pitot pressure = 320 kPa, static temperature = 450 K, density = 0.0492 kg/m³, γ = 1.40.

Drag Measurements in Shock Tunnel

Nitrogen was used as the test gas in the T4 shock tunnel to minimize chemical reactions, thereby simplifying comparison of drag measurements with theory. Eight test section stagnation enthalpies were used, from 2.6 to 33 MJ/kg. The test section conditions were computed from measurements of primary shock speed, test section pitot pressure, shock tube filling pressure and nozzle stagnation pressure after primary shock reflection.

Figures 7 and 8 show two representative results for the 15° cone. Each comprises plots of force balance output, test section pitot and nozzle stagnation pressure histories and the ratio of test section pitot pressure to stagnation pressure, allowing for the flow transport time through the nozzle. Also plotted is the prediction of cone drag from the inviscid Taylor-Maccoll²¹ theory for a perfect gas (frozen chemistry) attached conical shock and no base pressure.

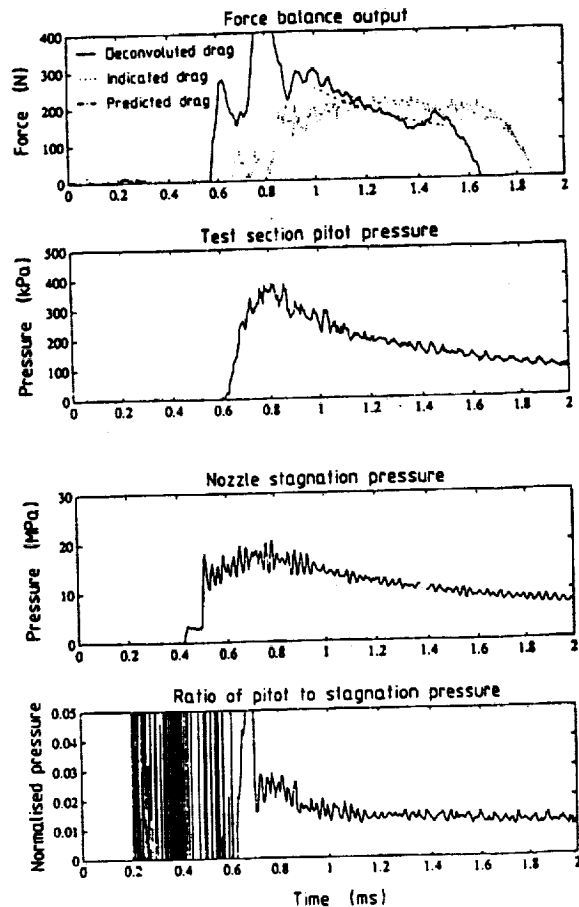


Fig. 8. Experimental results with 15° cone for nozzle stagnation enthalpy of 17.2 MJ/kg and the following test section conditions: Mach number = 5.4, velocity = 5000 m/s, static pressure = 6.86 kPa, pitot pressure = 256 kPa, static temperature = 2090 K, density = 0.0105 kg/m³, γ = 1.32.

The test section conditions in the captions of Figures 7 and 8 correspond to conditions that existed at the start of 'steady' flow in the test section, as determined from the constant ratio of pitot pressure to stagnation pressure. The start of the line for predicted drag marks the beginning of 'steady' flow and shows the predicted drag for the computed test section conditions. The predicted drag at other times is obtained by scaling the test section conditions according to the measured instantaneous pitot pressure. The oscillations at the beginning of the normalized pressure trace are due to division by zero and have no physical significance.

Figure 7 indicates that the deconvoluted drag follows the test section pitot pressure after about 100 μ s from the peak of the pitot pressure. Because of its 400 μ s mechanical time constant, the uncompensated balance is not able to follow the fast initial development of the flow over the model but it is sufficiently fast to follow the flow during the period of 'steady' flow. Later the uncompensated balance overshoots due to the delay in transmission of the unloading wave as the tunnel stagnation pressure falls. The deconvoluted drag measurement follows the pitot pressure until the arrival of the stress wave reflected from the free end of the sting.

Accuracy

The repeatability of the technique was assessed for the 15° cone by comparing deconvoluted drag histories for multiple shock tunnel tests at the same nominal conditions. This does not account for any systematic error due to inaccuracy of the finite element model. However, the accuracy of this model was confirmed by the dynamic calibration (Fig. 6). Figure 9 compares the deconvoluted drag histories from five tests at the conditions in the caption for

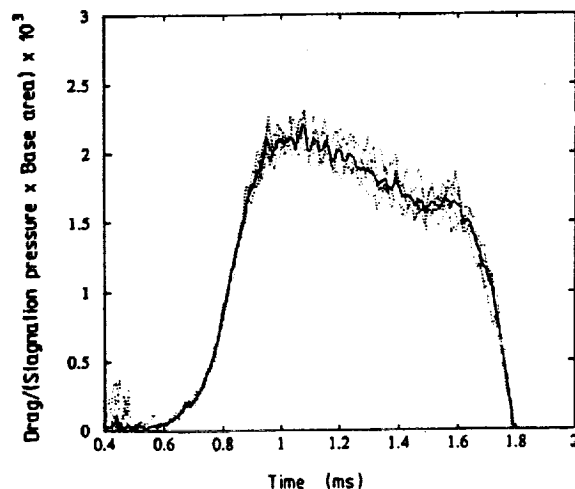


Fig. 9. Comparison of deconvoluted drag histories with 15° cone from repeated tests at conditions nominally identical to those defined in the caption to Fig. 7. Superimposed dotted lines are for five tests. Solid line is the average of five tests.

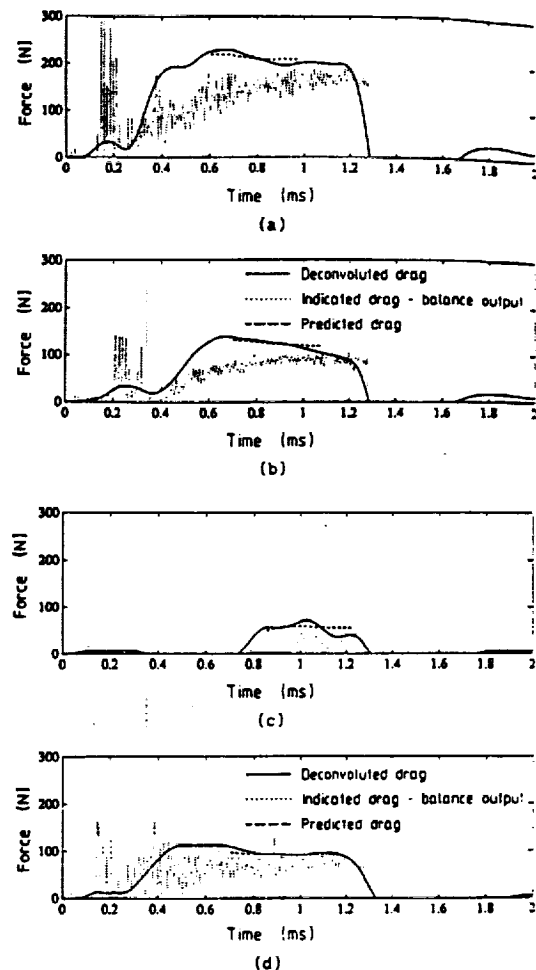


Fig. 10. Experimental results for 5° cone :

- (a) Nozzle stagnation enthalpy of 19.3 MJ/kg
Test section conditions :
Mach number = 5.03 , velocity = 5340 m/s.
static pressure = 38.0 kPa, pitot pressure = 1170 Pa , static temperature = 2880 K.
density = 0.0433 kg/m³, γ = 1.33.
- (b) Nozzle stagnation enthalpy of 7.78 MJ/kg
Test section conditions :
Mach number = 5.90, velocity = 3670 m/s.
static pressure = 21.2 kPa, pitot pressure = 1060 kPa, static temperature = 967 K.
density = 0.0738 kg/m³, γ = 1.33.
- (c) Nozzle stagnation enthalpy of 4.7 MJ/kg.
Test section conditions :
Mach number = 6.16, velocity = 2880 m/s.
static pressure = 7.32 kPa, pitot pressure = 443 kPa, static temperature = 530 K.
density = 0.0465 kg/m³, γ = 1.33.
- (d) Nozzle stagnation enthalpy of 25.7 MJ/kg
Test section conditions :
Mach number = 4.8, velocity = 5700 m/s.
static pressure = 17.4 kPa, pitot pressure = 614 kPa, static temperature = 3330 K.
density = 0.0159 kg/m³, γ = 1.33.

Figure 7. To eliminate the effect of slight variations in test conditions for each test, the drag data has been normalized by the instantaneous stagnation pressure and the cone base area. On the basis of these results, the technique applied to the 15° cone is conservatively estimated to give results repeatable to ± 10 percent under the operating conditions used.

To assess accuracy further the method was extended to the more complicated measurement problem posed by the 5° cone. Because of the smaller base area, signals had at most one-half the level of those for the 15° cone. This resulted in a poor signal-to-noise ratio, necessitating a refinement of the filtering process incorporated in the inversion process. A digital, second-order low-pass Butterworth filter with a corner frequency of 1.5 kHz was used to filter the deconvoluted time history of drag. Sample results from a series of tests²⁰ are shown in Figure 10. The theoretical prediction was modified to include a skin friction component. In this challenging situation the drag balance continued to exhibit acceptable accuracy.

VI. Conclusions

A prototype drag balance has been developed and its use demonstrated in a free piston shock tunnel. The time history of the drag applied to the model is inferred from the output of strain gauges that respond to the passage of stress waves along the sting. Tests with a 15° cone indicate that drag measurements agree with predictions for a model on which drag due to skin friction is small. The uncertainties of about 10 percent are acceptable, considering the penalty imposed by the short test time and the harsh operating environment. The method is also seen to work acceptably well when skin friction on a 5° cone is no longer negligible and the signals are much smaller. Results to date indicate that any accuracy limits encountered are due to the electronics employed, rather than to any deficiency in the principle of the balance.

A finite element representation is needed to obtain an accurate impulse response function for the deconvolution procedure. For situations in which the drag is not dependent significantly on the loading distribution, impulse response functions might be obtained from the dynamic calibration procedure described above, but care would be needed to ensure sufficiently fast removal of the load.

The use of non-metallic materials such as nylon is worth investigation because much shorter response times can then be obtained¹⁴. However, the effects of material damping would need careful consideration. In principle, the basic technique of the balance is extendible to measurement of drag in the presence of lift, and to simultaneous measurement of lift, drag and moments.

Acknowledgements

This study was supported by Australian Research Council Grant A4 851508P. The work on the 5° cone was supported by NASA under grant NAGW-674. The authors are grateful for suggestions from Prof. R.J. Stalker of the Department of Mechanical Engineering, The University of Queensland.

References

- ¹Bernstein, L., "Force Measurement in Short-Duration Hypersonic Facilities," AGARDograph No. 214, Dept. of Aeronautical Engineering, Queen Mary College, University of London, 1975.
- ²Ledford, R.L., Smotherman, W.E. and Kidd, C.T., "Recent Developments in Heat-Transfer-Rate, Pressure and Force Measurements for Hot-Shot Tunnels," *IEEE Trans. on Aerospace and Electronic Systems*, Vol. AES-4, 1968, pp. 202-209.
- ³Beaussier, J., "A Six-Component Balance," *IEEE Trans. on Aerospace and Electronic Systems*, Vol. AES-4, 1968, pp. 210-217.
- ⁴Duryea, G.R. and Martin, J.F., "An Improved Piezo-electric Balance for Aerodynamic Measurements," *IEEE Trans. on Aerospace and Electronic Systems*, Vol. AES-4, 1968, pp. 351-359.
- ⁵Kussoy, M.I. and Horstmann, C.C., "Cone Drag in Rarefied Hypersonic Flow," *AIAA Journal*, Vol. 8, No. 2, Feb. 1970, pp. 315-320.
- ⁶Duryea, G.R. and Sheeran, W.J., "Accelerometer Force Balance Techniques," *3rd International Congress on Instrumentation in Aerospace Simulation Facilities*, Brooklyn, N.Y., 1969.
- ⁷Reddy, N.M., "Aerodynamic Force Measurements in the IISc Hypersonic Shock Tunnel," *Proc. 15th International Symposium on Shock Tubes and Waves*, Sydney, Australia, 1985, pp. 358-362.
- ⁸Bernstein, L. and Stott, G.T., "A Laser-Interferometric Trajectory-Following System for Determining Forces on Freely Flying Models in a Shock-Tunnel," *Proc. 13th International Symposium on Shock Tubes and Waves*, Niagara Falls, N.Y., 1981.
- ⁹Hopkinson, B., "A Method of Measuring the Pressure Produced in the Detonation of High Explosives and by the Impact of Bullets," *Phil. Trans. Roy. Soc. (London)*, Ser. A, Vol. 213, 1914, p. 437.
- ¹⁰Kolsky, H., "An Investigation of the Mechanical Properties of Materials at very High rates of Loading," *Proc. Roy. Soc. (London)*, Sect. B, Vol. 62, 1949, pp. 676-700.
- ¹¹Lindholm, U.S., "High Strain Rate Tests, in R.F. Bunshah (ed.), *Techniques of Materials Research*, Vol. V, Part 1, Interscience, New York, 1971.
- ¹²Bathe, K.T., *Finite Element Procedures in Engineering Analysis*, Prentice-Hall, Englewood Cliffs, N.J., 1982.
- ¹³Press, W.H., Flannery, B.P., Teukolsky, S.A. and Vetterling, W.T., *Numerical Recipes: The Art of Scientific Computing*, Cambridge University Press, London, 1986.
- ¹⁴Sanderson, S.R., "Drag Measurement Techniques for Short Flow Duration Hypervelocity Shock Tunnels," M.Eng.Sc. Thesis, Dept. of Mechanical Engineering, The University of Queensland, Queensland, Australia, 1989.
- ¹⁵Goodier, J.N., Jahsman, W.E. and Ripperger, E.A., "An Experimental Surface-Wave Method for

Recording Force-Time Curves in Elastic Impacts," *Journal of Applied Mechanics*, Vol. 26, March 1959, pp. 3-7.

¹⁶Stump, B.W. and Johnson, L.R., "The Determination of Source Properties by the Linear Inversion of Seismograms," *Bulletin of the Seismological Society of America*, Vol. 47, 1977, pp. 1489-1502.

¹⁷Michaels, J.E. and Pao, Y.H., "The Inverse Source Problem for an Oblique Force on an Elastic Plate," *Journal of the Acoustical Society of America*, Vol 77, 1985, pp. 2005-2011.

¹⁸Robinson, E.A., *Multichannel Time Series Analysis with Digital Computer Programs*, Holden-Day, San Francisco, Ca., 1967.

¹⁹Papoulis, A., *Probability, Random Variables and Stochastic Processes*, McGraw-Hill, New York, N.Y., 1984.

²⁰Tuttle, S.L., "A Drag Measurement Technique for Hypervelocity Impulse Facilities," M.Eng.Sc. Thesis, Dept. of Mechanical Engineering, The University of Queensland, Queensland, Australia, 1990.

²¹Taylor, G.I. and Maccoll, J.W., "The Air Pressure on a Cone Moving at High Speed," *Proceedings of The Royal Society (London)*, Ser. A, Vol. 139, 1932, pp. 278-297.

DRAG AND THRUST MEASUREMENT TECHNIQUES

FOR FREE PISTON SHOCK TUNNELS

BY : S.L. TUTTLE

SUPERVISOR : J.M. SIMMONS

DRAG MEASUREMENT ON A FIVE DEGREE CONE

Drag, including skin friction, has been measured on a 5° cone, 425 mm in length. The drag measurement technique described in "A Drag Measurement Technique for Free Piston Shock Tunnels" has been further refined. It was mentioned that the more complicated measurement problem posed by the 5° cone necessitated the inclusion of Butterworth low pass filtering of the deconvoluted drag signal. This was performed with the Wiener filter in its original place (smoothing the measured drag before deconvolution) as proposed originally. Thus, in order to obtain the results shown in the aforementioned paper, a double filtering technique was required.

Subsequently, it was found that the Wiener filter could be omitted and the original, extremely noisy, raw measured drag could be deconvoluted. Only after the deconvolution process was the Butterworth low pass filter used to smooth out the data. In other words, all filtering can be left until after all manipulation to the measured data has been done, so that a completely original, unaltered, measured signal is deconvoluted, and the whole process is once more a single filter procedure. Filtering is performed in the time domain. Negligible time delay is introduced by the filter chosen (second order Butterworth low pass filter with a cut-off frequency of 1.5 kHz). The rate of change of the signal during the test time is slow enough that the cut-off frequency does not reduce the response of the system in this region. Only the initial rise of the drag signal is slightly rounded by the filter.

The attached plots show the degree of accuracy attainable on the 5° cone with ordinary foil resistance strain gauges. (Note : a drag of 50 N corresponds to a strain of $3 \mu\epsilon$, persisting for several hundred microseconds with a signal-to-noise ratio of approximately unity).

All attempts to improve signal-to-noise ratio electrically resulted in an order of magnitude increase in this ratio. This was achieved during dynamic calibration of the balance outside the shock tunnel. It was found, subsequently, that the signal-to-noise ratio of the strain

measurements was strongly flow dependent, and that poor signals would have to be tolerated under many tunnel operating conditions.

THRUST MEASUREMENT ON A SCRAMJET NOZZLE

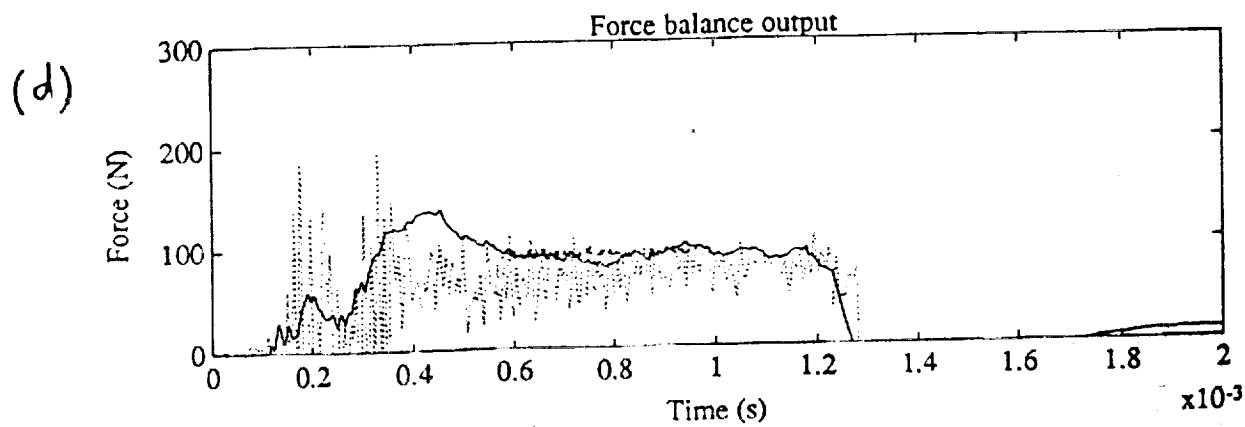
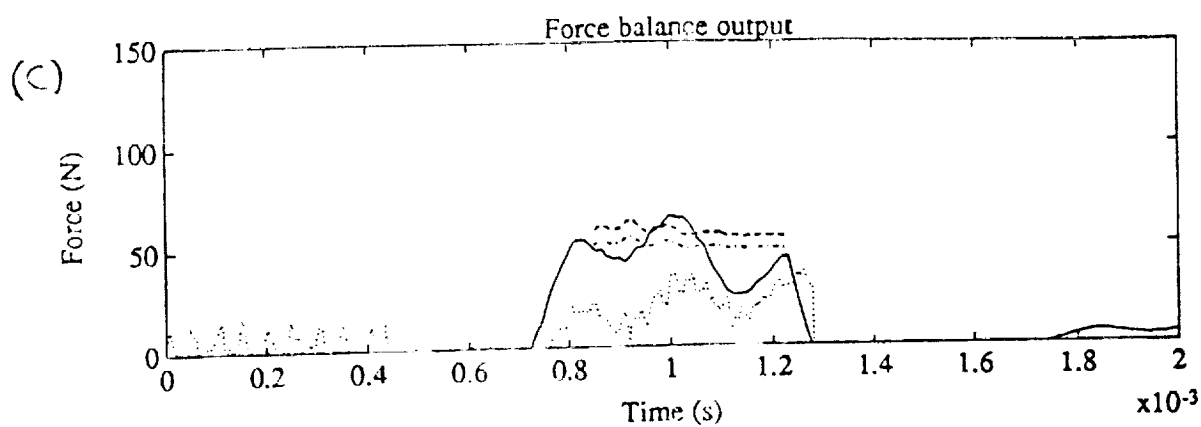
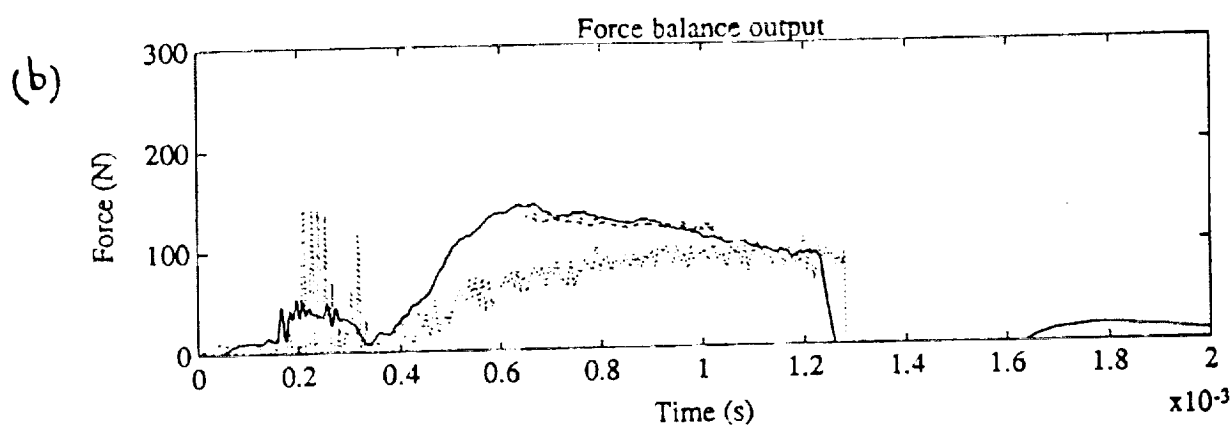
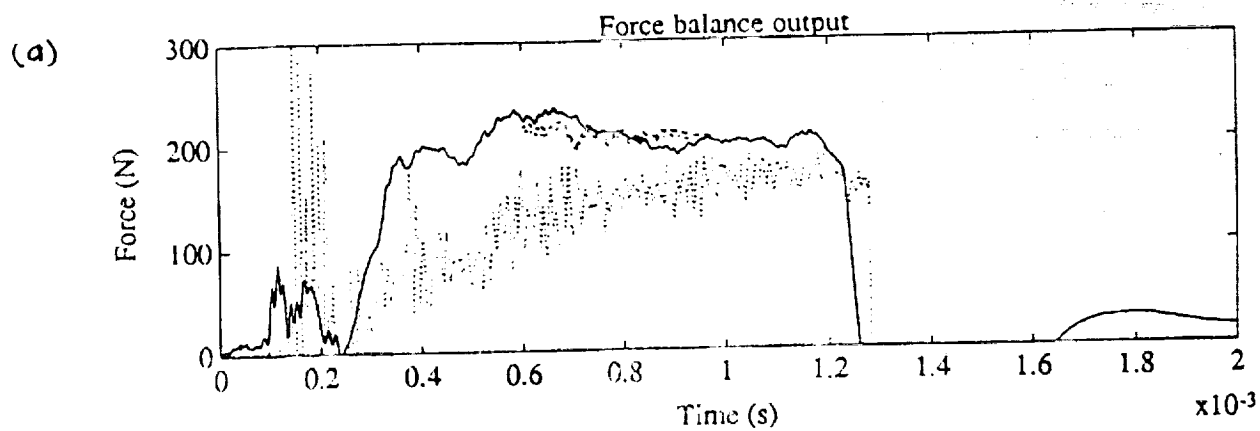
The force balance technique is now being applied to the measurement of the net thrust produced by a two dimensional symmetric nozzle attached to a rectangular cross-sectioned scramjet. Although symmetry of the system means the net force is co-axial with the nozzle-duct axis, the inclined nozzle walls mean that at least two internal stress components are present. This complicates design and measurement of the net thrust (which will give rise to some axial, compressive stress wave). The measurement of this in the presence of possible large transverse flexural stress waves is currently being studied.

REFERENCES

1. S.R.Sanderson, J.M.Simmons, S.L.Tuttle, *A Drag Measurement Technique for Free Piston Shock Tunnels*, AIAA Conference Paper, Reno, Nevada, 1991

Experimental results for 5° cone

- (a) Nozzle stagnation enthalpy of 19.3 MJ/kg
Test section conditions :
Mach number = 5.03 , velocity = 5340 m/s.
static pressure = 38.0 kPa, pitot pressure
= 1170 Pa , static temperature = 2980 K.
density = 0.0433 kg/m³ , γ = 1.33.
- (b) Nozzle stagnation enthalpy of 7.78 MJ/kg
Test section conditions :
Mach number = 5.90, velocity = 3670 m/s.
static pressure = 21.2 kPa, pitot pressure
= 1060 kPa, static temperature = 967 K.
density = 0.0738 kg/m³ , γ = 1.33.
- (c) Nozzle stagnation enthalpy of 4.7 MJ/kg.
Test section conditions :
Mach number = 6.16, velocity = 2980 m/s.
static pressure = 7.32 kPa, pitot pressure
= 443 kPa, static temperature = 530 K.
density = 0.0465 kg/m³ , γ = 1.33.
- (d) Nozzle stagnation enthalpy of 25.7 MJ/kg
Test section conditions :
Mach number = 4.8, velocity = 5700 m/s.
static pressure = 17.4 kPa, pitot pressure
= 614 kPa, static temperature = 3330 K.
density = 0.0159 kg/m³ , γ = 1.33.



A SKIN FRICTION GAUGE FOR USE IN HYPERVELOCITY IMPULSE FACILITIES

G.M. Kelly*, J.M. Simmons** and A. Paull***
The University of Queensland
Queensland, Australia

Introduction

Hypervelocity impulse facilities, such as free piston shock tunnels and expansion tubes, have an important role in the development of technologies for hypersonic flight. They are capable of generating the high enthalpy flows associated with external aerodynamics of space planes at near orbital velocities and the internal aerodynamics of scramjet propulsion systems. Important model test parameters are drag and skin friction but their measurement is complicated greatly by the very short test times of impulse facilities. Skin friction measurement is also made difficult because the wall pressure can be an order of magnitude greater than the wall stress generated by skin friction. Skin friction gauges for use in conventional shock tunnels have been reported¹. However, their ability to perform satisfactorily in the very short duration flows associated with free piston shock tunnels and expansion tubes does not appear to have been demonstrated.

This paper reports the development of a transducer capable of measuring skin friction with a rise time of about 20 μ s. Results prove the effectiveness of the concept when used to measure skin friction on a flat plate.

Gauge Design

The gauge design is shown schematically in Figure 1. It comprises a thin metal disk or thermal cover (10 mm diameter and 0.4 mm thick) mounted flush with the surface of the model and bonded to a stack of two piezoelectric transducer elements (each 7 mm by 7 mm and 1.5 mm thick). The material

*Ph.D Student, Department of Mechanical Engineering

**Dean, Faculty of Engineering. Member AIAA

***Research Fellow, Department of Mechanical Engineering

chosen for the elements was the piezoceramic PZT-7A. Its rigidity and density were such that for the configuration in Figure 1, gauge natural frequencies were above 300 kHz. In theory the elements, appropriately orientated and with electrodes on the appropriate surfaces, respond only to the shear force generated by skin friction, but in practice, pressure sensitivity (normal to the disk) was found to be significant. For this reason the two-element gauge was designed, with one piezoceramic element inverted with respect to the other. One element provides an output e_1 proportional to the sum of the effects of skin friction τ and pressure p applied to the disk and the other provides an output e_2 proportional to the difference ((1) and (2) below). A weighted summation of the two outputs therefore provides a direct measurement of shear stress.

$$e_1 = a_1 \tau + b_1 p \quad (1)$$

$$e_2 = a_2 \tau - b_2 p \quad (2)$$

A calibration procedure would involve applying a known transient shear stress, with $p = 0$, to the transducer to determine constants a_1 and a_2 , and a transient pressure, with $\tau = 0$, to the transducer to determine the ratio of constants b_1/b_2 . Hence, an unknown shear stress τ can be determined from (3) and simultaneous measurements of outputs e_1 and e_2 .

$$e_1 + (b_1/b_2)e_2 = (a_1 + (b_1/b_2)a_2) \tau \quad (3)$$

Piezoceramics exhibit a 'Curie' temperature above which they begin to depolarize. To avoid this the thickness of the thermal cover and its material were chosen to prevent unacceptable levels of conductive heat transfer from the hot test gas in the boundary layer. Several materials were evaluated. Invar was finally chosen because it has a very small coefficient

of thermal expansion, thereby preventing the transducer elements from being strained due to thermal expansion of the disk.

The impulsive nature of the flow in free piston shock tunnels results in stress waves in the model, with the skin friction gauge being exposed to a vibration-induced acceleration environment. To counteract this, rubber vibration isolation was included in the design (Figure 1). The technique effectively lowered acceleration induced output from the gauge to a level that could be handled by filtering during signal processing.

The shear stress levels on the model were typically 1250 Pa but for some of the flow conditions they were as low as 200 Pa. Since the charge produced by the piezoceramic elements is small (of the order of 5 pC for some conditions) amplification of the signal was required. To minimize noise contamination a charge amplifier was located as close as possible to the site of signal detection. It was housed directly beneath the gauge in a chamber which was vented to atmospheric pressure and completely isolated from the test section flow. This was done to remove the effect the test flow may have had on the electronics.

Results

To determine b_1/b_2 a small shock tube was used to apply a transient pressure to the gauge. A technique for transient shear stress calibration yielding a_1 and a_2 is being developed. It is based on sudden removal of a weight attached to the disk with a thread and needs further refinement. However, the following results are not dependent upon it. They can be viewed as a demonstration of the correct functioning of the gauge, or alternatively, as a calibration of the gauge against a value of skin friction determined from the theory for a simple compressible flat plate boundary layer and known shock tunnel test section conditions.

Table 1 The four test conditions

	1	2	3	4
Stagnation Enthalpy (MJ/kg)	12.07	9.507	7.34	5.76
Stagnation Temperature (K)	6348	5287	4373	3763
Stagnation Pressure (MPa)	5.88	3.62	1.63	0.77
Temperature (K)	3383	2262	1952	1463
Pressure (kPa)	114	65.8	27.4	12.1
Density (kg/m ³)	0.107	0.079	0.046	0.027
Velocity (m/s)	3486	3134	2789	2444
Mach No.	3.096	3.129	3.198	3.216

Figure 2 is a typical digitally filtered response from the skin friction gauge (see Table 1 for test conditions with air as the medium); i.e. it is a plot of $e_1 + (b_1/b_2)e_2$ against time and from (3) should be proportional to the shear stress on the gauge. The data was sampled at 1 μ s intervals. The flow is established in the test section in about 20 μ s at which time the gauge registers a constant mean value with small fluctuations superimposed. (Note that the gauge gives a negative output for positive skin friction). This 'steady' flow lasts for about 200 μ s after which large fluctuations appear and the response departs from the steady mean value. To prove that these fluctuations were associated with the flow and not with the gauge, a commercial piezoelectric pressure transducer was mounted in a second flat plate model to measure static pressure on the surface. The second flat plate model had substantially different geometry and different flow-induced stress wave reflection times but the onset of large fluctuations occurred in the unfiltered outputs from both the pressure transducer and one piezoceramic element at the same time, about 250 μ s after the start of the flow. We conclude that the large-scale unsteadiness after 250 μ s is due either to shock wave reflections resulting from the impulsive flow meeting the back face of the dump tank or to the arrival of the helium driver gas. However,

in the available 200 μ s of useful test time, the skin friction gauge indicated steady boundary layer flow (Figure 2).

Figure 3 displays the skin friction gauge averaged output voltage in the 200 μ s test time plotted against theoretical shear stress values obtained using the method of van Driest². The test section stagnation pressure ranged from 0.77 MPa to 5.88 MPa. The flow Mach number was nominally 3.2. The relationship is linear, confirming the fact that shear stress has effectively been isolated from the unwanted contributions due to pressure, temperature and flow-induced vibration. One of the major problems encountered in the development of the gauge was the decoupling of pressure and shear stress. For the range of conditions considered, pressure varies as a nonlinear function of shear stress. Hence, if the gauge was responding to pressure the linear relationship in Figure 3 would not occur. Using the nominal manufacturer's sensitivities for the piezoceramic material, calculations indicate that the gauge outputs for the theoretical shear stresses should lie along the second straight line in Figure 3. This small difference is not surprising and further confirms the proper functioning of the gauge.

Conclusions

Tests of a prototype skin friction gauge at Mach 3.2 in a small free piston shock tunnel have demonstrated the effectiveness of the design concept and the calibration against theoretical skin friction values in a simple flow. The gauge has a rise time of about 20 μ s, sufficiently short for most shock tunnel applications and approaching the rise times needed for expansion tube applications.

Acknowledgements

This work was supported by the Australian Research Council under grant A5852080 and by NASA under grant NAGW-674. The authors wish to acknowledge

the invaluable technical contribution of Mr John Brennan and the scholarship support from Zonta International Foundation.

References

¹Dunn, M.G., "Current Studies at Calspan Utilizing Short-Duration Flow Techniques", Proceeding of 13th International Symposium on Shock Tubes and Waves, Niagara Falls, N.Y., 1981, State University of New York Press, Albany, N.Y., 1981, pp.32-40.

²van Driest, E.R. "Investigation of Laminar Boundary Layer in Compressible Fluids Using the Crocco Method"; NACA, TN 2597, January, 1952.

CAPTIONS FOR FIGURES

Fig. 1 Schematic of skin friction gauge

Fig. 2 Uncalibrated time-history of filtered gauge output for the following test section conditions : Mach number = 3.1, velocity = 3486 m/s, static pressure = 114 kPa, stagnation enthalpy = 12.1 MJ/kg, temperature = 3383 °K

Fig. 3 (a) Measured gauge output (Volts) and (b) predicted gauge output versus theoretical shear stress for test section stagnation pressures from 0.77 MPa to 5.88 MPa. Line (b) is determined from nominal manufacturer's sensitivities for the piezoceramics.

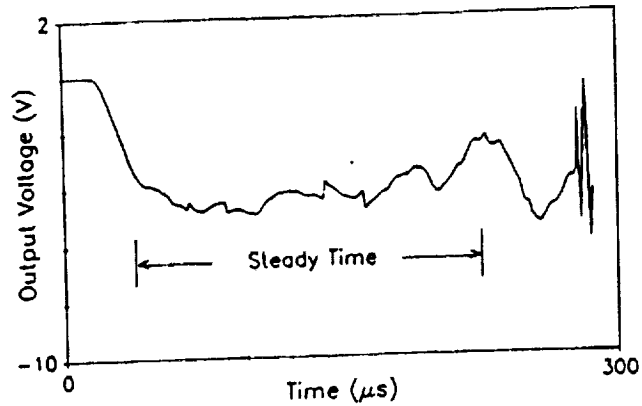


Fig. 2 Uncalibrated time-history of filtered gauge output for the following test section conditions : Mach number = 3.1, velocity = 3486 m/s, static pressure = 114 kPa, stagnation enthalpy = 12.1 MJ/kg, temperature = 3383 °K

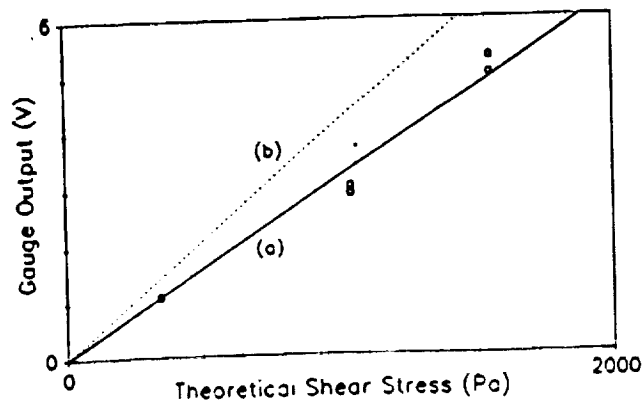


Fig. 3 (a) Measured gauge output (Volts) and (b) predicted gauge output versus theoretical shear stress for test section stagnation pressures from 0.77 MPa to 5.88 MPa. Line (b) is determined from nominal manufacturer's sensitivities for the piezoceramics.

High enthalpy, hypervelocity flows of air and argon in an expansion tube

A. J. NEELY, R. J. STALKER and
A. PAULL

Department of Mechanical Engineering,
The University of Queensland, Australia

ABSTRACT

An expansion tube with a free piston driver has been used to generate quasi-steady hypersonic flows in argon and air at flow velocities in excess of 9 km/s. Irregular test flow unsteadiness has limited the performance of previous expansion tubes, and it has been found that this can be avoided by attention to the interaction between the test gas accelerating expansion and the contact surface in the primary shock tube. Test section measurements of pitot pressure, static pressure and flat plate heat transfer are reported. An approximate analytical theory has been developed for predicting the velocities achieved in the unsteady expansion of the ionising or dissociating test gas.

NOTATION

E	thin film output voltage
E_a, E_b	dissociation energies per molecule
E_s	ionisation energy per molecule
h	specific enthalpy
k	thermal conductivity
K	law of mass action coefficient
m	mass
P	gas pressure
Pr	Prandtl number
q	gas velocity
\dot{q}	heat transfer rate
r	mixture ratio
R	universal gas constant
R	gas constant per unit mass
s	entropy per unit mass
T	gas temperature
T_a, T_b	characteristic dissociation temperature
T_s	characteristic ionisation temperature
t	time
U	gas velocity
u	internal energy per unit mass

x	displacement
α	ionisation, dissociation fraction
α_R	temperature coefficient of resistance
γ	ratio of specific heats
ρ	gas density
μ	dynamic viscosity

Subscripts and superscripts

1..20	gas states
e	edge of the boundary layer
r	recovery
o	initial
w	wall
*	reference

1. INTRODUCTION

The expansion tube provides an alternative to the shock tunnel as a means of producing high enthalpy, hypersonic flows⁽¹⁾. Both use a shock tube as the basic source of test gas. However, whereas the shock tunnel employs a steady expansion through a nozzle to accelerate the test gas to hypersonic speeds, the expansion tube uses an unsteady expansion in a constant area tube. This has the advantage that both the stagnation enthalpy and the effective reservoir pressure of the test flow are increased through the expansion. It has the disadvantage that the test times are less than those for a reflected shock tunnel, although they are generally greater than for a non-reflected shock tunnel.

The facility was first proposed by Resler and Bloxson⁽²⁾ in the early 1950s. A detailed theoretical study of the device by Trimpi⁽³⁾ in the early 1960s suggested the ability to produce a large range of quasi-steady flow conditions simply by varying the filling pressures in each section of the device. Subsequent experimental work⁽⁴⁻⁶⁾ demonstrated an inability to produce the variety of quasisteady flow conditions first thought possible. The large scale 6-inch expansion tube later built at NASA Langley could only be made to produce a quasi-steady flow over a very narrow range of test conditions for each test gas⁽⁷⁾. A typical test section centreline pitot pressure history from the Langley facility is illustrated in Fig. 1.

The addition of a free piston driver to an expansion tube has been shown to increase the performance of the facility^(8,9).

Manuscript received 20 February 1991, revised version received 15 April 1991, accepted 1 May 1991.
Paper No 1821.

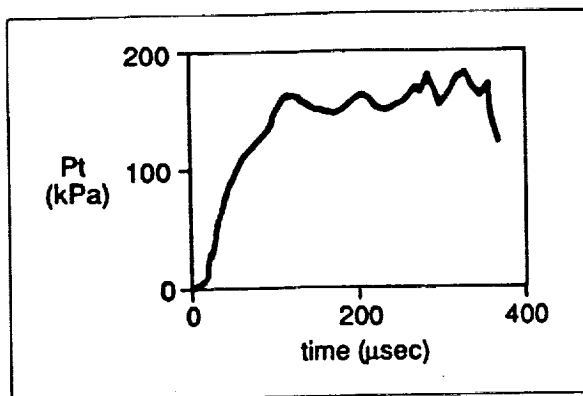


Figure 1. Typical centreline pitot pressure time history for air test gas and helium acceleration gas from the Langley 6 inch expansion tube (from Ref. 7, Fig. 6).

This increased performance and a greater understanding of the factors limiting the test flow time in the expansion tube^(10, 11) has renewed interest in the device as a facility for hypervelocity aerothermodynamic research, and has led to this study of the test section flows generated by the expansion tube.

Unlike a steady flow expansion, the stagnation enthalpy does not remain constant in an unsteady expansion, and it is necessary to find a means of calculating the test section velocity, which does not rely upon knowledge of the stagnation enthalpy generated in the shock tube. For a perfect gas, this can be done by a straightforward analysis, involving integration of the differential equations governing the unsteady expansion. This is not possible for high enthalpy flows, where the real effects of dissociation and/or ionisation must be taken into account. Rather than reverting to a relatively complex numerical analysis, this problem is resolved, here, by developing a simplified, approximate analytical model for calculating the velocity.

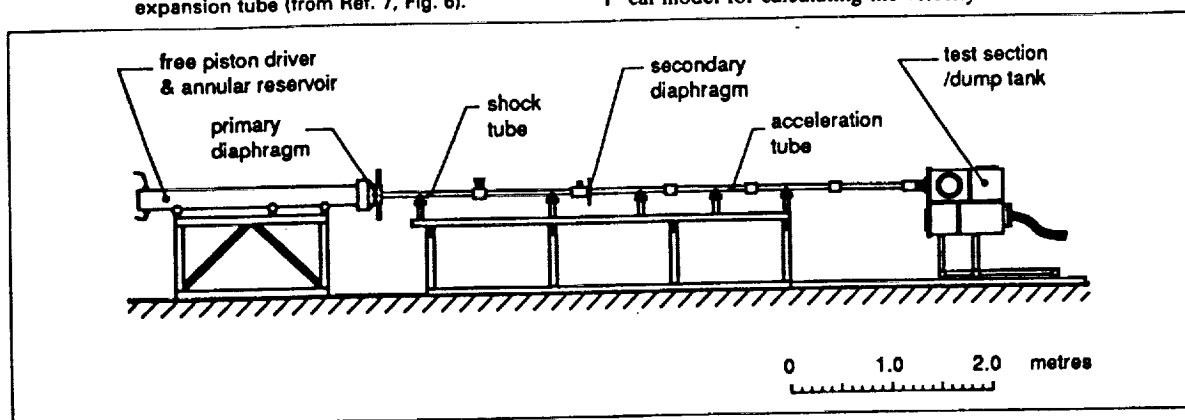


Figure 2(a). Layout of TQ expansion tube.

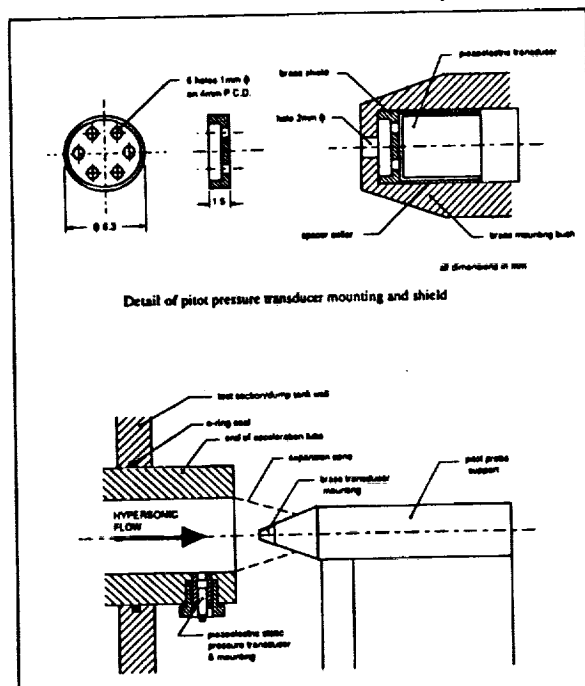


Figure 2(b). Pitot pressure and static pressure transducer positioning and mounting detail.

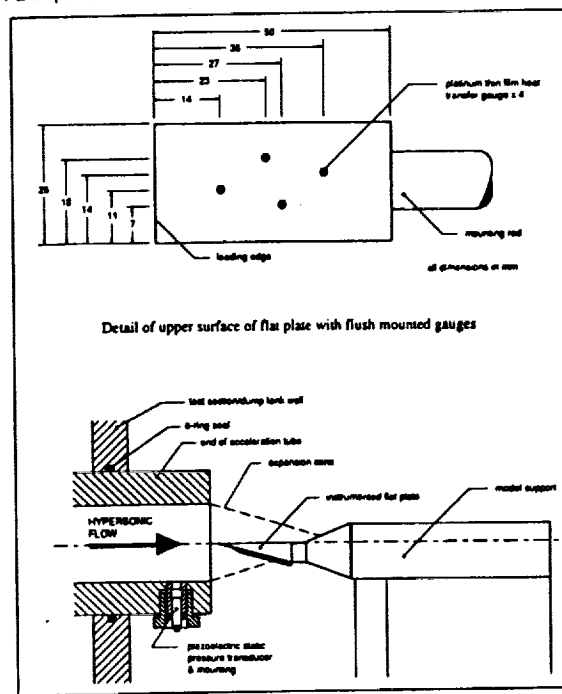


Figure 2(c). Position and detail of zero-incidence flat plate in the test section.

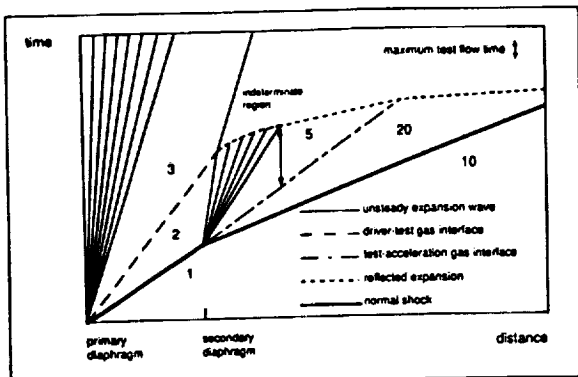


Figure 3. Wave diagram for expansion tube flow process.

2. APPARATUS

High enthalpy flow conditions were produced in the TQ expansion tube at the University of Queensland. The layout of the free piston driven expansion tube is shown in Fig. 2(a). The free piston driver has a compression tube with an internal diameter of 100 mm and is 2.3 m in length. Both the shock tube and acceleration tubes have constant internal diameters of 37 mm and are 2.08 m and 3.36 m long respectively. Typical quiescent filling pressures are listed in Tables 1 and 2.

High temperature, high pressure driver gas bursts a primary diaphragm (usually 1 mm mild steel) and drives a shock wave through the test gas held in the shock tube. At the end of the shock tube the shock wave bursts the secondary diaphragm (cellophane, approx 230 μm) and is accelerated to a higher velocity. The test gas that follows the acceleration gas is expanded unsteadily in the acceleration tube. The hypersonic test gas exits the acceleration tube and flows over the model mounted in the test section (Figs 2(b), 2(c)). A wave diagram of the flow process is shown in Fig. 3.

The facility is instrumented for measurement of the flow conditions in the tube. Seven ionisation detection gauges are positioned along the length of the tunnel for measurement of the shock speeds in the shock and acceleration tubes via time of flight calculations. Piezoelectric pressure transducers are used to measure the wall static pressure at the exit of the acceleration tube and the centerline pitot pressure in the test section (Fig. 2(b)). For the measurement of heat transfer rates in the flow the pitot pressure probe is replaced with a zero incidence flat plate with four flush mounted thin film resistance thermometers (Fig. 2(c)).

3. FLOW CONDITIONS

To investigate the real gas effects of dissociation and ionisation in high enthalpy flows in an expansion tube, air and argon are used as the test gases. Argon, a monatomic gas, is used to examine the effect of ionisation on the flow. Air, considered here to be a mixture of two diatomic gases, oxygen and nitrogen, is used to examine the effect of dissociation on the flow.

Initially only a limited number of air test conditions had been established in the TQ expansion tube facility^(8,9) and only two argon conditions had been found. Guided by the theory of test time maximisation developed by Paull⁽¹⁰⁾, a search was made for new test conditions using argon as the test gas.

Paull's theory calculates the test time of the flow as the interval between the passage of the secondary gas interface between the acceleration and test gases, and the arrival of the trailing edge of the unsteady expansion, or the reflected wave emanating from the interaction of the upstream head of the unsteady expansion with the driver-test gas interface in the shock tube (Fig. 3).

The latter effect allows flow disturbances, which are known to exist in the driver gas at the interface, to follow the reflected wave into the test gas. Paull's theory shows that these disturbances cannot pass from the driver gas into the test gas when the test gas speed of sound is substantially higher than in the driver gas, and the shock tube operating parameters here are such that this condition is satisfied. The reflected expansion lowers the test gas speed of sound, and thus allows the disturbances to pass through to the test region.

By adjusting the filling pressures in each section, the run condition may be varied so that the maximum period of undisturbed test flow, indicated on the wave diagram (Fig. 3), coincides with the passage of the test flow through the test section. Charts of test time contours may be plotted against run condition parameters to aid in the determination of the optimum run conditions.

Pitot pressure and static pressure histories recorded at the exit of the acceleration tube are used to confirm the presence of a period of uniform flow required for a useful test condition. Some of the static pressure records exhibit 'ringing' at the frequencies governed by the characteristics of the pressure transducer and the data recording system, and this may be ignored. On the other hand, during the test time, the pitot pressure records exhibit a superimposed oscillation with a period of the order of 20 μs , which may be compared with a similar oscillation, at a period of about 90 μs , in the pitot pressure record from the Langley tunnel (Fig. 1). These are thought to originate from a gas dynamic source. As explained by Paull⁽¹¹⁾ they are associated with weak disturbances in the shock heated test gas which tend to be focused to a single frequency by the unsteady expansion. In the

TABLE 1
Averaged test conditions for ionising argon

CONDITION	1	2	3	4	5	6
Driver Gas	He	He	He	He	He	He
Fill Pressures						
Compression tube (kPa)	130	130	130	130	130	130
Shock Tube (Pa)	2000	2000	2933	4000	6666	6666
Acceleration Tube (Pa)	11	17	18	27	37	53
Shock Tube Flow						
Shock Velocity (ms^{-1})	5662	5273	5346	5017	4767	4560
Flow Velocity (ms^{-1})	4833	4442	4498	4151	3876	3667
Temperature (K)	16 746	15 922	16 431	15 900	15 657	15 042
Pressure (kPa)	879	753	1134	1344	1981	1793
Density (kgm^{-3})	0.219	0.203	0.296	0.371	0.571	0.545
Ionisation fraction	0.153	0.117	0.119	0.089	0.065	0.051
Test Flow						
Shock Velocity (ms^{-1})	10 075	8976	9394	9110	8453	7331
Flow Velocity (ms^{-1})	9154	8431	8715	8528	7951	6868
Pressure (Pa)	11 441	14 669	17 814	22 875	28 627	31 239
Temperature (K)	7515	6964	6529	5827	4364	4178
Density ($\times 10^{-2} \text{kgm}^{-3}$)	0.732	1.012	1.310	1.838	3.151	3.595
Ionisation fraction	6.07e-4	1.86e-4	8.98e-5	1.44e-5	3.21e-8	1.06e-8
Stagn. Enth. (MJ kg^{-1})	45.8	39.1	41.4	39.5	33.9	25.8
Reynolds No. ($\times 10^6 \text{m}^{-1}$)	0.400	0.531	0.736	1.070	1.992	2.010
Mach Number	5.67	5.43	5.80	5.92	6.46	5.70

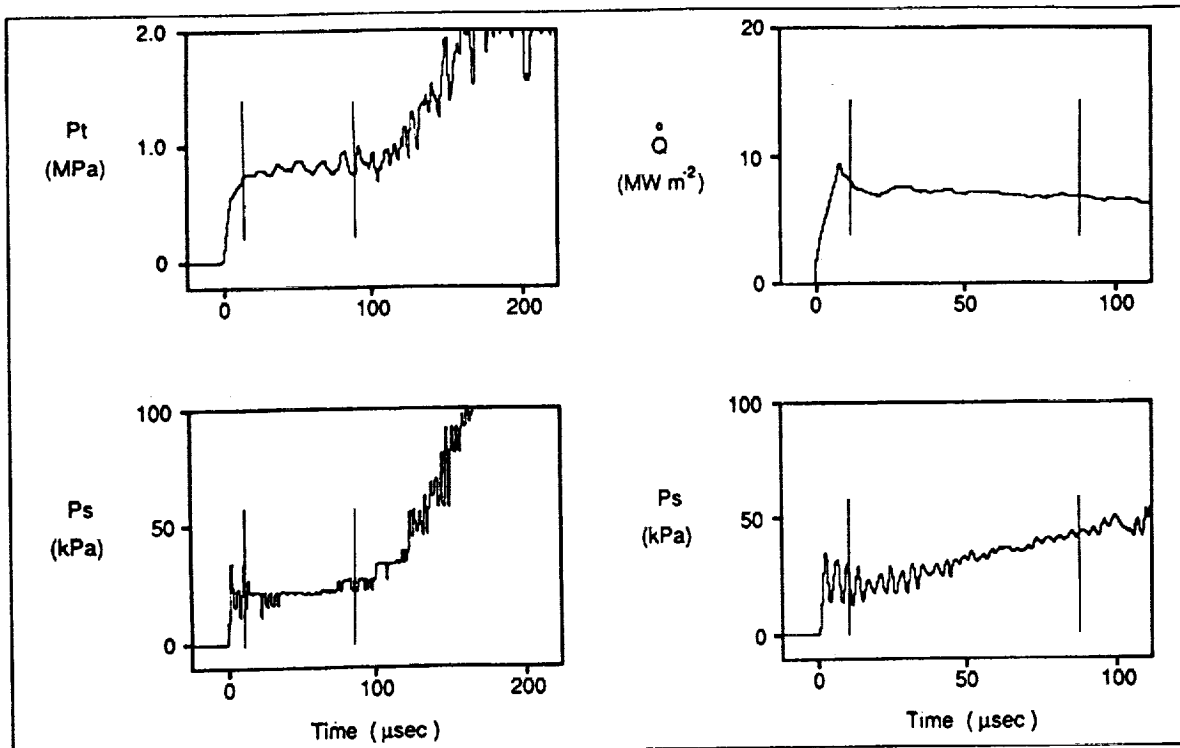


Figure 4(a). Pitot pressure (P_t) and matching static pressure (P_s) histories, and heat transfer rate (\dot{Q}) and matching static pressure (P_s) histories, for a high enthalpy air condition.

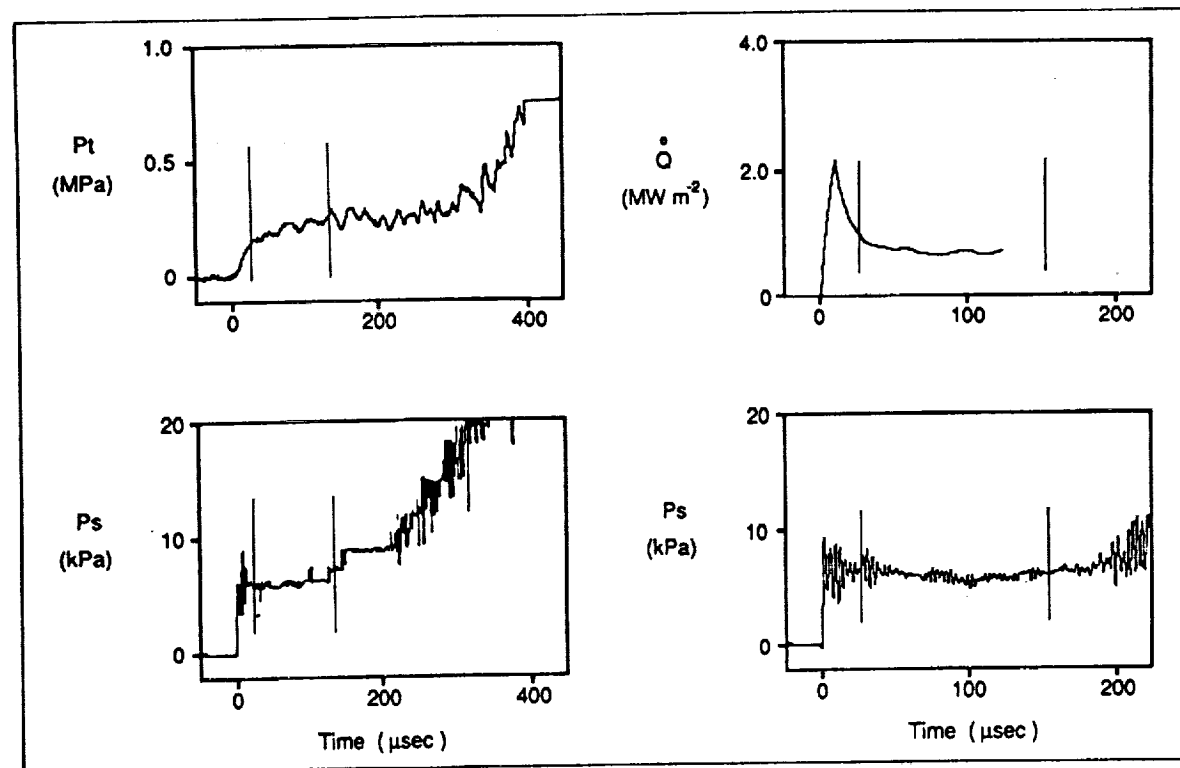


Figure 4(b). Pitot pressure (P_t) and matching static pressure (P_s) histories, and heat transfer rate (\dot{Q}) and matching static pressure (P_s) histories, for a low enthalpy air condition.

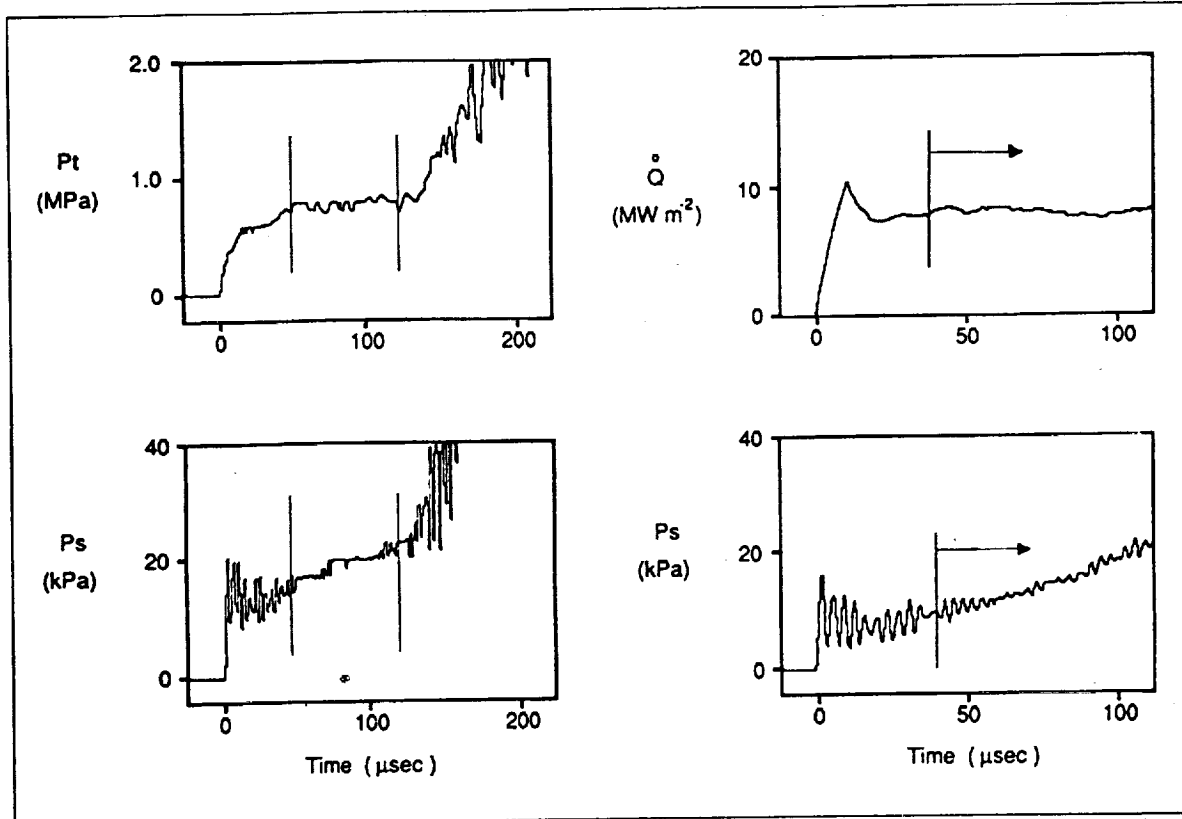


Figure 4(c). Pitot pressure (P_t) and matching static pressure (P_s) histories, and heat transfer rate (\dot{Q}) and matching static pressure (P_s) histories, for a high enthalpy argon condition.

present tests, they give rise to a fluctuation of approximately $\pm 5\%$ and for most high enthalpy aerodynamic testing purposes, this may be ignored.

Heat transfer rate histories, although less sensitive to flow variations, are also used to confirm this quasi-steady flow. Typical pressure and heat transfer rate traces for a high and a low enthalpy air condition and a high enthalpy argon condition are illustrated in Figs 4(a), 4(b) and 4(c).

The data acquisition equipment was run at 2 MHz for the heat transfer rate experiments and at 1 MHz for the pitot pressure experiments, resulting in different time bases in each case shown in Fig. 4. Some shot to shot variation is also visible when the static pressure traces are compared for each condition. The periods of quasi-steady flow are indicated on each trace. The duration of the quasi-steady flows are approximately 60 μs for the high enthalpy air condition, 100 μs for the low enthalpy air condition and 80 μs for the high enthalpy argon condition.

Six conditions in each test gas were obtained with a number of shots fired at each condition. These conditions are summarised in Tables 1 and 2. There is some overlap of test conditions with different initial conditions found to produce similar test flows.

The argon conditions are medium to high enthalpy shots with stagnation enthalpies in the range 26 to 46 MJ/kg. The air shots are a mixture of low enthalpy and high enthalpy shots. The low enthalpy shots are at stagnation enthalpies around 9 MJ/kg, while the high enthalpy shots are at enthalpies in the range 42 to 48 MJ/kg. The run conditions for the two gases cover a range of Mach numbers and Reynolds numbers.

TABLE 2
Averaged test conditions for dissociating air

CONDITION	1	2	3	4	5	6
Driver Gas	He	He	He	He	Air	Ar
Fill Pressures						
Compression tube (kPa)	130	130	130	130	174	130
Shock Tube (Pa)	3466	3466	6666	6666	1733	3466
Acceleration Tube (Pa)	17	27	27	40	9	33
Shock Tube						
Shock Velocity (ms^{-1})	5512	5459	5192	5091	2219	2373
Flow Velocity (ms^{-1})	5003	4951	4685	4583	1865	2002
Temperature (K)	6753	6698	6583	6410	2338	2616
Pressure (kPa)	1114	1092	1890	1813	86	195
Density (kgm^{-3})	0.436	0.433	0.793	0.777	0.126	0.257
N dissociation fraction	0.129	0.121	0.079	0.063	0	0
O dissociation fraction	0.995	0.995	0.989	0.986	0.015	0.016
Test Flow						
Shock Velocity (ms^{-1})	9888	9295	9323	8917	4345	4123
Test Velocity (ms^{-1})	9035	8630	8673	8368	4076	3743
Pressure (Pa)	18 474	24 898	25 065	34 704	1985	6013
Temperature (K)	3748	3862	3463	3532	892	1097
Density ($\times 10^{-2} kgm^{-3}$)	1.453	1.892	2.230	3.026	0.744	1.909
N dissociation fraction	0	0	0	0	0	0
O dissociation fraction	0.847	0.876	0.617	0.622	0	0
Stagn. Enth. (MJ kg $^{-1}$)	47.7	44.4	44.0	41.6	9.3	8.8
Reynolds No. ($\times 10^6 m^{-1}$)	1.513	1.855	2.325	3.0125	0.7760	1.6295
Mach Number	7.50	7.04	7.63	7.29	7.11	6.05

4. MODELLING THE FLOW PROCESSES

It is assumed that all the flow processes occurring in the expansion tube take place with the gas in thermodynamic equilibrium. This applies to the flow immediately after the normal shock in the shock tube, and to the unsteady expansion in the expansion tube.

For the normal shock, the pressure levels are such that both air and argon attain thermodynamic equilibrium within a millimetre or so downstream of the shock⁽¹⁾. For the unsteady expansion the situation is less certain, but Jones⁽⁴⁾ and Moore⁽¹²⁾ have demonstrated that for air, the flow can be more closely modelled by equilibrium theory than by using the non-equilibrium assumption of frozen flow, whilst Miller⁽⁷⁾ has shown the same applies to carbon dioxide. Since the ion-electron recombination processes in argon tend to be faster than the atomic recombination processes in air or carbon dioxide, it seems reasonable to assume that it also follows an equilibrium path in the expansion.

4.1 Thermodynamic Relations

Simple thermodynamic models are used to describe the thermodynamic behaviour of each of the test gases. Thus argon is treated as an ionising monatomic gas in which ionisation of the atom takes place from the ground state, and electronic excitation is ignored, as described by the Saha model. Air is treated as a mixture of two ideal dissociating gases, as described by Lighthill⁽¹³⁾.

An equation of state for these models can be written as

$$P = \rho R' T \{1 + \alpha_a + r(1 + \alpha_b)\} \quad (1)$$

$$\text{with } R' = \frac{IR}{(m_a + r m_b)}$$

where IR is the Universal gas constant per mol, r is the ratio of the total number of 'b' atoms in a sample to the total number of 'a' atoms (with the total taken to include both the molecular and atomic form), m_a and m_b are the masses of the molecules in the air and the atoms for argon, and for argon $r = 0$.

The corresponding expression for the internal energy per unit mass is

$$u = \frac{3}{2} R' T \{1 + \alpha'_a + r(1 + \alpha'_b)\} + R' \left\{ \frac{E_a}{IR} \alpha_a + r \frac{E_b}{IR} \alpha_b \right\} \quad (2)$$

where $\alpha'_a = \alpha'_b = 1$ for air, and $\alpha'_a = \alpha_a$ for argon. E_a and E_b are dissociation energies per molecule for air and E_a is the ionisation energy for argon.

The law of mass action gives the ionisation or dissociation fractions as

$$\frac{\alpha_i^2}{(1 - \alpha_i)} = K_i \frac{T^e}{p R'} \exp \left(\frac{E_i}{RT} \right) \quad (3)$$

where the subscript i is used to represent the compound a or b , and $e = 0$ for the two components of air, and $e = 1.5$ for argon.

An expression for entropy change is obtained by writing the differential relation

$$T ds = du + P d \left(\frac{1}{\rho} \right) \quad (4)$$

where ds is the entropy change per unit mass, then substituting from (1), (2) and (3) and integrating to obtain

$$\begin{aligned} \frac{s - s_0}{R'} = & l(1 + r) \ln \left(\frac{T}{T_0} \right) - 2 \ln \left(\frac{1 - \alpha_a}{1 - \alpha_{a0}} \right) + 2 \ln \left(\frac{\alpha_a}{\alpha_{a0}} \right) \\ & + n(\alpha_a - \alpha_{a0}) + \left(\frac{1 + \alpha_a}{T} - \frac{1 + \alpha_{a0}}{T_0} \right) \frac{E_a}{IR} \\ & - 2r \ln \left(\frac{1 - \alpha_b}{1 - \alpha_{b0}} \right) + 2r \ln \left(\frac{\alpha_b}{\alpha_{b0}} \right) + r(\alpha_b - \alpha_{b0}) \\ & + r \left(\frac{1 + \alpha_b}{T} - \frac{1 + \alpha_{b0}}{T_0} \right) \frac{E_b}{IR} \quad (5) \end{aligned}$$

where $l = 3$ for air and $l = 0$ for argon, while $n = 1$ for air and $n = 2.5$ for argon. It should be noted that for air the entropy per unit mass is usually normalised with respect to the gas constant per unit mass, which is given here by

$$R = \frac{IR(1 + r)}{(m_a + r m_b)} = (1 + r) R'$$

In order to express Equation (5) in this form it is only necessary to divide by $(1 + r)$.

4.2 Flow Calculations — Normal Shock

The conditions behind the primary shock are determined in the usual manner, combining the above thermodynamic relations with equations expressing the balance of mass, momentum and energy, and employing an iterative process to solve the resultant set of simultaneous equations. As an alternative, this set of equations may be used to prepare charts of normal shock properties, which then can be used for rapid determination of the post shock conditions.

4.3 Flow Calculations — Unsteady Expansion

The thermodynamic conditions obtained in expansion of the test gas to a given pressure can be derived by noting that the gas is assumed to be in equilibrium during the expansion, and therefore it is an isentropic process. Thus Equation (5) can be used to establish a relation between T and α , allowing P and ρ to be determined from Equations (1) and (3). It then remains only to establish the flow velocity corresponding to these conditions.

Consideration of continuity and momentum for an adiabatic unsteady expansion in a constant area tube⁽¹⁴⁾ yields the differential relation

$$\left(\frac{dP}{dp} \right)^{1/2} \frac{dp}{p} = -dq \quad (6)$$

By using the above equations to determine dP/dp , this equation can be integrated numerically to yield the velocity. However, the inviscid isentropic model of the expansion which is employed here can only be expected to yield

approximate velocities anyway and, with this in mind, it is more convenient to develop an approximate theory which yields an expression for the velocity change through the expansion in a closed analytical form.

Using Equation (4) with $ds = 0$, Equation (6) becomes

$$\left(\frac{\rho}{P}\right)^{1/2} \left(\frac{\rho}{P} \frac{dP}{d\rho}\right)^{1/2} du = -dq \quad (7)$$

Since the expansion is isentropic, $\rho/P \, dP/d\rho$ becomes the isentropic exponent. For a perfect gas, without ionisation or dissociation, it is equal to the ratio of specific heats, which does not exceed 5/3, and is reduced to values closer to unity when ionisation or dissociation occurs. Thus

$$\left| \frac{\rho}{P} \frac{dP}{d\rho} - 1 \right| < 1$$

and the second term on the left side of Equation (7) may be expanded in a Binomial series, to yield

$$\left(\frac{\rho}{P}\right)^{1/2} \left\{ 1 + \frac{1}{2} \left(\frac{\rho}{P} \frac{dP}{d\rho} - 1 \right) \right\} du = -dq \quad (8)$$

where only the first order term in $(\rho/P \, dP/d\rho - 1)$ has been retained. It may be shown that the error in q incurred by neglecting the higher order terms is less than 5% for an ionising monatomic gas, and less than 2% for an ideal dissociation gas.

Now noting that

$$\left(\frac{\rho}{P} \frac{dP}{d\rho} - 1\right) du = d\left(\frac{P}{\rho}\right)$$

for an isentropic expansion, equation (8) becomes

$$\left(\frac{\rho}{P}\right)^{1/2} du + \frac{1}{2} \left(\frac{\rho}{P}\right)^{1/2} d\left(\frac{P}{\rho}\right) = -dq \quad (9)$$

Argon Test Gas

For argon, substituting from Equations (1) and (2), while writing $\alpha_s = \alpha$, and $Ea/RT = T_i$, the characteristic ionisation temperature, Equation (9) becomes, after integration

$$4 \left\{ \left(\frac{P_o}{P}\right)^{1/2} - \left(\frac{P}{P_o}\right)^{1/2} \right\} + \int_{T_i}^{\infty} \frac{\sqrt{R'} T_i d\alpha}{\sqrt{T(1+\alpha)}} = q - q_o \quad (10)$$

where the subscript o signifies the initial condition. It can be seen that the contribution to the velocity change through the expansion is divided into two parts. One part is represented by the second term on the right hand side of the equation, and is the contribution due to recombination. The first term is that due to the expansion of the test gas alone, which accelerates the test gas even in the absence of the heat release associated with recombination. It might be noted that if the analysis were carried out for a perfect gas, then the coefficient outside the brackets would be $2\sqrt{\gamma/(\gamma-1)}$ which for $\gamma = 5/3$, yields a value of 3.87, rather than the approximate value of 4 shown in Equation (10).

In order to evaluate the integral in Equation (10), a simple relation between the temperature and the ionisation fraction is required. Plots of T against α are shown in Fig. 5(c), where it can be seen that for constant entropy, the relationship

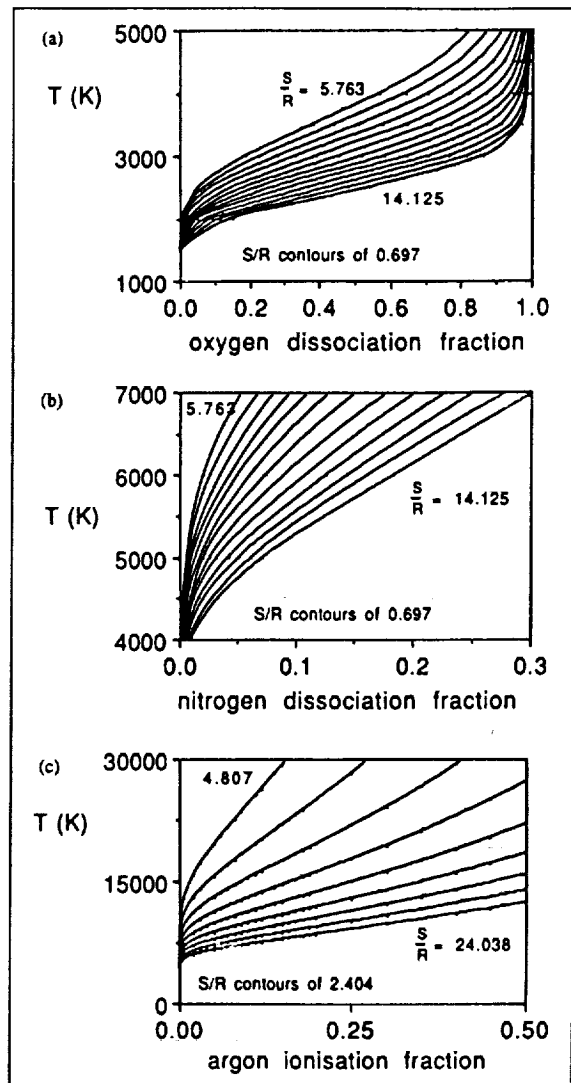


Figure 5. Plots of variation of (a) oxygen dissociation fraction, (b) nitrogen dissociation fraction and (c) argon ionisation fraction, with gas temperature at constant entropy (relative to STP).

between these two variables is approximately linear. Therefore the relation

$$T = C\alpha + B$$

is used, with the value of C and B chosen to match a line at an appropriate entropy in Fig. 5(c). Substitution of this relation into Equation (10), and evaluation of the integral, yields

$$\frac{\sqrt{R'} T_i}{C} \ln \left\{ \frac{2 \sqrt{\alpha_o^2 + (1 + \frac{B}{C}) \alpha_o + \frac{B}{C}} + 2\alpha_o + 1 + \frac{B}{C}}{2 \sqrt{\alpha^2 + (1 + \frac{B}{C}) \alpha + \frac{B}{C}} + 2\alpha + 1 + \frac{B}{C}} \right\} + 4 \left\{ \left(\frac{P_o}{T_o}\right)^{1/2} - \left(\frac{P}{T}\right)^{1/2} \right\} = q - q_o \quad (11)$$

Air Test Gas

For air, putting $Ea/IR = T_a$, and $E_b/IR = T_b$, the characteristic dissociation temperatures for oxygen and nitrogen respectively, Equations (1) and (2) may again be substituted into Equation (9) to yield, after integration

$$7 \left\{ \left(\frac{P_o}{\rho_o} \right)^{1/2} - \left(\frac{P}{\rho} \right)^{1/2} \right\} - 3 \sqrt{R'} \int_a^\infty \frac{d(T(\alpha_a + r\alpha_b))}{\sqrt{T(1 + \alpha_a + r(1 + \alpha_b))}} + \sqrt{R'} \int_a^\infty \frac{T_a d\alpha_a + T_b r d\alpha_b}{\sqrt{T(1 + \alpha_a + r(1 + \alpha_b))}} = q - q_o \quad (12)$$

where $\alpha = \alpha_a$ or α_b , and $\alpha_o = \alpha_{a_o}$ or α_{b_o} . It is seen that in comparison with Equation (10), the second term on the left hand side represents an additional effect of dissociation. This is related to the change in the number of gas particles per unit mass, and is only roughly one tenth of the magnitude of the third term on the left hand side, which is the recombination term. In obtaining a first approximation to the velocity it could be neglected, but it is included here in order to improve the accuracy. It is worth noting again that, if the analysis were carried out for a Lighthill gas in the undissociated state, with $\gamma = 4/3$, then the coefficient outside the brackets in the first term would be 6.93, rather than the value of 7 which is shown.

The unsteady expansion, which in general is taken to begin with a mixture of fully dissociated oxygen and partially dissociated nitrogen, and to end with a mixture of undissociated nitrogen and oxygen, is divided into three stages.

The first stage considers the unsteady expansion in the presence of monatomic oxygen, which acts as an inert diluent. This expansion proceeds from a level of partial dissociation of the nitrogen to an 'intermediate point', where the nitrogen can be assumed to be totally recombined. In this first stage the oxygen is assumed to remain totally dissociated, and acts as an inert diluent.

The second stage considers the unsteady expansion of dissociated oxygen in the presence of fully recombined nitrogen which acts as the inert diluent. The expansion of the oxygen occurs from a totally dissociated state.

The third stage considers the expansion of the fully recombined nitrogen and oxygen, behaving as a perfect gas with a ratio of specific heats of 4/3.

Of course, an expansion may not pass through all these stages, but the analysis can be readily adjusted to account for this simply by omitting the relevant stages, and by adjusting the limits of integration in Equation (12) (Fig. 6).

Thus Equation (12) can be written

$$7 \left\{ \left(\frac{P_o}{\rho_o} \right)^{1/2} - \left(\frac{P}{\rho} \right)^{1/2} \right\} + I_b + I_a = q - q_o \quad (13)$$

where I_b and I_a represent the contributions of the second and third terms on the left hand side of Equation (12) in the first and second stage respectively. The method by which I_b and I_a are determined follows that for argon. Plots of T against α_a and α_b (Fig. 5(a) & (b)) show that, at constant entropy, an approximately linear relationship exists over most of the range of α_a and α_b . Thus, using the relation

$$T = C_b \alpha_b + B_b$$

for nitrogen recombination stage (i.e. the first stage), the

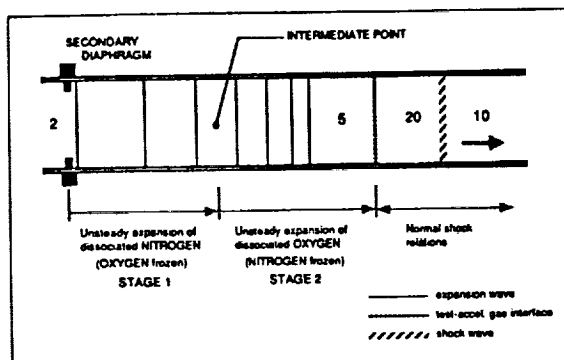


Figure 6. Two stage expansion model for air as a mixture of oxygen and nitrogen.

integrations in Equation (12) may be performed to yield

$$\sqrt{\frac{rR'}{C_b}} \left\{ T_b + 3 \frac{1+r}{r} C_b \right\} \ln \left\{ \frac{2 \sqrt{r C_b X_o} + 2r C_b \alpha_{b_o} + (2+r) C_b + r B_b}{2 \sqrt{r C_b X} + 2r C_b \alpha_b + (2+r) C_b + r B_b} \right\} - 6 \sqrt{R'} (\sqrt{X_o} - \sqrt{X}) \quad (14)$$

where $X = (C_b \alpha_b + B_b) (2 + r + r \alpha_b)$, and X_o is the value of X when $\alpha_b = \alpha_{b_o}$.

Similarly, using the relation

$$T = C_a \alpha_a + B_a$$

for the oxygen recombination stage (i.e. the second stage), the integrations in Equation (12) may again be performed to yield

$$\sqrt{\frac{R'}{C_a}} (T_a + 3 (1+r) C_a) \ln \left\{ \frac{2 \sqrt{C_a X_o} + 2C_a \alpha_{a_o} + (1+r) C_a + B_a}{2 \sqrt{C_a X} + 2C_a \alpha_a + (1+r) C_a + B_a} \right\} - 6 \sqrt{R'} (\sqrt{X_o} - \sqrt{X}) \quad (15)$$

where $X = (C_a \alpha_a + B_a) (1 + r + \alpha_a)$, and X_o is the value of X when $\alpha_a = \alpha_{a_o}$.

Remembering that \bar{P}/ρ is calculated from the exact isentropic relations, which also yield the values of α_b and α_a which are inserted into Equations (14) and (15), Equations (13), (14) and (15) may be combined to yield the velocity in the expansion.

5. IMPLEMENTATION OF FLOW MODELS

The flow models for the ionising and dissociating gases were applied to the run conditions described in Section 3. The states of the test gas at the end of the shock tube and at the exit of the acceleration tube were calculated and are set out in Tables 1 and 2.

For the high enthalpy argon conditions, equilibrium calculations showed that ionisation fractions of between 5 and 16% were induced in the test gas after shock heating in the shock tube. Essentially full recombination was predicted to occur in the unsteady expansion in the acceleration tube with

the ionisation fractions falling to well below a tenth of a per cent. Thus the test gas produced by these high enthalpy runs, although at elevated temperatures, is not ionised.

Essentially complete dissociation of the oxygen component of the air is predicted to occur for the high enthalpy air conditions in the shock tube. Dissociation fractions from 6 to 13% are predicted for the nitrogen component. Total recombination of the nitrogen occurs in the unsteady expansion in the acceleration tube, while the dissociation fraction of the oxygen only falls to between 62 and 88%. The test gas produced under these flow conditions thus has a highly dissociated oxygen component.

The shock heating of the test gas in the shock tube, for the low enthalpy air conditions is not severe enough to induce significant dissociation of the nitrogen component. The dissociation fraction of the oxygen component is approximately 1.5%. Processing by the unsteady expansion in the acceleration tube induces complete recombination of the oxygen. The low enthalpy flow conditions thus produce test flows of undissociated air.

6. COMPARISON OF IDEAL AND ACTUAL PERFORMANCE

Calculations of the ideal performance of the unsteady expansion process in the expansion tube are made from the known conditions at the end of the shock tube. The expansion process is allowed to proceed to the calculated pressure level behind the secondary shock.

The calculations of ideal performance exceed the velocities calculated directly from observed shock speeds (Fig. 7). This suggests energy is being lost in the expansion process. This energy loss could be attributed to viscous attenuation of the flow in the acceleration tube. No account of viscous effects is taken in any of the calculations. The high temperatures of the test gas and the levels of dissociation and ionisation of the gas suggest also the possibility of energy loss through radiation through the tube walls, before the gas can be cooled by the expansion.

Grey body calculations for the flow of air in the expansion tube indicate that the energy loss through radiation is not significant. Work by Logan *et al.*⁽¹⁵⁾ on shock heated argon at roughly equivalent temperatures and electron densities to those considered here, indicates a drop in total enthalpy of no more than 20% in the test gas in the shock tube. The primary source of energy loss would thus appear to be viscous attenuation of the flow down the acceleration tube. Unlike a shock tunnel, the radiation losses at high enthalpies in an expansion tube remain minor.

Measured static and pitot pressures are compared with values calculated from the observed shock velocities using equilibrium theory, for all the test flow conditions (Fig. 8). Agreement between the two methods of determining the static pressure levels in the flow is reasonable with measured pressures tending to be lower than those predicted generally by no more than 20%. Agreement is best for the lower enthalpy air conditions.

Measured pitot pressure levels are generally around 30% lower than predicted levels and in some cases only 50% of the predicted value (Fig. 8). Predictions of the pitot pressure are made from the calculated values of test gas velocity and the thermodynamic state of the gas. The pitot pressure is approximately proportional to the product of the flow density and the square of the flow velocity.

$$\text{i.e. } P_5 = 0.9 \rho_5 U_5^2$$

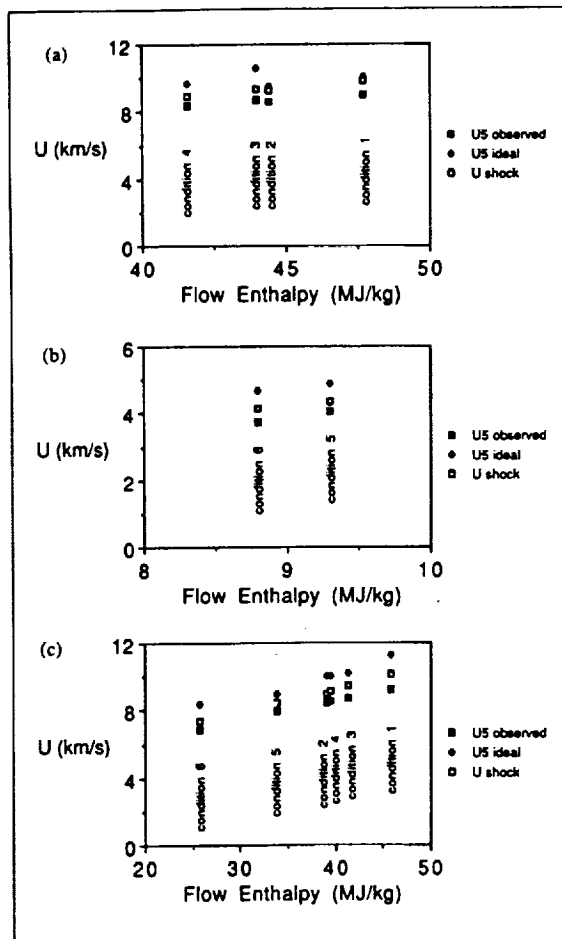


Figure 7. Comparison of the ideal velocity calculated through the expansion (U_5 ideal) with the observed shock velocity (U shock) and the velocity calculated across the shock (U_5 observed) for (a) high enthalpy air, (b) low enthalpy air and (c) high enthalpy argon conditions.

Although the relation is sensitive to any error in the measured velocity these errors are negligible. Assuming an accurate measurement of the pitot pressure the results indicate that the calculated value of the density is too high. This discrepancy could be due to shock reflection from the cellophane secondary diaphragm just before it ruptures, which could increase the entropy of the test gas, thereby increasing the temperature and lowering the density at a given static pressure.

7. HEAT TRANSFER RATES

Heat transfer rates for a number of flow conditions were measured using platinum thin film resistance thermometers mounted flush in the surface of a small flat plate (Fig. 1(c)). The flat plate was positioned centrally in the flow at the exit of the acceleration tube.

The numerical relation set out by Shultz and Jones⁽¹⁶⁾ and corrected in Ref. 17 is used to integrate the voltage/temperature history.

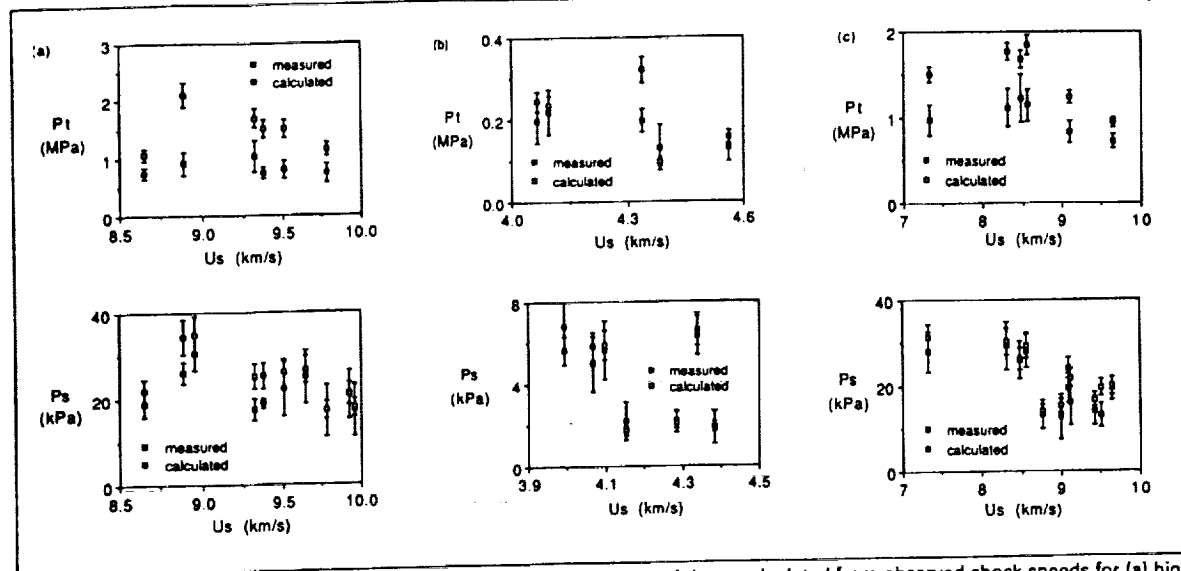


Figure 8. Comparison of measured pitot (Pt) and static (Ps) pressures and those calculated from observed shock speeds for (a) high enthalpy and (b) low enthalpy air and (c) high enthalpy argon conditions.

$$\dot{q}_n(t) = \frac{2 \sqrt{p} c k}{\sqrt{\pi} \alpha_R E_0} \left[\sum_{i=1}^n \frac{E(t_i) - E(t_{i-1})}{(t_n - t)^{1/2} + (t_n - t_{i-1})^{1/2}} \right] \quad (16)$$

Heat transfer rates for comparison with experimental measurements are calculated using the empirical relation for a laminar boundary layer⁽¹⁸⁾ as the local Reynolds number for the small flat plate are well within the laminar flow regime.

$$\dot{q}_w = \frac{0.332}{P_r^{2/3}} \rho^* U_e (H_r - H_w) \left[\frac{\rho^* U_e x}{\mu^*} \right]^{-1/2} \quad (17)$$

with Reference values (*) calculated at a reference enthalpy

$$h^* = 0.5(h_e + h_w) + 0.22(h_e - h_e) \quad (18)$$

The calculations are based upon the test conditions determined using the equilibrium method described previously. The free stream flow velocities used in the calculations are those derived from the observed secondary shock speeds, since the velocities derived from the performance calculations are known to be overestimated.

Calculations of local conditions on the flat plate are based upon the weak interaction principle⁽¹⁹⁾. The dynamic viscosity of the free stream is determined using the Sutherland Viscosity Law⁽²⁰⁾. The specific heat at constant pressure for the flow is calculated using the empirical curve fit data from the NENZEF predictive code⁽²¹⁾.

Comparison of measured heat transfer rates and laminar predictions confirms the heat transfer as a laminar boundary layer process (Fig. 9). Observed heat transfer rates are up to 25% lower than predicted values. This is consistent with an over prediction in the flow density suggested by the comparison of the pitot pressure levels. The heat transfer rate is proportional to the square root of the free stream density.

8. CONCLUSIONS

A number of high enthalpy quasi-steady test flow conditions using air and argon as the test gases have been established in the TQ expansion tube facility. Centreline pitot pressure and wall static pressure histories and centreline heat transfer rate histories, to a flat plate at zero incidence, confirm the existence of these quasi-steady flows.

Equilibrium approximate analytical relations which consider the real gas effects of ionisation and dissociation can be derived to model both the flow across the normal shocks and the unsteady expansion in the acceleration tube.

Calculations predict large levels of oxygen dissociation of up to 88% in the high enthalpy test conditions for air (48 MJ/kg), implying that 6% of the total free stream stagnation enthalpy is in the form of dissociation energy. This may be compared with a reflected shock tunnel for which, typically, 20% of a similar stagnation enthalpy would be in the form of dissociation energy. The low enthalpy conditions for air (9 MJ/kg) are free from dissociation. It is calculated that high enthalpy flows of argon (46 MJ/kg) are fully recombined by the unsteady expansion in the acceleration tube producing non-ionised flows.

Approximate estimates of the ideal performance of the unsteady expansion indicated velocities close to those which were measured. The loss of flow energy which did occur could be attributed to viscous attenuation and in the case of argon, radiation from the flow.

Static pressure levels measured directly fall slightly below those deduced from the observed shock speeds. Measured pitot pressures of as low as 50% of the levels deduced from the predicted flow conditions and the observed velocity indicate an over prediction of the flow density by ideal equilibrium theory. Deduction of the thermodynamic state of the test flow from direct measurements of velocity, static and pitot pressures remains the most reliable method of calculation. Steady heat transfer rates were established for the test conditions and measured rates were equal to or slightly less than laminar boundary layer predictions. These results indicate that expansion tubes can be used to generate hypersonic flows at speeds in excess of Earth orbital velocity.

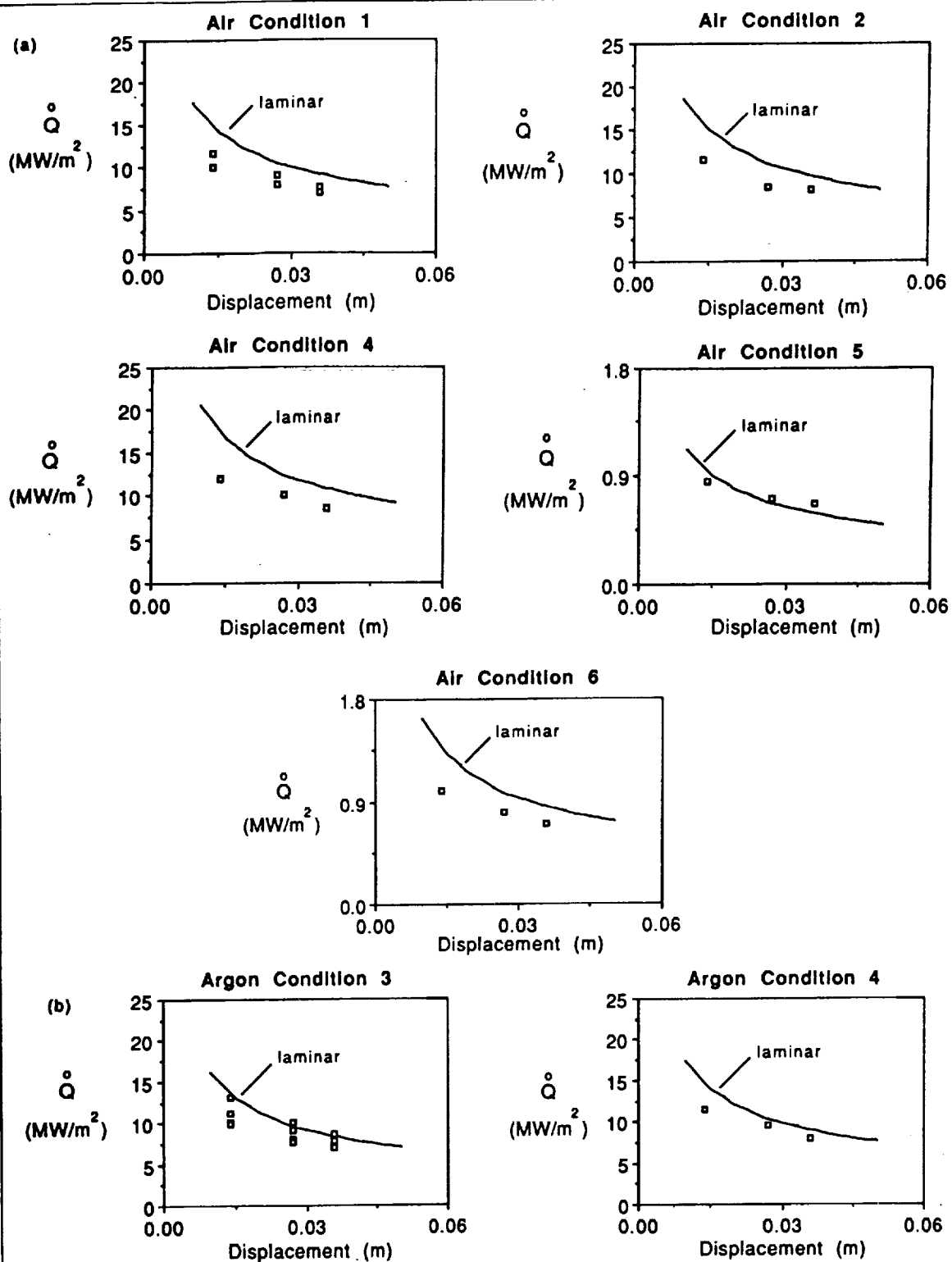


Figure 9. Comparison of observed flat plate heat transfer rates as a function of displacement from the leading edge, with empirical laminar predictions for (a) air conditions and (b) argon conditions.

ACKNOWLEDGEMENTS

The authors gratefully acknowledge the financial support provided through NASA grant NAGW-674, and by the Australian Research Council.

REFERENCES

1. STALKER, R. J. Hypervelocity aerodynamics with chemical nonequilibrium, *Ann Rev Fluid Mech*, 1989, 21, pp 37-60.
2. RESLER, E. L. and BLOXSOM, D. E. Very High Mach Number Flows By Unsteady Flow Principles, Cornell University Graduate School of Aeronautical Engineering, limited circulation monograph, January 1952.
3. TRIMPI, R. L. A Preliminary Theoretical Study of the Expansion Tube, A New Device For Producing High-Enthalpy Short-Duration Hypersonic Gas Flows, NASA Technical Report R-133, 1962.
4. JONES, J. J. Some performance characteristics of the LRC 3¼-inch pilot tube using an unheated hydrogen driver, Fourth Hypervelocity Techniques Symposium, Tullahoma, Tennessee, 1965, pp 7-26.
5. SPURK, J. H. Design, operation, and preliminary results of the BRL expansion tube, Fourth Hypervelocity Techniques Symposium, Tullahoma, Tennessee, 1965, pp 112-114.
6. NORFLEET, G. D., LACEY, J. J. and WHITFIELD, J. D. Results of an experimental investigation of the performance of an expansion tube, Fourth Hypervelocity Techniques Symposium, Tullahoma, Tennessee, 1965, pp 49-110.
7. MILLER, C. G. Operational Experience in the Langley Expansion Tube with Various Test Gases, NASA TM 78637, 1977.
8. STALKER, R. J., PAULL, A. and STRINGER, I. Experiments on an Expansion Tube with a Free Piston Driver—Phase 1, Department of Mechanical Engineering Report, The University of Queensland, 1987.
9. PAULL, A., STALKER, R. J. Experiments on an Expansion Tube with a Free Piston Driver—Phase 2, Department of Mechanical Engineering report, The University of Queensland, 1989.
10. PAULL, A. Theoretical Analysis of Test Conditions in an Expansion Tube, Department of Mechanical Engineering report, The University of Queensland, 1989.
11. PAULL, A. and STALKER, R. J. The effect on an acoustic wave as it traverses an unsteady expansion, *Phys Fluids A* (accepted for publication).
12. MOORE, J. A. Description and Initial Operating Performance of the Langley 6-inch Expansion Tube Using Heated Helium Driver Gas, NASA TM X-3240, 1975.
13. LIGHTHILL, M. J. Dynamics of a dissociating gas. Part I Equilibrium flow, *J Fluid Mech*, January 1957, 2, (1), pp 1-32.
14. STALKER, R. J. An Approximate Theory of Equilibrium One-Dimensional Steady And Unsteady Expanding Flows of an Ideal Dissociating Gas, N.R.C. MT-45, National Research Council of Canada, Ottawa, June 1961.
15. LOGAN, P. F., STALKER, R. J. and MCINTOSH, M. K. A shock tube study of radiative energy loss from an argon plasma, *J Phys D: Appl Phys*, 1977, 10, pp 323-337.
16. SCHULTZ, D. L. and JONES, T. V. Heat Transfer Measurements In Short Duration Hypersonic Facilities, AGARDograph No. 165, February 1973.
17. MORGAN, R. G. and STALKER, R. J. Shock tunnel measurements of heat transfer in a model scramjet, *J Spacecraft Rockets*, Sept-Oct 1986, 23, (5), pp 470-475.
18. ECKERT, E. R. G. Engineering relations for friction and heat transfer to surfaces in high velocity flow, August 1955, *J Aeronaut Sci*, pp 585-587.
19. COX, R. N. and CRABTREE, L. F. *Elements of Hypersonic Aerodynamics*, English Universities Press, London, 1965.
20. WHITE, F. M. *Viscous Fluid Flow*, McGraw-Hill, New York, 1974.
21. LORDI, J. A., MATES, R. E. and MOSELLE, J. R. Computer Program for the Numerical Solution of Nonequilibrium Expansions of Reacting Gas Mixtures, NASA, CR 472, 1966.

TEST FLOW DISTURBANCES IN AN EXPANSION TUBE

A. Paull and R. J. Stalker

Mechanical Engineering Department
University of Queensland, Australia

Abstract

The operation of an expansion tube is investigated with particular attention to the test flow disturbances which have limited their utility in the past. New theoretical bounds are obtained for the duration of uniform test flow and are seen to be in good agreement with data derived from centreline pitot pressure measurements. The test flow durations are predicted by using conventional one-dimensional ideal gas relations across shocks and unsteady expansions, together with shock tube boundary layer entrainment effects. It is found that high frequency flow disturbances in the driver gas can penetrate the shock tube driver-gas interface when the driver gas Mach number is less than that in the test gas and that these disturbances then are manifested in the expansion tube test flow. Results from three different facilities are shown to display frequency focusing - the effect on acoustic waves produced by an unsteady expansion.

1. Introduction

An expansion tube is an impulse hypersonic facility which can produce high enthalpy quasi-steady flows. An expansion tube's central advantages over the more widely used reflected shock tunnel are substantial gains in both stagnation enthalpy and effective stagnation pressure and a decrease in dissociation levels due to a decrease in chemical freezing. These advantages are obtained because the expansion tube accelerates the test gas through an unsteady expansion, whereas the reflected shock tunnel utilizes a supersonic nozzle which produces a steady expansion of gases from conditions of high temperature and pressure.

A number of expansion tube have been built, however most have since been discarded as only a narrow window of test conditions for each test gas was ever obtained. This is contrary to prior theoretical results (Trimpi (1962)) which indicate that a large variety of test conditions are available.

The new analysis presented here explains the discrepancy between Trimpi's theoretical maximum test time and the observed test times. This analysis explains why the window of steady test conditions is small and indicates how this window can be widened so as these facilities could be used for a variety of hypersonic research. In addition to the theoretical results, centreline pitot pressure measurements for an air test gas are also

presented.

2. General Theory

An expansion tube consists of three consecutive sections; the compression, the shock tube and the acceleration tube (see Figure 1). The acceleration tube empties unrestrictively into a dump tank-test section. Initially the three sections are separated by two diaphragms. The heavier of these is the primary diaphragm which resides between the compression and shock tubes while the shock and acceleration tubes are initially separated by the secondary diaphragm. Ideally the secondary diaphragm is massless. The three regions are initially filled with the driver, test and acceleration gases, respectively.

Figure 1 incorporates a free piston driver (Stalker 1966) which is used to increase the driver gas pressure sufficiently to rupture the primary diaphragm. This produces a shock which travels through the test gas towards the secondary diaphragm. It is assumed that the shock ruptures the secondary diaphragm without reflecting, instantaneously accelerates, then travels down the acceleration tube with constant velocity. The test gas follows the shock and accelerates through an unsteady expansion centred at the secondary diaphragm. The test time is the period of steady flow following the arrival of the test-acceleration gas interface at the test section. (See Figure 2).

There are two distinct ranges of flow conditions in which different mechanisms limit the test time. These flow regimes will be referred to as the high enthalpy conditions and the low enthalpy conditions. To a good approximation, the high and low enthalpy conditions are respectively generated when the driver gas sound speed is less than and greater than the test gas sound speed.

At high enthalpy conditions the test time is predicted using ideal one-dimensional gas dynamics as used by Trimpi (1962). Trimpi's analysis assumes the test time is limited by the arrival at the test section of the unsteady expansion generated when the secondary diaphragm ruptures. It can be seen from Figure 2 that this is only correct if the acceleration tube is sufficiently short so that the reflection of the unsteady expansion off the driver-test gas interface arrives at the test section after the downstream edge of the unsteady expansion. Trimpi's analysis assumes the location of the driver-test gas interface can be predicted using inviscid one-dimensional gas theory. If this assumption were correct this interface would be sufficiently upstream so that the

reflection of the unsteady expansion would not normally limit the test time. However, Mirels (1964) has shown that the boundary layer entrains mass and acts like a mass sink. This significantly decreases the distance between the shock and the interface in the shock tube. Hence, the unsteady expansion produced when the secondary diaphragm ruptures can reflect off the driver-test gas interface and arrive at the test section before the unsteady expansion's downstream edge. The analysis presented here predicts the location of the driver-test gas interface using Mirels' theory and then analytically determines the trajectory of the leading edge of the reflected expansion.

At low enthalpy conditions and during the steady test period predicted by the above analysis the observed flow can still be unacceptably noisy. It is argued here that the dominant part of this noise can be modelled as acoustic lateral waves which are generated in the driver gas. These are transmitted through the driver-test gas interface into the test gas before the secondary diaphragm ruptures. It is important to recognize that the mechanisms for generating this noise are also present for the high enthalpy conditions. The noise is not transmitted through the interface at the high enthalpy conditions because the test gas sound speed is greater than the driver gas sound speed. For this mismatch of sound speeds it will be shown that the interface acts as a low frequency filter and totally reflects low frequency lateral waves.

All noise sources observed in the driver gas have not been positively identified, however, it will be shown that a significant portion can be attributed to noise generated in the primary diaphragm rupturing process. Furthermore, the filtering of the diaphragm noise is sufficient to produce acceptable test conditions.

A further process which disrupts the test time is produced when the unsteady expansion centred at the secondary diaphragm produces a large drop in the sound speed of the test gas. It has been shown by Paull and Stalker (1991) that all frequency components of noise transmitted through the expansion will be "focused" into a narrow bandwidth of frequencies. This results in a pronounced disturbance downstream of the expansion and thus, the test flow is rendered useless. Frequency focusing is discussed here in more detail and in the context of the more general theory.

3 High Enthalpy Conditions

At high enthalpy conditions the test time will be limited by either the downstream edge of the unsteady expansion centred at the secondary

diaphragm rupture time or the downstream edge of the reflection of the upstream edge of this expansion off the driver-test gas interface. The theoretical test time is obtained by assuming the flow is one-dimensional ideal and inviscid in all calculations except that which determines the location of the driver-test gas interface. This is obtained using Mirels' (1964) ideal gas theory for boundary layer entrainment.

For a one-dimensional ideal inviscid gas

$$u \pm \frac{2}{\gamma-1} a = \text{const.}, \quad (3.1\pm)$$

along the characteristics

$$\frac{dx}{dt} = u \pm a, \quad (3.2)$$

where u is the gas velocity, a is the local sound speed and γ is the specific heat ratio. It follows (Whitham (1974)) that within a centred unsteady expansion

$$u = \frac{\gamma-1}{\gamma+1} u_3 + \frac{2}{\gamma+1} \left(a_3 + \frac{x}{t} \right), \quad (3.3)$$

and

$$a = \frac{2}{\gamma+1} a_3 + \frac{\gamma-1}{\gamma+1} \left(u_3 - \frac{x}{t} \right), \quad (3.4)$$

where subscript 3 refers to the conditions upstream of the expansion (see Figure 2). The origin of the (x,t) space is at the rupture of the secondary diaphragm.

3.1. Test time bounds

If the test time is limited by the downstream edge of the unsteady expansion then the test time, T , is the time elapsed between the arrival of the test-acceleration gas interface and this edge. This interface and edge have velocities u_5 and $u_5 - a_5$ respectively, where subscript 5 refers to the test gas conditions downstream of the expansion. Hence, the test time is

$$T = \frac{x_A a_5}{u_5(u_5 - a_5)}, \quad (3.5)$$

where x_A is the length of the acceleration tube.

If the test time is limited by the reflected expansion then the test time is determined analytically as a function of the elapse time, t_0 , between rupture of the secondary diaphragm and arrival of the driver-test gas interface at the upstream edge of the unsteady expansion. Within the expansion the characteristic curve which marks the downstream edge of the reflected expansion is obtained analytically from integration of (3.1^{*}) with u and a given by (3.3) and (3.4), respectively. The intersection of this trajectory and the trajectory of the expansion's downstream edge determines the time for the reflected expansion's downstream edge to emerge from the expansion. The time elapsed between this event and rupturing of the secondary diaphragm is

$$t_1 = t_0 \left(\frac{a_5}{a_3} \right)^{\frac{\gamma+1}{2(1-\gamma)}}. \quad (3.6)$$

The reflected expansion's downstream edge then travels in the uniform flow ahead of the expansion with constant velocity $u_5 + a_5$ until it reaches the test section or the test-acceleration interface. In the latter case there is no test time, otherwise the test time is

$$T = \frac{a_5}{u_5 + a_5} \left(2t_1 - \frac{x_A}{u_5} \right). \quad (3.7)$$

It can be seen from (3.1^{*}), which relates conditions either side of the expansion, (3.6) and (3.7) that the nondimensional test time T/t_0 is a function of the sound speed ratio a_5/a_3 and the nondimensional acceleration tube length $X = x_A/(a_3 t_0)$. The nondimensional acceleration tube length is the ratio of acceleration tube length to the effective inviscid test gas slug length in the shock tube when the secondary diaphragm ruptures. For strong shocks it follows that this nondimensional test time is a function of the shock speed ratio U_{sa}/U_s and the nondimensional acceleration tube length, where U_{sa} and U_s are the shock speeds in the acceleration and shock tubes respectively.

Figure 3 displays the nondimensional test time as a function of shock speed ratio for different nondimensional acceleration tube lengths for a specific heat ratio of 1.4. In the regions where the test time is monotonically increasing the test time is limited by the downstream edge of the unsteady expansion and is determined from (3.5). When the test time is monotonically decreasing the test time is limited by the reflected unsteady expansion and is determined from (3.6) and (3.7).

It can be seen that the reflected expansion severely limits the test time and the conditions at which an expansion tube can be practically operated.

3.2. Maximum test time

From inspection of Figures 2 and 3 it can be seen that the maximum test time available for a given acceleration tube length is obtained when the reflected expansion and the unsteady expansion arrive at the test section simultaneously. The maximum test time is indicated by the dotted line in Figure 3. By equating (3.5) and (3.7) it can be shown that the maximum test time is

$$T_m = \frac{t_0}{M_5} \left(\frac{a_2}{a_5} \right)^{\frac{\gamma+1}{2(\gamma-1)}} \quad (3.8)$$

where $M_5 = u_5/a_5$ is the local Mach number of the test gas. From the substitution of (3.8) for T in (3.5) it follows that this maximum test time is achieved if the nondimensional length of the acceleration tube is

$$X = (M_5 - 1) \left(\frac{a_2}{a_5} \right)^{\frac{3-\gamma}{2(\gamma-1)}} \quad (3.9)$$

Hence, to obtain the maximum test time, the filling pressures and acceleration tube length must be chosen so that (3.9) is satisfied.

3.3. Boundary layer entrainment

In all the experiments reported here Mirels' (1964) turbulent boundary layer analysis for an ideal gas and strong shocks has been used to determine the location and velocity of the driver-test gas interface. This analysis indicates that a turbulent boundary layer theory is required if $P_4 r_0 > 0.085$ m.kPa (where r_0 is the tube radius). In the experiments reported here $P_4 r_0 > 0.062$ m.kPa. Hence, although some experiments are in the transitional region the majority should have turbulent boundary layers.

The elapse time t_0 between rupture of the secondary diaphragm and the arrival of the interface at the unsteady expansion head is determined by assuming that the interface travels with constant velocity u_1 after the diaphragm ruptures. The position of the unsteady expansion head is obtained as a function of time from the characteristic equation (3.1').

It is assumed that after the diaphragm ruptures the gas velocity between the shock and the interface varies linearly with distance. This approximation is made to obtain a simple analytical relationship between t_0 and the properties of the gas behind the shock. A more accurate method would be to use the gas velocity provided by Mirels (1964). For this linear approximation the gas velocity encountered by the expansion head is

$$u = \frac{u_1 - u_{30}}{l}(x_1 - x) + u_1, \quad (3.10)$$

where l is the separation of the shock and interface when the diaphragm ruptures, x_1 is the position of the interface relative to an origin located at the diaphragm and u_{30} is the gas velocity immediately after the primary shock. The positive x -direction is in the flow direction. If the interface travels with constant velocity then

$$x_1 = u_1 t - l. \quad (3.11)$$

The substitution of (3.11) into (3.10) gives the gas velocity upstream of the expansion as a function of position and time. If it is also assumed that the sound speed is constant and equal to a_3 then an estimate of the trajectory of the unsteady expansion's upstream edge is obtained from the integration of the characteristic equation (3.1) with the velocity given by (3.10). The intersection of this curve and the straight line (3.11) gives an elapse time t_0 of

$$t_0 = \frac{1}{u_1 - u_{30}} \ln \left(\frac{a_3 + u_1 - u_{30}}{a_3} \right). \quad (3.12)$$

3.4. Interface detection

In section 7 the location of the interface has to be determined from pitot pressure measurements. Since there is a change in Mach number across the interface there should, theoretically, be a change in the pitot pressure measurement at the interface. This is indeed observed, however, in addition, under certain conditions the mixing of the driver and test gases can produce at the interface a region of low density gas (Levine (1970)). This region would produce a dip in the pitot pressure record.

In section 7 the interface was identified by first making a theoretical

prediction using Mirels' (1964) analysis. Then a dip and or a step change in the pitot pressure was sought near this predicted location.

4. Acoustic Wave Theory.

The noise observed in the flow at low enthalpy conditions is assumed to be small perturbations of both velocity and pressure about a steady mean. Whitham (1972) shows that the velocity and pressure can be written as

$$\underline{u} = \underline{u}_0 + \nabla\phi, \quad (4.1)$$

and

$$p = p_0 - \rho_0 \frac{\partial\phi}{\partial t}, \quad (4.2)$$

respectively, where the potential function ϕ is a solution to the wave equation, \underline{u}_0 , p_0 and ρ_0 are the unperturbed velocity, pressure and density respectively and t is time.

It will be assumed that the noise observed experimentally has properties consistent with those potential functions which are only dependent on time, radial distance, r , and axial distance, x . These functions have the form

$$\phi = J_0(\lambda r) \exp(i\omega(t \pm \beta x/a)), \quad (4.3)$$

where J_0 is the zero th. order Bessel function of the first kind, a is the local sound speed, ω is the fundamental frequency and the dispersive term is

$$\beta = \left[1 - (\lambda a/\omega)^2 \right]^{1/2}. \quad (4.4)$$

The spatial origin is fixed in a frame in which the gas is at rest. The permissible values of λ are obtained by imposing the no-penetration boundary condition,

$$\frac{\partial\phi}{\partial r}(r_0, t) = 0. \quad (4.5)$$

It follows that λr_0 is equal to any of the infinite number of discrete zeros of the first order Bessel function of the first kind, J_1 . The first zero of J_1 occurs when λr_0 equals zero. $J_0(0)=1$, hence, from (4.3) this solution is radially independent. Solutions of this form are called longitudinal waves. All other solutions are radially dependent and will

be referred to as lateral waves.

4.1. Doppler shifts

It is assumed in (4.3) that x has its origin fixed in a frame in which the unperturbed gas is at rest. However, in a laboratory the unperturbed gas is in motion relative to the observer. Thus, a Doppler shift in the frequency is observed.

If the unperturbed gas moves with a velocity u relative to the laboratory then, by using the exponent in (4.3), it can be shown that the frequency observed in the laboratory would be

$$\nu = \omega (1 \mp u\beta/a) / 2\pi. \quad (4.6)$$

In the case of a longitudinal wave ($\beta=1$) the Doppler shift is only dependent upon the local Mach number u/a . In contrast, the form of β ensures that the Doppler shift for lateral waves is dependent on both the sound speed and gas velocity independently.

When an acoustic wave encounters an unsteady expansion solutions of the form (4.3) are not directly applicable in the expansion because the unperturbed state is not steady. However, these acoustic wave solutions can be used to determine the shift in frequency which would be observed as the acoustic wave traverses the expansion. Following the approach used by Godunov (1959) the expansion is divided along the characteristic lines into discrete steady regions and acoustic theory is applied within these regions. Between these regions there is a discontinuity in both sound speed and gas velocity. Furthermore, the discontinuity itself has a velocity which is different to both the gas velocities of its adjacent regions.

The shift in frequency across the expansion is obtained by first determining the frequency shift across an interface separating two steady regions, subscripted 1 and 2, which have different sound speeds and gas velocities. The interface has a velocity different to the gas velocities in both regions. An acoustic wave described by (4.3) is incident in region 1 and is transmitted through the interface into region 2.

The interface is a boundary for region 2 upon which conditions are imposed which uniquely determine the solution to the wave equation in region 2. In the case when there is no discontinuity in the gas velocities and the interface is fixed relative to the gas it can be seen by equating the time coefficients in the exponent of (4.3) from either

side of the interface that the fundamental frequency is the same in both regions. However, in the more complex situation where there is a discontinuity in the gas velocity this is not the case. The interface is the boundary which drives the solution in region 2, hence, the fundamental frequency in region 2 must be chosen so that it is equal to the frequency which is observed at the interface. That is to say, the frequency as observed in the frame of the interface shall be continuous across the interface. Hence, from (4.6) the fundamental frequencies either side of the interface are related by

$$\omega_1 (1 + (u_1 - v)\beta_1/a_1) = \omega_2 (1 + (u_2 - v)\beta_2/a_2), \quad (4.7)$$

where v is the interface velocity.

In the case of the unsteady expansion the interface is a characteristic which separates two regions subscripted i and $i+1$. $i=0$ refers to the steady region upstream of the expansion. The characteristic is propagating upstream and therefore has velocity $u_i - a_i$, hence, from (4.7) the fundamental frequencies are related by

$$\omega_i (1 + \beta_i) = \omega_{i+1} (1 + (u_{i+1} - u_i + a_i)\beta_{i+1}/a_{i+1}) . \quad (4.8)$$

The sound speeds and gas velocities of the two regions are related by (3.1'). Eliminating the velocity terms in (4.8) it follows that

$$\omega_i (1 + \beta_i) = \omega_{i+1} \left(1 + \left(1 - \frac{\gamma+1}{\gamma-1} \frac{da_i}{a_{i+1}} \right) \beta_{i+1} \right) . \quad (4.9)$$

where $da_i = a_{i+1} - a_i$. The limit in which the number of discrete steady regions approach infinity and the discontinuities approach zero is then taken. The relationship obtained from (4.4) between the infinitesimal change in the fundamental frequency and the infinitesimal changes in the dispersive term and the sound speed is then used to develop an integral relationship between the sound speed and the dispersive term within the expansion. This relationship can be integrated to give

$$\frac{\beta - (\gamma-1)/2}{\beta - 1} = \frac{\beta_0 - (\gamma-1)/2}{\beta_0 - 1} \left(\frac{a}{a_0} \right)^{(3-\gamma)/(\gamma-1)} . \quad (4.10)$$

Figure 4 plots the dispersive term as a function of the sound speed for different values of β_0 . It can be seen that in the limit as the sound

speed approaches zero β approaches $(\gamma-1)/2$ independent of β_0 . It could be said that the frequencies are "focused" by the unsteady expansion. From (4.4) and (4.6) in the laboratory frame of reference the focus frequency is

$$\nu = \frac{\lambda(a + (\gamma-1)u/2)}{2\pi(1-((\gamma-1)/2)^2)^{1/2}} \quad (4.11)$$

From (3.1') it can be seen that this frequency is only dependent upon the steady state conditions upstream of the expansion, the lateral wave mode and the specific heat ratio.

If all components of noise described by (4.3) were to traverse an unsteady expansion across which the sound speed dropped sufficiently, then at the downstream end of the expansion discrete narrow bands of frequencies corresponding to different modes should be observed.

Focusing of the dispersive term across an unsteady expansion occurs because both the sound speed decreases and the gas velocity increases.

If an interface is stationary with respect to the gas either side and a decrease in the sound speed is the only physical quantity to change across the interface then from (4.4) the value of the dispersive term must increase. However, if a velocity increase is the only change across the interface then the equality (4.7) is preserved by a decrease in the value of the dispersive term (and therefore the fundamental frequency).

Within an unsteady expansion where both the velocity and sound speed change, the fundamental frequency shift derived from (4.7) is dependent upon a velocity change which is multiplied by the dispersive term. Hence, if the dispersive term is small, the change in the velocity is less significant and therefore the value of the dispersive term is driven by the change in sound speed. Therefore, it increases. In contrast if the dispersive term is sufficiently large so that the velocity change drives the change in the dispersive term then the dispersive term decreases. The net result is that the values of the dispersive term converge to one value.

4.2. Reflection and transmission coefficients

It will become apparent that the sound speeds either side of the driver-test gas interface plays a major role in determining the amplitude of the noise transmitted into the test gas.

If the sound speed changes across an interface between two mediums then

an acoustic wave approaching the interface will be both reflected and transmitted. If the interface is stationary relative to the two mediums the fundamental frequencies of the incident, reflected and transmitted waves are the same.

In the case of a longitudinal wave the reflection and transmission coefficients are obtained by assuming the velocity and pressure are continuous across the interface. From (4.1) and (4.2) the reflection and transmission coefficients are

$$C_R = \frac{\beta_1 a_1 \gamma_2 - \beta_2 a_2 \gamma_1}{\beta_1 a_1 \gamma_2 + \beta_2 a_2 \gamma_1}, \quad (4.12)$$

and

$$C_T = 2 \frac{a_2}{a_1} \frac{\beta_1 a_2 \gamma_1}{\beta_1 a_1 \gamma_2 + \beta_2 a_2 \gamma_1}, \quad (4.13)$$

respectively, where β_1 and β_2 equal one and subscripts 1 and 2 refer to the medium in which the wave is incident and transmitted respectively. In the case of a lateral wave it can be seen from (4.1) that there are two nonzero velocity components. It is impossible to collectively satisfy continuity across the interface of both velocity components and the pressure. To overcome this dilemma and to be consistent with the boundary condition (4.5) it will be assumed that slip can occur at the interface so that the axial velocity is the only component which is continuous across the interface. If the sound speed of the medium into which the wave is transmitted is less than ω/λ , so that β_2 is real, it can be shown as above that the reflection and transmission coefficients are (4.12) and (4.13) respectively. However, if the sound speed of the medium into which the wave is transmitted is sufficiently large so that a_2 is greater than ω/λ then β_2 is imaginary and exponential decay of the transmitted solution occurs. In this case the transmission coefficient (which determines the amplitude of the transmitted wave at the interface) is

$$C_T = 2 \frac{a_2}{a_1} \frac{\beta_1 a_2 \gamma_1}{\left[(\beta_1 a_1 \gamma_2)^2 - (\beta_2 a_2 \gamma_1)^2 \right]^{1/2}}, \quad (4.14)$$

and the reflection coefficient is one. Figures 5 and 6 are the transmission and reflection coefficients as functions of sound speed

ratio across the interface for different values of the incident wave dispersive term. In Figure 5 it can be seen that the transmission coefficient has a cusp for each value of the incident dispersive term. If the sound speed ratio is greater than that at the cusp the transmitted wave decays and the transmission coefficient is given by (4.14). For sound speed ratios less than that at the cusp the transmitted wave does not decay and the transmission coefficient is given by (4.13). Experimentally it is important to know the lowest frequency which does not decay when transmitted into a medium with a higher sound speed. The lowest frequency is that for which β_2 equals zero. From (4.4), β_2 equals zero if ω equals λa_2 . The substitution of this value of the fundamental frequency into (4.4) gives the value of the corresponding incident dispersive term,

$$\beta_1 = \left(1 - \left(\frac{a_1}{a_2} \right)^2 \right)^{\frac{1}{2}}. \quad (4.15)$$

Experimentally the media move relative to the laboratory. If, relative to the laboratory, ν_L is the frequency measured in the incident medium which corresponds to the lowest frequency that is unattenuated, then from the substitution of (4.15) into (4.6) with the fundamental frequency determined from (4.4) it follows that

$$\frac{\nu_0}{\nu_L} = \frac{M_2}{M_1} \left(1 \mp M_1 \left(1 - \left(\frac{M_2}{M_1} \right)^2 \right)^{\frac{1}{2}} \right)^{-1}, \quad (4.16)$$

where

$$\nu_0 = \frac{\lambda a_1}{2\pi}, \quad (4.17)$$

is the lowest frequency which can be observed from the laboratory in the incident medium. $M_1 = u_1/a_1$ and $M_2 = u_2/a_2$ are the local Mach numbers of the two media relative to the laboratory. Figure 7 displays the ratio ν_0/ν_L as a function of the Mach number ratio across the interface for different values of M_1 for waves travelling in the flow direction, (4.16⁺). In the experiments considered here the frequencies of the waves travelling upstream are too small to be considered as disruptive to the flow.

5. Driver Gas Calculations

The analysis of section 7 requires knowledge of the driver-gas sound

speed. In some experiments the centreline pitot pressure, static pressure P_s , and shock speed, U_s , were measured. In these cases Rayleigh's pitot pressure formula (Liepmann and Roshko (1967))

$$P_T = P_s M^2 \left(\frac{\gamma+1}{2} \right)^{\frac{\gamma+1}{\gamma-1}} \left(\gamma - \frac{\gamma-1}{2} M^{-2} \right)^{\frac{1}{1-\gamma}}, \quad (5.1)$$

is used to determine the local Mach number, M , of the driver gas. The driver gas sound speed is obtained from this Mach number by assuming the driver gas velocity is equal to the test gas velocity, which is determined from real gas calculations (McIntosh (1968)) based on the measured shock speed.

Where these measurements were not available it will be assumed that the mechanism through which the driver gas is accelerated is as follows.

The driver-gas is compressed adiabatically in the compression tube by the free piston until the primary diaphragm ruptures. At this time the driver gas is assumed to be at rest. The cross-sectional area ratio of the compression tube is 7.2 times greater than the shock tube. Hence, it is assumed that the driver gas then undergoes a steady subsonic expansion to the entrance of the shock tube where the flow is assumed to be sonic. This point will be defined as the throat. From the throat the driver gas accelerates through an unsteady expansion to the velocity deduced from the measured shock speed. In all calculations the driver gas is assumed to be perfect.

If P_0 and a_0 are the driver gas pressure and sound speed before compression then

$$a_1 = a_0 \left(\frac{P_1}{P_0} \right)^{\frac{\gamma-1}{2\gamma}}, \quad (5.2)$$

where P_1 and a_1 are the pressure and sound speed in the compression tube when the primary diaphragm ruptures. (See Figure 2). For a large area ratio between compression and shock tubes the sound speed at the throat is approximately

$$a_t = \left(\frac{2}{\gamma+1} \right)^{\frac{1}{2}} a_1. \quad (5.3)$$

The driver gas sound speed in the shock tube is related to the sound speed at the throat by (3.1+). As the flow at the throat is sonic it then follows that

$$a_2 = \frac{\gamma+1}{2} a_t - \frac{\gamma-1}{2} u_2 . \quad (5.4)$$

6. Test Time Limitations at High Enthalpies.

From Figure 3 it can be seen that for sufficiently large acceleration tube shock speeds the test time is limited by the the leading edge of the unsteady expansion. If the conditions in the shock tube are unchanged and the acceleration tube shock speed is decreased then the test time should increase to its maximum. With a further decrease in acceleration tube shock speed the test time should decrease to zero as it is terminated by the reflection of the unsteady expansion off the driver-test gas interface. Figures 8A-8D are centreline pitot pressure records which display these phenomena. The shock tube length, x_s , was 2.08 m and the acceleration tube length was 3.18 m. The driver gas was argon. It was compressed from 120 kPa to the primary diaphragm rupture pressure of 34.5 MPa. The test and acceleration gases were air. The shock tube filling pressure was 3.4 ± 0.15 kPa and the shock tube shock speed was 2400 ± 200 m/s. The acceleration tube filling pressure was varied between 5.4 ± 1 Pa and 66 ± 1 Pa which produced a variation in acceleration tube shock speed between 4400 m/s and 3700 m/s respectively. The theoretical locations of the downstream edge of the expansion and its reflection off the driver-test gas interface are marked with the letters "E" and "R" respectively. Figure 9 displays the predicted test time as a function of acceleration tube filling pressure for the above shock tube conditions. On this figure is also placed the measured values of the test time taken from Figures 8A-8D. It can be seen that there is good agreement between prediction and measurement. In Figure 8A the expansion limits the test time. The predicted test time in this case is not as good as in Figures 8B-8D where it is limited by the reflected expansion. However, by inspection of Figure 9, when the test time is limited by the expansion a small error in the acceleration tube filling pressure will produce a large variation in the test time.

7. Acoustic Wave Results

In this section experiments are presented which show that the oscillatory noise which is detrimental to the expansion tube test flow can be modelled as first order lateral acoustic waves, a large proportion of which are generated in the driver gas.

Initially the secondary diaphragm was removed so that the expansion tube was simply a shock tube. The exit centreline pitot pressure and exit wall pressure were measured (see Figures 10A and 10B) along with the times at which the shock arrived at different locations along the tube. This experiment was done to measure the spectral decomposition of the noise in the driver gas. The results of these experiments are then used to predict the attenuation of the noise which would occur in the expansion tube.

7.1 Validation of Mach number predictions

To predict the attenuation of the noise transmitted into the test gas it is essential to know the Mach numbers and velocities of both test and driver gases. The Mach number of the test gas is obtained from real gas calculations based on shock speed and shock tube filling pressure, however, the Mach number of the driver gas must be determined from pitot and static pressure measurements using Rayleigh's pitot pressure formula. The accuracy of this method is established by comparing the real gas predicted Mach number with that determined from the wall and pitot pressure measurements made in the test gas.

The driver gas was helium and was compressed from 130 kPa to 34.5 MPa at which point the primary diaphragm ruptured. The shock tube was filled with air to 2.66 kPa. Figures 10A and 10B respectively display the pitot and static pressures as a function of time. The shock speed measured over the last 350mm of the shock tube was 4000 m/s.

Real gas calculations predict that the velocity of the test gas following the shock is 3600 m/s, the Mach number is 2.7, the static pressure is 450 kPa and the equilibrium specific heat ratio is 1.22. The location of the driver-test gas interface was determined as in section 3.4 and is concluded to be coincident with the large dip in the pitot pressure 43 μ s after the shock. The pitot and static pressures measured between 14 μ s and 40 μ s after the shock are 4133 ± 300 kPa and 473 ± 30 kPa respectively. Using these measured pressures and a specific heat ratio of 1.22, Rayleigh's pitot pressure formula (5.1) predicts a Mach number of 2.66 ± 0.18 , which is in good agreement with the theoretical value of 2.7.

7.2. Driver gas flow properties

In section 7.3 the gas speed and local Mach number are required in the relatively steady period between 200 and 456 μ s after the shock. In addition, an estimate of the sound speed at the throat is needed.

The average pitot and wall pressures in the period between 200 and 456 μ s after the shock are 3780 kPa and 720 kPa, respectively. Hence, from (5.1) the average local Mach number is 1.80.

The gas velocity over this period is deduced from (3.1⁺), the shock speed and the driver gas local Mach number at the interface. From the previous section the test gas velocity is 3600 m/s. This is assumed to be equal to the driver gas velocity at the interface. Clear of the interface transients (80 μ s after the shock) the unperturbed (or average) driver gas pitot and wall pressures are 4037 kPa and 494 kPa, respectively. Hence, from (5.1) with $\gamma=5/3$ the unperturbed local Mach number of the driver gas at the interface is 2.29.

From Figure 10B it can be seen that there exists a compression in the driver gas starting at the interface. This disturbance is possibly caused by the acceleration of the driver-test gas interface. Whatever its cause may be, it will be assumed that the sound speed and gas velocity can be related throughout the disturbance by (3.1⁺). It therefore follows from the velocity at the interface and the above local Mach number predictions that in the period between 200 and 456 μ s after the shock the unperturbed gas speed is 3120 m/s.

The driver gas sound speed at the throat can be obtained by two independent methods. Either the compression tube filling pressure and the primary diaphragm rupture pressure can be used to predict the throat sound speed from (5.2) and (5.3) or the sound speed and gas velocity at the interface can be used in conjunction with (5.4) to determine what the throat sound speed must be for the driver gas to have these properties.

The measured values of compression tube filling pressure, P_0 , and the primary diaphragm rupture pressure P_1 are 130 kPa and 34.5 Mpa respectively, hence, if the driver gas sound speed before compression, a_0 , is assumed to be 1008 m/s then from (5.2) and (5.3) the driver gas sound speed at the throat should be 2665 m/s. The velocity and Mach number at the interface are 3600 m/s and 2.29, respectively, hence, by (5.4) the sound speed at the throat is required to be 2079 m/s. The source of this discrepancy is not known, however, it is conceivable that the compression in the free piston driver is non-adiabatic. Notwithstanding it will be assumed that the value deduced from the shock speed measurement, 2080 m/s, is the better estimate.

7.3. Noise spectral decomposition and source.

A spectral decomposition of the pitot pressure driver gas noise was taken

between 200 μ s and 456 μ s after the shock and is displayed in Figure 11. This region was chosen as the unperturbed wall pressure is reasonably steady.

It can be seen that the spectrum has maxima in the ranges 0-5 kHz, 50-70 kHz and 74-120 kHz. The noise which is detrimental to the flow quality is the 50 kHz and above components.

From the flow properties deduced in the previous section it can be shown from (4.4) and (4.6) with $\beta=0$ that first order lateral wave exists at frequencies greater than 55 kHz. Thus it is possible for the majority of the detrimental noise to be first order lateral waves.

The origin of the noise is also of interest. One obvious source of noise is when the primary diaphragm ruptures. If acoustic waves generated at the throat are transmitted through the unsteady expansion centred at this diaphragm then as shown in section 4.1 every frequency of each acoustic wave mode would approach the frequency (4.11) where λ is determined by the mode. Hence, for a velocity of 3120 m/s and a Mach number of 1.8 the first order lateral waves should approach 94.2 kHz.

However, the focusing effect of the unsteady expansion centred at the throat is weak because the sound speed ratio across the expansion is 0.83. Furthermore, for a monotonic gas the power to which this ratio is raised in (4.10) is only two. Therefore a band of frequencies would be expected after the unsteady expansion.

If the lowest frequency first order lateral wave ($\beta=0$) was excited at the throat then downstream of the expansion this component can be shown from (4.4) and (4.6) to have a frequency of 70 kHz and this would be the lowest frequency in the band.

It can be seen in Figure 11 that the 74-120 kHz range has a definite peak between 90 kHz and 94 kHz which would be consistent with weak focusing of first order lateral waves originating at the throat. Furthermore, the lowest frequency of this range is also consistent with being produced at the throat. Hence, it is concluded that this part of the spectrum is first order lateral waves which in the main originate at the throat.

The origin of the 50-70 kHz components are not known. However, it will be seen in the next section that in the experiments reported here they do not govern the bounds for acceptable test conditions.

7.4. Driver-test gas interface; Helium driver

In section 4.2 it was seen that a lateral wave incident upon the driver-test gas interface will be attenuated in the test gas if the local

Mach number of the test gas is sufficiently less than that of the driver gas. Due to the relatively short test gas slug length it is difficult to see from shock tube pitot pressure results whether or not the noise observed in the driver gas is transmitted into the test gas. However, the effect of the interface can be seen in expansion tube results where the test gas slug has been expanded.

Figure 12 displays the expansion tube centreline pitot pressure records for different shock tube filling pressures. Table 1 tabulates the driver and test gas flow properties in the shock tube either side of the driver-test gas interface.

The test gas sound speed and velocity were obtained from real gas calculations based on the measured shock speed. The test gas velocity was assumed to be equal to the driver gas velocity at the interface. The driver gas sound speed was then determined from (5.4) where the throat sound speed was assumed to be 2080 m/s. From Table 1 it can be seen that the lateral wave disturbances should be attenuated at the two higher shock speeds and no attenuation should occur for the smallest shock speed. Furthermore, from Figure 7, for a driver gas Mach number of approximately three, the test gas Mach number need be only 2% less to attenuate frequencies twice as high as the lowest frequency lateral wave ν_0 . Hence, from Figure 12, as $\nu_0=55$ kHz, a 2% decrease in local Mach number would attenuate the majority of the noise produced in the driver gas.

This is displayed in Figures 12A and 12B where there is respectively a 36% and 18% decrease in local Mach number and there is only minimal noise in the test time. It can be seen in Figure 12C where the test gas local Mach number is greater than the driver gas local Mach number that significant noise disrupts the flow.

7.5. Test-acceleration gas interface.

The results of the previous section indicate that the noise which disrupts the test gas has properties consistent with lateral waves produced in the driver gas. A significant result which confirms the existence of lateral waves in the test gas is displayed in Figures 13A and 13B. Figure 13B is a reproduction of results obtained by Norfleet et.al. (1965) Fig. 26. These figures are the centreline pitot pressure record from different expansion tubes, both of which used air test and acceleration gases.

From Figure 2 it can be seen that the acceleration gas which arrives at

the test section before the test gas would, in general, have a different sound speed to that of the test gas. The steps in Figures 13A and 13B are produced because of this difference in sound speed. To the right of the step is the test gas and to the left is the acceleration gas. In Figure 13A the pitot pressure measured in the acceleration gas is approximately half that in the test gas. Hence, the acceleration gas sound speed is approximately $2^{1/2}$ that of the test gas. Therefore, as the acceleration gas sound speed is greater than the test gas sound speed the interface will act as a filter to lateral waves. From the measured shock speed of 3700 m/s and (4.16⁺) it can be shown that $v_0/v_L \approx 0.2$, hence, a significant band of frequencies will be attenuated.

In contrast, from (4.13) the transmission coefficient for a longitudinal wave would be approximately 1.6. Thus, an increase in the relative size of the disturbance to the unperturbed state should be observed if the disturbance is a longitudinal wave.

From Figures 13A and 13B it is observed that effectively no disturbances are transmitted into the acceleration gas in either facility. Thus, it must be concluded that this disturbance can not be modelled as longitudinal waves, but is consistent with the properties of lateral waves.

7.6 Driver-test gas interface; Argon driver.

In section 7.4 helium was used as a driver gas. As a result the sound speed of the driver gas was relatively high at the throat. In this section expansion tube experiments are presented for an argon driver gas to display the effect that the lower sound speed driver has on the noise transmitted through the interface.

Figure 14B is the centreline pitot pressure record for an argon driver. Table 2 tabulates the properties of the driver and test gases. Due to the lack of shock tube pitot pressure measurements the driver gas properties were obtained assuming the driver gas was adiabatically compressed in the compression tube, as outlined in section 5.

The value of v_L/v_0 for the driver-test gas interface determined from (4.16⁺) and Table 2 is 3.9 compared with 3.23 for the helium driver used for Figure 12B. Hence, a slightly more favorable ratio exists for the argon driver and yet there is significantly more noise in the test gas. This occurs because the argon driver gas sound speed is about one third of the helium driver gas sound speed. Hence, from (4.17) the highest attenuated frequency for the argon driver is approximately one third less

than that of the helium driver. Therefore, the higher frequencies associated with diaphragm rupture are not completely attenuated.

For completeness it should be understood that different driver gas sound speeds at the throat will produce different ranges of frequencies which are incident upon the driver-test gas interface. It is assumed that the frequencies relative to the laboratory produced when the primary diaphragm ruptures are functions of tunnel and diaphragm geometry. Thus, provided these geometries remain the same, the band of frequencies relative to the tunnel which are induced into the driver gas are identical at the throat for all driver gas sound speeds. However, since the Doppler effect on lateral waves is sound speed and gas velocity dependent and not simply Mach number dependent the fundamental frequencies induced into the driver gas at the throat will depend on the sound speed at the throat. This in turn produces a different range of frequencies which will be incident to the driver-test gas interface.

It is assumed that the frequency range 74-125 kHz with a peak at 92 kHz in Figure 11 is produced by the primary diaphragm. Following the above assumptions, for Figure 14B, the primary diaphragm would produce a band of frequencies from 67-117 kHz with a peak at 85 kHz in the shock tube at the driver-test gas interface. The highest attenuation frequency determined from equation (4.16⁺) for this condition is 78 kHz. Hence, it can be seen that only a portion of the diaphragm noise, which does not include the peak, would be attenuated under these circumstances.

Figure 14C was produced by increasing the shock speed in the shock tube by lowering the shock tube filling pressure. There was also a minor change in the driver gas filling pressure. The overall effect is to dramatically increase the highest attenuated frequency. For this condition the primary diaphragm would produce a band of frequencies in the driver gas from 63-107 kHz with a peak at 78 kHz. The highest attenuation frequency determined from (4.16⁺) is 133 kHz. Hence, it can be seen that all the noise would be attenuated at the driver-test gas interface. This is reflected in the experimental results.

An interesting phenomenon occurs in Figure 14A. From Table 2 it would appear that the shock tube conditions for both Figures 14A and 14B are almost identical and yet a vastly different result occurs. The acceleration tube filling pressures were different in the two cases, but it is not believed that this is the cause of the amplification of the noise. It can be seen from Figure 5 that for a given sound speed ratio

across the interface the transmission coefficient peaks when the incident frequency is the lowest unattenuated frequency. For Figure 14A if $\beta_2=0$ then from (4.15) and Table 2, $\beta_1=0.7$. It follows from Figure 5 that the transmission coefficient for the lowest unattenuated frequency is 5.1. Hence, a significant amplification of this frequency occurs. Furthermore, it can be seen from Figure 5 that a small change in β_1 results in a sizable decrease in the transmission coefficient. Therefore, a very unstable situation occurs.

It is interesting to note that for Figure 14A the primary diaphragm would produce a band of frequencies in the range 68-118 kHz with a peak at 86 kHz. The lowest unattenuated frequency is 82 kHz. Hence, the peak frequency is closer to the lowest unattenuated frequency than it is for Figure 14B. Therefore, a possible cause of the large noise in Figure 14A is the strong amplification of the most dominant component of noise produced when the primary diaphragm ruptures.

7.7. Frequency focusing

Expansion tube centreline pitot pressure measurements are shown in Figures 15A and 15B. The sound speed ratios across the expansion centred at the secondary diaphragm are 0.46 and 0.67, respectively, for a perfect gas with $\gamma=1.4$. The conditions upstream of the expansion are the same. From Figure 4 it can be seen that significantly more focusing should occur at the lower sound speed ratio. This is reflected in the experimental results. In Figure 15A it can be seen that a structured disturbance does occur downstream of the expansion, whereas in Figure 15B the disturbance is less structured. If the shock speed prior to secondary diaphragm rupture is used to predict the values of u and a upstream of the expansion then from (4.11), for a perfect gas with $\gamma=1.4$, the period corresponding to a fully focused first order lateral wave is $21\mu\text{s}$. Real gas calculations which assume the flow is frozen within the expansion predict a more strongly focused disturbance, due to the decrease in specific heat ratio, with a period of $25\mu\text{s}$. The measured value taken between $170\mu\text{s}$ and $220\mu\text{s}$ in Figure 15A is $21\pm 2\mu\text{s}$.

The effect of focusing has also been observed in the facilities used by Miller (1977) and Norfleet et.al (1965). The inside diameters of these facilities are 0.152 m and 0.102 m respectively. The inside diameter of the facility which produced Figure 15A is 0.036 m. Figures 15C and 15D are the pitot pressure records obtained by Miller and Norfleet (Fig.25), respectively. For a fully focused first order lateral wave the period of

the disturbance in Miller's experiment should be 104 μ s and in Norfleet's experiment it should be 69 μ s. This compares satisfactorily with the measured values of approximately 100 μ s (average of the period between 130 μ s and 330 μ s, Figure 15C) and 89 μ s (average over the period between 160 μ s and 340 μ s, Figure 15D), respectively.

8. Conclusions

It has been shown that the test time in an expansion tube is limited by the following three mechanisms

(i) The downstream edge of the unsteady expansion centred at the secondary diaphragm,

(ii) the downstream edge of the reflection of the upstream edge of this expansion off the driver-test gas interface and

(iii) noise generated in the driver gas which can be modelled as first order lateral acoustic waves.

Noise which exists in the test gas prior to expansion can be more disruptive if the sound speed drop across the unsteady expansion centred at the secondary diaphragm is sufficient to produce focusing.

Maximum test times are obtained when conditions are chosen so that the expansion and its reflection off the driver-test gas interface arrive simultaneously at the test section. Furthermore, the driver conditions should be chosen so that there is a sufficient increase in sound speed across the driver-test gas interface to filter out the noise in the driver gas. This increase has to be greater when the driver gas sound speed is decreased.

9. Acknowledgements

The authors wish to acknowledge the financial support of NASA Langley Research Center Grant No. NAGW 674. The authors also wish to acknowledge C. Gourlay for his insight into the significance of the reflection of the unsteady expansion off the driver-test gas interface and I. Stringer for his help in gathering data.

Table 1.

Figure	U_{∞} (m/s)	$U_{\infty a}$ (m/s)	U_3 (m/s)	a_3 (m/s)	a_2 (m/s)	P_4 (kPa)	P_7 (Pa)
11A	5270	9200	4814	1588	1164	3.46	16
11B	4800	8970	4325	1572	1327	6.65	17
11B	3650	7640	3291	1138	1672	13.2	16

Table 2.

Figure	P_0 (kPa)	P_4 (kPa)	P_7 (kPa)	U_{∞} (m/s)	U_3 (m/s)	M_3	M_2
12A	125	13.7	17	2050	1714	1.98	2.76
12B	130	13.7	32	2000	1668	1.96	2.70
12C	120	3.46	33	2350	1995	2.12	3.79

10 References

Godunov, S.K.

1959, A difference method for numerical calculation of discontinuous solutions of the equation of hydrodynamics. Mat. Sb. (N.S.) 47 (89) pp.271-306.

Levine, M.A.

1970, Turbulent mixing at the contact surface in a driven shock wave. Phys. Fluids, 13, pp.116-1171.

Liepmann, H.W. and Roshko, A.

Elements of Gas Dynamics, pp 149 (Wiley, N.Y., 1967).

Lordi, J.A., Mates, R.E., and Moselle, J.R.

1966, Computer program for numerical solution of nonequilibrium expansions of reacting gas mixtures. NASA CR-472.

McIntosh, M.K.

1968, Computer program for the numerical calculation of frozen and equilibrium conditions in shock tunnels. Dept. of Physics, A.N.U. Canberra Aust. (Modification of code produced by Lordi et.al (1966)).

Miller, C.G.

1977, Operational experience in the langley expansion tube with various test gases. Fig. 6, $p_{10}=15 \mu\text{m}$. NASA Tech. Mem. 78637, Dec.

Mirels, H.

1964, Shock tube test time limitation due to turbulent-wall boundary layer. Vol 2, No.1 AIAA pp.84-93.

Norfleet, G.D, Lacey, Jr, J.J., Whitfield, J.D.

1965, Results of an experimental investigation of the performance of an expansion tube. 4 Th. Hypervelocity Tech. Symp., A.E.D.C. Tullahoma, Tennessee, Nov. pp.49-110.

Paull, A. and Stalker, R.J.

1991, The Effect on an acoustic wave as it tranverses an unsteady expansion. To be published in Phys. Fluids A.

Stalker, R.J.

1966, The free piston shock tunnel. Aeronautical Quarterly, V17. pp.351-370.

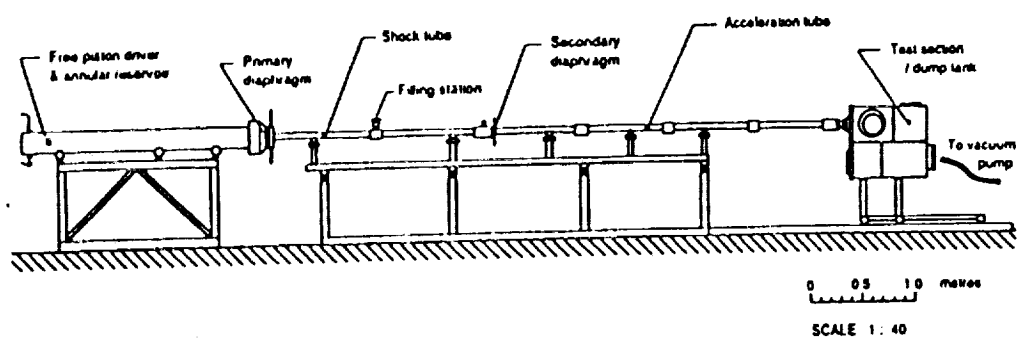
Trimpi, R.L.

1962, A Preliminary theoretical study of the expansion tube, a new device for producing high-enthalpy short-duration hypersonic gas flows. NASA TR R-133.

Whitham, G.B.

Linear and Nonlinear Waves, pp.157,158 (Wiley, N.Y., 1974).

Figure 1. Schematic of an expansion tube.



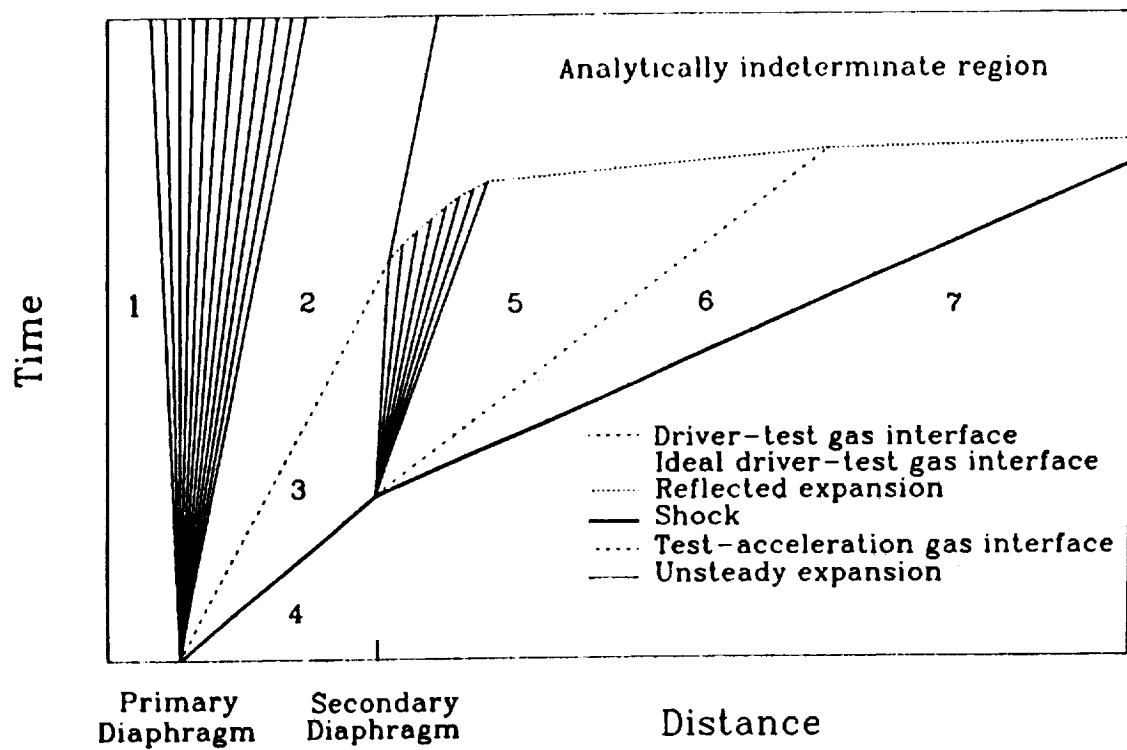


Figure 2. X-t diagram for an expansion tube.

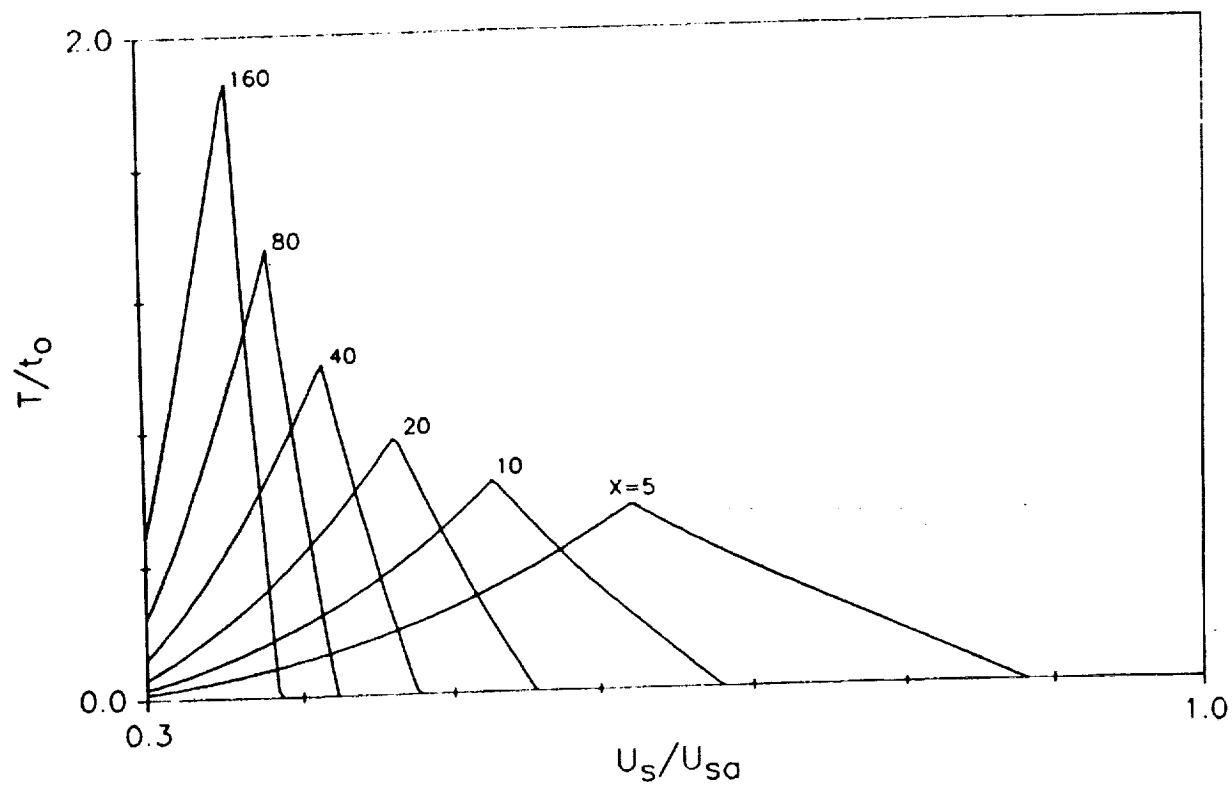


Figure 3. Nondimensional test time for different nondimensional acceleration tube lengths as a function of the ratio of shock speeds in the shock and acceleration tubes for strong shocks with $\gamma=1.4$.

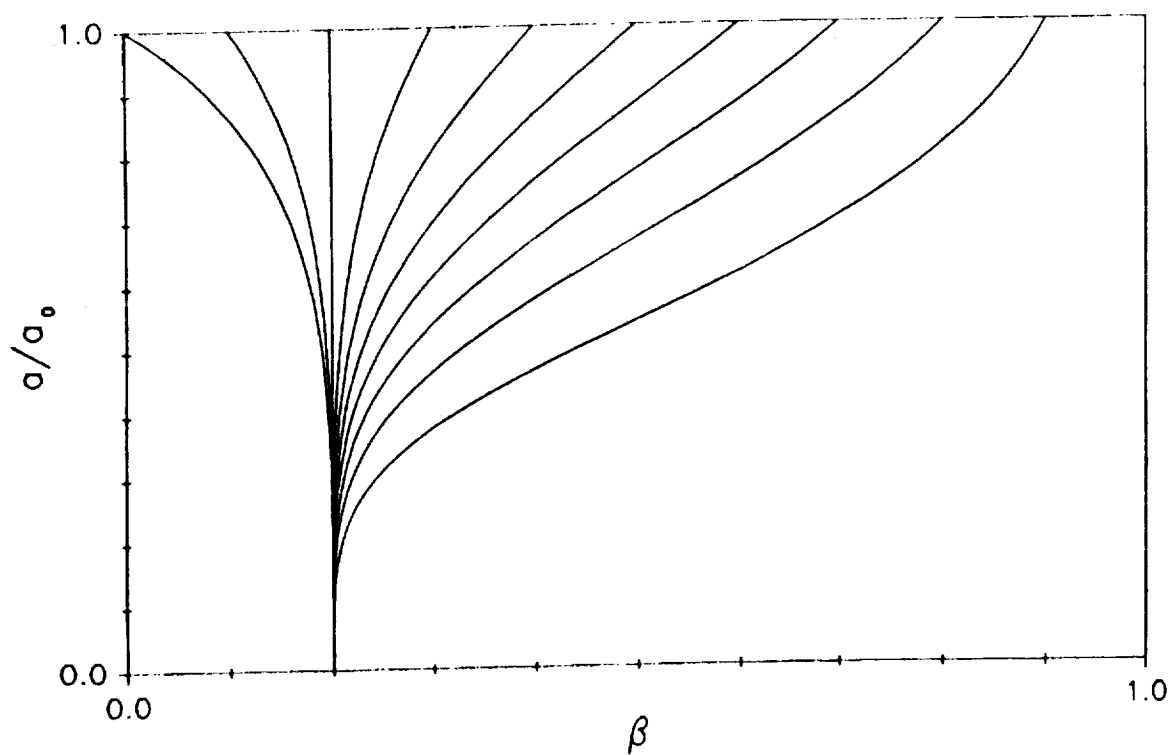


Figure 4. Dispersive term as a function of sound speed ratio across a centred unsteady expansion for different initial values of the dispersive term. $\gamma=1.4$.

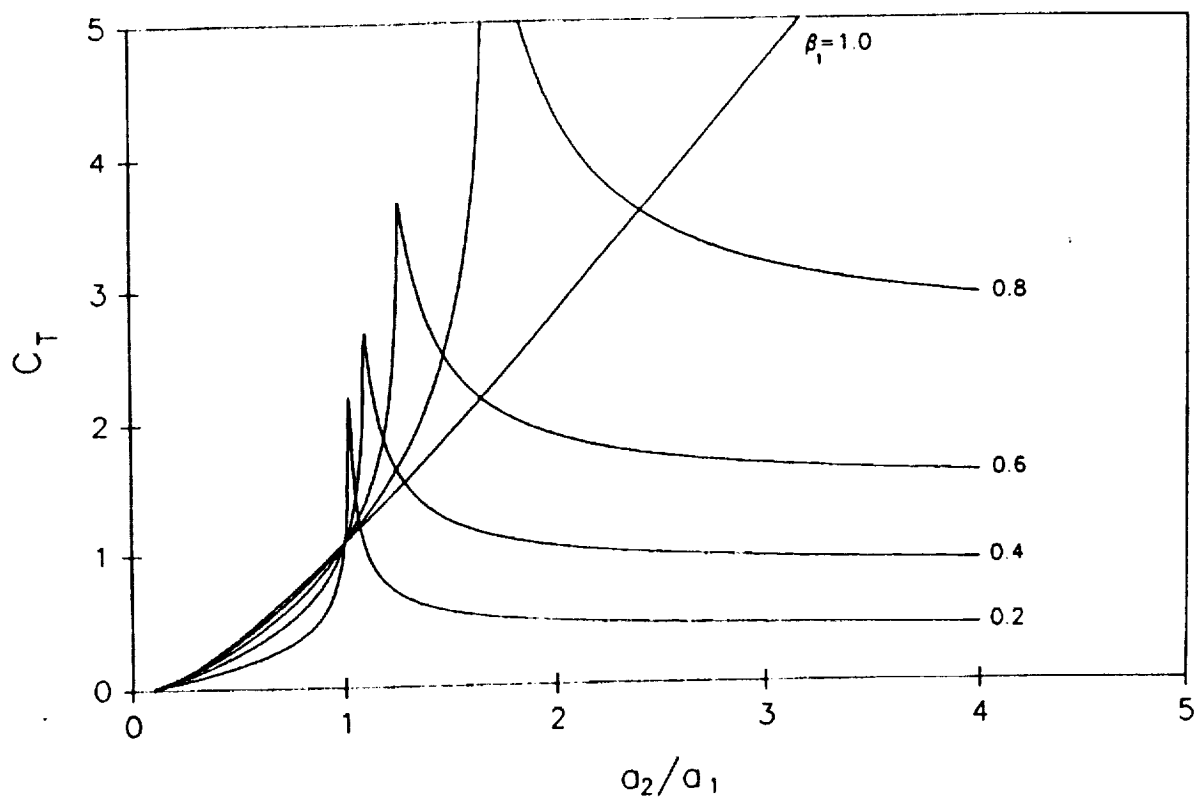


Figure 5. Transmission coefficients for different dispersive terms as a function of sound speed ratio across an interface. $\gamma_1=5/3$. $\gamma_2=7/5$.

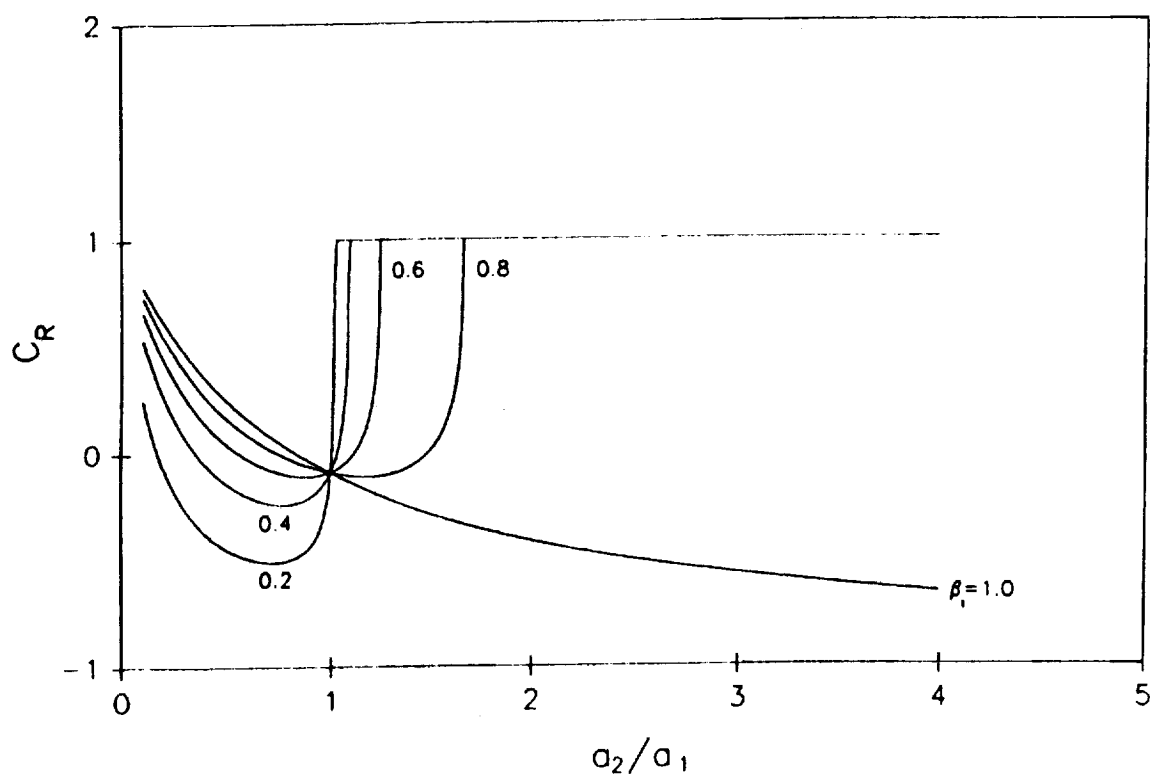


Figure 6. Reflection coefficients for different dispersive terms as a function of sound speed ratio across an interface. $\gamma_1=5/3$. $\gamma_2=7/5$.

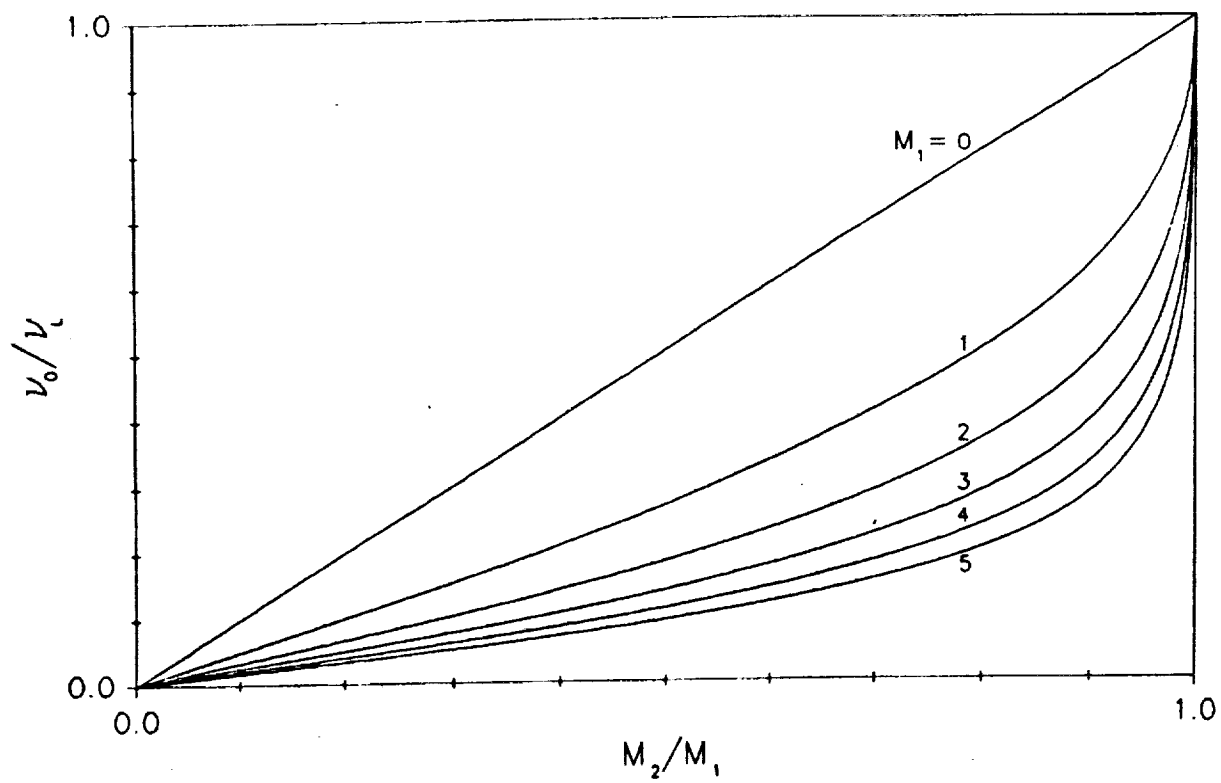


Figure 7. The ratio of the lowest possible lateral wave frequency to the lowest frequency lateral wave which does not decay when transmitted, as a function of local Mach number ratio across the interface, for different values of the local Mach number of the incident region.

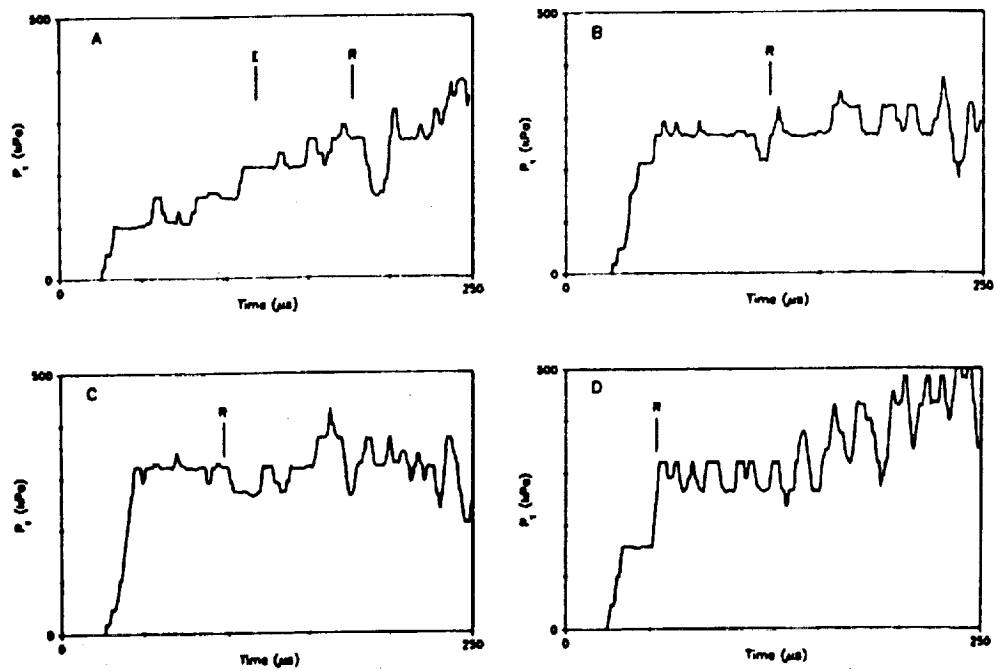


Figure 8A-8D. Expansion tube centreline pitot pressure records. Argon driver, air test and acceleration gases, $P_0=130$ kPa, $P_1=34.5$ Mpa, $P_4=3.4$ kPa, $U_g=2400$ m/s.

A. $P_7=5.4$ Pa. B. $P_7=16$ Pa C. $P_7=26$ Pa. D. $P_7=66$ Pa.

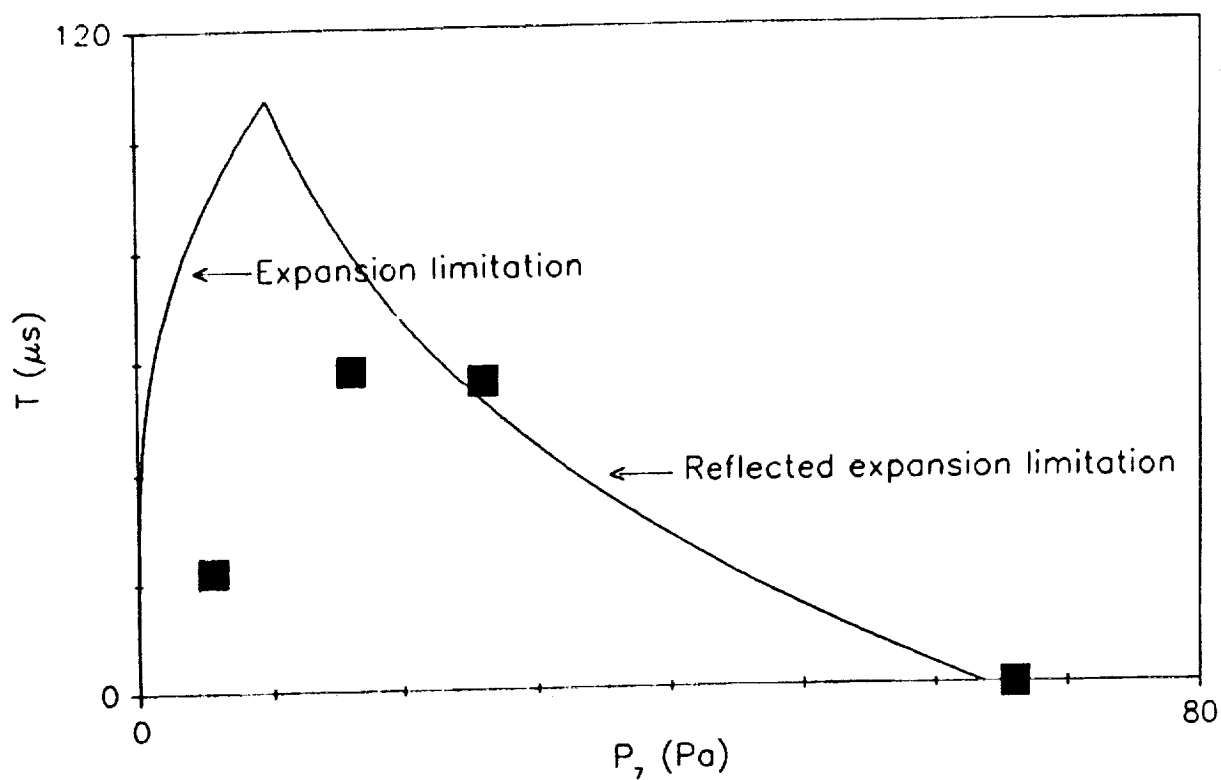


Figure 9. Test time as a function of acceleration tube filling pressure. Air test and acceleration gases. Squares: -Test time as measured from Figure 8. $P_4=3.4$ kPa. $U_s=2400$ m/s. $\gamma=1.4$. $r_0=18$ mm. $x_s=3.18$ m. $x_a=2.08$ m.

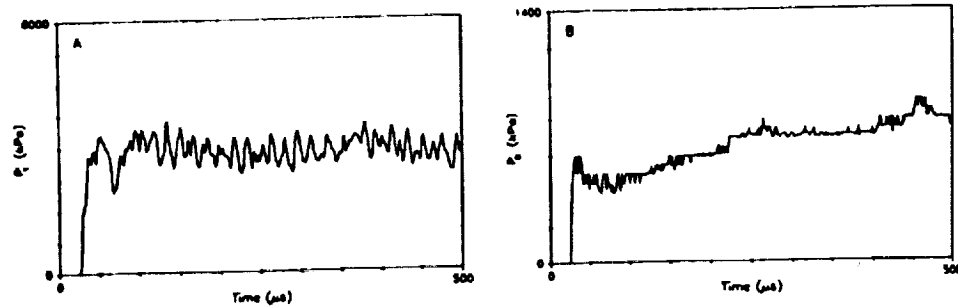


Figure 10A-10B. Shock tube centreline pitot pressure and static pressure records. Helium driver, air test and acceleration gases. $P_0=130$ kPa. $P_1=34.5$ MPa. $U_g=4000$ m/s. $P_4=2.66$ kPa.

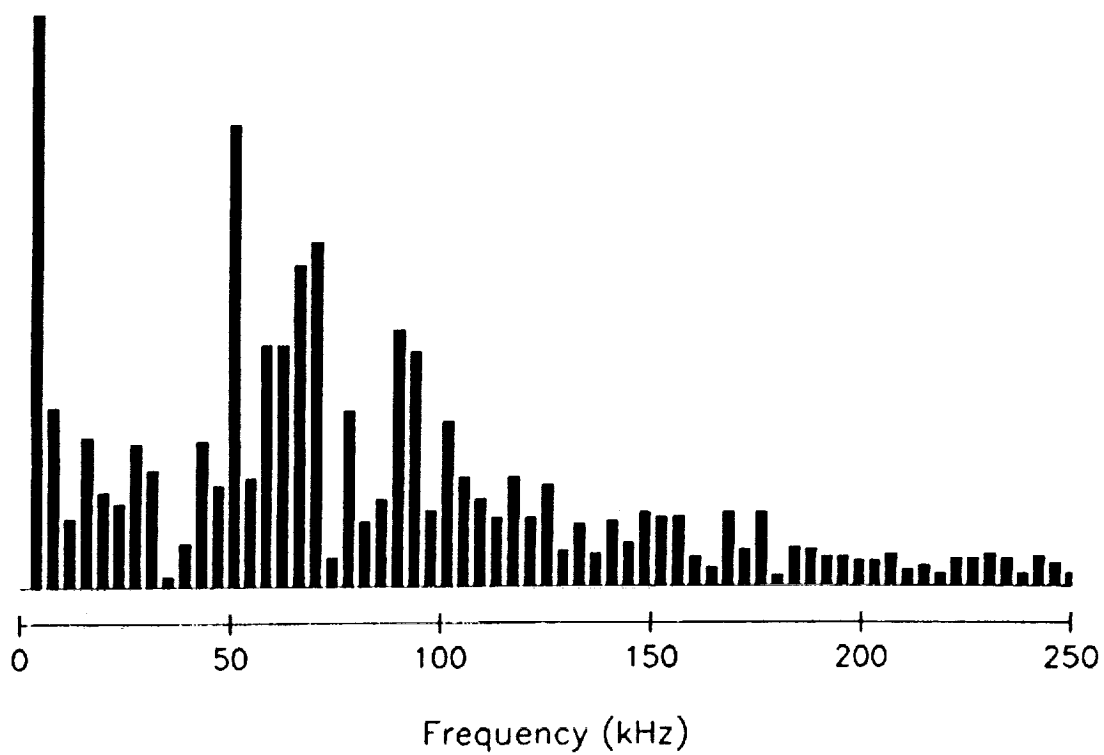


Figure 11. Spectral decomposition of pitot record Figure 10A between 200 and 456 μ s after shock.

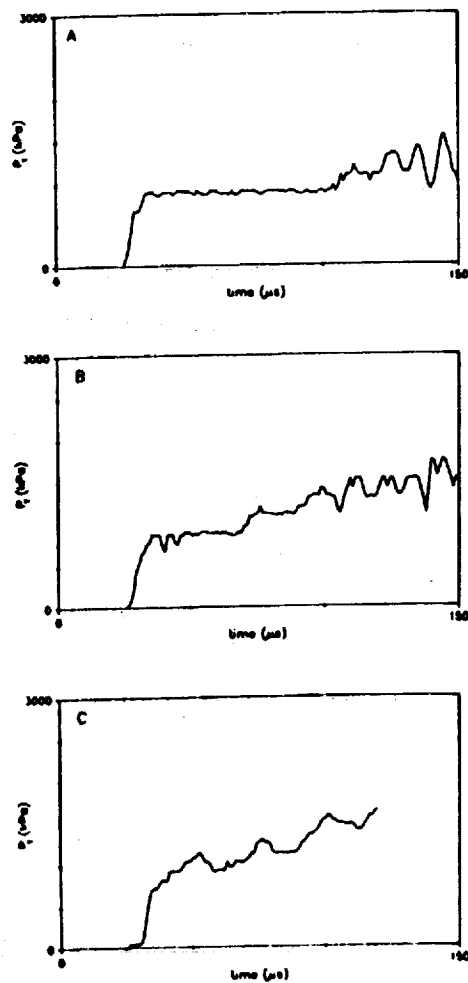


Figure 12A-12C. Expansion tube centreline pitot pressure measurements. Helium driver, air test and acceleration gases. $P_0=130$ kPa. $P_1=34.5$ Mpa. See Table 1.

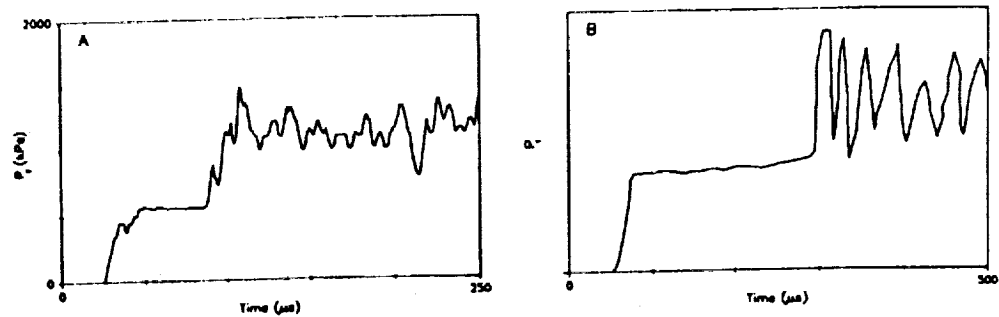


Figure 13A-13B. Expansion tube centreline pitot pressure measurements displaying the effect of the test-acceleration gas interface on the noise.

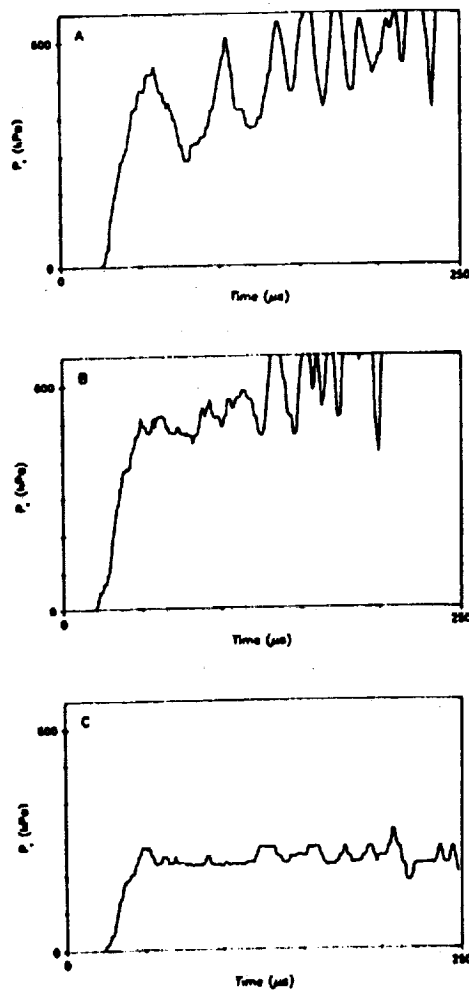


Figure 14A-14C. Expansion tube centreline pitot pressure measurements. Argon driver gas, air test and acceleration gases. $P_1=34.5$ Mpa. See Table 2.

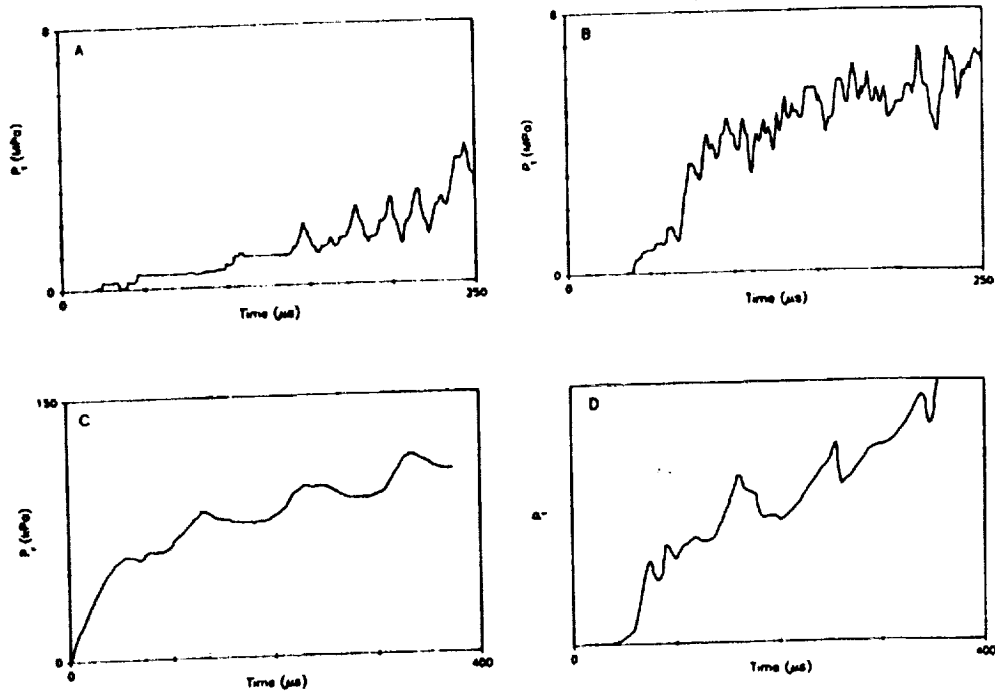


Figure 15A-15D. Expansion tube centreline pitot pressure measurements.
Air test and acceleration gases.

- 15A. $U_g=2410$ m/s. $U_{ga}=5970$ m/s. $a_3/a_5=0.46$. $r_0=0.018$ m
15B. $U_g=2500$ m/s. $U_{ga}=4680$ m/s. $a_3/a_5=0.67$. $r_0=0.018$ m

... ..

LEEWARD HEAT TRANSFER COMPARISON BETWEEN T4 DATA AND STS-3 FLIGHT DATA

by

Robert M Krek & R.J. Stalker

When the United States Space Orbiter first reentered the Earth's atmosphere, a forward shift in the center of pressure was experienced. To compensate for this shift the Orbiter body flap was deflected to twice the angle predicted.

Preflight predications of the orbiter aerodynamics were based on extensive wind tunnel tests, which were then extrapolated to flight conditions via the use of analytical and CFD methods. These methods were unable to simulate the real gas aerodynamics that the Orbiter experienced.

The T4 Shock Tunnel is a facility that is able to simulate the enthalpies and pressures that are experienced in the reentry to Earth's atmosphere from Low Earth Orbit. The experiments were conducted on a scale model of the Orbiter (1:185). The model was tested at various Reynolds numbers, Stagnation enthalpies and angles of incidence.

The data is then compared with conventional wind tunnel data and results obtained from the flights of the Shuttle Orbiter. In this report the leeward surface heat transfer results obtained from T4 experiments are compared with STS-3 results for $\alpha = 40^\circ$ (α is the angle of incidence).

Figure 1 shows plots comparing flight data with T4 data for turbulent and laminar leeward flow. Figure 1a shows the turbulent case, plotting $q/q_\infty Re_{NS}^{0.3}$ versus x/L , where q_∞ is the stagnation point heat transfer to a scaled one foot radius sphere and Re_{NS} is the normal shock Reynolds number. The results are plotted as $q/q_\infty Re_{NS}^{0.3}$ to remove the dependence of Reynolds number. Flight data was available (Throckmorton and Zoby) at stagnation enthalpies of 9.9 and 6.5 MJ/kg and compared with tunnel data at a stagnation enthalpy of 8.1 MJ/kg. With the Reynolds number dependence removed, it can be seen that the tunnel and flight data are consistent for a turbulent leeward flow (figure 1a).

Figure 1b shows plots for a laminar leeward flow in which the normalised heat transfer is independent of Reynolds number, and therefore q/q_∞ is plotted in figure 1b. The flight laminar flow data is available only at the high stagnation enthalpies (28.6 & 16.3 MJ/kg) and is consistent with T4 data obtained at 2.7 and 6.0 MJ/kg. The last measuring stations for the T4 results suggest that transition to a turbulent flow is occurring. The high stagnation enthalpy case for the T4 results

(24.7 MJ/kg) seem to indicate that transition has occurred, but it is believed that a laminar flow still exists for this condition and is being investigated at this time.

Comparison between flight and T4 results for both a turbulent and laminar leeward flows are shown to be consistent. The T4 shock tunnel can therefore be seen to be a reliable facility in which to simulate reentry flows from Low Earth Orbit similar to those experienced by the Shuttle Orbiter.

REFERENCE

Throckmorton, D.D., & Zoby, E.V., 1983 *Orbiter Entry Leaside Heat Transfer Data Analysis*. J. Spacecraft & Rockets, Vol. 20, No. 6, pp. 524-530.

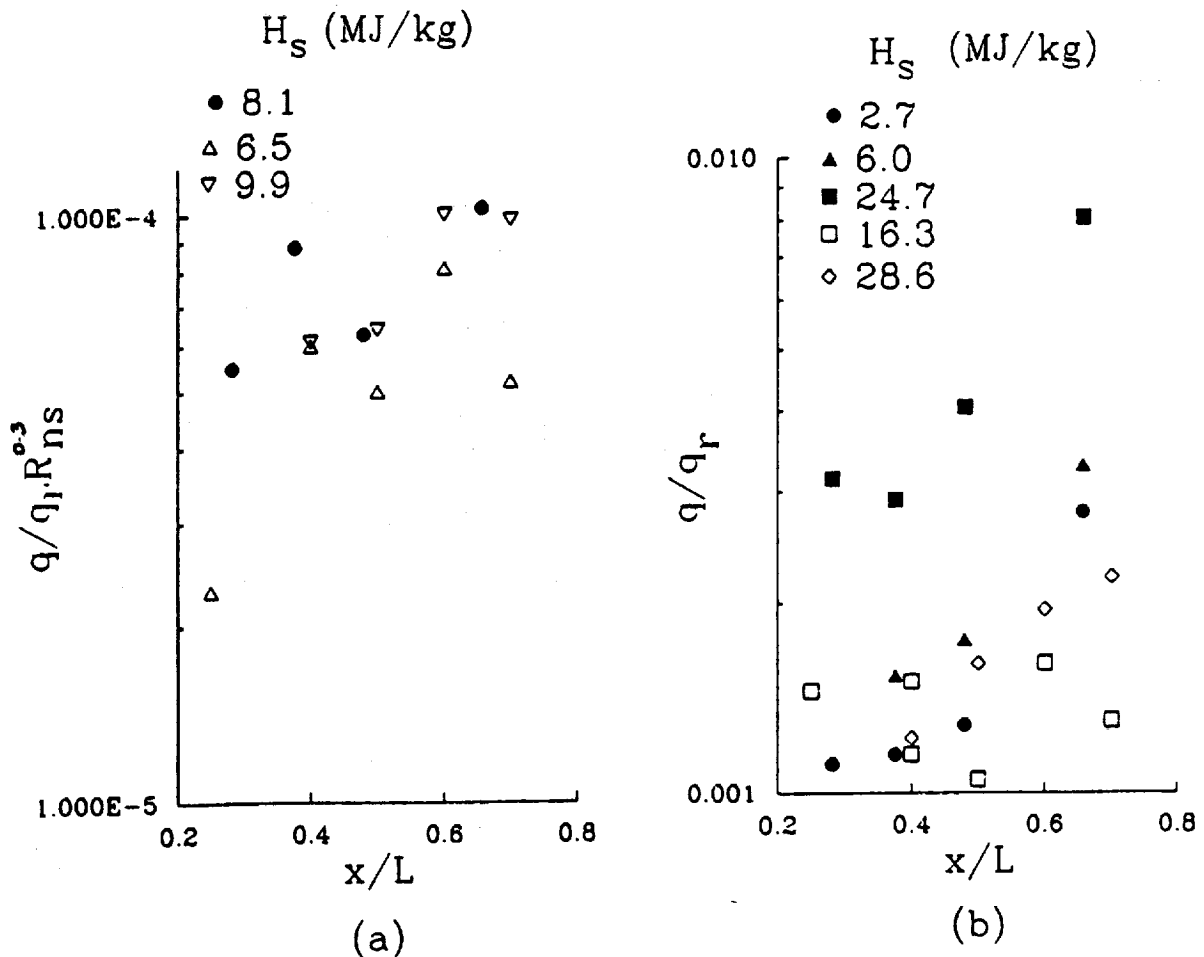


Figure 1 Leeward Heat Transfer - Comparison with Flight.
Filled Symbols - T4 Data. Open Symbols - STS-3.
(a) Turbulent Flow. (b) Laminar Flow.

REPORT DOCUMENTATION PAGE			Form Approved OMB No. 0704-0188	
Public reporting burden for this collection of information is estimated to average 1 hour per response, including the time for reviewing instructions, searching existing data sources, gathering and maintaining the data needed, and completing and reviewing the collection of information. Send comments regarding this burden estimate or any other aspect of this collection of information, including suggestions for reducing this burden, to Washington Headquarters Services, Directorate for Information Operations and Reports, 1215 Jefferson Davis Highway, Suite 1204, Arlington, VA 22202-4302, and to the Office of Management and Budget, Paperwork Reduction Project (0704-0188), Washington, DC 20503.				
1. AGENCY USE ONLY (Leave blank)		2. REPORT DATE February 1993		3. REPORT TYPE AND DATES COVERED Contractor Report, CY 1990
4. TITLE AND SUBTITLE Shock Tunnel Studies of Scramjet Phenomena, Supplement 6			5. FUNDING NUMBERS 505-70-62-02 NAGW-674	
6. AUTHOR(S) M. Wendt, M. Nettleton, R. G. Morgan, K. Skinner, R. Casey, R. Stalker, C. Brescianini, A. Paull, G. Allen, M. Smart, N. Akman, N. Ward, S. Tuttle, J. Simmons, S. Sanderson, G. Kelly, A. Neely, R. Krek				
7. PERFORMING ORGANIZATION NAME(S) AND ADDRESS(ES) University of Queensland Department of Mechanical Engineering St. Lucia, Queensland AUSTRALIA			8. PERFORMING ORGANIZATION REPORT NUMBER	
9. SPONSORING / MONITORING AGENCY NAME(S) AND ADDRESS(ES) National Aeronautics and Space Administration Langley Research Center Hampton, VA 23681-0001			10. SPONSORING / MONITORING AGENCY REPORT NUMBER NASA CR-191428	
11. SUPPLEMENTARY NOTES Langley Technical Monitor: R. Clayton Rogers Interim Report 0 Supplement 6, NAGW-674				
12a. DISTRIBUTION / AVAILABILITY STATEMENT Unclassified - Unlimited Subject Category 34			12b. DISTRIBUTION CODE	
13. ABSTRACT (Maximum 200 words) Reports by the staff of the University of Queensland on various research studies related to the advancement of scramjet technology are presented. These reports document the tests conducted in the reflected shock tunnel T4 and supporting research facilities that have been used to study the injection, mixing, and combustion of hydrogen fuel in generic scramjets at flow conditions typical of hypersonic flight. In addition, topics include the development of instrumentation and measurement technology, such as combustor wall shear and stream composition in pulse facilities, and numerical studies and analyses of the scramjet combustor process and the test facility operation. This research activity is Supplement 6 under NASA Grant NAGW-674.				
14. SUBJECT TERMS Scramjets, pulse facilities, hypersonic, hypervelocity, shock waves, combustion, shock tubes			15. NUMBER OF PAGES 279	
			16. PRICE CODE A13	
17. SECURITY CLASSIFICATION OF REPORT Unclassified	18. SECURITY CLASSIFICATION OF THIS PAGE Unclassified	19. SECURITY CLASSIFICATION OF ABSTRACT Unclassified	20. LIMITATION OF ABSTRACT	